Sheffield Hallam University

The Adaptation of a Millifluidics System for Ex Vivo Drug Absorption Studies

SPENCER, Chloe Elizabeth

Available from the Sheffield Hallam University Research Archive (SHURA) at:

https://shura.shu.ac.uk/34336/

A Sheffield Hallam University thesis

This thesis is protected by copyright which belongs to the author.

The content must not be changed in any way or sold commercially in any format or medium without the formal permission of the author.

When referring to this work, full bibliographic details including the author, title, awarding institution and date of the thesis must be given.

Please visit https://shura.shu.ac.uk/34336/ and http://shura.shu.ac.uk/information.html for further details about copyright and re-use permissions.

The Adaptation of a Millifluidics System for Ex Vivo Drug Absorption Studies

Chloe Elizabeth Spencer

A thesis submitted in partial fulfilment of the requirements of Sheffield Hallam University for the degree of Doctor of Philosophy

The work in this thesis was carried out in collaboration with CRODA Inc, USA.

June 2024

Candidate Declaration

I hereby declare that:

1. I have not been enrolled for another award of the University, or other academic or professional organisation, whilst undertaking my research degree.

2. None of the material contained in the thesis has been used in any other submission for an academic award.

3. I am aware of and understand the University's policy on plagiarism and certify that this thesis is my own work. The use of all published or other sources of material consulted have been properly and fully acknowledged.

4. The work undertaken towards the thesis has been conducted in accordance with the SHU Principles of Integrity in Research and the SHU Research Ethics Policy.

5. The word count of the thesis is 53,701.

Name	Chloe Elizabeth Spencer
Award	PhD
Date of Submission	11/06/2024
Research Institute	Health & Wellbeing
Director(s) of Studies	Professor Malcolm Clench Dr Vikki Carolan

Dedicated in loving memory to

Ernest Albert Spencer

1929 - 2024

Acknowledgments

Throughout my university years I had often voiced that I wanted to complete a PhD before I turned 30 years old. However, the decision to apply for this PhD project was a difficult one for me; with a previous PhD rejection already and a major hint of imposter syndrome creeping in, I was doubtful that I would be accepted for the position. I want to firstly thank my partner, Ryan Walters and the university girls Charlotte Cowell, Natalie Carter and Courtney Allen for their unwavering support and encouragement that helped me take the leap and apply (and get through the interview preparations!!).

I want to express my utmost gratitude to Professor Malcolm Clench, Dr Catherine Duckett, Stephen Rumbelow and Steve Mellor for believing in me and trusting me with this project. I would also like to thank the BBSRC and CRODA for the funding and scholarship which made this PhD a possibility for me.

I am indebted to my support system back home who have been my backbone throughout all of my endeavours, not just the PhD. To the best Mum and Dad, thank you for the constant encouragement, keeping me level-headed and taking my incessant phone calls to rant and ramble. I hope that I make you proud. To my girls, Chloe Hodson and Courtney Aitken, thank you for understanding the stress and busy schedules over the last few years but sticking by me no matter what. To my uni girls, thank you for always having my best interests at heart and letting me know when I'm overdoing it. I am so lucky to have the most amazing friends who show me nothing but love and support. For organising the perfect distractions that seem to melt all stress away. To my loving partner Ryan, I can't thank you enough for sticking by me all these years (you should be the one getting a PhD for that alone). Thank you for putting up with the late nights, the stress, the nervous retching, relentless perfectionism and everything in between. Thank you for making my PhD that bit easier, being my housemaid and private chef at times. I am so lucky to have such a supportive group of loved ones, that I can count on to pick me up when I'm down and celebrate my wins. I really couldn't do it without you all by my side.

I would like to thank all of the PhD students and technical staff for making my time in the BMRC a pleasant one despite being on the rollercoaster that is a PhD. I have been lucky enough to meet and get to know some amazing people over the years that have made the experience a memorable and enjoyable one from nights out to conferences. I would like to give special acknowledgements to my lab-partner in crime Josh Millar for keeping me sane as well as, Kelly Capper-Parkin, Muna Nuh Ali, Tim Wooton, Joe Ready, Amy Grayson, Lucy Dascombe and Madalena De Oliveria for their moral support and friendship over the years. Thank you to everyone that has listened to me venting, its been a tremendous help in getting me through hard times which I am so grateful for. I would like to acknowledge Josh, Madalena, Cristina Russo, Cameron Heaton, Lucy Flint, Rohith Krishna, Sophie Pearce and Veronika Tibljas for all of your

help and support within the lab. From the technical team, I would like to give special acknowledgements to Jonathan Foster, Jef Clark, Mick Cox and Celine Soulihol for all of your invaluable help and support in the lab. The lab would simply not function without you all, you are a true credit to the BMRC. Thank you for not only the tremendous technical support but also the knowledge and tricks that I have learnt from you all over the years.

I want to give a massive thanks to Dr Catherine Duckett for her time as my second supervisor. You were always my inspiration for 'women in science' before the PhD and became an important confidant and friend throughout it. While I'm gutted you didn't get to see me through to the end, I'm thankful for your support and caring nature which helped me greatly on my PhD journey. I would also like to thank Dr Vikki Carolan for seamlessly stepping into my project and supporting me when you weren't expected to.

I cannot express enough how thankful I am to Professor Malcolm Clench who went above and beyond the requirements of a supervisor and was a pillar of support and encouragement in the hardest period of my life. It goes without saying that I would have crumbled without your patience and understanding through my (many) tears. Your moral support not only guided me through those tough times but helped me to secure a PhD at the same time; for that, I will be forever grateful. I want to thank you for your advice and mentoring which has undoubtedly moulded me into the strong person I am now who can handle absolutely anything (once I've cried it out my system). All seriousness aside, I am assuming that I will remain the only student you've had to play 'God is a DJ' for to distract from crying. I hope that some of my 'Chloeisms' have made up for the spell of doom and gloom that appeared to follow me for a while. All I am going to say is that I hope when you hear 'macho man' playing, you think of me!!

Finishing my PhD will always be bittersweet for me; reflecting on the (ridiculous amount of) unfortunate circumstances that made my PhD inevitably more challenging but also, realising (and admiring) a newfound strength and resilience I didn't know I was capable of. I remember those who were there cheering me on from the beginning but unfortunately couldn't be there to see me through to the end. To Dave, the only person who has made me feel every emotion under the sun yet still holds a large part of my heart. It still hasn't hit home that you won't be here to torment me with the nickname 'Dr Big Arms' (you started that a little prematurely) but I want to thank you for forcing me to discover my inner resilience, although I'd much rather you were still here. Last but not least, I would like to thank my Grandad. I hope that you realised the impact that you had on my pursuit for further education and my drive to keep pushing with my career. I miss the excitement and pride when you spoke of my courses and future plans which motivated me to push myself harder. Even in the most difficult times, I never truly considered quitting as telling you I'd given up was something I couldn't bear. We talked of dedicating my thesis to you on your birthday; I was so excited to tell you I'd made it and that you were the inspiration and driving force for this chapter of my life. As promised, this one's for you.

i. Abstract

Before human trials are feasible, all drugs and their excipients must undergo vigorous scrutiny to assess potential health implications, safety, dosage and efficacy. Traditionally in all stages of drug research and development, the most predominant means of testing new drugs and formulations was by the in vivo study of animals. As time has progressed, the use of animals in research has become less accepted by society. A shift in public opinion ultimately led to a ban on testing cosmetic products and ingredients on animals. The clear sign of changing times has seemingly had an effect on many researchers in the pharmaceutical field who are turning their focus to developing and optimising animal-free models. An impressive 60% of the global market is accounted for by oral dosage forms; however, the complexity of the oral drug absorption route is difficult to replicate and has led to the development of many different types of gastrointestinal (GI) models. The choice of GI model is heavily debated among researchers with each model carrying its own benefits and limitations. Here, a modified millifluidics device containing viable ex vivo tissue combined with mass spectrometry imaging (MSI) and liquid chromatography tandem mass spectrometry (LC-MS/MS) has demonstrated its potential to be a useful workflow in drug absorption studies. The combination of MSI and LC-MS/MS has been used to explore the absorption of atorvastatin through porcine intestinal tissue along with the influence of relevant excipients. The adapted system has demonstrated the effect of excipients such as Mapcho-12 and DEGEE under different pH environments. The current adaptations made to the system pave the way for comparative studies to be performed within the same system using more valuable animal-free alternatives such as organoids and human biopsies. In turn, the model could help to bridge the gap for researchers exploring animal-free models. Further work has been identified to further improve the system which should be carried out before moving to more precious samples. The modular nature of the commercial system allows for further easy modifications to be made.

ii. Contents

iii. List of Figures

iv. List of Tables

v. Abbreviations

α-CHCA: α-Cyano-4-hydroxycinnamic acid

µg: Microgram

µL: Microlitre

µm: Micrometre

2D: Two dimensional

3D: Three dimensional

ACN: Acetonitrile

API: Active pharmaceutical ingredient

ATP: Adenosine triphosphate

au: Arbitrary units

BCS: Biopharmaceutics classification system

Caco-2: Colorectal adenocarcinoma

Calcein-AM: Calcein acetoxymethyl ester

CEM: Chain ejection model

CFD: Computational fluid dynamic

cm^2: Centimetre squared

cm/s: Centimetre per second

CO_2: Carbon dioxide

CRM: Charge reduction model

CYP: Cytochrome

d5: Deuterated by 5

Da: Dalton

DAPI: 4′,6-diamidino-2-phenylindole

DC: Direct current

DEGEE: Diethylene glycol monoethyl ether

DESI: Desorption electrospray ionisation

DHB: 2,5-Dihydroxybenzoic acid

DMEM/F12: Dulbecco's Modified Eagle Medium / Nutrient Mixture F-12

DP: Drug product

EFP: Encoded frequent pushing

ESI: Electrospray ionisation

EU: European Union

FBS: Fetal bovine serum

FNA: Fine needle aspiration

GI: Gastrointestinal

h: hour

H_2O_2: Hydrogen peroxide

HMG-CoA: 3-hydroxy-3-methyl-glutharyl-coenzyme A

HT29-MTX: Human colorectal adenocarcinoma methotrexate

IEM: Ion evaporation model

ITO: Indium tin oxide

IV: Intravenous

KRS: Bicarbonate-buffered krebs-ringer solution

LC: Liquid chromatography

LC-MS/MS: Liquid chromatography tandem mass spectrometry

LDH: Lactate dehydrogenase

LSE: Living skin equivalent

M: Molar

m/z: Mass-to-charge

mg: Milligram

mM: Millimolar

mm: Millimetre

mL: Millilitre

MALDI: Matrix-assisted laser desorption ionisation

MDa: Megadalton

$MgSO_4$: Magnesium sulphate

MRM: Multiple reaction monitoring

MRT: Multi reflecting time-of-flight

MS: Mass spectrometry

MSI: Mass spectrometry imaging

MTBE: Methyl-Tert-Butyl Ether

NaCl: Sodium chloride

nm: Nanometre

P_{app}: Apparent permeability index

P_{eff}: Effective permeability

PBS: Phosphate-buffered saline

PFA: Paraformaldehyde

PI: Propidium iodide

ppm: Parts per million

QMSI: Quantitative mass spectrometry imaging

QV600 LLI: Quasi Vivo 600 liquid-liquid interphase

QWBA: Quantitative whole-body autoradiography

RF: Radio frequency

ROI: Region of interest

rpm: Revolutions per minute

SNEDDS: Self-nanoemulsifying drug delivery system

TEER: Trans-epithelial electrical resistance

TOF: Time-of-flight

UV: Ultra-violet

v/v: Volume to volume

w/v: Weight to volume

×g: G force

Chapter 1:

Introduction

1.1 Oral Drug Absorption Route

A substantial portion of the global market is accounted for by the pharmaceutical industry, with its worth estimated to be several hundreds of billions of pounds and climbing (*Global pharmaceutical industry - statistics & facts.* 2019). Of the numerous dosage forms available, it has been reported that over 60% of drugs on the market are of an oral dosage form (Masaoka et al., 2006). Oral drugs boast a high patient compliance which is undoubtedly related to the painless and non-invasive nature of the route (Lin & Wong, 2017). The popularity of oral administration is shared by patients and healthcare providers alike. For both parties, oral drugs are highly convenient as they allow self-administration which does not require the assistance of a trained professional or the need for a hospital visit (Abuhelwa et al., 2017).

Compared to administration routes such as intravenous (IV) injection, the oral administration route is very complex. For IV injection, the drug is delivered directly to the blood stream whereas oral drugs must overcome many obstacles before reaching systemic circulation. Oral drugs enter via the oral cavity and travel through the gastrointestinal (GI) tract. In order of procession, the GI tract consists of the oral cavity, pharynx, oesophagus, stomach, small intestine, large intestine and rectum. The small intestine alone accounts for a staggering 297-1056 cm of the GI tract (Homayun et al., 2019). The already vast surface area of the small intestine lumen is further increased by the presence of transverse folds known as plicae circulares; these are shown schematically in Figure 1.1. Due to the large surface area and high residence time in this organ, most drug absorption occurs in the small intestine.

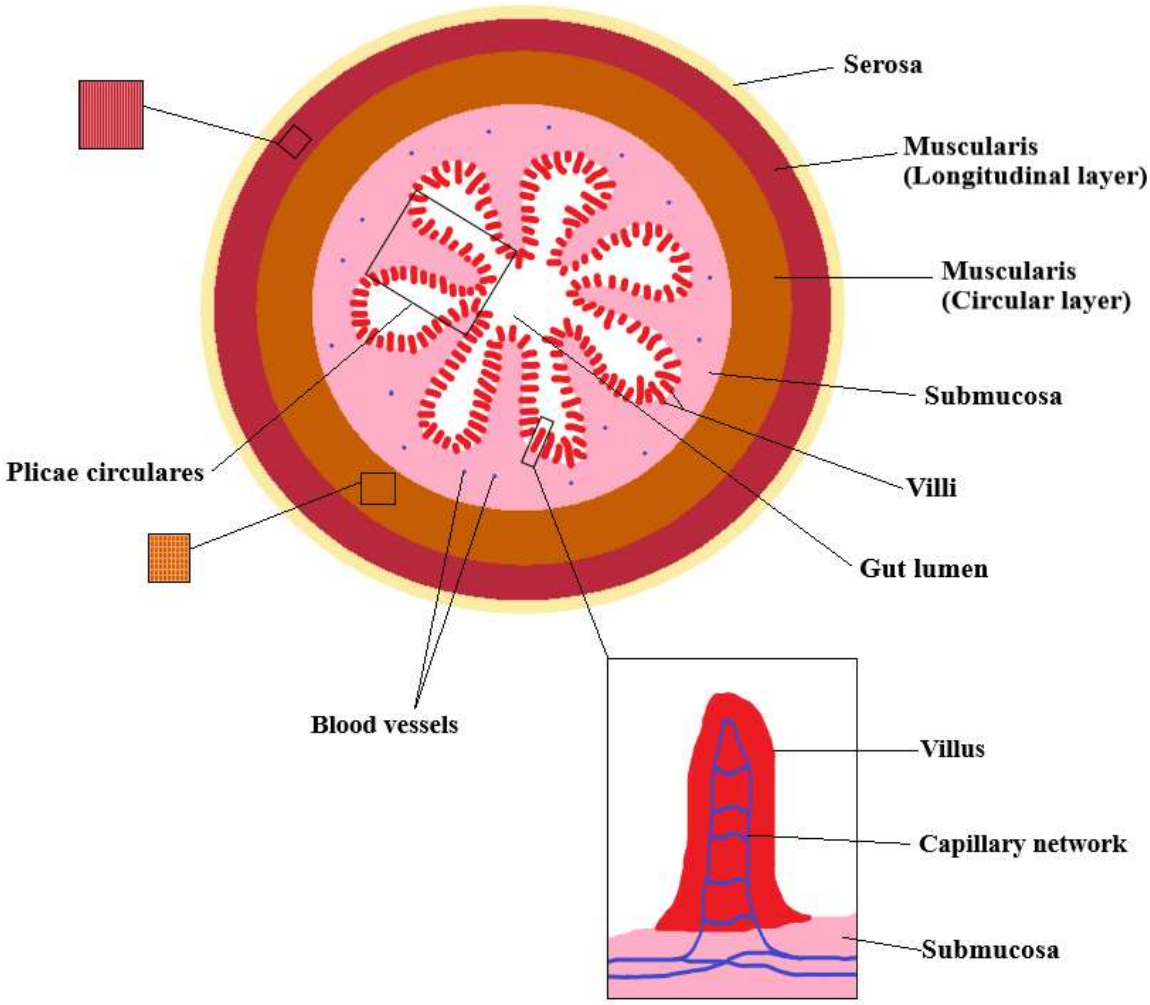

Figure 1.1: *A cross-section of the small intestine showing the key layers and circular folds known as plicae circulares as well as the capillary network in the villi and submucosa.*

Regardless of the large absorptive area and ample opportunity, the absorption of oral drugs can be greatly hindered if not formulated correctly. Before reaching the small intestine, oral drugs must navigate through several, hollow organs, all of which serve different functions and thus, differ in structure and environment. As a consequence of this, oral drugs face a host of challenges and biological barriers that fluctuate along the GI tract. Many of the fluctuating environmental factors experienced along the GI tract heavily influence drug absorption and integrity (Homayun et al., 2019).

Extreme fluctuations in the luminal pH occur along the GI tract and pose as a significant biological barrier to oral drugs. Once the drug has passed the neutral environment in the oral cavity and oesophagus, it will enter the stomach. In this organ, the presence of stomach acid and other gastric juices create extremely acidic conditions as low as pH 1

(Homayun et al., 2019). The low pH causes oral drugs to denature and thus, reduces the amount of drug that has reached its site of action. In addition to this, oral drugs can also become denatured by digestive enzymes such as pepsin which are found in the gastric acid. Further luminal enzymes such lipase and protease are present in the GI tract; these are secreted into the small intestine via the pancreas (Qiu et al., 2017). The purpose of luminal enzymes is to break down molecules for digestion however, they can also cause some drug classes to be released early which in turn, would reduce the amount of drug that has reached its site of action (Qiu et al., 2017). The small intestine expresses intestinal metabolic enzymes such as cytochrome P450s which are reported to have a major impact on the bioavailability of some drug classes due to first-pass metabolism (Lennernas, 2003). For drug classes such as statins, this is particularly detrimental as a portion of the drug would become metabolised prior to reaching the liver and thus, less of the active ingredient would reach its intended target.

While drugs must be formulated to withstand the fluctuating pH and digestive enzymes in the gut, the active ingredient must be soluble in the gastric fluid in order to be absorbed into the appropriate organ. As the acidic gastric fluid passes from the stomach, the small intestine has its own barriers to protect itself from the corrosive effects. Brunner glands found in submucosal layer of the duodenum section of the small intestine produce an alkaline mucus that coats the surface of the tissue. Beneficially, the sticky mucus lining not only protects the tissue but also, traps digested compounds and extends their time in the GI tract. However, the presence of a thick mucus layer impedes the absorption of drug molecules and in some cases, has been proven to affect the bioavailability of oral drugs (Boegh et al., 2015).

Therefore, oral drugs must be carefully formulated to prevent premature release under extreme conditions but also, to ensure that the drug can be readily released and absorbed at the site of action.

1.2 Excipients

The complexity of the oral administration route means that an equally complex formulation is required to maximise the successful delivery of the active pharmaceutical ingredient (API) to its intended site of action and achieve the desired therapeutic effect. A pharmaceutical formulation consists of several different types of excipients with varying functionalities. Pharmaceutical excipients are defined as “pharmacologically

inert ingredients added intentionally to a drug product (DP) for various functional roles" (Qiu et al., 2017). Examples of excipient categories are coating agents, antioxidants and disintegrants which work together to stabilise the API and ensure a timely release from an oral dosage form. Coating the dosage form is a crucial step with multiple purposes which include protecting the drug from degradation and controlling drug release with a pH sensitive coating (Darji et al., 2017). Antioxidants are used to improve drug stability by preventing oxidation (Goel et al., 2024). Traditional disintegrants, such as starch, allow an oral solid dosage form to rapidly break down following administration to facilitate rapid dissolution into the GI fluid (Darji et al., 2017). Companies that manufacture excipients, such as CRODA, market novel excipients that exhibit permeation enhancing properties in addition to refined versions of common excipients such as polysorbate-80. Commercially available permeation enhancers from CRODA include DEGEE and Mapcho-12. The exact mechanism of action for all chemical permeation enhancers is not fully known however, there are many suggested mechanisms. It is heavily believed that many permeation enhancers operate by interacting and extracting intercellular lipids to facilitate transport of drugs through the membrane (Nicolazzo et al., 2005). Other mechanisms include increasing drug retention at the mucosal surface as well as interactions between the excipient and epithelial proteins that lead to enhanced permeation (Nicolazzo et al., 2005).

1.2.1 DEGEE

Diethylene glycol monoethyl ether (DEGEE) is an ethylene oxide derivative and its structure is shown in Figure 1.2. DEGEE is a pharmaceutical excipient that is ideal for topical and transdermal applications but reportedly, is suitable for oral dosage forms too (*Super refined™ DEGEE* . 2024). DEGEE has historically been used as a strong solubiliser and co-solvent in many pharmaceutical applications (Ha et al., 2020). More recently, the excipient has been shown to enhance permeation. One study evaluated the effect of DEGEE in the formulation of methotrexate and found that with 2% DEGEE present, higher percutaneous absorption was observed which made methotrexate a stronger candidate for clinical treatment of psoriasis (Javadzadeh & Hamishehkar, 2010). Another study investigated the effect of several excipients on the absorption of genistein from a topical gel into human skin; when 25% w/v DEGEE was incorporated into the formulation, the permeability constant was 1.5-fold higher than the control

formulation thus demonstrating the permeation enhancing qualities of the excipient (Chadha et al., 2010).

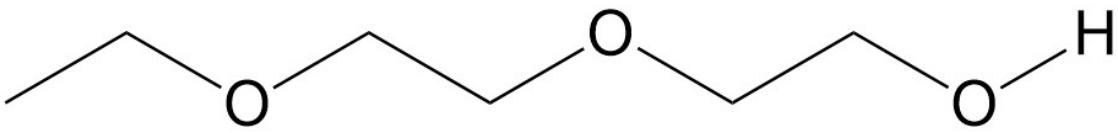

Figure 1.2: *The chemical structure of diethylene glycol monoethyl ether (DEGEE)*

1.2.2 Mapcho-12

The chemical name for mapcho-12 is n-dodecylphosphocholine and it is a more stable, structural analogue of lauroyl lysophosphatidycholine (*Mapcho®-12.* 2024). This lipophilic excipient is a saturated aliphatic chain with both a choline and phosphate group; the chemical structure of mapcho-12 is shown in Figure 1.3. Mapcho-12 is an excipient that has been shown to enhance drug absorption and permeation (Liu et al., 1999). One study investigated the effect of mapcho-12 on the permeability of hydrophilic compounds across caco-2 cell monolayers; the findings demonstrated the ability of mapcho-12 to improve paracellular permeation by means of modulating tight junctions (Liu et al., 1999). Additionally, the study touched on the importance of evaluating the overall effect of excipients and found that increased potency of the drug led to cellular toxicity (Liu et al., 1999). Another group formulated a glucagon nasal powder with mapcho-12 and performed a medley of in vivo studies on laboratory animals using standard and excessive doses of the formulation; the study concluded that the excipient was unlikely to pose any safety concerns and that the formulation was well tolerated by the animals (Reno et al., 2015).

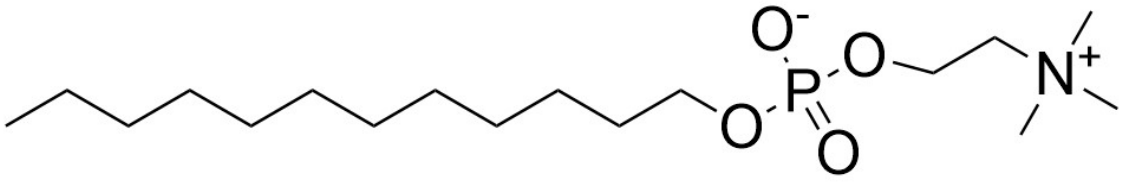

Figure 1.3: *The chemical structure of n-dodecylphosphocholine (mapcho-12).*

1.2.3 Polysorbate-80

Polysorbate-80 is a common excipient which is derived from polyethoxylated sorbitan and oleic acid. The chemical structure of the polymer is shown in Figure 1.4.

Polysorbate-80 acts as a surfactant which makes it an effective solubilising agent and it is widely used in the pharmaceutical industry.

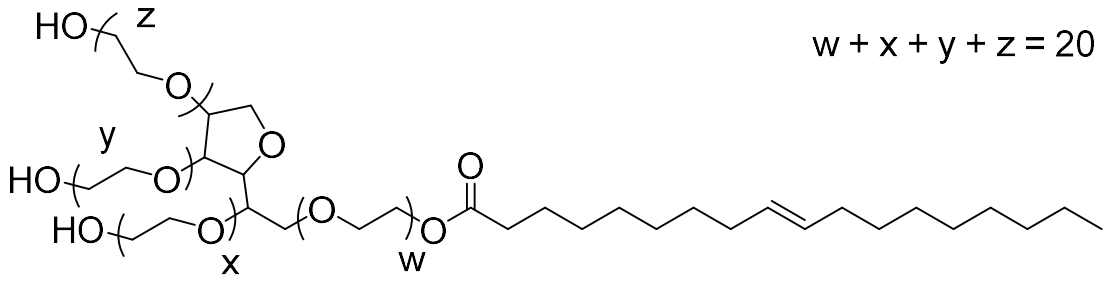

Figure 1.4: *The chemical structure of polysorbate-80.*

The solubility of an API in the gastric fluid is crucial for permeation. The relationship between solubility and permeability is important to understand when designing oral drug formulations. Many research groups have commented on the interesting interplay between solubility and permeability. One research group investigated the effects of increasing the concentration of known solubilisers on the intestinal permeability of carbamazepine; the study concluded that as the solubility of carbamazepine was increased, the intestinal permeability declined (Dahan et al., 2016). Alternatively, the group found that the increased solubility of rifaximin, by addition of a solubiliser, led to increased permeation (Dahan et al., 2016). The article stressed the importance of studying the solubility-permeability interplay for different drug and excipient combinations (Dahan et al., 2016). Another research group focused on the effect of polysorbate-80 on the absorption of micelle-free drugs; this study also demonstrated a solubility-permeation interplay (Kaneda et al., 1974).

Polysorbate-80 has been extensively researched and is approved as an excipient with solubilising abilities; the excipient is commonly formulated with the prescription drug, Lipitor, which has been used throughout the work reported in this thesis.

1.3 Atorvastatin

Lipitor, otherwise known as atorvastatin, is a synthetic lipid-lowering agent belonging to the statin family. Statins are the gold standard for the management of hypercholesterolemia (Reig-López et al., 2021). Hypercholesterolemia is a disorder where low-density lipoprotein levels are too high in the body and lead to a build-up of fatty plaque in the arteries which increases the likelihood of a heart attack or stroke. The

statin family work by inhibiting the enzyme, 3-hydroxy-3-methyl-glutharyl-coenzyme A (HMG-CoA) reductase, which is responsible for the synthesis of cholesterol (Reig-López et al., 2021). Atorvastatin, the most prescribed statin worldwide, is administered in the active hydroxy-acid form as a calcium salt. The structure of atorvastatin calcium salt is shown below in Figure 1.5.

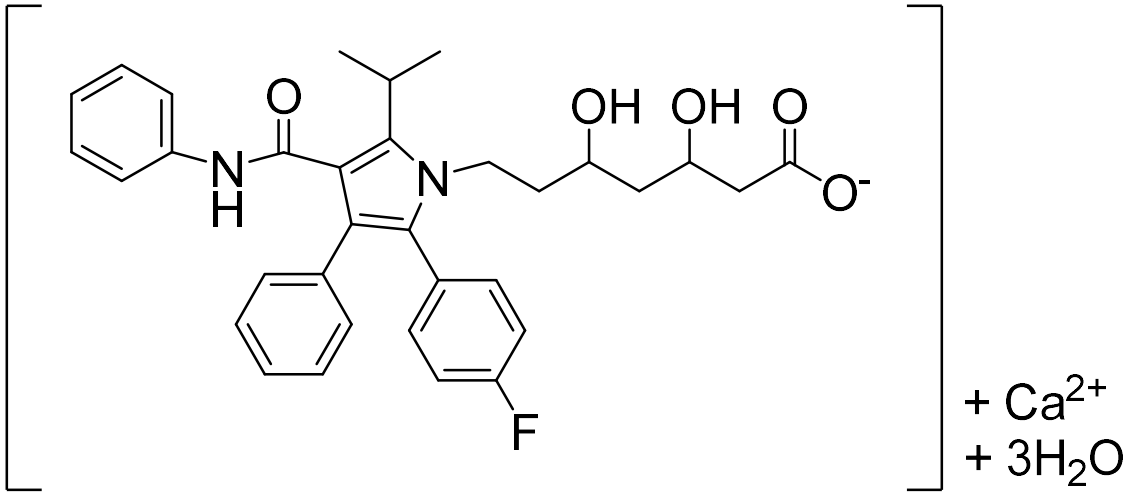

Figure 1.5: *The chemical structure of atorvastatin calcium.*

Under the Biopharmaceutics Classification System (BCS), drugs are assigned to different classes based on their solubility and permeability. Atorvastatin has been assigned to class II because of its poor solubility in gastrointestinal fluid (Reig-López et al., 2021). Historically, the permeability of a drug in human participants was established by measuring the rate of drug loss during intestinal perfusion; this value is known as the regional in vivo human intestinal effective permeability (Peff) (Dahlgren et al., 2014). For alternative models, the degree of permeability of a drug is assessed using the apparent permeability index (Papp) (Ravikanth & Ramanamurthy, 2018). As well as the amount of drug that has permeated, the Papp value takes into consideration the surface area exposed to the drug, the length of exposure and the starting concentration of the drug (Arnold et al., 2019). Class II drugs exhibit high permeability however, the bioavailability of atorvastatin can be as low as 12% despite being absorbed rapidly; the concentration of the drug in the plasma is reported to reach its peak within 0.5 – 3 hours (Lennernas, 2003). Pre-systemic metabolism is known to be responsible for the extremely poor bioavailability of atorvastatin.

1.3.1 Metabolism

Atorvastatin is metabolised by several different reactions including, but not limited to, glucuronidation, lactonisation and cytochrome P450-mediated oxidation. The administered calcium salt of the hydroxy acid is quickly converted to atorvastatin acid. From this form, atorvastatin acid can be metabolised by the CYP3A4 enzyme into either 2-hydroxy-atorvastatin acid or 4-hydroxy-atorvastatin acid (Lennernas, 2003). These active metabolites are isomers of each other and thus, have the same molecular weight. Atorvastatin acid and its metabolites can be reversibly converted to inactive lactone forms by lactonisation and returned to the acid form by hydrolysis (Lennernas, 2003). The chemical structures and metabolic pathway are illustrated in Figure 1.6.

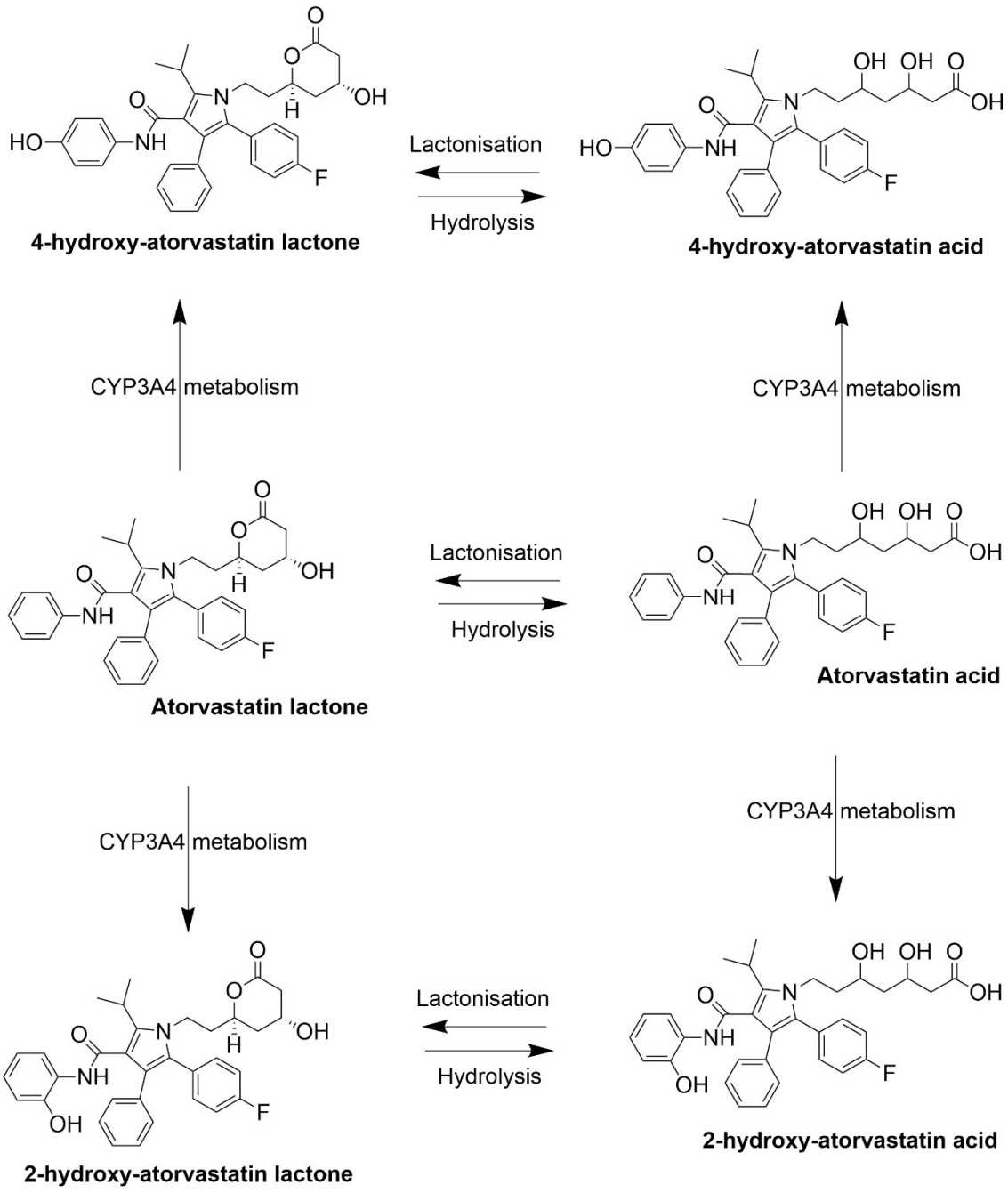

Figure 1.6: *The metabolic pathway of atorvastatin. The chemical structure of atorvastatin and its metabolites have been labelled in bold. Figure adapted from Lennernas, 2003.*

As demonstrated above, CYP3A4 has been proven to be involved in the major metabolic pathway of atorvastatin. While the highest concentration of the CYP3A4 enzyme is in the liver, which is the site of action for atorvastatin, it is also present in the gut wall (Lennernas, 2003). Consequently, atorvastatin is subjected to extensive first

pass metabolism prior to reaching the liver. Therefore, less of the active drug reaches the site of action and thus, significantly reduces its bioavailability.

1.3.2 Absorption Routes

For the fraction of atorvastatin that has not been metabolised in the apical enterocyte membrane along the gut wall, permeation through the gut wall occurs by diffusion and carrier-mediated uptake.

P-glycoproteins are transporter proteins present in the cell membrane that are widely expressed in the intestinal epithelium. The protein acts as an efflux pump that moves substances out of cells; this process is strictly dependent upon ATP. A recent study explored the effect of this protein on the permeation of atorvastatin using caco-2 cell lines; it demonstrated that due to P-glycoprotein efflux, permeation in the basolateral-to-apical direction was significantly higher than the desired absorptive direction (Wu et al., 2000).

Statins can absorb through the intestine by two different types of diffusion; these are paracellular and passive diffusion. Paracellular diffusion allows small drugs to be transported through the intestine via the tight junctions in between cells (Qiu et al., 2017). Absorption is dependent on the amount and size of junctional gaps as well as the quality of transmembrane proteins which regulate the barrier (Qiu et al., 2017). Due to the lipophilic properties of atorvastatin, the preferred method of diffusion is passive. Passive diffusion is a process where molecules move freely across a membrane from a higher concentration to a destination with a lower concentration. The driving force for passive diffusion is concentration gradient and so, no ATP is required for this process.

Of all the absorption mechanisms known for atorvastatin, only passive diffusion remains active when the tissue becomes non-viable making it an ideal drug for proof-of-concept studies since frozen tissue is desirable in the development and refinement stages of an ex vivo model.

1.4 GI Models

The Kassem research group prepared and optimised a self-nanoemulsifying drug delivery system (SNEDDS) for atorvastatin which included the excipients, polysorbate-80 and DEGEE. This formulation was administered to a group of laboratory rats in addition to a standard suspension of atorvastatin. The study found that the rats given the

optimised SNEDDS exhibited much higher oral bioavailability and therapeutic efficacy of atorvastatin (Kassem et al., 2018). While this study reported the successful development of a formulation that showed great promise, the research required in vivo study on animals. Traditionally, this was the accepted norm for all stages of drug research and development. However, as time and technology has progressed, the use of living animals is considered less acceptable, especially in the earlier stages of drug research.

The implementation of EU directive 76/768/EEC, which banned testing cosmetic products and ingredients on animals, was a clear statement of changing times (Russo, Lewis et al., 2018). It could be sensibly assumed that this movement caught the attention of many research groups and sparked a movement towards animal-free studies. Despite the extortionate investments that go into the research and development of preclinical models, high attrition rates make the approval of new drugs a long and expensive process (Ewart et al., 2021). A contributing factor to this failure has been linked to the limited predictive validity of preclinical models such as traditional cell culture and animal models (Ewart et al., 2021).

Realistic replication of the oral route is complex to say the least. Compared to other administration routes, the oral route is comprised of numerous organs all with differing structure and dramatically fluctuating in environment; not to mention the variability in the oral route between individuals. In addition to this, within an individual, factors such as the gastric emptying rate are highly variable and influenced by variables such as food intake, illness and emotional state. A number of studies have been conducted focused on the effect that the gut microbiome has on drug absorption. Examples have been identified in which gut microbes have caused both direct and indirect metabolism of pharmaceutical drugs (Tsunoda et al., 2021). Despite this, there are many instances in which the specific species and strains responsible remains unclear (Tsunoda et al., 2021). While the gut microbiome has been proven to affect drug absorption, it remains a large source of variability due to changes within and between individuals relating to genetics, diet, health and an individual response to drugs (Tsunoda et al., 2021). Therefore, creating a realistic model that provides comparable data to those from in vivo studies has proven challenging. While the current GI models available provide useful information for drug absorption studies, each have their own limitations.

1.4.1 Caco-2 Cell

The most established cell model for oral drug absorption studies is the colorectal adenocarcinoma (caco-2) cell line. Caco-2 cell monolayers are cultured in a cell culture insert and left in a static set up or transferred to a dynamic system. This particular cell line is considered to be the gold standard for drug permeation studies through the intestinal membrane. Caco-2 cells can be differentiated and express some efflux transporters which is desirable since these membrane proteins can affect the absorption of drug classes such as statins. Conventional caco-2 cells lack important features of the GI tract such as the cytochrome P450 enzymes e.g. CYP3A4. As previously discussed, the CYP3A4 enzyme plays a major role in the metabolism of statins such as atorvastatin. Thus, making the standard caco-2 cell line an unrealistic model for drug absorption studies using drug classes such as statins. Very recent advances have seen the development of a caco-2 cell line that can express CYP3A4 in levels similar to those in the small intestine of an adult human (Ichikawa et al., 2021).

Important structures such as Brunner's glands and goblet cells are also absent from the standard caco-2 cell model. Brunner's glands and goblet cells are naturally found in the small intestine and are responsible for the secretion of mucus. As previously touched upon, the presence and quantity of mucus in the small intestine is known to affect drug absorption. Therefore, without the mucus barrier, drug permeability is often overestimated. To combat this issue, the caco-2 cell line can be co-cultured with a human colon adenocarcinoma cell line, HT-29MTX, derived from goblet cells (Kleiveland, 2015). The HT-29MTX cell line secretes mucus and so, when combined with the caco-2 cells, forms a layer on the surface of the epithelial cells. Thus, bringing the now modified caco-2 cell model closer to the human in vivo situation.

The ongoing advancements in GI models such as the caco-2 cell line show great promise in what can be achieved in this area. However, a general limitation with all cell lines is the lack of physiological similarities to the real-life scenario.

1.4.2 Organoids

The development of organoids addresses the lack of structure in 2D cultured cell lines. Organoids are a type of 3D cell culture model which are typically derived from patient stem cells or even biopsies (Spencer et al., 2020). Stem cells have the ability to differentiate and organise themselves into miniature organs and tissues by aggregation

when under the correct conditions (Yang et al., 2023). Organoids take on many of the morphological features of the corresponding organ or tissue which makes them closer to the human in vivo situation than 2D cell models. Human gastric and intestinal organoids have been successfully created from pluripotent stem cells as adult stem cells taken from tissue (Zhang et al., 2020). The development and optimisation of GI organoids have led to major improvements in disease modelling and allowed extensive study into mechanisms within the GI tract.

Compared to other organoids, the GI architecture is not as simple to develop in the sense of allowing drug administration. In general, the GI organoid culture system forms a spherical structure in which the lumen is fully enclosed within the organoid (Zhang et al., 2020). In terms of drug absorption studies, the GI lumen cannot be easily accessed by drugs and their formulations; this is far from the in vivo situation in which luminal contents would flow over the apical surface inside the lumen (Zhang et al., 2020). Some research groups have recently begun to develop alternative systems that allow access to the luminal surface. The Wang research group designed a scaffold that was similar in structure to a crypt-villus (Wang et al., 2018). The scaffold was made from collagen-coated polydimethylsiloxane and could be loaded with cells to create a three-dimensional self-renewing intestinal epithelium with full accessibility to its surface (Wang et al., 2018).

Organoids have shown outstanding potential to be an excellent alternative to 2D cell models however, for GI organoids in particular, more work is needed to make them a rival model for preclinical oral drug absorption studies. Within the last 15 years, organoid research began to increase rapidly after a ground-breaking article was published; it highlighted that intestinal cryptvilli units could be generated from a single stem cell using a newly developed matrigel-based 3D culture system (Sato et al., 2009). The exponential projection in organoid research and culture exerts an exciting confidence that there is much more to come from this sector. Nevertheless, research using human material will always be limited to an extent as it is heavily reliant on the donation of stem cells and biopsies from patients and participants.

1.4.3 Ex vivo models

Ex vivo studies employ and maintain tissue, taken from a live subject, outside of the body in an in vitro environment. These types of models are considered a stepping stone

between in vivo animal experiments and cell culture in vitro models. While an ex vivo model still utilises animal tissue, these methods significantly reduce the number of animal sacrifices required in addition to the discomfort that would be experienced during in vivo experimentation. From one animal, it is possible to study multiple variables at once thus, vastly decreasing the number of animals required for sacrifice.

Although it would be possible to conduct these studies on human tissue, the logistics and availability of acquiring suitable human tissue means that this model is almost exclusively performed using animal tissue. The physiology of the oral route in humans shares striking similarities to that of the pig. In addition, humans and pigs share a similar omnivorous diet as well as digestive and metabolic processes (Patterson et al., 2008). Therefore, pigs have been considered the best non-primate, animal model for nutritional studies (Patterson et al., 2008). The Arnold research group found excellent correlations between the known drug permeability coefficient in humans to the experimental permeation values collected from a porcine model (Arnold et al., 2019). Pig tissue is readily available from abattoirs with some parts of the GI tract considered byproducts of meat production and thus, no animals needed to be sacrificed specifically for these studies.

While each GI model has its own benefits, it is heavily debated amongst researchers whether animal studies are a necessity in drug absorption studies to attain a closer resemblance to the real-life scenario. It is without doubt that an ex vivo model would be significantly closer in physiology to the human in vivo situation however, this leaves further room for debate. Drug absorption studies performed on an ex vivo intestinal model would be susceptible to higher variation than other in vitro models that use cell culture due to factors discussed previously. Within the intestine, the plicae circulares are not uniform across the surface meaning that the small area taken for the model may differ greatly in surface area to the next. Further variation will be experienced between different individual animals used for the study as discussed previously. Many researchers have seemingly overcome this by stipulating techniques which minimise variation and make the tissue samples more uniform. Instructions such as avoiding plicae circulares and Peyer's patches in addition to rinsing the lumen of the intestine which, inevitably, removes mucus and other luminal contents; all of which are known to have an effect on drug absorption (Arnold et al., 2019). However, it could be argued that in the instance of drug absorption and formulation, it is critical to acknowledge the level

of natural variation within and between individuals and factor this into research for future dosing and formulation purposes.

An undebatable advantage of ex vivo modelling compared to other in vitro models is that no long culture periods are needed which makes studies faster and much less susceptible to detrimental infection that can lead to experiment loss.

1.4.3.1 Ussing Chamber

Commonly used in drug transport studies, the Ussing chamber is designed with two adjacent compartments that are completely separated by a sheet of tissue clamped in between. Intestinal tissue is typically prepared for the Ussing chamber by opening the intestine up along the length of the mesenteric border to form a sheet before carefully removing the muscle-serosal layer; see illustration in Figure 1.7. The luminal side of the intestinal sheet is clamped facing into the donor compartment and the serosal side facing the acceptor compartment. For drug absorption experiments, the donor compartment is pulsed with a drug containing solution. If the drug permeates through the tissue, it is collected in the acceptor circuit. The chamber is fitted with probes to monitor tissue integrity throughout the experiment. Each semi-static compartment is bubbled with oxygen and carbon dioxide.

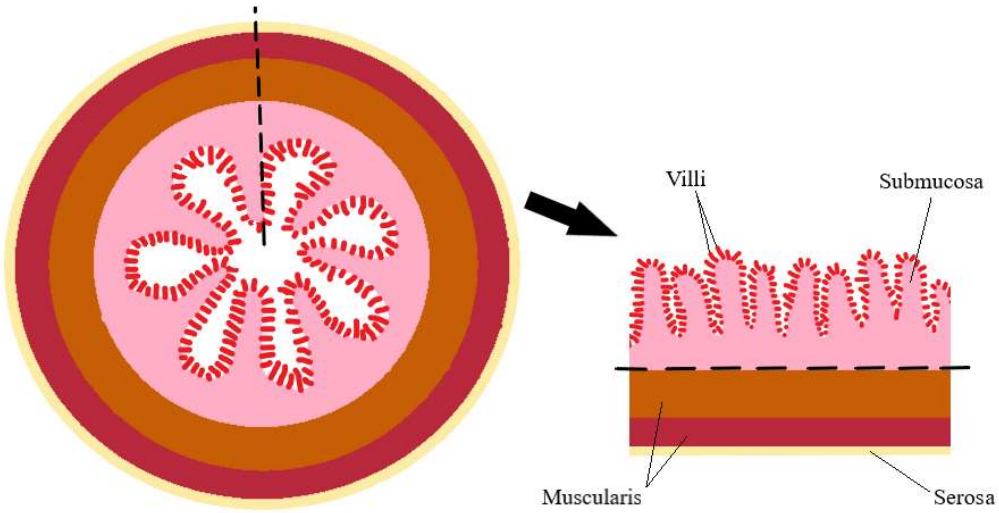

Figure 1.7: *A diagram showing a cross section of small intestine. A black dashed line is used to indicate where the tissue should be cut to prepare for an Ussing chamber. The arrow points to how the tissue should look after cutting and opening the intestine. An*

additional dashed line shows where the tissue should be cut to remove the muscle-serosal layers for ex vivo studies.

The Ussing chamber is a very similar system to the Franz cell with the only real difference being the orientation of the tissue; the compartments in the Franz cell are positioned on top of one another rather than adjacently. Both the Ussing chamber and Franz cell have been used in drug absorption studies for many decades now and proven itself to provide valuable information on drug transport across epithelial tissues. In a rare and lengthy study with data collected over 15 years, AstraZeneca compiled extensive human intestinal data using the Ussing chamber (Sjöberg et al., 2012). Human duodenum, jejunum and ileum tissues collected from 159 donors following a variety of surgeries were studied in the Ussing chamber (Sjöberg et al., 2012). Amongst the many parameters explored, permeability measurements of 28 drugs were carried out on sections of the small intestine (Sjöberg et al., 2012). This large-scale study using human tissue in the Ussing chamber allowed a database to be created that could be used by other researchers as a baseline to compare other models to.

It has been demonstrated that the Ussing chamber can house viable porcine intestinal tissue for a duration suitable to perform drug absorption studies (Arnold et al., 2019). The Arnold research group were able to successfully study the effect of P-glycoprotein transport and pre-systemic CYP3A4 metabolism on a number of oral drugs. The use of ex vivo tissue in the Ussing chamber allowed structures native to the gut wall to be studied in their natural state (Arnold et al., 2019).

1.4.3.2 Microfluidic & Millifluidic Systems

Both microfluidic and millifluidic devices work on a similar principle to the Ussing chamber however on a much smaller scale. The device is a two-compartment system separated by ex vivo tissue (or another model) that rests on a semi-permeable membrane within a cell culture well; an example of this has been greatly detailed and illustrated in throughout Chapter 3. A manipulatable flow continuously recirculates through narrow tubing in each compartment and flows over the tissue. For gut models specifically, many researchers have identified the need to mimic peristaltic movements to create a more realistic model; this motion can be easily achieved with the flow through these devices (Thomas et al., 2023). An additional feature of these devices is the ability to connect them to others and create a multi-organ system. This possibility was

successfully demonstrated by the Shim research group who demonstrated two-way communication between ex vivo tumour and lymph node tissue using a microfluidic chip model (Shim et al., 2020). Multi-organ communication would be particularly desirable for oral drug research considering the various organs that the drug must pass through to reach the site of action.

Ultimately, microfluidic and millifluidic systems are fairly versatile in that they can be equipped to house organoids and other 3D constructs. Thus, allowing the system to be optimised using cheaper, less complex substrates before moving to much more expensive and complex structures. Additionally, this allows comparative studies between ex vivo tissue and 3D constructs such as organoids to occur in the same environment. A recent research study has showcased a microfluidic device that was capable of both in vitro and ex vivo drug permeability studies (Hemmilä et al., 2020). The device, which accurately mimicked in vivo experimental conditions, was shown to produce permeability values that correlated well with those collected using the Ussing chamber (Hemmilä et al., 2020).

The only difference between a microfluidic and millifluidics device is the scale of the system; microfluidic devices use tubing with a diameter less than 1 millimetre and ex vivo tissue at diameters less than 10 millimetres. Millifluidic devices have wider tubing and can house larger pieces of tissue. Subsequently, the narrow tubing in these devices, especially microfluidic systems, is susceptible to bubble formation. The presence of bubbles within the system can cause variation in the system pressure and ultimately, lead to leakage if the pressure is raised too high. The low volume in the tubing makes the presence of even tiny bubbles more impactful. Microfluidic and millifluidics devices require careful set up and monitoring to reduce bubble formation and identify any leaks within the system.

A major drawback to all ex vivo models is the integrity and viability of the tissue. In comparison to other models that use cell culture, ex vivo models cannot be used for long term studies. All ex vivo tissue has a limit to the time that it can survive outside of the body even with the correct care and supplementation and thus, there is a limit to the type of studies that it is suitable for. Different types of tissue experience different periods of viability; for instance, brain tissue is known to have the shortest viability time while spinal disc can remain viable for days. It is critical to establish the viability period for the tissue type used to ensure it will be sufficient for the study in hand. Additionally,

the conditions the tissue is subject prior to and within the model can have a dramatic effect on viability. For instance, muscle-serosal layer removal from intestinal tissue for ex vivo models can lead to a rapid decline in viability (Arnold et al., 2019). Therefore, efforts should be made to assess the viability of tissue within the specific model set up. Where possible, steps should be taken to minimise stress on the tissue to maximise viability.

1.4.3.3 Viability Assessment

In terms of tissue, viability refers to the percentage of healthy, living cells within a given amount of tissue. As stipulated above, it is crucial to assess whether tissue has remained viable throughout the entirety of an experiment; the only exception here would be instances where frozen tissue is being used and so viability is not expected. If ex vivo tissue becomes non-viable during the course of a drug absorption experiment, the mechanisms available for absorption become severely restricted and thus, distort the findings of the study.

There are several methods to assess the viability of tissue in real-time. A popular method is to take trans-epithelial electrical resistance (TEER) measurements, which quantify the integrity of the cells (Srinivasan et al., 2015). For ex vivo models, measurements are taken by placing electrodes into the solutions surrounding the tissue where it can monitor TEER continuously throughout the experiment. TEER electrodes are built into Ussing chambers and many microfluidic devices. In some instances, TEER measurements may not be the most appropriate method if the model has not been designed to incorporate the electrode probes.

Viability assays are a means of assessing tissue viability either in-line or post-experiment. A common viability assay involves the quantification of lactate dehydrogenase (LDH) (Kaja et al., 2018). LDH is used to help cells generate energy and so, an increase in LDH levels strongly implies tissue deterioration and death (Kaja et al., 2018). To perform this assay, an aliquot of the solution surrounding the tissue is taken. The aliquot can be taken at different time points during the experiment or before and after the experiment. The absorbance of the solution is used to quantify the LDH level. When large volumes of liquid surround the tissue, the LDH levels become too diluted for this method to be effective.

Alternatively, viability assays can be used in conjunction with immunological staining. LIVE/DEAD staining is a common technique that uses the fluorescent dyes calcein AM, propidium iodide (PI) and DAPI to highlight live cells, dead cells and nuclei, respectively (Bulin et al., 2017). Once viewed using confocal microscopy, the ratio of living to dead cells can be easily established and thus, assess the viability of the tissue. . A potential problem with immunological staining on tissue rather than cells is that auto-fluorescence can be a major issue. Some tissue types exhibit auto-fluorescence to a higher degree than others which create false readings and so, not all stains will be suitable. AlamarBlue is another popular cell viability assay that utilises fluorescence. This assay uses the resazurin-to-resorufin conversion as a cell health indicator as living cells are known to reduce resazurin to resorufin (Dinh et al., 2023). The resazurin present in the assay is blue with no fluorescence and is easily distinguishable from resorufin; this is red and highly fluorescent (Dinh et al., 2023). An issue with using cell viability assays such as these with tissue is its thickness. As the assay is performed on living tissue rather than formalin-fixed, the tissue must be soaked to allow the active ingredient to penetrate through the whole tissue. Dependent on tissue type and thickness, issues can arise from the extra time needed for the active ingredient to penetrate through the full thickness of the tissue.

Another common viability assay using immunological techniques is the caspase-3 assay. Caspase-3 is a protease that plays a direct role in cell apoptosis or in other words, programmed cell death (Nichani et al., 2020). Therefore, detection of this molecule is often used as a measure for cell viability (Nichani et al., 2020). To detect and visualise caspase-3 by confocal microscopy, anti-caspase-3 antibodies are added to the tissue where they will bind to caspase-3. The tissue is then rinsed of excess primary antibody before the addition of a secondary antibody with a fluorescent tag. The tissue is generally counterstained with DAPI which identifies the nuclei in each cell. Therefore, cells that have undergone apoptosis can be visualised against the number of cells present under a confocal microscope thus, establishing viability. In addition to this, the DAPI stain will highlight the shape of the nuclei which in turn, can be an indicator of other types of cell death such as necrosis. Immunological staining for viability can be a much more labour-intensive process than it is for cells. In the case of basic cell culture, the staining can be performed directly onto unaltered cells whereas for tissue, this is not possible. Dependent on the thickness, the stain cannot fully penetrate through to the

centre of the tissue. Therefore, the tissue must be fixed to maintain the status of viability before sectioning. Inevitably, the need for fixing and sectioning limits this viability assay to post-experiment for ex vivo tissue models.

From the relatively brief evaluation of some of the GI models available, it is evident that advantages and limitations can be attributed to each and every GI model. The choice of GI model may be limited due to the purpose of the study but ultimately, more personal circumstances can mould the decision. Factors such as available funding, ethical standpoint, personnel expertise and available facilities all play a role in choosing the right GI model for that research group. Additionally, the accessibility to different analytical instruments may influence that decision too.

1. 5 Mass Spectrometry Fundamentals

Mass spectrometry is a popular analytical technique in which ions generated from a sample are separated based on their relative mass and charge prior to detection. Various configurations of mass spectrometers have been developed but all follow the same basic principles. A mass spectrometer is comprised of an ionisation source, mass analyser, detector and data system as illustrated in Figure 1.8. In general terms, once a sample enters the mass spectrometer it is converted into gaseous ions by the ionisation source. The ions are then accelerated by an electric field towards the mass analyser. Ions travel through the mass analyser and become separated based on their mass and charge. Consequently, ions hit the detector at different times relevant to their mass-to-charge (m/z) ratio. The detector translates this information into a mass spectrum that shows ion intensity against their m/z ratio.

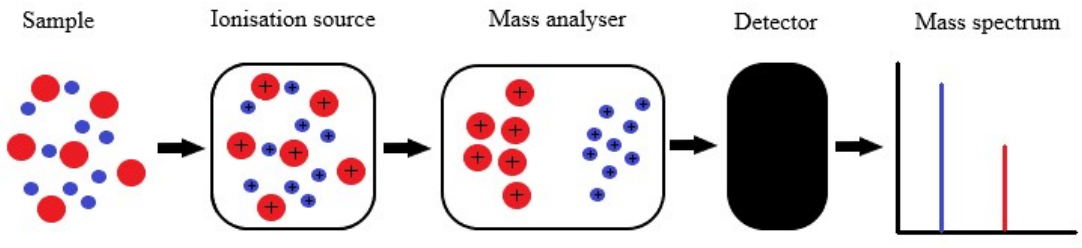

Figure 1.8: *A basic diagram showing the fundamentals of mass spectrometry.*

1.5.1 Ionisation Sources

Multiple ionisation sources exist that can be coupled to a mass spectrometer. Each ionisation source has different characteristics which are desirable for different sample types and applications. An example of this would be the scarcity of the sample; ionisation sources can be either hard or soft which refers to the degree of fragmentation inflicted and thus, the extent of sample destruction. Another factor would be the desired analyte; some molecules are not ionisable and thus, require assistance in order to be detected by a mass spectrometer.

1.5.1.1 MALDI

Matrix-assisted laser desorption ionisation (MALDI) is a soft ionisation technique that inflicts minimal fragmentation on a sample. Exclusively to this ionisation technique, the sample must be co-crystallised with matrix. With the assistance of the matrix, MALDI is able to convert non-volatile and thermally labile molecules that would otherwise not be ionised, into gaseous ions that remain intact. In order to be effective, the matrix must exhibit strong UV absorption at the wavelength that corresponds to the laser used in the source. Additionally, the matrix must be compatible with the desired analyte to allow co-crystallisation.

Co-crystallisation is crucial as the whole principle of MALDI is reliant on the matrix promoting ionisation and desorption of the analyte. Careful preparation of the sample and the matrix is required before it enters the mass spectrometer. The matrix must be evenly distributed amongst the sample; dependent on sample type this can include standard mixing together or evenly coating the sample surface. The matrix is allowed to dry which in turn, forms small uniform crystals if done correctly. Once dried, the sample can be transferred into the mass spectrometer. Under the vacuum conditions in the MALDI source, the surface of the matrix-coated sample is struck by a laser which induces rapid heating of the matrix crystals. The large accumulation of energy is absorbed by the matrix molecules that subsequently become excited and enter the gaseous state. After the initial ionisation of the matrix molecules, it is widely accepted that a secondary ionisation step occurs between the expanding plume of desorbed material created by the matrix and surrounding molecules. The exact mechanism is not fully understood, yet many feasible theories have been proposed. Nevertheless, both

matrix and analyte ions have been generated and accelerated into the mass analyser. A workflow for a tissue section has been shown in Figure 1.9.

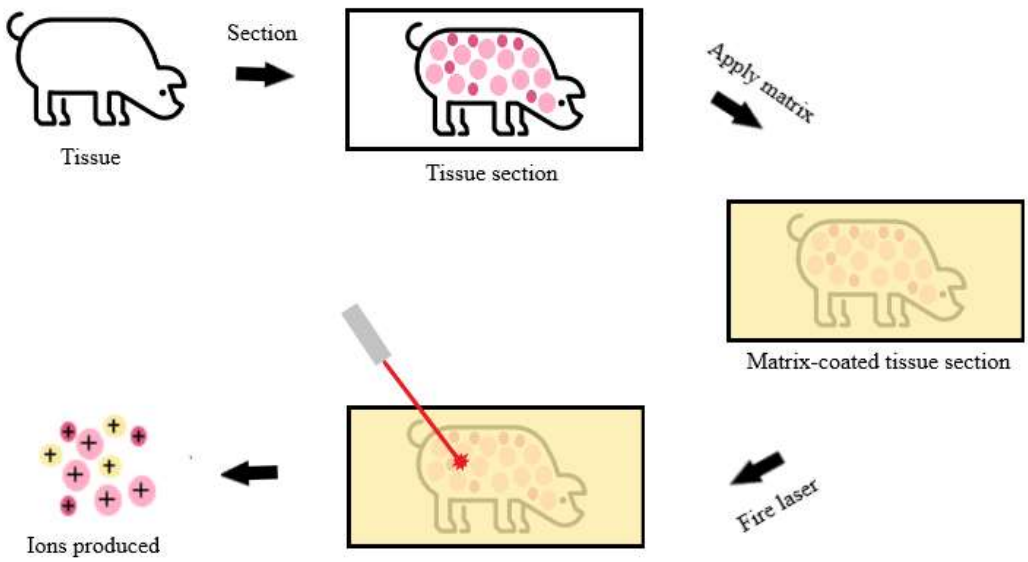

Figure 1.9: *A workflow showing the process of ionising tissue by MALDI.*

Further improvements to the sensitivity of MALDI have led to the development of MALDI-2. After the initial laser is fired, a secondary laser positioned adjacent to the sample is then fired at the plumb of desorbed material causing further ionisation of any remaining neutral molecules (*timsTOF fleX MALDI-2.* 2024). A transfer of charge to any remaining neutral analyte molecules increases the sensitivity of the ionisation method (*timsTOF fleX MALDI-2.* 2024).

Since the only difference between MALDI and MALDI-2 is the addition of another laser, the sample preparation remains the same. For the analysis of whole tissue sections as illustrated above, the sample should be evenly coated with matrix, rather than mixed. Sublimation is one of many established matrix application methods for producing a coating of matrix on a tissue section (Hankin et al., 2007). Sublimation is an ideal matrix deposition technique as the matrix undergoes a direct transition from the solid state to a gas state. During sublimation, the liquid state is bypassed and therefore, will not cause delocalisation on the sample. The typical sublimation apparatus has been illustrated in Figure 1.10.

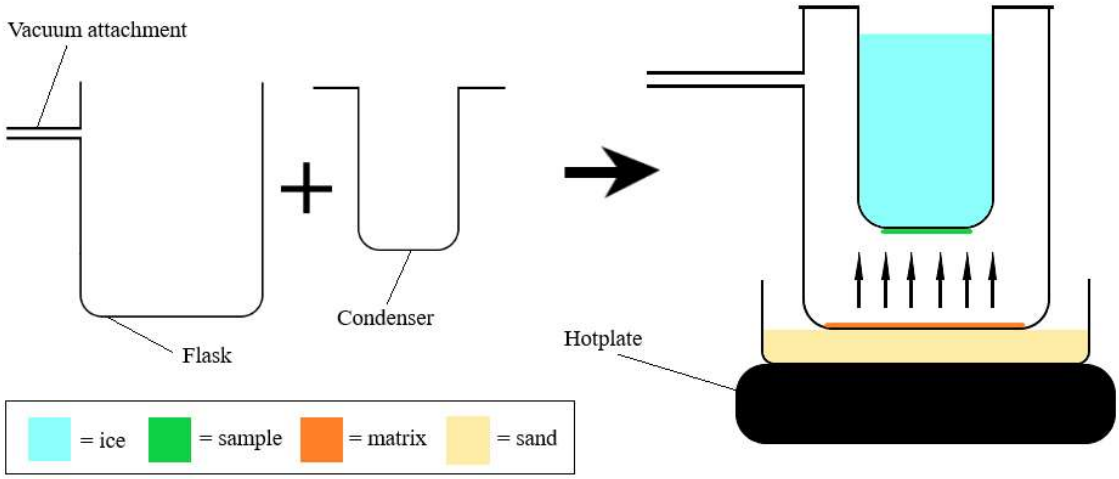

Figure 1.10: *A diagram showing the two parts of a sublimation kit. The sublimation kit is shown fully assembled with the matrix and sample inside the flask which is being heated by the sand.*

The sublimation apparatus is comprised of two parts, the condenser and the flask, which are separate entities. Matrix is evenly distributed in the bottom of the flask. The sample mounted onto a glass slide is fixed to the underside of the condenser with the sample facing the matrix. The two parts are then connected and placed under vacuum using the attachment built-in to the flask. The condenser is then filled with ice to create a cool environment around the sample. The flask is then rested on a temperature-controlled sand bath, heated by a hotplate. The principle behind this technique is that with the heat and vacuum conditions, matrix will sublime and deposit on the cold sample slide. A drawback to this method is the potential for many variables in parameters such as the sand temperature and even distribution of the matrix.

An alternative matrix deposition technique uses an automated sprayer such as the HTX TM-Sprayer (HTX Technologies, North Carolina, USA). The HTX TM-Sprayer is a means of evenly depositing matrix by spraying the matrix in solution through a heated nozzle directly onto the tissue. Advanced sprayers such as the HTX TM-Sprayer are fully automated and allow complete control over the specific amount of matrix in each deposition as well as the drying time of the matrix thereby creating reproducible deposits. Although drying time is a controllable feature, the matrix still enters the liquid phase thus, leaving the potential for some degree of analyte delocalisation.

A very basic matrix deposition method is manual spotting. A manual single channel pipette is used to deliver a precise volume of matrix onto the sample. Manual spotting is

infrequently used for depositing matrix on tissue and is more commonly used with a liquid sample or standard. There are two ways this can be performed; the sample can be spotted and allowed to dry before applying the matrix spot. Or alternatively, both the sample and matrix can be spotted together while wet and mixed with the pipette. Either of these ways are subject to irregularities in crystal formation and reproducibility. Therefore, this technique is mainly used for quick development of a method for instance, spotting standards to test the sensitivity of a mass spectrometry method.

1.5.1.2 ESI

Electrospray ionisation (ESI) is a soft ionisation technique that operates at atmospheric pressure and produces intact ions with multiple charges. Samples are required to be in a liquid state before entering the ESI source. An analyte solution is injected into the ESI source through a narrow, heated metal capillary along with a solvent mobile phase. The analyte solution travels through the capillary, into the desolvation chamber via the sampling cone. A high voltage is applied to the capillary which generates an electrical field along its length and causes a charge to accumulate on the surface of the liquid at the end of the capillary. With increased voltage applied, the liquid protruding from the capillary tip elongates until it forms a Taylor cone (Hoffmann & Stroobant, 2007). Consequentially, highly charged droplets are released which divide into smaller droplets that explode in an aerosol formation. Simultaneously, a flow of nebulising gas, usually nitrogen, is employed in the coaxial direction which restricts the expelled droplets into a narrower path, as illustrated in Figure 1.11.

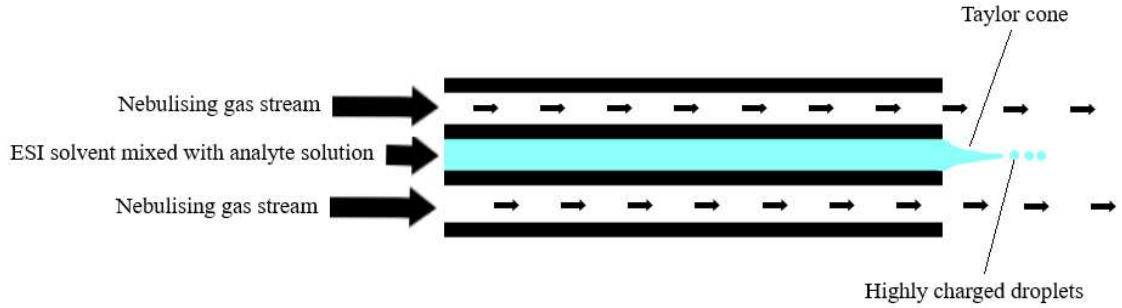

Figure 1.11: *A diagram showing the structure of an ESI capillary and the formation of the Taylor cone.*

The exact mechanism for the formation of multiply charged ions is not yet known however, three mechanisms have been proposed. These include the chain ejection model (CEM), the charge reduction model (CRM) and the ion evaporation model (IEM)

(Hoffmann & Stroobant, 2007). The IEM mechanism will be discussed here in greater detail as it is most associated with small molecules and thus, more relevant to the work presented in this thesis (Iribarne & Thomson, 1976).

When the spray droplets enter the desolvation chamber, the solvent begins to evaporate. The combination of heat and a stream of drying gas applied in the perpendicular direction causes the volume of each droplet to reduce. As the volume of the droplet shrinks, repulsive forces between the charges increase until the Rayleigh instability limit is reached (Hoffmann & Stroobant, 2007). At the Rayleigh instability limit, the surface tension of the droplet is equivalent to Coulombic repulsion (Hoffmann & Stroobant, 2007). Once the volume of the droplet is reduced further and surpasses the Rayleigh limit, a Coulombic explosion occurs leading to the formation of smaller droplets (Hoffmann & Stroobant, 2007). The process continuously repeats with the smaller droplets until only the analyte remains in the gaseous state; this has been illustrated in Figure 1.12. The entrance to the mass analyser receives an oppositely charged voltage to draw the multiply charged ions that have been generated towards it.

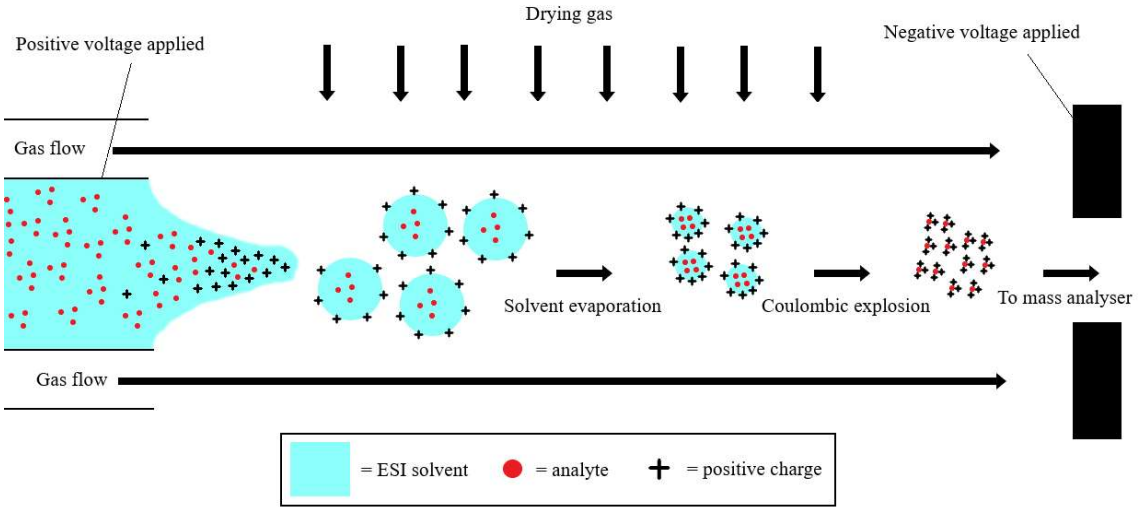

Figure 1.12: *A diagram showing the Ion Evaporation (IE) ionisation process in the ESI source.*

The multiple charges lower the mass-to-charge ratio and thus, enable a much wider mass range to be detected; this is highly beneficial as the detectable mass range can be extended up to MDa, thus enabling intact proteins to be observed (Hoffmann & Stroobant, 2007).

1.5.1.3 DESI

Desorption electrospray ionisation (DESI) is a non-destructive ambient ionisation technique that allows samples to become ionised in their native state. Similar to ESI, a stream of solvent is forced through a capillary where it forms charged droplets and ions that are ejected from the tip of the capillary in an aerosol formation. The capillary is angled onto the surface of a sample so that the spray of solvent wets the sample. An influx of nitrogen gas runs coaxially to the capillary which focuses the spray. The analyte becomes desorbed into secondary charged droplets which are then angled towards an ion transfer line leading to the mass analyser, as illustrated in Figure 1.13.

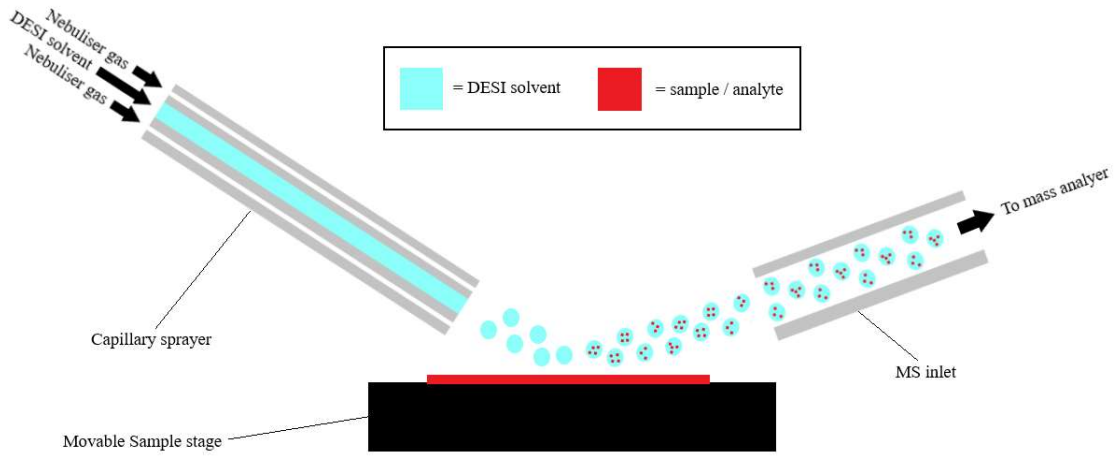

Figure 1.13: *A diagram showing ionisation occurring in the DESI source.*

The angle of the spray is critical to maximise the amount of analyte that reaches the MS inlet. Due to operating under atmospheric pressure, the angle can be easily changed in situ by moving the sample stage in the x, y and z directions or by altering the angle of the capillary. A benefit of working under atmospheric pressure is that virtually any sample can be deposited on the sample stage as long as it fits.

1.5.2 Mass Analysers

Following ionisation, the next stage in mass spectrometry is separation. The ions produced are separated in a mass analyser based on their mass and charge. Typically, ions are accelerated by an electric field before travelling the length of the mass analyser towards the detector. When a constant kinetic energy is applied to ions, they will travel at different speeds dependent on their mass and charge. Heavier and more highly

charged ions will travel faster than smaller ions with less charge. There are many different mass analysers commercially available which operate on different principles; the work reported in this thesis solely uses mass analysers based on the time-of-flight principle and thus will be described in greater detail.

1.5.2.1 TOF

Time of flight (TOF) is a one of the simplest mass analysers. Ions are initially accelerated into the TOF by an electrical field whereby all ions acquire the same level of kinetic energy. The TOF itself is a field free region in which accelerated ions enter and become separated due to travelling at different velocities. The ions travel the length of the TOF to the detector; the longer the distance travelled, the more separated the ions become. This process has been illustrated below in Figure 1.14. The m/z of each ion can be determined by the length of time it takes for the ion to travel through the TOF and reach the detector.

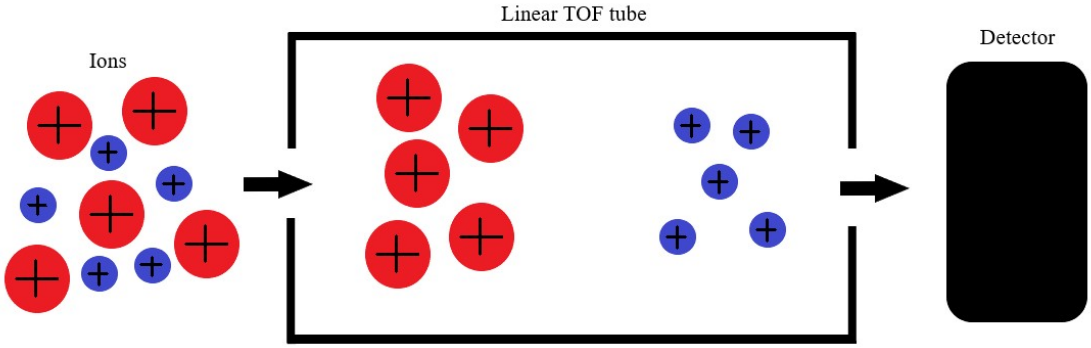

Figure 1.14: *A diagram showing the set up and separation inside a linear TOF.*

The TOF can be used in two modes: linear or reflectron mode. The linear TOF provides a simple, straight flight path as described and illustrated above. Reflectron mode follows the same principle however, the ion flight path is significantly increased within the same area. Upon initiating reflectron mode, an electrostatic reflector, or ion mirror, positioned to offset ions from reaching the primary detector is activated and reflects ions back through the TOF towards a secondary detector; this has been illustrated in Figure 1.15. Ultimately, reflectron mode increases the flight path which leads to greater ion separation and thus, improves mass resolution without the need for increasing the size of the mass spectrometer.

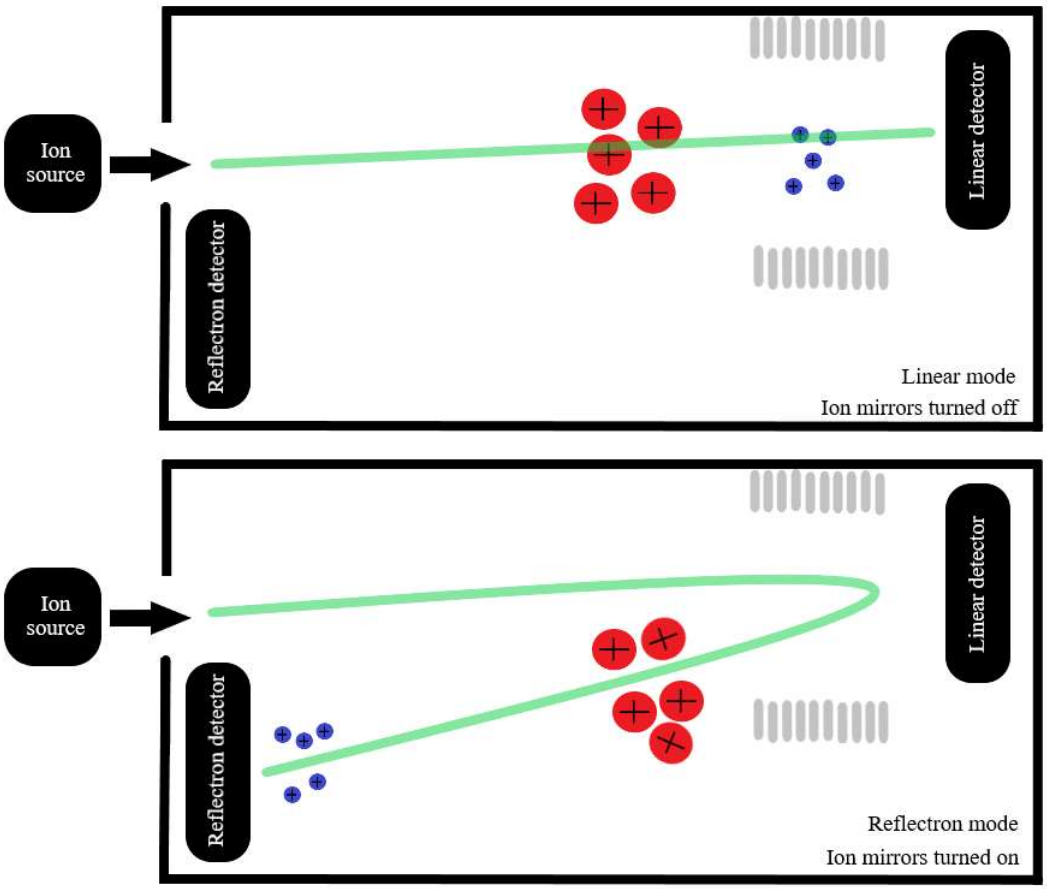

Figure 1.15: *A diagram showing the set up a TOF in two modes: linear and reflectron.*

1.5.2.2 MRT

Multi reflecting time-of-flight (MRT) is a novel mass analyser with a tremendously long ion flight path that delivers exceptional mass resolution and mass accuracy. The impressive flight path is achieved by multiple grid-less mirrors and periodic lenses organised in close proximity that deflect the ion path twenty-three times across the length of the mass analyser. At the final periodic lens, the ion path trajectory is altered to allow the ion to return to the detector located next to the ion entrance; in this process the ion path is deflected a further twenty-three times meaning ions will undergo a total of forty-six deflections. By the time the ion reaches the detector, its flight path has been exponentially increased. This process has been illustrated in Figure 1.16. A disadvantage to an extensive flight path is that some ions can be lost during flight reducing the sensitivity of the mass analyser. In an attempt to counteract this, LECO Inc developed 'Encoded Frequent Pushing' which was shown to recover some sensitivity of the mass analyser (LECO Corporation, 2018).

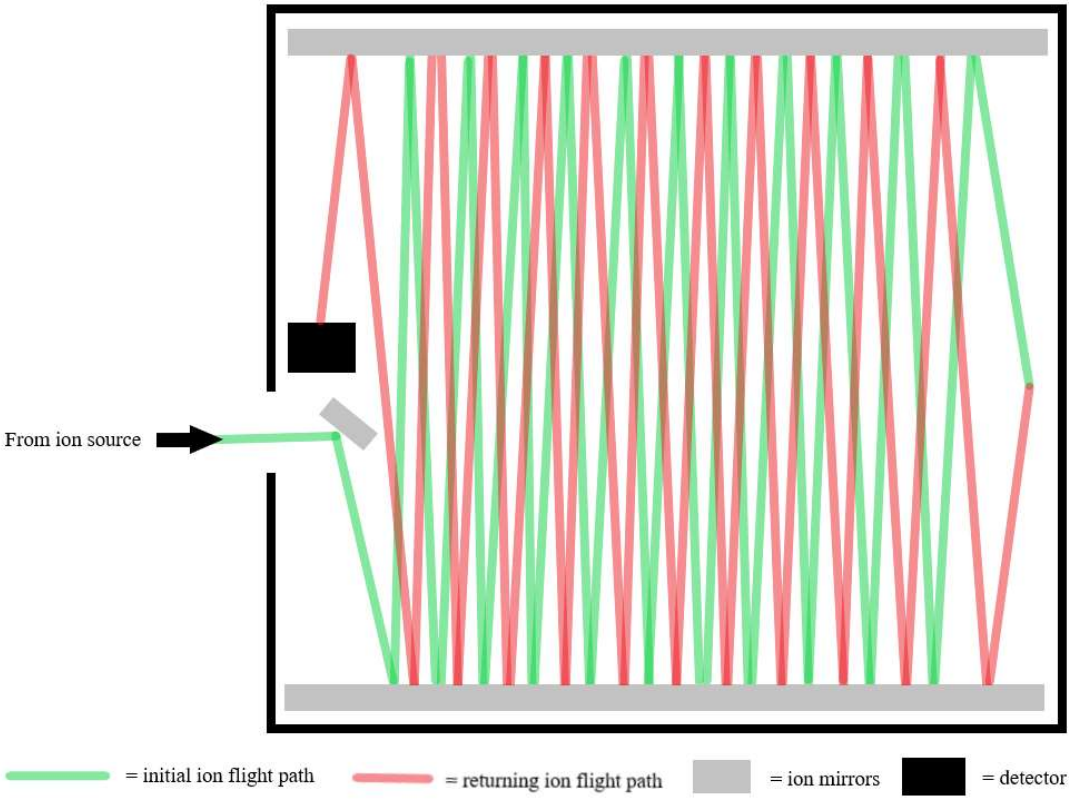

Figure 1.16: *A schematic representing the flight path for ions in the Waters MRT mass analyser. Not shown on the diagram, seemingly overlapping flight paths are kept separate by periodic lenses.*

1.5.2.3 Quadrupole

The quadrupole is a mass analyser that consists of four rods that are organised parallel to each other as shown in Figure 1.17. A focused beam of ions are directed through the centre of the quadrupole. Fixed alternating direct current (DC) and radio frequency (RF) potentials are applied to the rods to generate an electrical current; ions gain energy as they pass through the electrical field and begin to oscillate. The alternating currents applied to the rods constantly change the trajectory of the ions travelling through the quadrupole, which determines whether the ions collide with the rods. If the electrical field generated by the rods is too large, the velocity and thus, trajectory of the smaller ions would cause them to collide with the rods and become neutralised. Ions with a stable trajectory will travel the length of the quadrupole and reach the detector. Larger ions are less affected by the electrical field than smaller ions; this has been illustrated in Figure 1.17. Fine tuning of the currents applied to the rods can allow ions in a specific

mass range or m/z value to pass through the quadrupole; this is known as a full scan and selected ion monitoring, respectively.

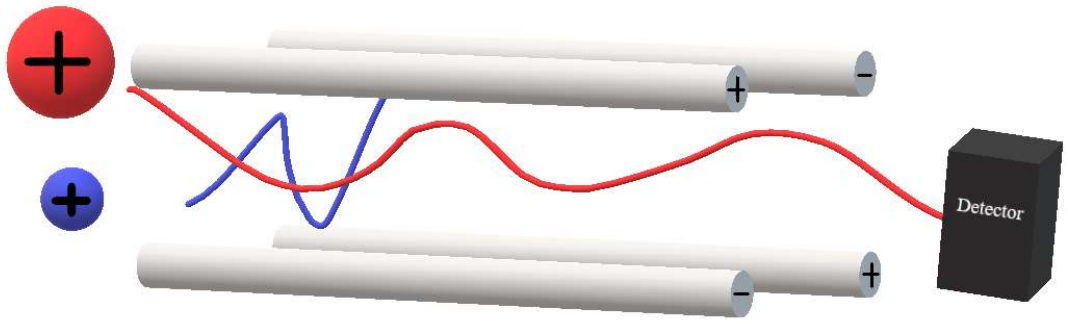

Figure 1.17: *A diagram of the quadrupole mass analyser. The red and blue ion pathway demonstrates a stable and unstable trajectory, respectively.*

1.6 LC-MS/MS

Liquid chromatography tandem mass spectrometry (LC-MS/MS) is a quantitative technique that allows quantification of analytes in a liquid state. An example of a liquid chromatography coupled tandem mass spectrometer is the Agilent 6420 triple quad; the schematic corresponding to this instrument has been shown in Figure 1.18. This instrument is comprised of a LC unit coupled to an ESI source and three quadrupoles.

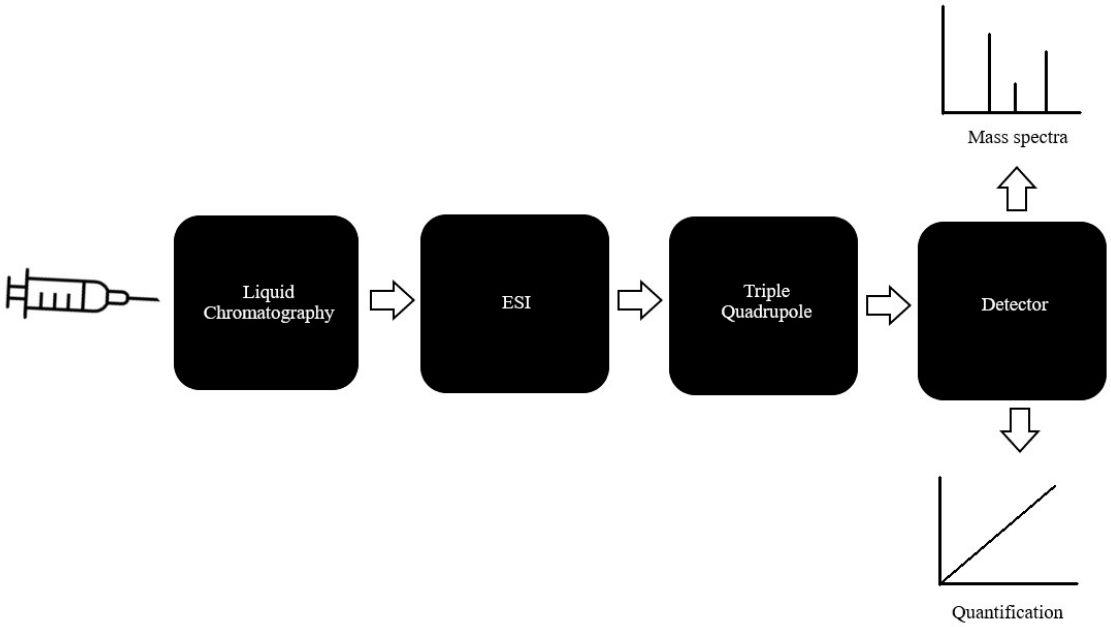

Figure 1.18: *A schematic showing the workflow for LC-MS/MS.*

A liquid sample is injected into the LC system with either a manual or automated syringe. Within the LC unit, a pump forces a solvent mobile phase through the tubing in the LC system and pushes the sample through the column. The column contains a packing material which is coated with a stationary phase that interacts with the sample-mobile phase solution; this causes analytes to separate based on physiochemical properties such as polarity. Components are eluted from the column at different times known as retention times; this is based on the interactions with the stationary phase. The components pass a detector where the retention time and abundance are measured. A more in-depth schematic of the LC unit has been shown in Figure 1.19.

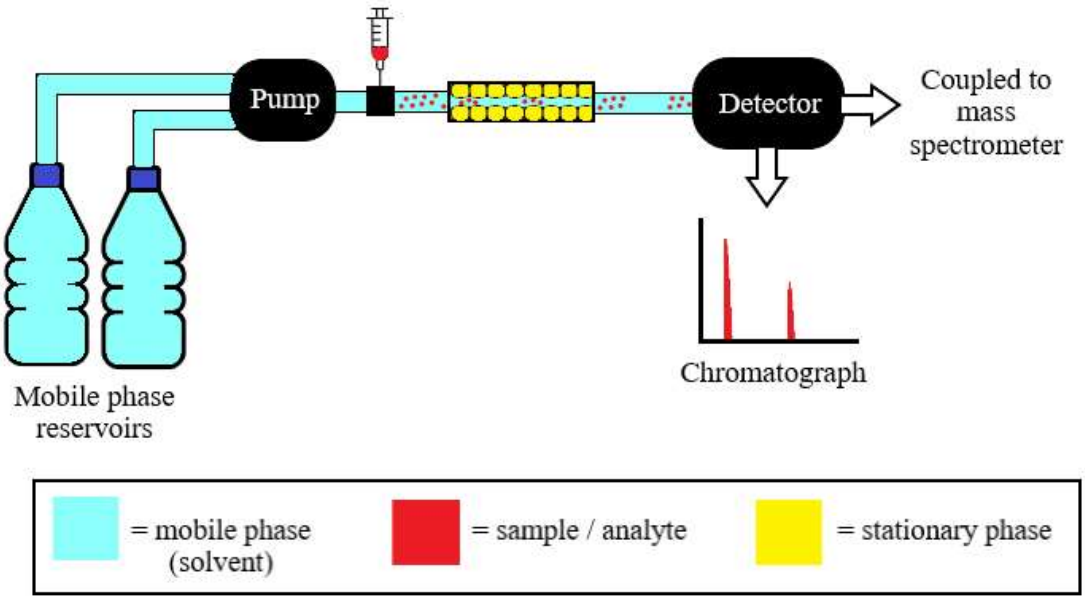

Figure 1.19: *A schematic showing the workflow of the LC unit coupled to a tandem mass spectrometer.*

Careful sample preparation is essential when analysing complex samples in a LC system. All samples should be a filtered and remain soluble when introduced into the mobile phase. An LC column is quite narrow and the presence of only a thin coating of the specialist stationary phase on the support material means that samples should be diluted into a specific concentration range so as to not overload the column. Additionally, thorough sample preparation is required to remove any compounds that are incompatible with the stationary and mobile phase as this can block the column and reduce its lifespan.

The now-separated components are introduced into the mass spectrometer via the ESI source where they become ionised. The ions enter a series of quadrupoles where they become further separated. As detailed previously, quadrupoles can be operated in two different modes known as full scan and select ion monitoring. When multiple quadrupoles are coupled together, different combinations of these modes create a range of different types of scans. These include product ion scan and multiple reaction monitoring (MRM) scan, to name a few.

A product ion scan allows all fragments of a specific ion to reach the detector. The product ion scan is achieved by tuning the first quadrupole to allow only select ions to pass through. The selected ions then enter the second quadrupole; this is not a true quadrupole and acts a collision chamber by fragmenting the ions. From this process, product ions are generated and pass into the third quadrupole. The final quadrupole is tuned to allow all product ions within a set range to reach the detector.

MRM scan allows specific ions and specific fragments to reach the detector; this mode allows accurate identification and quantification as the parent-to-fragment ion transition is unique. For MRM mode, the first quadrupole is tuned to allow only select ions to pass through the quadrupole. The selected ions are fragmented in the second quadrupole (collision cell). From this process, product ions are generated and pass into the third quadrupole. The final quadrupole is tuned to only allowed specific product ions to pass through and reach the detector. The product ion and MRM scan have been illustrated in Figure 1.20.

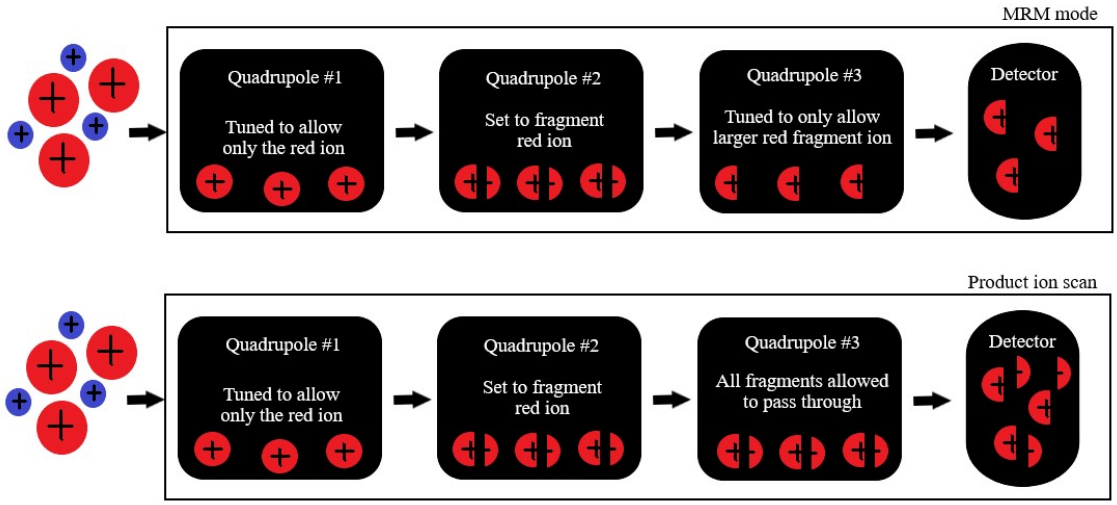

Figure 1.20: *A schematic describing the workflow for MRM mode and product ion scan on a tandem mass spectrometer.*

1.6.1 Applications

LC-MS/MS has become increasingly popular in drug absorption studies. A major advantage of LC-MS/MS is its ability to accurately detect and quantify multiple analytes in a single acquisition. As an example, the Larger research group routinely used an LC-MS/MS method to simultaneously detect and quantify three drugs from a caco-2 cell model in order to ascertain the Papp value for each substance (Larger et al., 2002). It is reported that the LC-MS/MS method is used routinely to perform checks on model reproducibility and the multi-analyte detection feature saves a lot of time compared to other techniques that are limited to single analyte detection (Larger et al., 2002). In addition to qualitative analyte detection, the quantitative abilities of LC-MS/MS make it ideal for establishing a mass balance simultaneously. Mass balances are routine in drug-related studies and ensure that the amount of drug added is suitably recovered. In studies such as those conducted by Larger et al., mass balances indicate loss of drug by degradation, metabolism or simply absorption into the walls of the transwell insert (Larger et al., 2002).

In many drug-related studies, it is crucial to establish a mass balance within a specific range. Kluxen et al., reported the accepted mass balance ranges expected by different authority bodies (Kluxen et al., 2019). The cosmetics-specific guidance body requires the overall recovery to fall within 85-115% whereas, the European food safety authority recommends a more stringent range between 95-105%. In other studies, experiments performed using in vitro models were only considered acceptable if the recovery fell between 85-115% (Gupta et al., 2020; Henneberger et al., 2019; Henriques et al., 2023).

Traditionally, LC-MS/MS has been used alongside quantitative whole-body autoradiography (QWBA) for imaging and quantifying oral drugs within tissue and similar specimens. While LC-MS/MS has many advantages over QWBA, there are limitations when it is used alone as it has no imaging capabilities. Therefore, an additional imaging technique is needed to provide spatial information in drug absorption studies.

1.7 MSI

Mass spectrometry imaging (MSI) is an analytical technique by which mass spectra are collected from multiple points on a sample. The mass spectra are stitched together by software that produces a visual image; each mass spectrum represents a pixel within the

image. The image is viewed by selecting a specific m/z value from the range collected; the image shows a map of the ion distribution with an appropriate colour scale indicating its relative intensity. Using the software, multiple ion maps from a single acquisition can be overlaid to show the distribution of different species in relation to each other. For example, a lipid and drug ion map could be overlaid to show the location of the drug in the tissue.

1.7.1 MALDI MSI

MALDI MSI is a technique that allows the spatial distribution of a wide range of analytes on a surface to be mapped and visualised. An example of a MALDI mass spectrometer is the Bruker Autoflex III Smartbeam. This instrument, illustrated in Figure 1.21, is comprised of a MALDI source that uses a 355 nm solid state laser coupled to a TOF mass analyser that operates in linear or reflectron mode. For the imaging of tissue, the sample must be sectioned to create a flat surface. For this technique, multiple mass spectra are generated by firing the laser in a raster along the surface of the tissue. The ions generated are separated in the TOF according to their mass and charge. When the ions reach the detector, their velocities are recorded and converted into a series of mass spectra. The use of additional software allows the mass spectra to be translated into images displaying relative intensities.

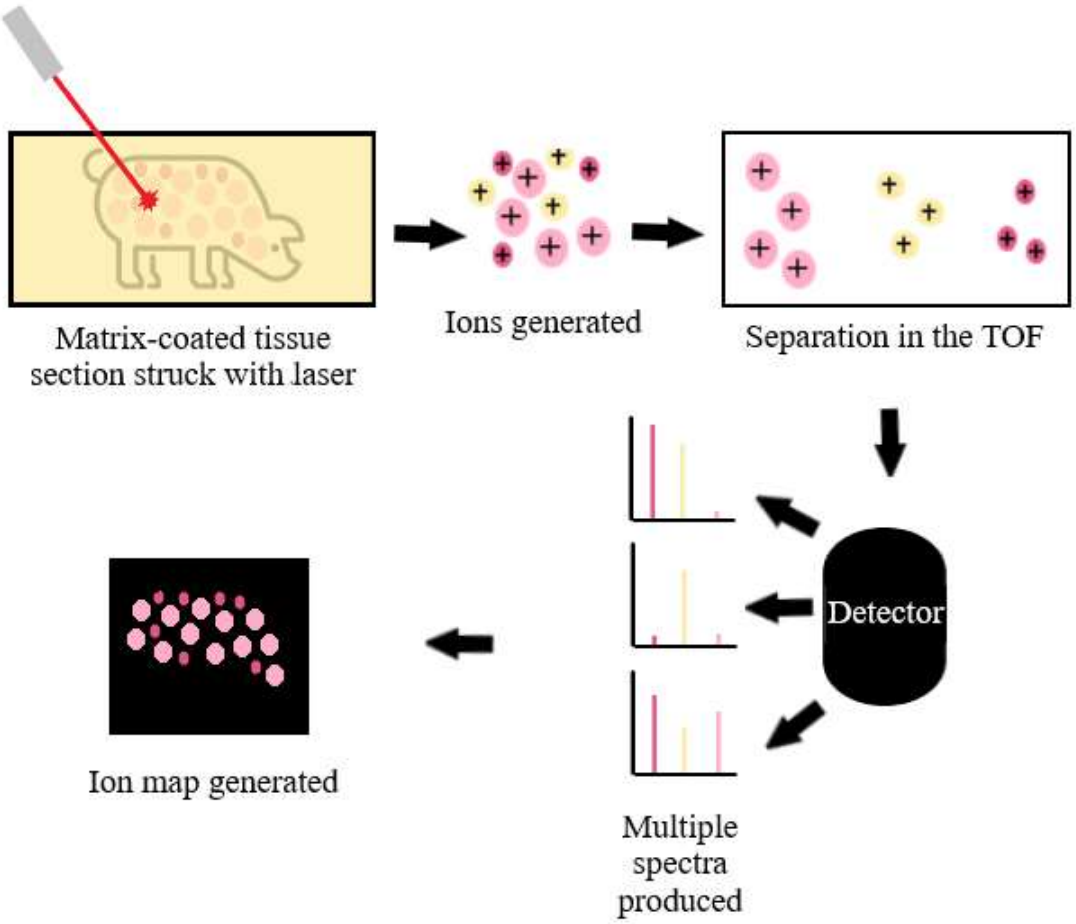

Figure 1.21: *A MALDI MSI workflow specific to the mass analyser on the Bruker Autoflex III Smartbeam.*

1.7.1.1 Applications

A benefit of MALDI MSI is that it allows the simultaneous detection of multiple compounds such as peptides, lipids and drugs which in turn, provides another layer of information to the spatial distribution of an analyte. Consequently, MALDI MSI is a powerful imaging technique commonly used to map the distribution of drugs through tissue. A drug development research group explored the potential for therapeutic peptides to be used in molecular-targeted therapy by administering octreotide to a group of mice (Takai et al., 2013). The liver and kidney from the dosed mice were then sectioned and imaged using MALDI MSI; the distribution of octreotide was successfully visualised in both organs (Takai et al., 2013). Additional steps were taken to allow quantification of the octreotide in the sections (Takai et al., 2013). In this instance, MALDI MSI was able to provide valuable spatial and quantitative information

on the distribution of the therapeutic peptide in biological tissue from an in vivo experiment.

In addition to biological drugs, MALDI MSI can identify crucial endogenous structures within the tissue such as biomarkers. The ability to discover biomarkers within tissue sections makes MALDI MSI an invaluable technique in cancer research where biomarker discovery is paramount. The Schwamborn research group analysed sections from healthy and cancerous prostate biopsies using MALDI MSI (Schwamborn et al., 2007). From this analysis, differences in protein expression were identified between the healthy and malignant tissue (Schwamborn et al., 2007). When the matrix was rinsed from the analysed sections and histologically stained, the cancerous and non-cancerous regions correlated with those identified from the MALDI MSI image (Schwamborn et al., 2007). Here, MALDI MSI demonstrated its potential clinical importance and ability to classify prostate tissue samples.

In addition to biomarker discovery, MALDI MSI has been used to simultaneously visualise disease biomarkers and their corresponding drug treatments to investigate whether the treatment has reached the infection site. Researchers affiliated with the Public Health Research Institute used MALDI MSI to analyse lung biopsies taken from tuberculosis lesions that had been treated with rifampicin (Blanc et al., 2018). Mycobacteria-specific lipid markers were identified in conjunction with metabolites associated with rifampicin; the infected area and drug metabolites were shown to be distributed in the same area which was later corroborated by histological staining of the same sections (Blanc et al., 2018). Therefore, MALDI MSI was able to confirm that the treatment had reached the site of action and had begun to metabolise.

MALDI MSI has been successfully employed to assess drug absorption through laboratory grown tissue in addition to ex vivo tissue. Russo et al., conducted a study which investigated the absorption of terbinafine from cream applied to a living skin equivalent (LSE) using MALDI MSI; it was observed that terbinafine had penetrated the surface of the LSE (Russo, Brickelbank et al., 2018). One drawback of MSI has historically been its limited quantitative abilities; the technique has commonly been referred to as ‘semi-quantitative’ and restricted to relative concentrations due to ion suppression effects (Tobias & Hummon, 2020). Recent advances in mass spectrometry have led to the development of quantitative MSI which requires additional steps compared to standard MSI. A range of serial diluted standards containing a relevant

internal standard need to be accurately spotted onto the tissue in order to create a calibration curve. Quantitative MSI was employed in the terbinafine study and enabled the drug concentration in the LSE to be determine (Russo et al., 2018). This was repeated for other LSEs that had been treated with different concentrations of terbinafine which enabled a useful, quantitative comparison. Studies such as this demonstrate that MSI can be performed in a quantitative manner when the correct experimental protocol is applied.

1.7.2 DESI MSI

DESI MSI is an ambient imaging technique that allows the spatial distribution of ions on the surface of a sample in its native state to be mapped and visualised. An example of a DESI mass spectrometer is the Waters Select Series MRT. This instrument, illustrated schematically in Figure 1.22, is comprised of a DESI source coupled to a quadrupole and MRT mass analyser.

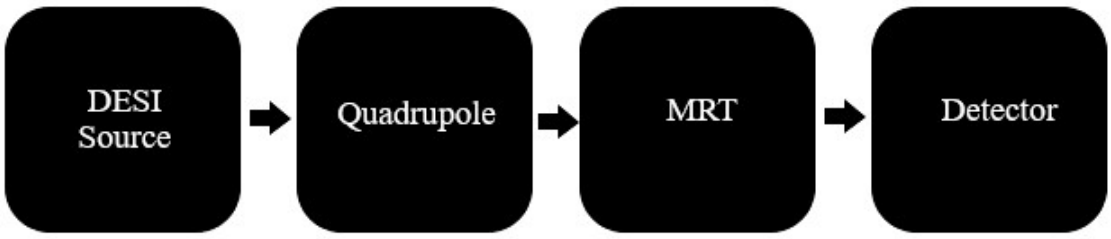

Figure 1.22: *A basic schematic of the main components in the Waters Select Series MRT.*

When imaging tissue sections using this technique, multiple mass spectra are generated when the DESI sprayer is moved over the surface of the tissue. The ions generated during this process are directed into the quadrupole and MRT where they are separated according to their mass and charge. When the ions reach the detector, their velocities are recorded and converted into a series of mass spectra. The use of additional software allows the mass spectra to be translated into images displaying relative intensities.

1.7.2.1 Applications

Historically, the gold standard imaging technique, QWBA, required radiolabelling to map the distribution of oral drugs in tissue. The major downfall of using radiolabels is that the experiment becomes limited to one analyte per experiment. Thus, drugs and tissue related ions could not be evaluated at the same time. Furthermore, the location of

the radiolabel is critical as the radiolabel can remain on the drug metabolite thus meaning it is impossible to distinguish between drug and metabolite signals. Like MALDI MSI, DESI MSI is a technique that does not require radiolabelling to observe analytes and allows simultaneous multi-ion detection. This feature, in combination with its ambient environment, makes it an ideal technique for whole-body analysis which is commonly used in early drug discovery and development. Recently, a research group successfully employed DESI MSI to investigate the distribution and metabolism of cyclosporine in whole body sections (Holm et al., 2022). Several laboratory rats were dosed with cyclosporine and sacrificed at different time points following administration; whole body sections were then collected and analysed using DESI MSI (Holm et al., 2022). The distribution of cyclosporine and its metabolites were successfully visualised in the whole-body sections and demonstrated how the distribution altered over time. The ambient conditions of DESI MSI allow more freedom in the sample holder and as such, it can accommodate larger samples such as rat whole-body sections.

A major benefit to DESI MSI is that minimal sample preparation is required compared to other techniques. This is particularly useful in a clinical setting as it allows for quick analysis. The Bensussan research group demonstrated the capabilities of DESI MSI in lung cancer diagnosis (Bensussan et al., 2020). Sections of healthy lung tissue along with those pre-diagnosed with varying subtypes of lung cancer were analysed by DESI MSI before standard histological staining (Bensussan et al., 2020). The mass spectra obtained were used to generate a statistical classification model to diagnose and subtype lung cancer; the model was successfully validated by inputting mass spectra acquired from fine needle aspiration (FNA) samples (Bensussan et al., 2020). The ability to correctly diagnose lung cancer from FNA samples highlights the real-life benefits of a non-destructive imaging technique that can simultaneously detect multiple ions in a timely manner.

DESI MSI has been successfully employed in drug absorption studies using ex vivo tissue. A recent research study was conducted using DESI MSI to explore the distribution of xenobiotics and endogenous lipids on an ex vivo skin model (Quartier et al., 2021). Three medicinal creams were applied to porcine skin in an ex vivo model. DESI MSI of the skin sections successfully demonstrated that the active ingredient in the cream had penetrated deep into the tissue for each cream (Quartier et al., 2021). Numerous endogenous compounds and excipients were simultaneously visualised in the

skin section which provided valuable detail on the penetration route exhibited by the active ingredient (Quartier et al., 2021). The simultaneous detection of a wide range of different molecules is highly desired in drug absorption studies as it provides further detail on penetration pathways which leads to better understanding.

Due to the growing number of successful studies using both MALDI and DESI MSI to detect and map xenbiotic distribution in ex vivo tissue, it was hypothesised that mass spectrometry imaging could provide important information relating to the absorption of oral drugs through the GI tract as well as aid in the optimisation of drug absorption systems.

1.8 Thesis Aims & Objectives

As discussed, there are many different well established GI models for the study of drug absorption, each with their own advantages and limitations. It is clear that recent developments in GI models have favoured animal-free techniques with the advancement of organoids becoming more prevalent; this movement can easily be anticipated given the ban of animal testing on cosmetic products. Nevertheless, much more work is needed for drug research to become predominately animal-free.

The overall aim of this thesis was to find a suitable GI model to act as a stepping stone between in vivo animal studies and animal-free techniques. The model would also need to be suitable for the study of oral drug absorption using a range of mass spectrometry techniques that have been previously discussed. The initial objective was to select a GI model that would be suitable for mass spectrometry imaging and optimise the system for drug absorption studies. The subsequent objective was to develop and optimise a mass spectrometry imaging method for the detection and visualisation of an oral drug within tissue. Another objective was to develop a mass spectrometry method to quantify the amount of drug from each component of the drug absorption experiment; this included the amount of drug that had permeated into the tissue and through it as well as assessing the total percentage of drug recovered from the experiment. The final objective was to perform a series of drug absorption experiments with different formulations to assess the effect of different excipients and, simultaneously, the performance of the optimised system.

The work reported in this thesis uses a pre-existing cell culture system that has been modified to create a versatile, millifluidics device capable of housing viable ex vivo

tissue for a suitable duration. The combination of MSI and LC-MS/MS has been used to explore the absorption of atorvastatin through porcine intestinal tissue along with the influence of relevant excipients. The adapted system has demonstrated the effect of excipients such as Mapcho-12 and DEGEE under different pH environments. Throughout the series of excipient studies performed, the adapted system demonstrated potential to be a versatile system although areas for further improvement were identified that should be addressed before trialling with more precious animal-free models such as organoids.

References

Abuhelwa, A. Y., Williams, D. B., Upton, R. N., & Foster, D. J. R. (2017). Food, gastrointestinal pH, and models of oral drug absorption. *European Journal of Pharmaceutics and Biopharmaceutics, 112*, 234-248.

Arnold, Y. E., Thorens, J., Bernard, S., & Kalia, Y. N. (2019). *Drug transport across porcine intestine using an ussing chamber system: Regional differences and the effect of P-glycoprotein and CYP3A4 activity on drug absorption*. MDPI AG. 10.3390/pharmaceutics11030139

Bensussan, A. V., Lin, J., Guo, C., Katz, R., Krishnamurthy, S., Cressman, E., & Eberlin, L. S. (2020). *Distinguishing non-small cell lung cancer subtypes in fine needle aspiration biopsies by desorption electrospray ionization mass spectrometry imaging*. Oxford University Press (OUP). 10.1093/clinchem/hvaa207

Blanc, L., Lenaerts, A., Dartois, V., & Prideaux, B. (2018). Visualization of mycobacterial biomarkers and tuberculosis drugs in infected tissue by MALDI-MS imaging. *Analytical Chemistry, 90*(10), 6275-6282.

Boegh, M., García-Díaz, M., Müllertz, A., & Nielsen, H. M. (2015). *Steric and interactive barrier properties of intestinal mucus elucidated by particle diffusion and peptide permeation*. Elsevier BV. 10.1016/j.ejpb.2015.01.014

Bulin, A., Broekgaarden, M., & Hasan, T. (2017). *Comprehensive high-throughput image analysis for therapeutic efficacy of architecturally complex heterotypic organoids*. Springer Science and Business Media LLC. 10.1038/s41598-017-16622-9

Chadha, G., Sathigari, S., Parsons, D. L., & Jayachandra Babu, R. (2010). *In vitropercutaneous absorption of genistein from topical gels through human skin*. Informa UK Limited. 10.3109/03639045.2010.525238

Dahan, A., Beig, A., Lindley, D., & Miller, J. M. (2016). The solubility–permeability interplay and oral drug formulation design: Two heads are better than one. *Advanced Drug Delivery Reviews, 101*, 99-107. 10.1016/j.addr.2016.04.018

Dahlgren, D., Roos, C., Sjögren, E., & Lennernäs, H. (2014). *Direct in vivo human intestinal permeability (peff) determined with different clinical perfusion and intubation methods*. Elsevier BV. 10.1002/jps.24258

Darji, M. A., Lalge, R. M., Marathe, S. P., Mulay, T. D., Fatima, T., Alshammari, A., Lee, H. K., Repka, M. A., & Narasimha Murthy, S. (2017). *Excipient stability in oral solid dosage forms: A review*. Springer Science and Business Media LLC. 10.1208/s12249-017-0864-4

Dinh, M. N., Hitomi, M., Al-Turaihi, Z. A., & Scott, J. G. (2023). Alamar blue assay optimization to minimize drug interference and inter-assay viability.10.1101/2023.03.16.532999

Ewart, L., Apostolou, A., Briggs, S. A., Carman, C. V., Chaff, J. T., Heng, A. R., Jadalannagari, S., Janardhanan, J., Jang, K., Joshipura, S. R., Kadam, M. M., Kanellias, M., Kujala, V. J., Kulkarni, G., Le, C. Y., Lucchesi, C., Manatakis, D. V., Maniar, K. K., Quinn, M. E., . . . Levner, D. (2021). *Qualifying a human liver-chip for predictive toxicology: Performance assessment and economic implications*. Cold Spring Harbor Laboratory. 10.1101/2021.12.14.472674

Global pharmaceutical industry - statistics & facts. (2019, Aug 13,). Statista. Retrieved Aug 19, 2020, from https://www.statista.com/topics/1764/global-pharmaceutical-industry/

Goel, R., Bhardwaj, S., & Bana, S. (2024). *Pharmaceutical excipients*. Elsevier. 10.1016/b978-0-323-91817-6.00003-6

Gupta, M. M., Khoorban, A., Ali, A., Ramlogan, O., & Talukdar, D. (2020). *Comparative quality control study of different brands of diclofenac sodium tablet available in local and government pharmacies by in-vitro testing*. Springer Science and Business Media LLC. 10.7759/cureus.11348

Ha, E., Lee, S., Choi, D. H., Jeong, S. H., Hwang, S., & Kim, M. (2020). Application of diethylene glycol monoethyl ether in solubilisation of poorly water-soluble drugs. *Journal of Pharmaceutical Investigation, 50*, 231-250. https://doi.org/10.1007/s40005-019-00454-y

Hankin, J. A., Barkley, R. M., & Murphy, R. C. (2007). Sublimation as a method of matrix application for mass spectrometric imaging. *Journal of the American Society for Mass Spectrometry, 18*(9), 1646-1652. 10.1016/j.jasms.2007.06.010

Hemmilä, S., Ruponen, M., Toropainen, E., Tengvall-Unadike, U., Urtti, A., & Kallio, P. (2020). *Microflow-based device for in vitro and ex vivo drug permeability studies*. Elsevier BV. 10.1177/2472630320916190

Henneberger, L., Mühlenbrink, M., Heinrich, D. J., Teixeira, A., Nicol, B., & Escher, B. I. (2019). *Experimental validation of mass balance models for in vitro cell-based bioassays*. American Chemical Society (ACS). 10.1021/acs.est.9b06144

Henriques, P., Bicker, J., Carona, A., Miranda, M., Vitorino, C., Doktorovová, S., & Fortuna, A. (2023). *Amorphous nasal powder advanced performance: In vitro/ex vivo studies and correlation with in vivo pharmacokinetics*. Springer Science and Business Media LLC. 10.1007/s40005-023-00630-1

Hoffmann, E. d., & Stroobant, V. (2007). *Mass spectrometry* (3. Aufl. ed.). Wiley-Interscience.

Holm, N. B., Deryabina, M., Knudsen, C. B., & Janfelt, C. (2022). *Tissue distribution and metabolic profiling of cyclosporine (CsA) in mouse and rat investigated by DESI and MALDI mass spectrometry imaging (MSI) of whole-body and single organ cryo-sections*. Springer Science and Business Media LLC. 10.1007/s00216-022-04269-z

Homayun, B., Lin, X., & Choi, H. (2019). Challenges and recent progress in oral drug delivery systems for biopharmaceuticals. *Pharmaceutics, 11*(3), 129. 10.3390/pharmaceutics11030129

Ichikawa, M., Akamine, H., Murata, M., Ito, S., Takayama, K., & Mizuguchi, H. (2021). *Generation of tetracycline-controllable CYP3A4-expressing caco-2 cells by the piggyBac transposon system*. Springer Science and Business Media LLC. 10.1038/s41598-021-91160-z

Iribarne, J. V., & Thomson, B. A. (1976). On the evaporation of small ions from charged droplets. *The Journal of Chemical Physics, 64*(6), 2287-2294. 10.1063/1.432536

Javadzadeh, Y., & Hamishehkar, H. (2010). *Enhancing percutaneous delivery of methotrexate using different types of surfactants*. Elsevier BV. 10.1016/j.colsurfb.2010.09.015

Kaja, S., Payne, A. J., Naumchuk, Y., & Koulen, P. (2018). *Quantification of lactate dehydrogenase for cell viability testing using cell lines and primary cultured astrocytes*. Wiley. 10.1002/cptx.21

Kaneda, A., Nishimura, K., Muranishi, S., & Sezaki, H. (1974). Mechanism of drug absorption from micellar solution. II. effect of polysorbate 80 on the absorption of micelle-free drugs. *Chemical & Pharmaceutical Bulletin, 22*(3), 523-528. 10.1248/cpb.22.523

Kassem, A. M., Ibrahim, H. M., & Samy, A. M. (2018). *Development and optimisation of atorvastatin calcium loaded self-nanoemulsifying drug delivery system (SNEDDS) for enhancing oral bioavailability: In vitro and in vivo evaluation*. Informa UK Limited. 10.1080/02652048.2017.1328464

Kleiveland, C. R. (2015). *Co-cultivation of caco-2 and HT-29MTX*. Springer International Publishing. 10.1007/978-3-319-16104-4_13

Kluxen, F. M., Grégoire, S., Schepky, A., Hewitt, N. J., Klaric, M., Domoradzki, J. Y., Felkers, E., Fernandes, J., Fisher, P., Mceuen, S. F., Parr-Dobrzanski, R., & Wiemann, C. (2019). *Dermal absorption study OECD TG 428 mass balance recommendations based on the EFSA database*. Elsevier BV. 10.1016/j.yrtph.2019.104475

Larger, P., Altamura, M., Catalioto, R., Giuliani, S., Maggi, C. A., Valenti, C., & Triolo, A. (2002). *Simultaneous LC−MS/MS determination of reference pharmaceuticals as a method for the characterization of the caco-2 cell monolayer absorption properties*. American Chemical Society (ACS). 10.1021/ac020265r

LECO Corporation. (2018). *Encoded frequent Pushing Improving duty cycle in the folded flight path high resolution time-of-flight mass spectrometry.* ().

Lennernas, H. (2003). Clinical pharmacokinetics of atorvastatin. *Clinical Pharmacokinetics, 42*(13), 1141-1160. 10.2165/00003088-200342130-00005

Lin, L., & Wong, H. (2017). Predicting oral drug absorption: Mini review on physiologically-based pharmacokinetic models. *Pharmaceutics, 9*(4), 41. 10.3390/pharmaceutics9040041

Liu, D., Lecluyse, E. L., & Thakker, D. R. (1999). *Dodecylphosphocholine-mediated enhancement of paracellular permeability and cytotoxicity in caco-2 cell monolayers*. American Geophysical Union (AGU). 10.1021/js990094e

Mapcho®-12. (2024, April,). Avanti Polar Lipids Products. https://avantilipids.com/product/850336

Masaoka, Y., Tanaka, Y., Kataoka, M., Sakuma, S., & Yamashita, S. (2006). *Site of drug absorption after oral administration: Assessment of membrane permeability and luminal concentration of drugs in each segment of gastrointestinal tract*. Elsevier BV. 10.1016/j.ejps.2006.06.004

Nichani, K., Li, J., Suzuki, M., & Houston, J. P. (2020). *Evaluation of Caspase-3 activity during apoptosis with fluorescence Lifetime-Based cytometry measurements and phasor analyses*. Wiley. 10.1002/cyto.a.24207

Nicolazzo, J. A., Reed, B. L., & Finnin, B. C. (2005). Buccal penetration enhancers—How do they really work? *Journal of Controlled Release, 105*(1-2), 1. 10.1016/j.jconrel.2005.01.024

Patterson, J. K., Lei, X. G., & Miller, D. D. (2008). *The pig as an experimental model for elucidating the mechanisms governing dietary influence on mineral absorption*. Frontiers Media SA. 10.3181/0709-mr-262

Qiu, Y., Chen, Y., Zhang, G., Yu, L., & Mantri, R. (2017). *Developing solid oral dosage forms* (2nd ed.). Mica Henley.

Quartier, J., Rao, W., Slade, S., Métral, F., Lapteva, M., & Kalia, Y. N. (2021). *DESI-MS imaging to visualize spatial distribution of xenobiotics and endogenous lipids in the skin*. Elsevier BV. 10.1016/j.ijpharm.2021.120967

Ravikanth, P. V., & Ramanamurthy, K. V. (2018). Permeability assessment of drug substances using in vitro and ex vivo screening techniques. *Innovations in Pharmaceuticals and Pharmacotherapy, 6*(2), 17-20.

Reig-López, J., García-Arieta, A., Mangas-Sanjuán, V., & Merino-Sanjuán, M. (2021). Current evidence, challenges, and opportunities of physiologically based pharmacokinetic models of atorvastatin for decision making. *Pharmaceutics, 13*(5), 709. 10.3390/pharmaceutics13050709

Reno, F. E., Normand, P., Mcinally, K., Silo, S., Stotland, P., Triest, M., Carballo, D., & Piché, C. (2015). *A novel nasal powder formulation of glucagon: Toxicology studies in animal models*. Springer Science and Business Media LLC. 10.1186/s40360-015-0026-9

Russo, C., Brickelbank, N., Duckett, C., Mellor, S., Rumbelow, S., & Clench, M. R. (2018). Quantitative investigation of terbinafine hydrochloride absorption into a living skin equivalent model by MALDI-MSI. *Analytical Chemistry, 90*(16), 10031-10038. 10.1021/acs.analchem.8b02648

Russo, C., Lewis, E. E. L., Flint, L., & Clench, M. R. (2018). Mass spectrometry imaging of 3D tissue models. *Proteomics, 18*(14), e1700462-n/a. 10.1002/pmic.201700462

Sato, T., Vries, R. G., Snippert, H. J., Van De Wetering, M., Barker, N., Stange, D. E., Van Es, J. H., Abo, A., Kujala, P., Peters, P. J., & Clevers, H. (2009). *Single Lgr5 stem cells build crypt-villus structures in vitro without a mesenchymal niche*. Springer Science and Business Media LLC. 10.1038/nature07935

Schwamborn, K., Krieg, R., Reska, M., Jakse, G., Knuechel, R., & Wellmann, A. (2007). Identifying prostate carcinoma by MALDI-imaging. *International Journal of Molecular Medicine, 20*(2), 155-159. 10.3892/ijmm.20.2.155

Shim, S., Belanger, M. C., Harris, A. R., Munson, J. M., & Pompano, R. R. (2020). *Two-way communication betweenex vivotissues on a microfluidic chip: Application to tumor–lymph node interaction*. Royal Society of Chemistry (RSC). 10.1039/c8lc00957k

Sjöberg, Å, Lutz, M., Tannergren, C., Wingolf, C., Borde, A., & Ungell, A. (2012). *Comprehensive study on regional human intestinal permeability and prediction of fraction absorbed of drugs using the ussing chamber technique*. Elsevier BV. 10.1016/j.ejps.2012.10.007

Spencer, C. E., Flint, L. E., Duckett, C. J., Cole, L. M., Cross, N., Smith, D. P., & Clench, M. R. (2020). Role of MALDI-MSI in combination with 3D tissue models for early stage efficacy and safety testing of drugs and toxicants. *Expert Review of Proteomics, 17*(11-12), 827-841. 10.1080/14789450.2021.1876568

Srinivasan, B., Kolli, A. R., Esch, M. B., Abaci, H. E., Shuler, M. L., & Hickman, J. J. (2015). TEER measurement techniques for in vitro barrier model systems. *Journal of the Association for Laboratory Automation (Charlottesville, Va.), 20*(2), 107-126. 10.1177/2211068214561025

Super refined™ DEGEE . (2024, April,). CRODA Pharma Product Finder. https://www.crodapharma.com/en-gb/product-finder/product/5421-super_1_refined_1_degee

Takai, N., Tanaka, Y., Watanabe, A., & Saji, H. (2013). Quantitative imaging of a therapeutic peptide in biological tissue sections by MALDI MS. *Bioanalysis, 5*(5), 603-612. 10.4155/bio.13.13

Thomas, D. P., Zhang, J., Nguyen, N., & Ta, H. T. (2023). *Microfluidic gut-on-a-chip: Fundamentals and challenges*. MDPI AG. 10.3390/bios13010136

timsTOF fleX MALDI-2. (2024, August). Bruker. https://www.bruker.com/en/products-and-solutions/mass-spectrometry/timstof/timstof-flex-maldi-2.html

Tobias, F., & Hummon, A. B. (2020). Considerations for MALDI-based quantitative mass spectrometry imaging studies. *Journal of Proteome Research, 19*(9), 3620-3630. 10.1021/acs.jproteome.0c00443

Tsunoda, S. M., Gonzales, C., Jarmusch, A. K., Momper, J. D., & Ma, J. D. (2021). Contribution of the gut microbiome to drug disposition, pharmacokinetic and pharmacodynamic variability. *Clinical Pharmacokinetics, 60*(8), 971. 10.1007/s40262-021-01032-y

Wang, Y., Kim, R., Gunasekara, D. B., Reed, M. I., Disalvo, M., Nguyen, D. L., Bultman, S. J., Sims, C. E., Magness, S. T., & Allbritton, N. L. (2018). *Formation of human colonic crypt array by application of chemical gradients across a shaped epithelial monolayer*. Elsevier BV. 10.1016/j.jcmgh.2017.10.007

Wu, X., Whitfield, L. R., & Stewart, B. H. (2000). Atorvastatin transport in the caco-2 cell model: Contributions of P-glycoprotein and the proton-monocarboxylic acid co-transporter.*17*, 209-215.

Yang, S., Hu, H., Kung, H., Zou, R., Dai, Y., Hu, Y., Wang, T., Lv, T., Yu, J., & Li, F. (2023). *Organoids: The current status and biomedical applications*. Wiley. 10.1002/mco2.274

Zhang, M., Liu, Y., & Chen, Y. (2020). *Generation of 3D human gastrointestinal organoids: Principle and applications*. Springer Science and Business Media LLC. 10.1186/s13619-020-00040-w

Chapter 2:

A Proof-of-Concept Study Performed within a QV600 LLI System Adapted to House Frozen Porcine Intestinal Tissue

The experimental data in this chapter was published as Spencer, C. E., Rumbelow, S., Mellor, S., Duckett, C. J., & Clench, M. R. (2022). Adaptation of the Kirkstall QV600 LLI Microfluidics System for the Study of Gastrointestinal Absorption by Mass Spectrometry Imaging and LC-MS/MS. *Pharmaceutics*, *14*(2), 364. https://doi.org/10.3390/pharmaceutics14020364

2.1 Introduction

Within the pharmaceutical industry, a variety of dosage forms have been developed for the purpose of administering medication. Amongst those, oral administration remains the most popular route with patients (Berben et al., 2018; Lin & Wong, 2017). The ease of delivery and non-invasive nature of oral drug delivery contribute to the high level of patient compliance experienced with this route. However, the study of drug absorption within the gastrointestinal (GI) tract is highly complex.

As detailed in Chapter 1, the oral route is comprised of several different organs meaning that there are varying tissue structures as well as fluctuating conditions to replicate in order to create a realistic model for study. It is critical that any model used to study drug permeation and absorption resembles real-life. The production and secretion of gastric acid within the stomach creates an extremely acidic environment ranging between pH 1-3 (Hsu et al., 2021) before rapidly increasing to pH 6 when passing through the duodenum of the small intestine; the pH neutralises during passage of the large intestine (Fallingborg, 1999). The importance of correctly modelling the pH extremes and fluctuations should not be overlooked as some drug classes could be released too early from their formulation or undergo degradation which would greatly reduce the amount of drug reaching the site of action (Qiu et al., 2017).

Specialised structures and mechanisms are needed to withstand the harsh conditions presented by extreme acidic environments. Specialised foveolar cells, exclusive to the stomach, produce mucus which lines the gastric mucosa and provides protection from the gastric acid (Hsu et al., 2021). In addition to this, the duodenum of the small intestine has Brunner's glands within its submucosa layer that secrete an alkaline mucus to protect the small intestine and help to neutralise the highly acidic contents that enter from the stomach (Sedano et al., 2015). The presence of mucus is an important feature of the small intestine that should not be disregarded when attempting to develop a realistic GI model. Mucus production can be highly variable between individuals as well as within individuals making it difficult to replicate and create reproducible data from. Nevertheless, mucus production is an important variable that ought to be included within a model when attempting to simulate real-life as it can greatly hinder drug absorption and permeation.

Another obstacle faced when attempting to model the oral administration route is the different mechanisms exhibited by organs along the tract. While the stomach and small intestine essentially share the same function of breaking down GI contents, they utilise different techniques to achieve this. Aided by digestive juices, the stomach has a unique muscle layer known as the oblique layer that uses grinding and mixing movements to break the stomach contents down (Hsu et al., 2021). The small intestine, on the other hand, lacks this specialised muscle layer and instead, utilises bile and enzymes to break down gastric contents whilst using peristaltic contractions to move them further along the tract. The difference in mechanisms for movement along the tract adds another layer of complexity to modelling the full GI tract as a multi-compartment model would be needed.

As mentioned in Chapter 1, circular folds in the lumen of the small intestine known as plicae circulares, found in part of the duodenum and the entirety of the jejunum and ileum, greatly increase the surface area of this organ and thereby, improve the rate of absorption (Collins et al., 2021). This makes the small intestine an ideal organ to focus on for drug absorption studies.

Despite the complexity of the GI tract hindering the development of alternatives to animal models for the study of drug absorption and excipient performance (Kaur et al., 2018), the need for realistic organ and tissue models is becoming more apparent as animal testing for research purposes is losing societal acceptance (Russo et al., 2018). Under the Cosmetic Directive 76/768/EEC, the EU prohibited testing cosmetic products and cosmetic ingredients on animals in 2004 and 2009, respectively. In 2013, a complete EU ban on animal testing for cosmetics came into full force which prohibits the marketing of any cosmetics in the EU that have been tested on animals. This movement has undoubtedly sparked concern within the pharmaceutical research industry with a significant rise in the amount of research studies that use animal testing alternatives (Russo et al., 2018). Well-established alternatives include the use of cultured cells and ex vivo tissue housed in microfluidic systems (Qiu et al., 2017).

For oral drug absorption and permeation research, a common cell line used are colorectal adenocarcinoma (Caco-2) cells. These cells are typically cultured within microfluidic devices or systems in order to study drug permeation and absorption. Caco-2 cells have been successfully used in a membrane bioreactor that was influenced by the QV600 LLI produced by Kirkstall Ltd. (York, UK) (Giusti et al., 2014). The feasibility

of the membrane bioreactor as a dynamic intestinal barrier model when combined with Caco-2 cells was successfully demonstrated (Giusti et al., 2014). Although this cell line is considered to be a gold standard, it lacks drug metabolizing P450 enzymes which are essential to accurately represent the absorption of drug classes such as statins (Berben et al., 2018; Küblbeck et al., 2016). Whilst P450 enzyme activity largely occurs in the liver, cytochrome P450 can be found in the epithelial cells of the GI tract (Qiu et al., 2017). Thus, monocultured cells are not the most suitable system for the study of every drug class.

The major benefit of using ex vivo intestinal tissue is that it maintains important morphological and physiological features of the intestine which aid drug absorption; including the plicae circulares that drastically increase the surface area in the intestine and thus, enhance drug absorption. A popular microfluidic system used to house ex vivo intestinal tissue is the Ussing chamber. Arnold et al. conducted a study focused on combining porcine intestinal tissue with the Ussing chamber to evaluate drug transport and absorption (Arnold et al., 2019). The study was successful and demonstrated that ex vivo porcine tissue was compatible with the Ussing chamber system. A limitation of this system is that the removal of the muscle-serosal layer (required for its usage) is complex and labour intensive (Clarke, 2009; Volpe, 2010). Additionally, the classic Ussing chamber model does not allow the simultaneous analysis of several tissue segments unlike more recently developed multichannel Ussing systems (although these are expensive). Ex vivo small intestine tissue can remain viable for up to 3 h which makes it ideal for drug absorption and permeation studies as drug absorption in the small intestine is rapid. However, this makes ex vivo models unsuitable for long-term exposure studies, unlike cell culture.

Three-dimensional cell models, such as organoids and organ-on-a-chip, combine some of the advantages of 2D cultured cells and ex vivo tissue while eliminating some associated limitations. Organoids are 3D structures that have been derived from patient stem cells or biopsies that can be grown to mimic a particular organ. Organoids contain significantly more morphological and physiological features of an organ than a 2D cell line, which is one of the major advantages that ex vivo tissue has over 2D cell lines. In addition, organoids, have an exceptional viability window in comparison to ex vivo tissue. Wetering et al., report that a healthy tissue-derived organoid is viable after 6 days of drug incubation (van de Wetering et al., 2015). This is significantly longer than the

viability of ex vivo tissue. Similarly, to 2D cell lines, the limitation of 3D cell models is the amount of time required to culture the cells until they are fully differentiated when compared to ex vivo studies. The animal tissue used for such studies can be quickly acquired from abattoirs or in-house laboratory animals on the day of study. Whereas, the culture of cells can take up to a number weeks; caco-2 cell culture requires 21 days to demonstrate characteristics of the small intestine, as an example (Natoli et al., 2012). Organ-on-a-chip technology such as microfluidic intestine chip models, are cells cultured in hollow microchannels within a microfluidic device. Primary human cells are cultured in the device which allows the formation of a structure that closely resembles the 3D architecture of real human organs (Kim & Takayama, 2015; Wnorowski et al., 2019). The miniature design of the device leads to the formation of bubbles which are easily formed but difficult to remove (Kim & Takayama, 2015). The presence of bubbles in the device can lead to detachment and damage to the cells (Kim & Takayama, 2015). Specialized microengineering skills are needed in addition to equipment such as pumps and cleanrooms, thereby making the model an expensive one (Kim & Takayama, 2015). Although relatively more expensive when compared to ex vivo model studies, organ-on-a-chip technology provides the possibility for longer experimentation time and for a morphology similar to that of the human organ.

All models discussed play a part in drug absorption studies, each with their own benefits and limitations when compared with another. The choice of model is unique to the individual based upon factors including, but not limited to, funding, available facilities, and the purpose of the experiment. In this chapter, an existing cell culture system known as the QV600 LLI system (Kirkstall Ltd., York, UK) has been successfully adapted to produce a millifluidics device that is compatible with ex vivo porcine intestinal tissue rather than cells alone.

The advantages of adapting the QV600 LLI to house larger samples such as ex vivo tissue is that this makes it a unique, versatile system that can hold ex vivo tissue, human biopsy tissue, and organoids as well as 2D cell lines. This allows contrasting sample types to be directly compared within the same environment and comparative studies to be performed. Another advantage of this system is that many accessories are commercially available to allow for example in situ sampling and closed or open circuit experiments to be performed. In addition to this, multiple chambers can be added to allow for different regions of the intestine to be studied simultaneously.

The adaptation of QV600 LLI was developed using ex vivo tissue rather than organoids or any other cell culture as the tissue was readily available and relatively inexpensive which was essential during the development stages. Unlike other commercially available microfluidic systems, the modified system is versatile and can house different sample types; this allows for comparative studies between opposing sample types within the same environment. In addition, its modular nature provides further flexibility in terms of the types of experiments that can be performed.

Using the adapted millifluidics device with ex vivo tissue, experiments were performed to study the absorption of the statin, Atorvastatin, through the apical layers of intestinal tissue. As discussed in Chapter 1, Atorvastatin is ideal for a proof-of-concept study using frozen tissue as it can move through tissue via passive diffusion. MALDI MSI has been applied to show the spatial distribution of Atorvastatin within the tissue. An LC-MS/MS method has been fully optimized to quantify the amount of Atorvastatin in the tissue, basal circuit and other relevant areas to complete a mass balance and thus, aid in the development of the millifluidics device. The LC-MS/MS method was developed in order to act as a validation method that will pave the way for the development of a successful QMSI method in future work.

2.2 Chapter Aims

The aim of the following chapter was to adapt an existing cell culture system into a cost-effective millifluidics system that could house ex vivo tissue and demonstrate its capabilities in drug permeation studies. The initial objective focused on adapting the system so that the acceptor and donor circuits were separated entirely; where the only possibility of the drug entering the acceptor circuit required the drug to pass through the ex vivo tissue rather than migrate around it. The final objective saw the adapted millifluidics system used to perform a set of absorption experiments ran in triplicate with differing amounts of excipient to investigate how this may affect permeation and thereby, demonstrate proof-of-concept.

2.3 Materials and Methods

2.3.1 Materials

Gibco BenchStable DMEM/F12, phosphate-buffered saline (PBS), 2-methylbutane 99+% extra pure, LC-Grade methanol, LC-Grade acetonitrile (ACN), and acetone were

purchased from Fisher Scientific Ltd**.** (Loughborough, UK). Atorvastatin calcium, α-Cyano-4-hydroxycinnamic acid (α-CHCA) and 2,5-Dihydroxybenzoic acid (DHB) were purchased from Sigma Aldrich (Dorset, UK). The deuterated internal standard, Atorvastatin-(anilide ring-d5) calcium salt was purchased from Merck Life Sciences (Dorset, UK). Formic acid 98% was purchased from Scientific Laboratory Supplies (Nottingham, UK). 18.2 MΩ × cm water was collected from an ELGA water purification system (Buckinghamshire, UK). Cryo-M-Bed was purchased from VWR International Ltd**.** (Lutterworth, UK). Porcine small intestine was provided by R.B Elliott & Son (Chesterfield, UK). Super refined Polysorbate (80) LQ was donated by CRODA (DE, USA).

2.3.2 Tissue Collection and Preparation

The duodenum region of the small intestine from an adult pig was collected and prepared within 1 h post-mortem. Using a scalpel, the intestine was cut down its length and opened into a flat sheet. The tissue was then snap-frozen in liquid nitrogen cooled 2-methylbutane and stored at −80 °C until needed. To prepare for drug absorption experiments, the frozen tissue was submerged in PBS until completely thawed. The serosal-muscle layer was carefully removed from the flat sheet of intestinal tissue with a scalpel. A 10 mm diameter tissue punch was then used to remove a disc from the remaining tissue.

2.3.3 Drug Absorption Experiments

The drug absorption experiments were performed in the Quasi Vivo® QV600 LLI system purchased from Kirkstall Ltd**.** (York, UK). The disc of tissue was adhered to a MilliCell insert with the basal layer facing the mesh. The insert was fitted into the chamber of the QV600 so that the upper (donor) circuit flowed above the tissue and the lower (acceptor) circuit flowed below the insert. Three chambers were set up within this system to allow three tissue discs to run simultaneously under the same experimental conditions; this has been illustrated in Figure 2.1.

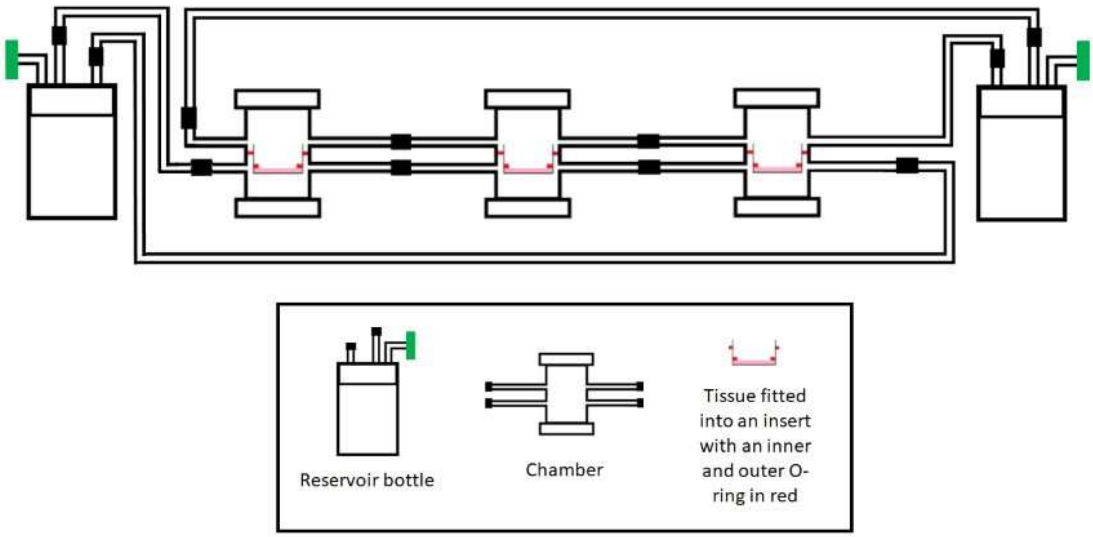

Figure 2.1: *A schematic of the Quasi Vivo® QV600 LLI with three tissue discs fitted into the chambers.*

The donor circuit was filled with 0.5 mg/mL of Atorvastatin in phosphate-buffered saline and the acceptor circuit was filled with Gibco BenchStable DMEM/F12. All air bubbles were removed while filling. Using a peristaltic pump, the flow rate of the donor and acceptor circuit was set to 0.2 mL/min and 0.1 mL/min, respectively, before the whole system was then transferred to an incubator for 6 h at 37 °C, 5% CO_2. The circuit fluids were collected, before removing the tissue discs, and stored at 5 °C. The tissue discs were rinsed with PBS before being snap-frozen in liquid nitrogen cooled 2-methylbutane and stored at −80 °C. The whole QV600 system was thoroughly cleaned using 70% methanol in water and then rinsed with PBS. The solutions used to clean the system and the PBS used to rinse the tissue were collected for the mass balance study and stored at 5 °C.

After the initial drug absorption experiment, a series of experiments were performed with varied concentrations of the excipient polysorbate-80 added to the donor circuit alongside 0.5 mg/mL of Atorvastatin. The experiment had otherwise run under the same conditions as described for the initial drug absorption experiment.

2.3.4 Cryosectioning

Tissue discs were transferred to the Leica CM 1950 Cryostat (Leica Microsystems, Milton Keynes, UK). The discs were mounted onto a cork ring using Cryo-M-Bed

embedding compound and were allowed to thermally equilibrate for 1 h. The chamber and specimen head temperature were set at −20 °C. Each tissue disc was cryosectioned into 14 µm sections and thaw mounted onto indium tin oxide (ITO) coated glass slides. The sections were then vacuum packed and stored at −80 °C.

2.3.5 Matrix Application

In total, 19 mg of DHB matrix was dissolved in 15 mL of acetone and added to the bottom of the sublimation apparatus (Sigma-Aldrich, Gillingham, UK). An ITO glass slide containing the tissue disc section was secured to the flat surface within the top section of the sublimation apparatus. The top and bottom of the sublimation apparatus were then assembled using the O-ring seal and the vacuum was applied to seal. Once the vacuum had stabilized at 5×10^{-2} Torr, the top was filled with ice and the temperature was set at 180 °C. The sublimation process was stopped after 15 min.

2.3.6 Mass Spectrometry Imaging

All tissue sections in this study were imaged using a Bruker Autoflex III mass spectrometer. The instrument calibration was performed with CHCA matrix. The MALDI MS images were acquired in positive ion mode focused on a range of *m*/*z* 120–1500 Da. The spatial resolution was set to 100 µm × 100 µm. Three separate sections from the same absorption experiment were imaged within the same batch.

2.3.7 Tissue Extraction and Sample Preparation

Each tissue disc was added to 30 mL of methanol: water (9:1, *v*/*v*) and homogenized. The donor circuit, acceptor circuit, and the solutions collected from rinsing the tissue and the system were each separately added 50:50 *v*/*v* to a solution of methanol: water (9:1 *v*/*v*). All of the solutions were then centrifuged for 5 min at 3000 ×*g*. The supernatant was collected for LC-MS/MS analysis. From a 50 µg/mL Atorvastatin stock solution, 6 standards and a blank were made ranging from 0–10 µg/mL. All standards and samples were prepared with an internal standard, 2.5 µg/mL of Atorvastatin-d5, matrix matched, and run-in triplicate.

2.3.8 LC-MS/MS

All LC-MS/MS experiments were performed using the Agilent 6420 triple quad mass spectrometer in negative ion mode. The analyser was set to detect the product ion of Atorvastatin-d5 calcium salt (*m*/*z* 562 -> *m*/*z* 458) and the product ion of Atorvastatin

calcium salt (*m*/*z* 557 -> *m*/*z* 453) in multiple reaction monitoring (MRM) mode. An Agilent EclipsePlusC18 RRHD 1.8 µm 2.1 × 50 mm column was used. The mobile phase consisted of water: ACN: methanol (41:19:40, *v*/*v*/*v*) with 0.005% formic acid and was used in isocratic mode at a flow rate of 0.275 mL/min.

2.3.9 Data Analysis

MALDI MS data were processed using the FlexImaging software from Bruker Daltonics. For the LC-MS/MS data, the chromatographic peaks for Atorvastatin and Atorvastatin-d5 were integrated and processed using the Agilent MassHunter Quantitative Analysis Version 8.09 software. This software was also used to create the calibration graph from the standards and calculate the concentration of all the samples. The back-calculations from software generated concentrations were performed manually.

The apparent permeability coefficient for transport across porcine intestinal tissue ($P_{app,pig}$) was determined for each drug absorption experiment performed in the study (Arnold et al., 2019). The following equation was used to determine the Papp,pig value for each experiment:

$$P_{\text{app,pig}} = \frac{dc}{dt} \times \frac{V}{A \times C_0} \left(\frac{cm}{s}\right)$$

where dc/dt is the change in the acceptor concentration calculated using the final concentration in the acceptor circuit divided by the length of the experiment (6 h), V is the volume in the donor circuit (30 mL), A is the exposed surface area (0.785 cm^2), and C_0 is the initial concentration of Atorvastatin in the donor circuit (500 µg/mL).

2.4 Results and Discussion

2.4.1 QV600 LLI Adaptation

The QV600 LLI system was adapted to hold an ex vivo intestinal tissue disc in a Millicell insert without allowing the donor and acceptor circuit to interact (Figure 2.2). A complete barrier between these circuits was essential as any leakage of the donor circuit into the acceptor circuit would give a false representation of the movement of Atorvastatin through the tissue. The intestinal tissue was cut into a disc using a biopsy punch that was slightly larger than the bottom of the insert. Thus, the tissue disc would cover the mesh layer at the bottom of the insert entirely. To prevent any movement or

shifting of the tissue disc during the experiment, the tissue disc was fixed to the mesh and in addition, a silicon O-ring was fitted into the insert and placed on top of the tissue to seal off the edges as they were the most susceptible to movement. The original set-up of QV600 LLI with cells advertised by Kirkstall Ltd. allowed for free movement between the two circuits. With the adaptation reported here for use with ex vivo tissue, the system was more susceptible to pressure build-ups when following the original set-up guidance which would lead to leaks between the two circuits. A different set-up method was established which reduced the pressure build-up during the initial system set-up and prevented leakages from occurring. The system was run with the flow rates in the donor and acceptor circuits calculated to be 0.2 mL/min and 0.1 mL/min, respectively.

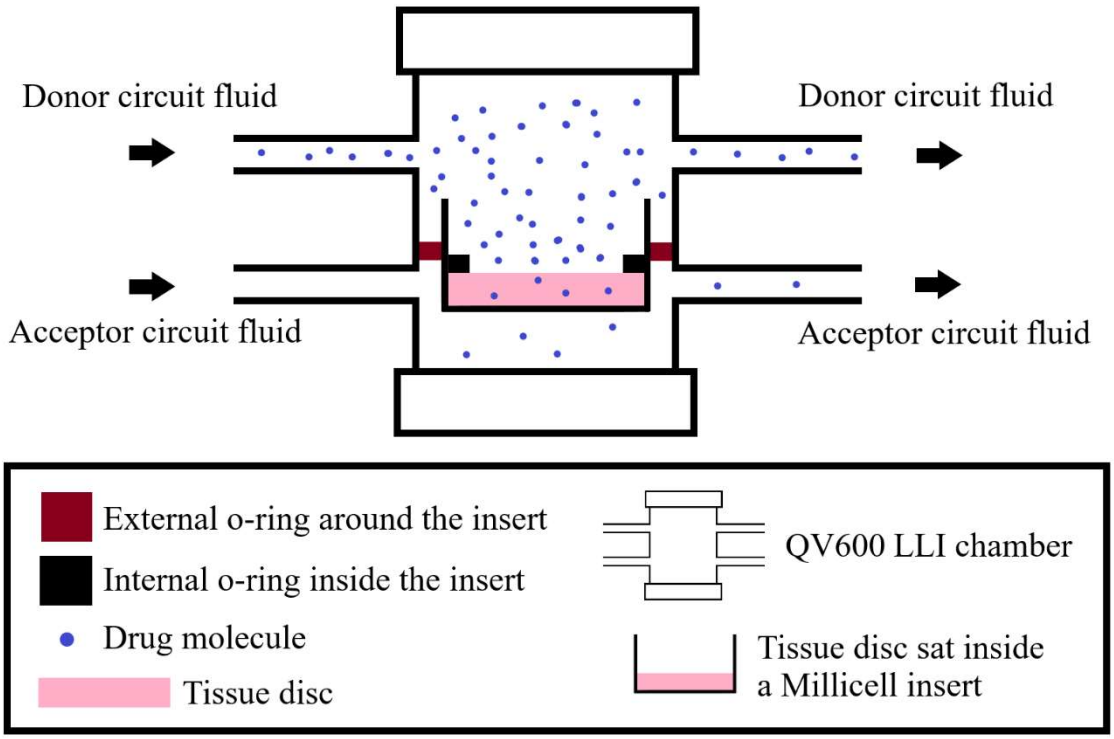

Figure 2.2: *Adaptation of the QV600 LLI (Kirkstall Ltd.) millifluidics cell culture chamber to hold ex vivo tissue.*

During the adaptation, development, and testing of the QV600 LLI, previously snap-frozen tissue was used. Therefore, there was no need to assess the viability of the tissue as this was lost during the freezing process. Thus, the experiment time was based upon the highest estimate for intestinal transit time which ranges between 3–6 h in the small intestine specifically (Slavin, 2013). Therefore, the experiments were performed for 6 h to ensure that the drug exposure time did not exceed what it would be in a whole organ.

This also would allow for time point studies to be conducted using sampling ports to assess how drug absorption is affected over time. It should be noted that once viable (rather than frozen) tissue is introduced into the system, the viability of the tissue will need to be assessed. Atorvastatin is rapidly absorbed after administration with a peak plasma concentration reported between 1–2 h which would make the study of Atorvastatin absorption appropriate for this millifluidics experimental set up as other ex vivo models have reported tissue viability up to 3 h (McIver & Siddique, 2021).

2.4.2 Development of MALDI MSI for the Detection of Atorvastatin

A MALDI MS method was developed to profile the protonated molecule, sodium, and potassium adducts of Atorvastatin at *m/z* 559, *m/z* 581, and *m/z* 597, respectively, in positive ion mode. Initially, several different MALDI matrices were trialled for the detection of Atorvastatin, including CHCA. The optimal matrix was found to be DHB. Atorvastatin was dissolved in methanol: water (9:1, *v*/*v*) to create a series of known standards to test the sensitivity of the profiling method. The method was continuously improved to detect the three Atorvastatin-related peaks in prepared standards as low as 0.01 mg/mL. The MALDI MS profiling method was then converted into a MALDI MS imaging method using FlexControl version 3.4 software.

The MALDI MS imaging method was then used to image 0.5 µL spots of known Atorvastatin standards that had been pipetted onto 14 µm sections of untreated duodenum intestinal tissue. The imaging method and matrix application were optimised to increase the signal from the protonated molecule, sodium, and potassium adducts of Atorvastatin when in the presence of tissue.

Once the imaging method was optimised, it was then ready to use for the imaging of tissue sections acquired from drug absorption experiments.

2.4.3 Development of LC-MS/MS for the Detection of Atorvastatin

An LC-MS/MS method was developed in MRM mode for the detection of Atorvastatin in tissue and liquid samples collected from the initial drug absorption experiment in the QV600 LLI. Matrix matched standards were prepared using the deuterated internal standard Atorvastatin-d5 to create a calibration graph for the quantification of

Atorvastatin in the tissue discs and each sample collected from the experiment. The samples collected were the donor circuit solution, the acceptor circuit solution, the solution used to rinse the tissue disc, the initial system rinse in 70% methanol, and the final system rinse in PBS. The amount of Atorvastatin in each sample was quantified and used to establish a mass balance. The mass balance was calculated to ensure that an acceptable amount of the drug had been recovered in order to be representative of the drug movement through the system. Acceptable mass balances were considered to be between 85–115% for the purpose of this study.

The tissue discs were rinsed to remove any excess Atorvastatin that had not absorbed into the tissue. The final system rinse was collected to ensure that the QV600 LLI was considered analytically clean for the next experiment and also, to confirm that all the drug had been recovered from the system by the system rinse in 70% methanol. The collection of these samples was essential for the calculation of the mass balance, although they provide no context to the movement of the drug.

Due to matrix effects from the DMEM, an extensive matrix matched formula was developed for the preparation of the samples. Despite this, matrix effects were still experienced when the drug had originally dissolved in DMEM such as in the acceptor circuit. Therefore, an additional set of calibration standards were made using a stock solution in which Atorvastatin had been dissolved in DMEM prior to matrix matching the standards.

In addition to performing a mass balance, the concentration of Atorvastatin in the acceptor circuit was calculated to determine the amount of drug that travelled through the tissue disc and thereby, accumulated in the acceptor circuit.

2.4.4 Removal of Muscle-Serosal Layer

The muscle-serosal layer was left intact for the initial imaging drug absorption experiment to aid the visualisation of the distribution of the Atorvastatin within the section when Peyer's patches are present. The experiment ran for 6 h with 0.5 mg/mL Atorvastatin passing over the surface of the apical layer of the duodenum intestinal tissue. The tissue discs from this experiment were cryosectioned and imaged using an optimised MALDI MS imaging method. The images generated from this experiment were reproducible in the three sections that were taken from one of the tissue discs, as shown in Figure 2.3.

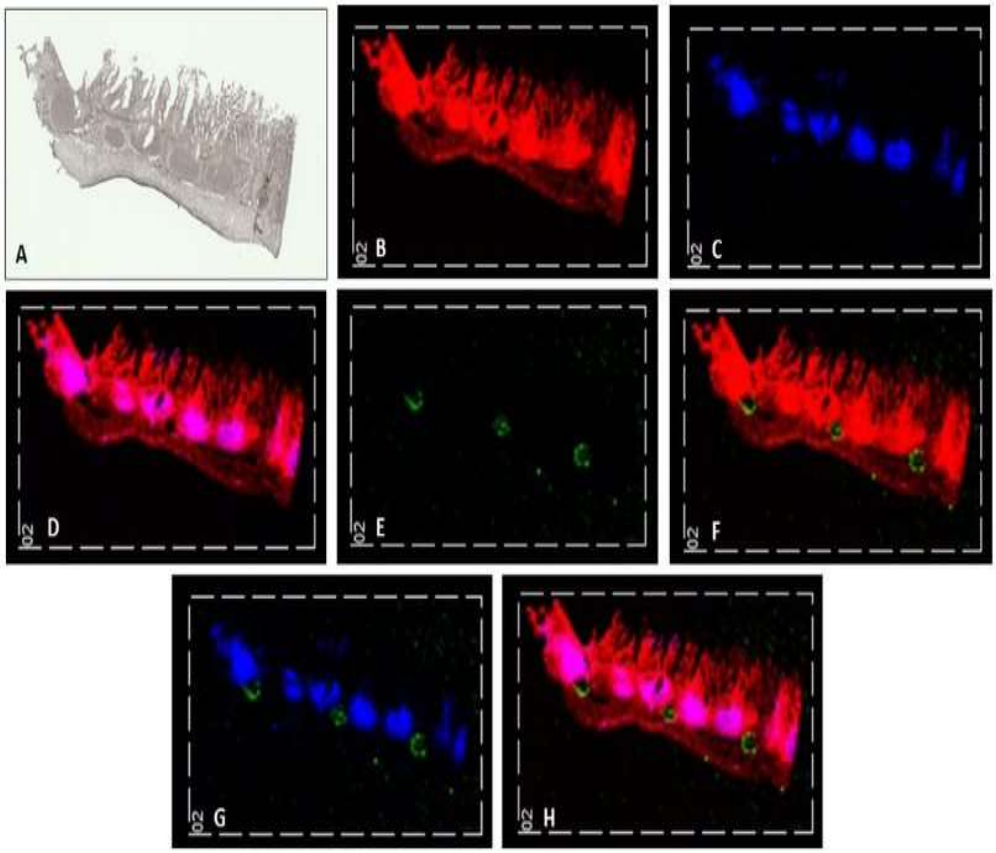

***Figure 2.3**: Using the QV600 LLI, intact porcine small intestinal tissue was treated with 0.5 mg/mL Atorvastatin over a 6 h period to investigate drug absorption. (A) A scanned image of the intestinal tissue section taken using a Super Coolscan 5000 ED Film Scanner with the apical layer facing upwards. (B) A MALDI-MS image showing cholesterol $[Chol+H-H_2O]^+$ at m/z 369 in red. (C) A MALDI-MS image showing the Peyer's patches at m/z 389 in blue. (D) A MALDI-MS image showing cholesterol $[Chol+H-H_2O]^+$ at m/z 369 in red and Peyer's patches in blue; overlapping ions are shown in pink. (E) A MALDI-MS image showing the sodium adduct of atorvastatin at m/z 581 in green. (F) A MALDI-MS image showing the sodium adduct of atorvastatin at m/z 581 in green and cholesterol $[Chol+H-H_2O]^+$ at m/z 369 in red. (G) A MALDI-MS image showing sodium adduct of atorvastatin (m/z 581) in green and Peyer's patches (m/z 389) in blue. (H) A MALDI-MS image showing the sodium adduct of atorvastatin at m/z 581 in green, cholesterol $[Chol+H-H_2O]^+$ at m/z 369 in red and Peyer's patches in blue; overlapping ions are shown in pink.*

The distribution of *m/z* 369 outlined the whole tissue section, showing unique characteristics of the section which can be identified by comparing Figure 2.3A and B. The distribution of *m/z* 389 outlines a collection of lymphatic vessels within the tissue

known as Peyer's patches. These two ions were overlaid with *m/z* 581, the sodiated adduct of Atorvastatin as shown in Figure 2.3H. The identification of tissue structures in addition to the drug molecule in the tissue section using the MALDI MS imaging method provides invaluable spatial information that gives an insight into drug distribution within the tissue. The sodiated adduct of Atorvastatin is shown distributed in between the Peyer's patches in the submucosal layer. In the image, the sodiated adduct appears to be pooled on top of the muscle-serosal layer and did not appear to have passed through the Peyer's patches.

The drug absorption experiment was repeated with the muscle-serosal layer carefully removed (as would be the case in the millifluidics device). The MALDI MSI images obtained are shown in Figure 2.4. Interestingly, here the 'pooling' of the drug (imaged in green) is not observed clearly demonstrating that the presence of the muscle-serosal layer in the absence of blood flow hinders the movement of Atorvastatin as might be expected.

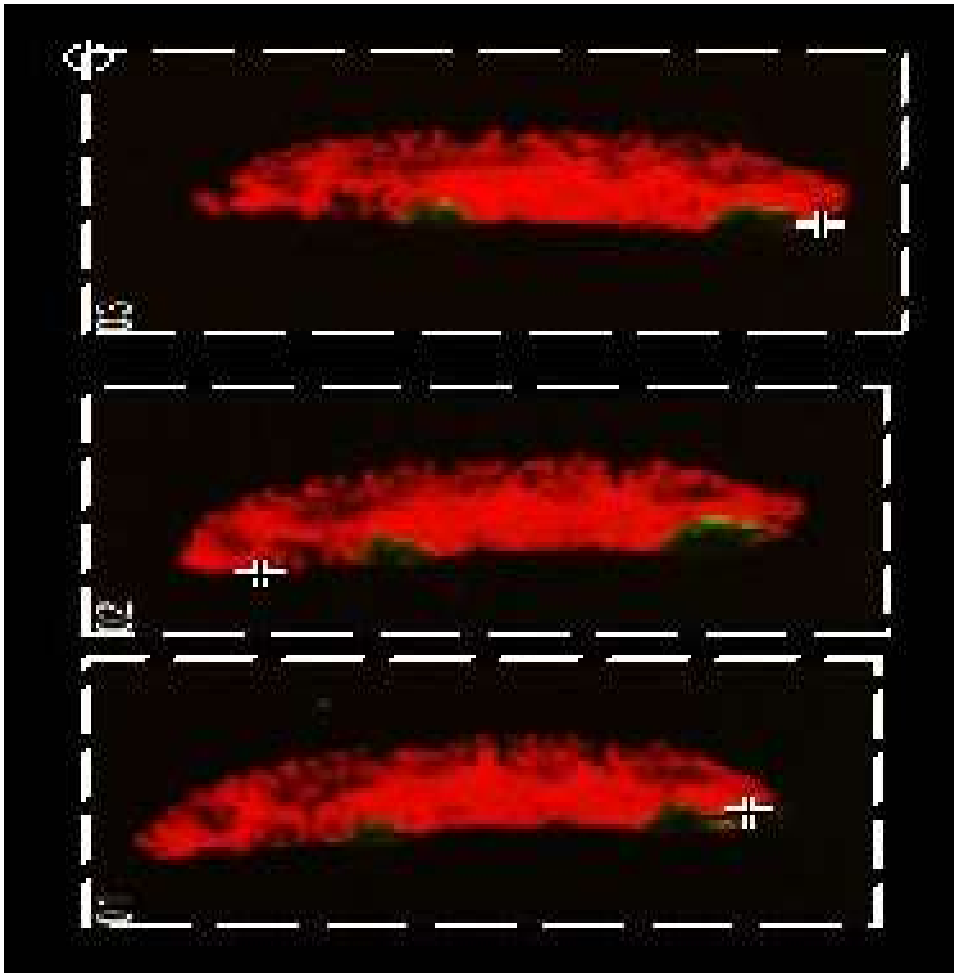

***Figure 2.4**: Using the QV600 LLI, porcine small intestinal tissue with the muscle-serosal layer removed was treated with 0.5 mg/mL Atorvastatin over a 6 h period to investigate drug absorption. A MALDI-MS image was generated showing cholesterol [Chol+H-H_2O]$^+$ at m/z 369 in red and protonated molecule of atorvastatin at m/z 559 in green.*

Additionally observable in these data is the variability of the tissue structure of sections taken from the duodenum of the same animal. In Figure 2.3, a number of Peyer's patches can be seen; however, in Figure 2.4, none are observable. This indicates that care must be taken when selecting tissue for the chambers as there is high variability even within the same region of the small intestine.

2.4.5 The Addition of Polysorbate-80 to the Adapted QV600 LLI

A series of experiments were performed as described in the section 2.3.3 with the muscle-serosal layer removed. The experiments varied by the addition of the CRODA

Inc product “Super Refined Polysorbate-80”. (Note: The specific concentrations and ingredients used in the refinement of the excipient are proprietary). An initial experiment was performed as a control with no excipient added to the donor circuit. Five additional experiments were performed with different volumes of the excipient added to the donor circuit; these consisted of 0.4% *v*/*v*, 0.8% *v*/*v*, 1% *v*/*v*, 1.5% *v*/*v*, and 2% *v*/*v* refined polysorbate 80.

In Figure 2.5, an apparent increase in the absorption of Atorvastatin can be seen when 0.4 % *v*/*v* polysorbate-80 is added to the donor circuit. Above this concentration, no obvious effect was observed by increasing the amount of polysorbate 80. This is in agreement with other published work (Kaneda et al., 1974). They commented that there were two levels of surfactant effect on the absorption of drugs in the intestine. An absorption enhancing effect at low concentrations and a small inhibiting effect at higher concentrations. Interestingly, these effects have also been observed in this proof-of-concept study even though previously frozen tissue (i.e., active transport mechanisms and functional metabolising enzyme would not be expected to be present) was used. However, even with this system what has been termed “a solubility–permeability interplay” is still observable (Dahan et al., 2016).

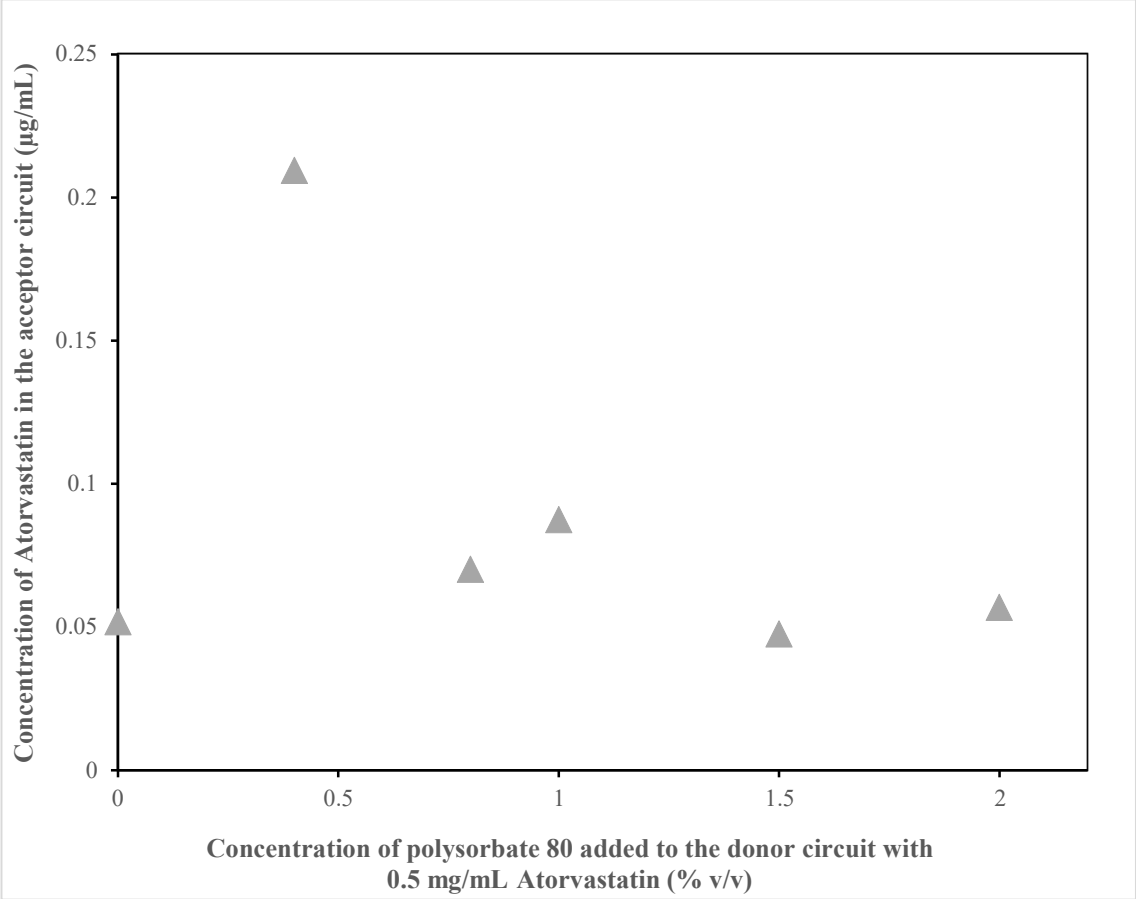

Figure 2.5: *A graph showing the concentration of atorvastatin recovered from the acceptor circuit against the concentration of Polysorbate-80 added to the donor circuit in that experiment. Each experiment, represented by the triangle marker, used previously frozen porcine small intestinal tissue from the same animal (specifically the duodenum)(n=1).*

Arnold et al. have conducted a study investigating the passive diffusion of eleven drugs through viable porcine intestines using an Ussing chamber system (Arnold et al., 2019). Apparent permeability coefficients ($P_{app,pig}$) were calculated and compared to known permeability coefficients determined in humans in vivo, $P_{eff,human}$. The study reports a range of $P_{app,pig}$ values for BCS class II drugs which span between 4.26×10^{-6} cm/s and 45.47×10^{-6} cm/s when in different donor circuit environments (Arnold et al., 2019). When comparing the $P_{app,pig}$ values for BCS class II drugs with those determined in this proof-of-concept study, the values are of a similar order of magnitude as those reported. Thereby providing confidence that the adapted QV600 LLI has great potential for use in this field of work when viable tissue/3D cell culture models are used. The relevant $P_{app,pig}$ values calculated for this study are shown in Table 2.1.

Table 2.1: *The apparent permeability coefficient values for the passive absorption of Atorvastatin through ex vivo porcine tissue from a series of drug absorption experiments conducted using the modified QV600 LLI system in the presence of increasing amounts of the solubilizing agent polysorbate 80. (With corresponding mass balance data) (n=1).*

Concentration of Excipient Added to Donor Circuit (% *v/v*)	Concentration of Atorvastatin in Acceptor Circuit (µg/mL)	Apparent Permeability Coefficient ($P_{app,pig}$) (10^{-6} cm/s)	Mass Balance (%)
0	0.052	0.234	95.2 ± 0.25
0.4	0.209	0.942	90.9 ± 0.67
0.8	0.074	0.336	95.9 ± 1.4
1	0.078	0.352	95.6 ± 2.6
1.5	0.046	0.207	94.3 ± 1.2
2	0.050	0.225	116.4 ± 1.1

It is important to highlight that the data provided in the proof-of-concept study have been acquired from ex vivo tissue that was previously frozen, whereas in the study of Arnold et al., viable tissue has been used (Arnold et al., 2019). Now that the proof-of-concept study has proven that the QV600 LLI can be successfully adapted to house ex vivo tissue and produce data comparable to permeation studies carried out by other ex vivo models, the next logical steps would be to repeat this study using ex vivo tissue that has not been previously frozen. The reason for this being that any P450 enzymatic activity within the small intestine would have been disabled during the freezing process. The presence of P450 enzymes in the small intestine contributes to the extensive metabolism of Atorvastatin prior to reaching systemic circulation, leading to the oral bioavailability of this drug reportedly as low as 14% (Lennernäs, 2009). From here, a direct comparison can be made between ex vivo tissue and the classical caco-2 cell line from within the QV600 LLI model. As the classical caco-2 cell line lacks P450 enzymes, it would be interesting to see the impact this could have on the permeation of Atorvastatin through the small intestine.

Due to the versatility of the QV600 LLI, this allows comparative studies to be performed within the same system as ex vivo human samples, cultured cells and

organoids could be held in individual chambers. This would make for an interesting comparison between the apparent permeability coefficients to human in vivo data, thereby giving an insight into how the different types of models compare with each other in terms of their comparability to human in vivo studies.

2.5 Conclusions

This proof-of-concept study has demonstrated that the adapted QV600 LLI system is suitable for studying drug absorption in the gastrointestinal tract using ex vivo porcine tissue. Initial studies carried out using formerly frozen tissue showed the expected effects of a solubilising excipient on drug absorption. Further work will be carried out to repeat this study using fresh porcine tissue and further demonstrate the potential of the system for excipient studies where active transport mechanisms exist. Further modifications to the system by the incorporation of sampling ports will also allow for time point studies. The adaptation for ex vivo tissue allows the study of natural tissue structure using imaging techniques which is important to assess tissue variability. The use of mass spectrometry imaging allows not only the study of drug distribution and tissue pathology, but with further development will allow the quantification of the drug directly within the tissue sections.

References

Arnold, Y. E., Thorens, J., Bernard, S., & Kalia, Y. N. (2019). *Drug transport across porcine intestine using an ussing chamber system: Regional differences and the effect of P-glycoprotein and CYP3A4 activity on drug absorption*. MDPI AG. 10.3390/pharmaceutics11030139

Berben, P., Bauer-Brandl, A., Brandl, M., Faller, B., Flaten, G. E., Jacobsen, A., Brouwers, J., & Augustijns, P. (2018). Drug permeability profiling using cell-free permeation tools: Overview and applications. *European Journal of Pharmaceutical Sciences, 119*, 219-233. 10.1016/j.ejps.2018.04.016

Clarke, L. L. (2009). A guide to ussing chamber studies of mouse intestine. *American Journal of Physiology: Gastrointestinal and Liver Physiology, 296*(6), G1151-G1166. 10.1152/ajpgi.90649.2008

Collins, J., Nguyen, A., & Nadireddy, M. (2021). *StatPearls: Anatomy, abdomen and pelvis, small intestine*. Treasure Island (FL): StatPearls Publishing.

Dahan, A., Beig, A., Lindley, D., & Miller, J. M. (2016). The solubility–permeability interplay and oral drug formulation design: Two heads are better than one. *Advanced Drug Delivery Reviews, 101*, 99-107. 10.1016/j.addr.2016.04.018

Fallingborg, J. (1999). Intraluminal pH of the human gastrointestinal tract. *Danish Medical Bulletin, 46*(3), 183-196. http://europepmc.org/abstract/MED/10421978

Giusti, S., Sbrana, T., La Marca, M., Di Patria, V., Martinucci, V., Tirella, A., Domenici, C., & Ahluwalia, A. (2014). A novel dual-flow bioreactor simulates increased fluorescein permeability in epithelial tissue barriers. *Biotechnology Journal, 9*(9), 1175-1184. 10.1002/biot.201400004

Hsu, M., Safadi, A., & Lui, F. (2021). *StatPearls: Physiology, stomach*. Treasure Island (FL): StatPearls Publishing.

Kaneda, A., Nishimura, K., Muranishi, S., & Sezaki, H. (1974). Mechanism of drug absorption from micellar solution. II. effect of polysorbate 80 on the absorption of micelle-free drugs. *Chemical & Pharmaceutical Bulletin, 22*(3), 523-528. 10.1248/cpb.22.523

Kaur, N., Narang, A., & Bansal, A. K. (2018). Use of biorelevant dissolution and PBPK modeling to predict oral drug absorption. *European Journal of Pharmaceutics and Biopharmaceutics, 129*, 222-246. 10.1016/j.ejpb.2018.05.024

Kim, S., & Takayama, S. (2015). Organ-on-a-chip and the kidney. *Kidney Research and Clinical Practice, 34*(3), 165-169. 10.1016/j.krcp.2015.08.001

Küblbeck, J., Hakkarainen, J. J., Petsalo, A., Vellonen, K., Tolonen, A., Reponen, P., Forsberg, M. M., & Honkakoski, P. (2016). *Genetically modified caco-2 cells with improved cytochrome P450 metabolic capacity*. Elsevier BV. 10.1016/s0022-3549(15)00187-2

Lennernäs, H. (2009). Ethanol−Drug absorption interaction: Potential for a significant effect on the plasma pharmacokinetics of ethanol vulnerable formulations. *Molecular Pharmaceutics, 6*(5), 1429-1440. 10.1021/mp9000876

Lin, L., & Wong, H. (2017). Predicting oral drug absorption: Mini review on physiologically-based pharmacokinetic models. *Pharmaceutics, 9*(4), 41. 10.3390/pharmaceutics9040041

McIver, L., & Siddique, M. (2021). *StatPearls: Atorvastatin*. Treasure Island (FL): StatPearls Publishing.

Natoli, M., Leoni, B. D., D'Agnano, I., Zucco, F., & Felsani, A. (2012). Good caco-2 cell culture practices. *Toxicology in Vitro, 26*(8), 1243-1246. 10.1016/j.tiv.2012.03.009

Qiu, Y., Chen, Y., Zhang, G., Yu, L., & Mantri, R. (2017). *Developing solid oral dosage forms* (2nd ed.). Mica Haley.

Russo, C., Lewis, E. E. L., Flint, L., & Clench, M. R. (2018). Mass spectrometry imaging of 3D tissue models. *Proteomics, 18*(14), e1700462-n/a. 10.1002/pmic.201700462

Sedano, J., Swamy, R., Jain, K., & Gupta, S. (2015). Brunner's gland hamartoma of the duodenum. *Annals of the Royal College of Surgeons of England, 97*(5), e70-e72. 10.1308/003588415X14181254790040

Slavin, J. (2013). 3 - health aspects of dietary fibre. *Fibre-rich and wholegrain foods* (pp. 61-75). Elsevier Ltd. 10.1533/9780857095787.1.61

van de Wetering, M., Francies, H., Francis, J., Bounova, G., Iorio, F., Pronk, A., van Houdt, W., van Gorp, J., Taylor-Weiner, A., Kester, L., McLaren-Douglas, A., Blokker, J., Jaksani, S., Bartfeld, S., Volckman, R., van Sluis, P., Li, V. W., Seepo, S., Sekhar Pedamallu, C., . . . Clevers, H. (2015). Prospective derivation of a living organoid biobank of colorectal cancer patients. *Cell, 161*(4), 933-945. 10.1016/j.cell.2015.03.053

Volpe, D. A. (2010). Application of method suitability for drug permeability classification. *The AAPS Journal, 12*(4), 670-678. 10.1208/s12248-010-9227-8

Wnorowski, A., Yang, H., & Wu, J. C. (2019). Progress, obstacles, and limitations in the use of stem cells in organ-on-a-chip models. *Advanced Drug Delivery Reviews, 140*, 3-11. 10.1016/j.addr.2018.06.001

Chapter 3:

Final Adaptations and Modifications to the QV 600 LLI Millifluidics System to House Fresh Viable Ex Vivo Porcine Intestinal Tissue

3.1 Introduction

While drug absorption studies can be performed employing non-viable tissue, the study would be heavily limited to the research of drugs that move by passive diffusion only. While passive diffusion is known to be a preferred route of absorption that remains functional in non-viable tissue, there are a number of other drug absorption mechanisms that are available to oral drugs (Qiu et al., 2017).

3.1.1 Absorption Routes

As detailed in Chapter 1, other categories of absorption include paracellular diffusion and carrier-mediated transport. Paracellular diffusion allows the transport of small hydrophilic and ionized drugs through tight junctions between cells. In addition to the amount and size of junctional gaps, the phenomenon is dependent upon the quality of the transmembrane proteins that regulate the barrier (Qiu et al., 2017). Thus, for this absorption route to be available, the tissue must be viable.

Carrier-mediated transport is an umbrella term for a number of other absorption mechanisms, including facilitated diffusion and active transport, that require carriers to mediate transport. The carriers needed for transport are primarily proteins and thus, require viable tissue (Mukherjee et al., 2017). Facilitated transport allows larger drug molecules to be transported across the membrane at a much faster rate. In addition to carriers, this mechanism requires a concentration gradient to function. Contrastingly, active transport is a mechanism that allows drug molecules to be transported across the membrane against a concentration gradient. However, for this to occur, ATP energy is required to activate the carrier transporters (Mukherjee et al., 2017). This type of energy would only be generated when the tissue is living (Dunn & Grider, 2024).

The additional absorption mechanisms require ATP energy and carrier transporters to be functional and therefore, necessitate the tissue to be viable.

3.1.2 Tissue Viability

To access the other absorption mechanisms and thus, broaden the use of an ex vivo gastrointestinal (GI) model, it should be capable of housing and maintaining viable tissue for a suitable amount of time. Tissue viability refers to the percentage of healthy cells within a given amount of tissue. The health of cells can be severely impacted by factors such as temperature, manual stress and time. When preparing porcine small

intestinal tissue for ex vivo models, it is commonly reported that the muscle-serosal layer is removed to reveal the arterial network within the mucosal layer (Ripken & Hendriks, 2015). The process of removing the muscle-serosal layer is widely considered destructive as well as a difficult procedure to perform. Thus, an assessment of the tissue viability before and after this procedure is advisable to assess its impact and ensure that the tissue remains viable. After such a procedure has been performed, the viability of the tissue could begin to rapidly decline; this should be carefully assessed to evaluate longevity.

It is crucial that the ex vivo tissue remains viable from the point of removal from the animal to the end of the experiment; this will ensure the absorption mechanisms available to the drug remain the same throughout. The duration of an absorption experiment should be relevant to the specific drug being investigated and the tissue type chosen. Information such as the peak plasma concentration should be taken into consideration when planning the length of an experiment. Once this has been established, the length of time the tissue remains viable for should be thoroughly evaluated. When contained within a closed system, factors such as pressure can cause stress to the cells within tissue and therefore, diminish viability. Thus, the effect of the system and any changes to the parameters should be carefully assessed to ascertain the effect this has on the viability of tissue. In addition, the length of time that the tissue can remain viable for within the system under these specified conditions should also be ascertained.

While data can be attained from other research studies, it is important that individual factors are taken into account when assessing the viability of tissue and thus, independent viability tests should be performed. The combination of the experimental conditions, system parameters, set up time, tissue preparation and transportation time have a unique impact on tissue viability. Therefore, adequate tests are essential to ensure that the viability of the tissue has not been severely impacted during the tissue preparation process or under the conditions within the system.

3.1.2.1 Tissue Viability Assessment

In contrast to cell culture, assessing the viability of ex vivo tissue has its own unique obstacles including the thickness of the tissue as well as an increase in autofluorescence. The viability of tissue can be assessed in a number of different ways however, in the

work reported here, caspase-3 and DAPI staining were chosen. The caspase-3 stain is an immunofluorescent stain that allows the visualisation of cell death caused by apoptosis; this is regarded to be the most common type of cell death. DAPI is used alongside this stain as it highlights the nuclei in each cell and thus, allows for the percentage of cell death to be established. In addition to this, the DAPI staining can be used to assess the morphology of the nuclei; this is particularly useful as nuclei shrinkage and debris is conclusive with cell death (Cummings & Schnellmann, 2013).

Caspase-3 and DAPI stain are suitable for tissue that has been fixed and cryosectioned, meaning this is an ideal technique for scenarios where viability can only be assessed after the experiment. The limited accessibility of the adapted millifluidics system later described meant it was not possible to use continuous in-line viability measurements without creating specially adapted equipment. In addition, the issues with pressure maintenance and build-up limit the number of viability assessment techniques that are possible.

3.1.3 Common Millifluidic System Challenges

While millifluidic systems have great benefits, as detailed in Chapter 1, like other model systems, they are not without challenges and limitations. A common issue experienced amongst microfluidic systems and millifluidic systems alike, is unintentional leakage. When leakage is experienced in such devices, this can result in the device not working correctly or giving false readings. It is therefore critical that the cause of the leak is identified and resolved. Visually apparent causes of leaks include physical actions such as bubble formation and vibrations. Both microfluidic and millifluidic systems are comprised of narrow tubing with a low total volume; while millifluidic systems are of a larger scale, they are still greatly subject to unwanted bubble formation. The presence of bubbles within the system leads to an increase in pressure. Alternatively, minor leaks can go undetected as they cannot be observed by the naked eye and thus, require internal monitoring of pressure, temperature and flow rate, to name a few. It is crucial that these challenges are identified and overcome as a rise in pressure can also alter the direction of the pressure gradient within the system.

3.1.4 Pressure Gradient

Within any system, there should be a pressure gradient across the tissue which drives the drug through. Solute passage tests were performed across an epithelial barrier within

a system very similar to that of the QV600 LLI by (Giusti et al., 2014). Using computational fluid dynamic (CFD) modelling and pressure measurements, the group assessed the effect of different flow rates and pressure differences within a bioreactor for maximum transport. The group were able to identify that when both circuits used the same flow rate and exhibited similar pressures, no driving pressure gradient force was present to aid mass transport. In addition, the group found that the solute exchange was at its maximum when there was high velocity flow over the membrane in addition to the pressure within the top chamber exceeding that within the bottom chamber (Giusti et al., 2014).

3.2 Chapter Aims

The aim of this chapter was to adapt and further optimise the QV600 LLI to be suitable for absorption experiments with fresh tissue. This was achieved by optimising both the system configuration, and the experimental timings to ensure that the tissue remained viable for the duration of the absorption experiment.

3.3 Materials and Methods

3.3.1 Materials

Gibco BenchStable DMEM/F12, phosphate-buffered saline (PBS), 2-methylbutane 99+% extra pure, LC-Grade methanol, LC-Grade acetonitrile (ACN), 4',6-diamidino-2-phenylindole (DAPI) and acetone were purchased from Fisher Scientific Ltd**.** (Loughborough, UK). Atorvastatin calcium, paraformaldehyde (PFA), Tween 20 and sucrose were purchased from Sigma Aldrich (Dorset, UK). The deuterated internal standard, Atorvastatin-(anilide ring-d5) calcium salt was purchased from Merck Life Sciences (Dorset, UK). Formic acid 98% was purchased from Scientific Laboratory Supplies (Nottingham, UK). 18.2 MΩ × cm water was collected from an ELGA water purification system (Buckinghamshire, UK). Cryo-M-Bed was purchased from VWR International Ltd**.** (Lutterworth, UK). The primary antibody (Rabbit Polyclonal anti-caspase-3 antibody), secondary antibody (Goat Anti-Rabbit IgG H&L Polyclonal (Alexa Fluor® 488) preadsorbed) and normal goat serum were purchased from Abcam (Cambridge, UK). Prolong Gold Antifade DAPI was purchased from Life Technologies (Paisley, UK). Porcine small intestine was provided by R.B Elliott & Son (Chesterfield, UK). Super refined Polysorbate (80) LQ was donated by CRODA (DE, USA).

3.3.2 Fresh Tissue Preparation

3.3.2.1 Collection Timings & Conditions

Animal tissue was collected from the abattoir at R B Elliot & Son Ltd (Chesterfield, UK). Porcine small intestine was retrieved immediately after removal from the animal. The tissue specification given to the abattoir was as follows: the intestine needed to be removed promptly (within 20 minutes) of animal sacrifice and supplied with a small portion of stomach still attached followed by ~ 30 cm of intestine. Intestine was collected daily from the abattoir contained in a plastic bag which was placed inside a cool bag directly on top of additional ice blocks. The cool bag was then transported to the laboratory. From point of collection, the tissue reached the lab within the hour.

3.3.2.2 Muscle-Serosal Layer Removal

Under a laminar flow hood, a ~ 5 cm wide section of small intestine was cut from the collected tissue. A visual examination was carried out when selecting tissue to avoid using any areas that could have been physically damaged during the removal process at the abattoir. Tissue was harvested from as close to the proximal end of the intestine as possible and did not exceed 25 cm from the pyloric sphincter; this ensured duodenal tissue retrieval. The ~ 5 cm section of small intestine was cut along its length to open the intestine into a sheet. The intestine was placed on ice with the muscle-serosal side facing down and left for approximately 3 minutes. Under a stereo microscope, the muscle-serosal layer was carefully removed from the intestine. Utilising the cold-induced separation of the layers at the edges of the tissue, each layer was clipped by tweezers and gently pulled taut while the blunt edge of a scalpel was gently run over the connecting join to separate the layers apart without damaging the tissue. The muscle-serosal layer was disposed of.

3.3.2.3 Tissue Adherence

Three 10 mm discs were cut from the remaining sheet of tissue using a biopsy punch. The location the discs were taken from was chosen at random; the only requirements being to avoid taking tissue from near the edge of the tissue or areas of obvious damage. Each tissue disc was then placed into a Millicell cell culture insert with the apical side facing upwards. Tweezers were used to ensure the disc covered the entirety of the mesh in the insert and left no gaps around the edges. The insert was then placed over the

ventilation system within the laminar flow hood for approximately 3 minutes. A 10 mm o-ring was then placed in the insert and carefully pushed into place to create a seal between the edge of the tissue disc and the side of the insert. During o-ring fitting, care was taken to not dislodge the tissue disc and keep the tissue disc flat to the insert mesh; the correct positioning is illustrated in Figure 3.1. A final 14 mm o-ring was fitted to the outside of the insert before fitting the insert into the QV600 LLI chamber.

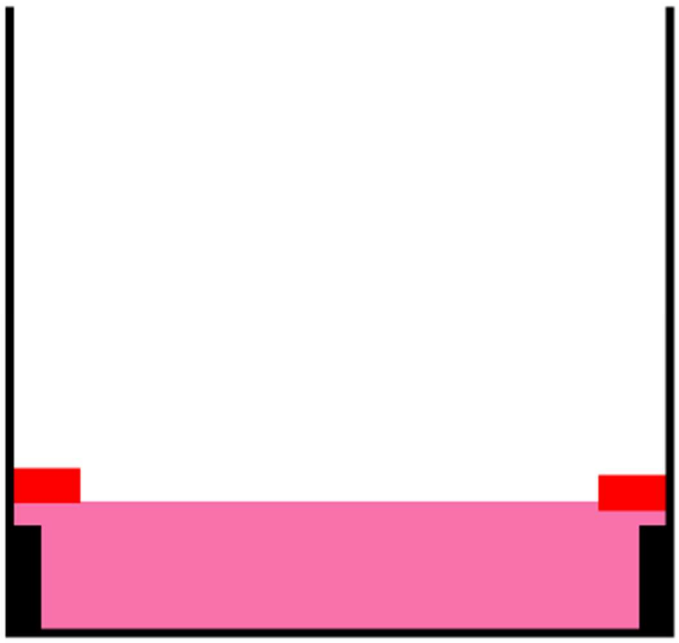

Figure 3.1: *The correct positioning of the tissue and internal o-ring within an insert illustrated with a diagram of the cross section of the insert. The tissue is represented by the pink rectangle and the red rectangles represent the internal o-ring.*

3.3.3 QV600 LLI Set Up & Adaptations

3.3.3.1 General Configuration

The QV600 LLI consisted of a peristaltic pump, three chambers, two reservoir bottles and two circuits created by silicon tubing and luer lock connectors. The two circuits were divided by an insert held within each chamber by an o-ring. The system was configured so that the peristaltic pump drew liquid from the reservoirs and pumped it around the system through each circuit with movements mimicking peristalsis. The liquid travelled through the tubing and filled each chamber in turn, before returning to the reservoir where it was recirculated. Each reservoir was fitted with an air filter.

Different thickness silicon tubing was used throughout the system to balance the millifluidics of the system; the configuration used can be seen in Figure 3.2.

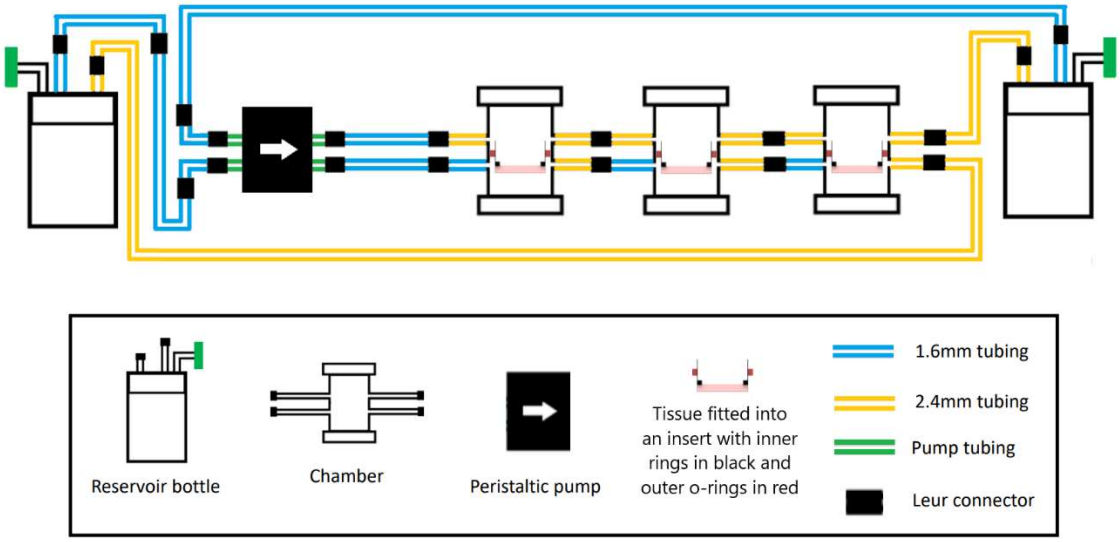

Figure 3.2: *A schematic showing the general configuration of the QV600 LLI with all components at the same level.*

The system was constructed as in Figure 3.2 prior to fresh tissue reaching the lab; with the exception being that no inserts were in the chambers. All work performed on the QV600 LLI was under a laminar flow hood and all components had been sterilised before use.

3.3.3.2 Peristaltic Pump Calibration

Following the Kirkstall Ltd protocol, the QV600 LLI was filled with PBS (Kirkstall Ltd., 2019). The peristaltic pump was switched on and PBS was allowed to circulate to dispel any air bubbles. The liquid was collected for 5 minutes into a pre-weighed weighing boat and re-weighed. This was repeated three times at three different pump settings. An average flow rate was established for each pump setting. A calibration curve was plotted using the pump setting against the average flow rate (mL/min).

3.3.3.3 System Priming

Prior to acquiring fresh tissue, the system was rinsed thoroughly with sterile PBS. A sterile pipette was used to remove any excess PBS. The inserts containing fresh tissue discs were fitted into the chambers prior to any further system priming. When fitting the inserts, it was ensured that the outer o-ring was in-between the two circuits and that the

top of the insert was lower than the entrance to the upper circuit tubing. The optimal insert positioning in the chamber has been illustrated in Figure 3.2.

Using a pipette, the upper (donor) circuit fluid was used to fill each insert only before closing the chambers. The donor circuit reservoir was then filled with the remaining fluid to give a total volume of 30 mL in the donor circuit. The donor circuit fluid consisted of 0.5 % Atorvastatin calcium made up in PBS; dependant on the experiment, differing volumes of Polysorbate-80 were also added to this circuit.

The lower (acceptor) circuit reservoir was then filled with 30 mL of DMEM/F12 and the air filter was temporarily removed. The acceptor circuit reservoir was lowered beneath the system and the peristaltic pump was then switched on; the pump was set to 1000 and 500 au for the donor and acceptor circuit, respectively. Whilst filling the acceptor circuit, the chambers were tilted and manipulated in an attempt to avoid bubble formation in the tubing and chambers; any bubbles formed were removed by tapping and tilting, if possible. Once the acceptor circuit had filled completely, the air filter was replaced, and the reservoir returned to the initial configuration. Once both circuits had filled, the pump settings were set for the experiment and the absorption experiment began.

3.3.4 Absorption Experiment

After the tissue discs were fitted into the chambers and the system had been primed, the system was transported into an incubator set to 37 °C, 5% CO_2 for 2 h. At the end of the experiment, the circuit tubing lines were drained before removing the inserts containing tissue. Each tissue disc was rinsed thoroughly with PBS before immediately being snap-frozen by liquid nitrogen whilst being submerged in 2-methylbutane. Each disc was stored separately at −80 °C. The donor and acceptor circuit reservoirs were emptied and stored at 4 °C. The entire system was flushed with 500 mL of 70% methanol in 50 mL increments. The system was subsequentially flushed with 50 mL of sterile PBS before being drained of all fluid using a Pasteur pipette and syringe. All solutions used for rinsing the tissue and cleaning the system were collected and stored at 4 °C.

3.3.4.1 Polysorbate-80 Study at Different Flow Rates

Two series of absorption experiments were conducted utilising a range of different concentrations of Polysorbate-80 in the donor circuit in addition to 0.5 mg/mL

Atorvastatin in PBS. The two-experiment series were performed with different flow rates across the circuits; the first series used pump settings 120 and 58 au in the donor and acceptor circuits, respectively. The second series used the same pump setting for the acceptor circuit but increased the donor pump setting to 580 au.

3.3.4.2 Tissue Extraction and Sample Preparation

The same method was used as described in section 2.3.7 to prepare the donor circuit, acceptor circuit, tissue discs, tissue rinsing solution, initial system rinse and final system rinse samples from each experiment.

3.3.4.3 LC-MS/MS Method

The same method was used as described in section 2.3.8

3.3.4.4 Data Analysis

As detailed in chapter 2, the LC-MS/MS data was automatically integrated and processed using the Agilent MassHunter Quantitative Analysis Version 8.09 software. This software was also used to create the calibration graph from the standards and calculate the concentration of all the samples. The back-calculations from software generated concentrations were performed manually. For each experiment, a mass balance calculation was carried out using these values.

The apparent permeability coefficient for transport across porcine intestinal tissue ($P_{app,pig}$) was determined for each drug absorption experiment performed in the study (Arnold et al., 2019). The following equation was used to determine the $P_{app,pig}$ value for each experiment:

$$P_{\text{app,pig}} = \frac{dc}{dt} \times \frac{V}{A \times C_0} \left(\frac{cm}{s}\right)$$

where dc/dt is the change in the acceptor concentration calculated using the final concentration in the acceptor circuit divided by the length of the experiment (2 h), V is the volume in the donor circuit (30 mL), A is the exposed surface area (0.785 cm^2), and C_0 is the initial concentration of Atorvastatin in the donor circuit (500 µg/mL).

3.3.5 QV600 LLI Final Modifications

3.3.5.1 Pressure Monitoring

The QV600 LLI was modified to utilise real-time pressure sensors. The Elveflow microfluidic pressure sensors (Elveflow, Paris, France) were added to each circuit between the peristaltic pump and the first chamber as demonstrated in Figure 3.3. The pressure sensors were attached to a laptop which ran the Elveflow Smart Interface software to provide real-time pressure monitoring. The sensors were used to monitor the pressure during the set up and entirety of an absorption experiment.

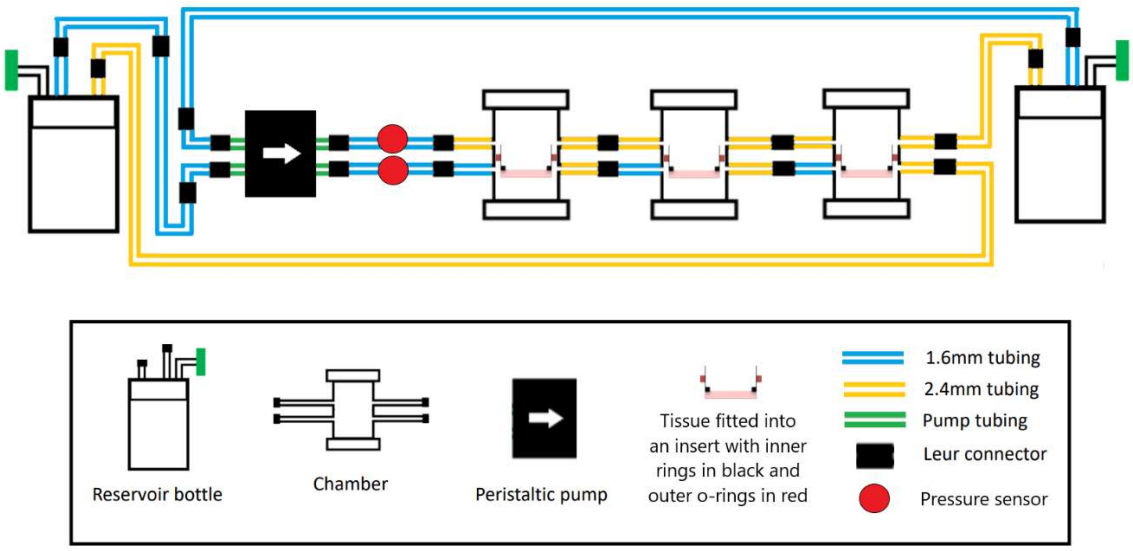

Figure 3.3: *A schematic showing the general configuration of the QV600 LLI with the addition of pressure sensors. All components of the system are shown at the same level.*

3.3.5.2 System Re-Configuration

The QV600 LLI was reconfigured to raise the entire system 20 cm higher than the acceptor circuit reservoir as shown in Figure 3.4. When performing absorption experiments in this configuration, the system was primed as described in section 2.3.3.3 with particular emphasis on the reservoir being returned to the 'initial configuration' referring to the new configuration described here.

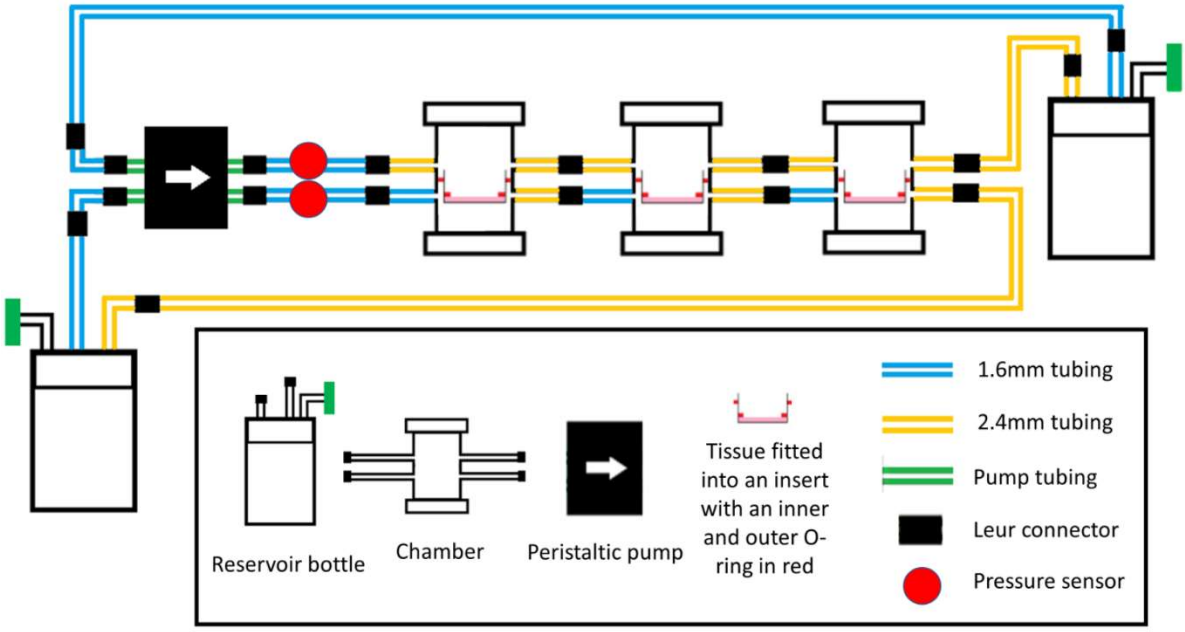

Figure 3.4: *A schematic showing the re- configured QV600 LLI. All components of the system are shown at the same level with the exception of the acceptor circuit reservoir being 20 cm lower than the rest of the system.*

3.3.5.3 Syringe Filling Method

Using a pipette, the upper (donor) circuit fluid was used to fill each insert before closing the chambers. The donor circuit reservoir was then filled with the remaining fluid to give a total volume of 30 mL in the donor circuit. The donor circuit fluid consisted of 0.5 % Atorvastatin calcium made up in PBS; dependant on the experiment, differing volumes of Polysorbate-80 were also added to this circuit.

The lower (acceptor) circuit reservoir was then filled with 30 mL of DMEM/F12 and the air filter was temporarily removed. A syringe was attached to the final female luer connector located just in front of the acceptor circuit reservoir and used to draw the acceptor circuit fluid from the reservoir, through the pump, the chambers and the remaining tubing. After attaching but prior to drawing the syringe, the clip on the pump tubing was released and the syringe filter was removed from the acceptor circuit. Whilst filling the acceptor circuit, the components were tilted and manipulated to avoid bubble formation in the tubing and chambers; any bubbles formed were removed by tapping and tilting, if possible. When attaching, using and detaching the syringe, the reservoir and syringe were kept lower than the system itself to prevent the tissue discs from becoming dislodged. Prior to detaching the syringe, the pump clip was closed. Upon

detaching the syringe, the tubing was instantly reconnected and the reservoir remained below the system to prevent the liquid from withdrawing. The peristaltic pump was then switched on; the donor and acceptor circuit pump settings were 1000 and 500 au, respectively. Once both circuits had filled, the pump settings were set for the experiment. The air filter was reattached to the acceptor circuit reservoir before returning to the initial configuration to start the absorption experiment.

3.3.5.4 Double O-ring Fitting

Three 10 mm discs were cut from the remaining sheet of tissue using a biopsy punch. The locations the discs were taken from were chosen at random; the only requirements being to avoid taking tissue from near the edge of the tissue or areas of obvious damage. Each tissue disc was then placed into a Millicell cell culture insert with the apical side facing upwards. Tweezers were used to ensure the disc covered the entirety of the mesh in the insert and left no gaps around the edges. An 8 mm rubber o-ring was placed in the center of the tissue disc before placing the insert over the ventilation system within the laminar flow hood for approximately 3 minutes. A 10 mm o-ring was then placed on top of the first o-ring. The second o-ring was carefully pushed into place to create a seal around the edge of the tissue disc, first o-ring and side of the insert. During o-ring fitting, care was taken to not dislodge the tissue disc and keep the tissue disc flat to the insert mesh; the correct positioning is illustrated in Figure 3.5. A final 14 mm o-ring was fitted to the outside of the insert before fitting the insert into the QV600 LLI chamber.

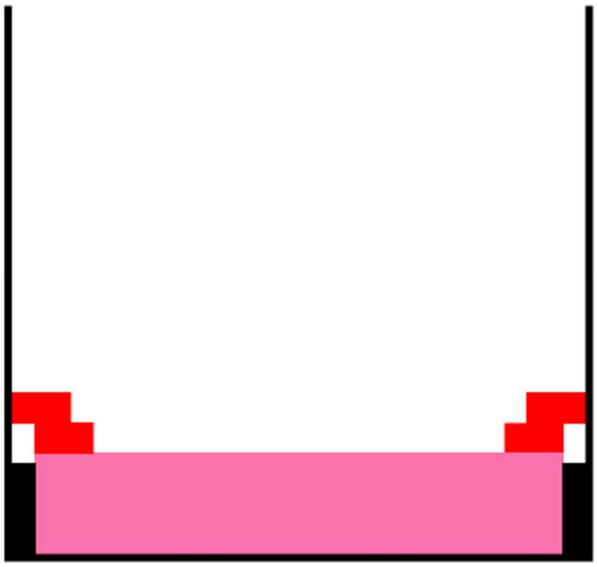

Figure 3.5: *The correct positioning of the tissue and two internal o-rings within an insert illustrated with a diagram of the cross section of the insert. The tissue is represented by the pink rectangle and the red rectangles represent the two internal o-rings stacked on top of each other.*

3.3.6 Viability Experiments

On two separate days, intestines were collected fresh from the abattoir from a total of six different pigs. On each day, an absorption experiment was performed, and several tissue samples were collected at different time points to assess the viability of the tissue. Tissue samples were collected at the following time points.

Day 1:

A. As soon as reached the lab with muscle intact
B. As soon as reached the lab with muscle intact but treated with 1.6 mM H_2O_2 for 1 h
I. Straight after muscle removal
D. Straight after the absorption experiment (2 h exposure to the system without muscle)
E. Straight after the absorption experiment (Kept out of the system in PBS with the muscle intact)

Day 2:

H. As soon as reached the lab with muscle intact

C. Straight after muscle removal
F. Straight after the absorption experiment (4 h exposure to the system)
G. Straight after the absorption experiment (Kept out of the system in PBS with the muscle intact)

3.3.6.1 Tissue Fixation

At each time point, the relevant tissue samples were washed with PBS before fixation in 4% PFA; they were incubated at room temperature for 1 h. All samples were washed twice in PBS and then stored in PBS at 4 °C until all samples from that day had reached the same step.

3.3.6.2 Preparation of Tissue Sections for Immunostaining

The fixed tissue samples were transferred to a tube containing 30% (w/v) sucrose and stored at 4 °C overnight until the tissue had sunk to the bottom. The tissue samples were individually snap-frozen by liquid nitrogen whilst being submerged in 2-methylbutane. Each sample was immediately transferred to a -80 °C freezer for storage until cryosectioning. The tissue samples were transferred to the Leica CM 1950 Cryostat (Leica Microsystems, Milton Keynes, UK). The samples were mounted onto a cork ring using Cryo-M-Bed embedding compound and were allowed to thermally equilibrate for 1 h. The chamber and specimen head temperature were set at −19 °C. Each tissue sample was cryosectioned into 8 µm sections and thaw mounted onto glass slides. The sections were placed in a slide box and stored at −80 °C.

3.3.6.3 Immunostaining

The slides were removed from the freezer and allowed to warm at room temperature for 30 minutes before starting the staining procedure. Meanwhile, blocking solution (1x PBS / 20% goat serum / 0.1% Tween 20) and staining solution (1x PBS / 5% goat serum / 0.1% Tween 20) were freshly prepared. In a humidity box, each tissue section was covered with ~ 200 µL blocking solution and left to incubate at room temperature for 20 minutes. The blocking solution was removed (by flicking the slide), and each section was covered with 0.25 % (v/v) primary antibody (Rabbit Polyclonal Anti-Caspase-3) in staining dilution. The slides were left to incubate in the humidity box overnight at 4 °C. The slides were washed twice for 5 minutes with the staining solution. Excess solution was removed (by flicking the slide) before covering the tissue sections with 0.2 % (v/v) secondary antibody (Goat Anti-Rabbit IgG H&L Polyclonal) in staining solution. The

slides were left in the humidity box to incubate at room temperature for 1 h. The tissue sections were washed for 5 minutes in PBS prior to counterstaining with 0.1 % v/v DAPI in PBS for 10 minutes. The slides were washed twice for 10 minutes with PBS. The slides were then mounted with pro-long old antifade DAPI and stored at 4 °C away from light.

3.3.6.4 Data Analysis

The slides were viewed under the Zeiss Laser Scanning Confocal Microscope (LSM800) to assess the fluorescence of the DAPI and the caspase-3 staining. Three random areas on the stained tissue section were captured and used for cell counting. ImageJ v1.54 software was used to count the stained cells and calculate the average percentage of apoptotic cells from each sample.

3.4 Results and Discussion

3.4.1 Fresh Tissue Preparation

When preparing the tissue, it was considered paramount to remove as much of the muscle-serosal layer as physically possible so that the model was closer to real-life scenarios and that the acceptor circuit was representative of the blood vessels outside of the submucosa. Compared to the muscle-serosal layer removal described in Chapter 2, it was much more challenging to remove this layer from fresh tissue. To aid with the removal of the muscle-serosal layer, it was discovered through trial and error that cooling the muscle-serosal layer directly on ice made for more successful and better-quality removal attempts. The cooling of the tissue caused a natural separation between the layers at the edges of the tissue; this is shown in Figure 3.6A. The separating edges meant that each side of the separating layers could be gripped easily with tweezers whilst being carefully coaxed apart. Although mucosal stripping is considered an invasive procedure, it is essential that damage is kept to an absolute minimum where possible as this could impact the viability of the tissue and, could allow the donor circuit fluid to leak through the damaged areas. To avoid excessive damage, the two layers were gently pulled taut in opposite directions using the tweezers whilst the blunt side of a scalpel was run along the join to encourage the layers to separate; this is partially demonstrated in Figure 3.6B.

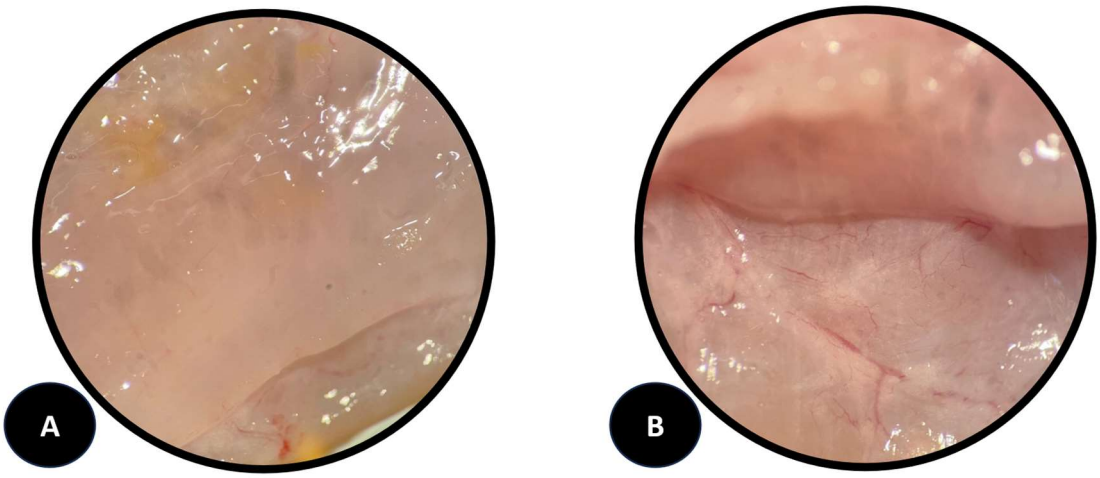

Figure 3.6: *Optical images taken of the intestinal tissue through a dissecting microscope during preparation. A) The tissue intact with separation of the layers starting at the edge with the muscle-serosal layer on top. B) Two layers being pulled in opposite directions to reveal the submucosa underneath.*

If cooled correctly, the blunt edge of the scalpel is enough to gently tease the layers apart. Using the sharp edge of the scalpel was avoided as it sometimes snagged the tissue or resulted in a partial removal of the serosal layer. In some instances, it was found that the sharp edge of the scalpel was needed when reaching areas of blood vessels as the connective tissue surrounding them can be rather tough; this was performed carefully and switched back to the blunt blade as soon as complete. The removal of the muscle-serosal layer was performed under a dissecting microscope; although it was still not possible to definitively guarantee the full removal of the layers by eye without staining, it was found that the microscope aided in identifying whether the same layer was being removed consistently throughout.

For each absorption experiment, three discs of tissue were acquired by biopsy punch. The location biopsies were taken from was randomised to avoid bias and to create an average although there were the following exceptions: biopsies were never taken from near the edge of the tissue or near areas where the sharp edge of the scalpel had to be used to avoid using damaged tissue. It is crucial that during the set-up and entirety of an absorption experiment, the tissue discs remain in place and act as a complete seal between the donor and acceptor circuit. If the donor circuit was to leak around the edges of the tissue, the amount of drug detected in the acceptor circuit would not be representative of the amount of drug that had absorbed through the tissue. Therefore, it

was paramount that the technique for fitting the tissue discs into the inserts was suitably optimised. As part of this optimisation it was found that the bottom submucosal layer of the tissue discs had to sit flat against the mesh within the insert and fill the entire surface with no gaps around the edges, as shown in Figure 3.7A-B. Additionally, when the internal O-rings had been fitted correctly, the tissue disc needed to remain flat and to the edge; as shown in Figure 3.7C-D.

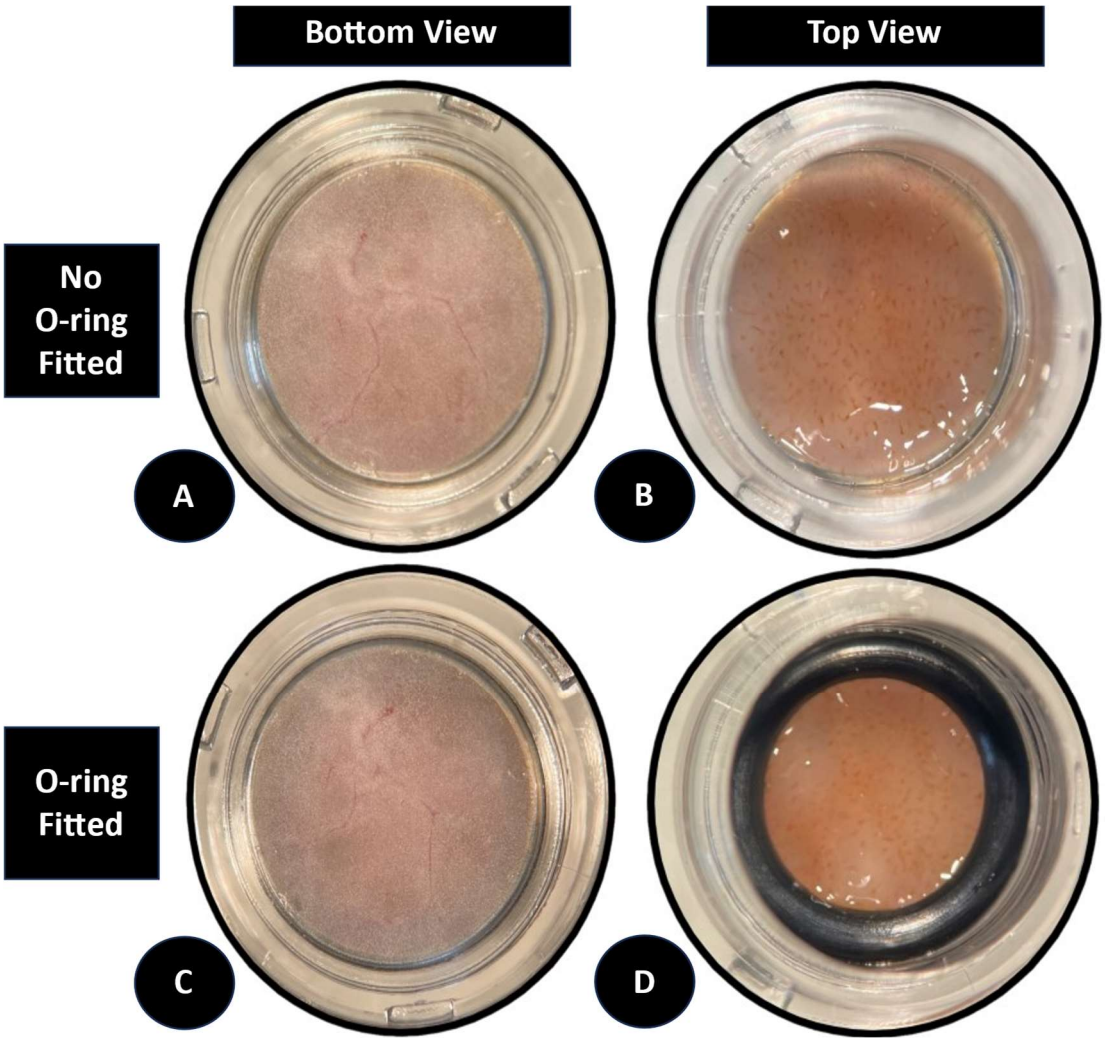

Figure 3.7: *A collection of optical images taken under a dissecting microscope showing how a correctly fitted tissue disc should look in the insert before and after O-ring fitting; images taken from different viewpoints of the insert. A) Bottom view of the tissue disc fitted into an insert prior to adding the internal O-ring. B) Top view of the tissue disc fitted into an insert prior to adding the internal O-ring. C) Bottom view of the tissue disc fitted into an insert with the internal O-ring in place. D) Top view of the tissue disc fitted into an insert with the internal O-ring in place.*

Through numerous trial and error experiments, it was observed that if the tissue disc was too wet, it would become dislodged whilst fitting the internal O-rings. To prevent this from happening, it was decided that no additional fluid would be added to the intestine during transportation and the tissue would be placed on ice to cool rather than being submerged in ice water. As the tissue disc would come into direct contact with the donor circuit fluid when fitted into the system, it was essential that the tissue discs were well adhered to the insert mesh. Despite having an internal O-ring holding the tissue discs into the insert, it was found that the discs were easily dislodged during the system priming process; this caused catastrophic mixing of the two circuits. Once fluid was introduced into the donor circuit, the fluctuating pressures experienced during system priming most likely exacerbated any weaknesses in the tissue adherence to the insert mesh. To overcome this issue, it was discovered that by allowing the tissue discs to sit in the insert for a suitable amount of time (approximately 3 minutes) over a sterile air vent, excess moisture was drawn from underneath the insert and a bond was formed between the tissue disc and insert mesh. It was important to get the drying time correct as in addition to losing critical viability time, leaving the tissue for too long meant that the tissue itself would start drying out. On the other hand, drying for an inadequate amount of time resulted in the tissue disc becoming dislodged during set-up or the absorption experiment. The appropriate drying time was unique for each disc and was determined by observation of the tissue texture and appearance. With optimal drying time and lack of added fluid, the absorption experiments were predominately successful when set up correctly.

3.4.2 QV600 LLI Set Up & Adaptations

The QV600 LLI system was originally designed and promoted for use with cell lines that would be cultured within an insert; the system worked under the principle that both circuit solutions could freely move between cells. Due to the thickness and structure of the tissue, free movement would only be possible around the edges of the tissue. Hence, the system was adapted as described in Chapter 2 to separate the circuits entirely. The adaptation caused a natural build-up of pressure in the acceptor circuit during the set-up process which was enough to dislodge the tissue discs if they were incorrectly fitted or if the system was filled too quickly. This was resolved for frozen tissue as described in Chapter 2 with a single o-ring fitting and by slowly filling the system circuits.

As the goal of this chapter was to implement fresh, viable tissue into the system, it was essential that the experiment was set-up in a time-efficient manner. While the gradual system filling process used in Chapter 2 was suitable for previously-frozen tissue experiments, it was deemed too time-consuming for fresh tissue experiments which led to an unnecessary loss of viability time. Even with the improvements to the tissue preparation method detailed in section 3.3.2, increasing the pump speed to fill the system caused the tissue discs to become dislodged sporadically. It was paramount that the set-up timings were optimised without jeopardising the barrier between the two circuits. Therefore, the system priming and filling technique were revisited.

When increasing the pump speed to fill the system more rapidly, it was observed almost consistently that the tissue would become dislodged in the same location within the system; even with the tissue disc being correctly fitted. The tissue disc would become dislodged when the acceptor circuit fluid had passed the final chamber and began to climb up the tubing towards the reservoir. It was presumed that the most likely cause was a detrimental rise in pressure as a result of expelling air against gravity. To test this theory, the acceptor circuit reservoir bottle was held below the level of the system before the final chamber was reached so that the liquid did not have to travel upwards whilst dispelling the remaining air from the system. The reservoir bottle was returned to the entire system level once all air had been expelled from the acceptor circuit. No movement of the tissue disc was observed when trialling this method.

Upon further testing, it seemed apparent that the expelling of air from the system would cause the pressure in the system to fluctuate until it was completely filled. There were infrequent occurrences in which the tissue became dislodged prior to the acceptor circuit fluid reaching the final chamber. It was observed that during these occurrences, significant bubbles had formed within the chambers while filling and were in the process of being teased out of the system via the tubing. Due to the inconsistency of bubble formation, unpredictable fluctuations in pressure within the system were suspected. Thus, in some instances the acceptor circuit pressure could have surpassed that of the donor circuit prior to reaching the final chamber and caused the seemingly ‘sporadic’ dislodgement of the tissue. Lowering the acceptor circuit reservoir prior to filling the system prevented excessive pressure build-up in the acceptor circuit and allowed for the system to be filled at a faster rate without dislodging the tissue discs.

Prior to starting an absorption experiment, the relationship between the peristaltic pump settings and the flow rate within the system were established. After a series of simple experiments detailed in section 3.3.3.2, the amount of water collected over set time periods was weighed to ascertain the flow rate. This was repeated three times at three different pump settings. The findings were plotted to give the calibration graph shown in Figure 3.8.

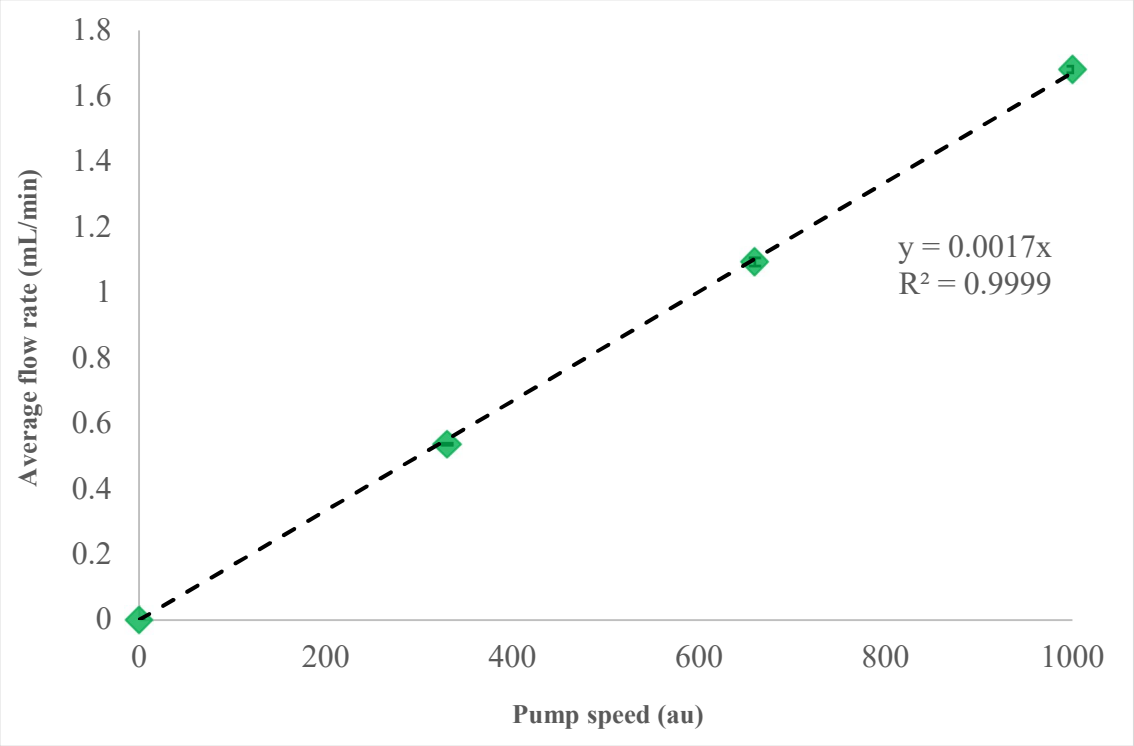

Figure 3.8: *The calibration graph, constructed from the peristaltic pump calibration detailed in section 3.3.3.2, showing the relationship between the pump speed and the flow rate within the circuit (n=3).*

Using the equation of the line of best fit, y = 0.0017 x, the theoretical flow rate could now be calculated for the dual circuits.

3.4.3 Absorption Experiments

Two series of absorption experiments were conducted with the sole differences being the flow rate gradients used. The first set of experiments were performed with the donor circuit being double that of the acceptor circuit. The pump settings used were 120 and 58 au for the donor and acceptor circuit, respectively. Using the calibration graph and

equation shown in Figure 3.8, this gave theoretical flow rates of 0.2 mL/min and 0.1 mL/min, respectively.

The purpose of the first set of experiments was to test the adaptations and functionality of the system and so, absorption experiments with and without 0.4% v/v Polysorbate-80 were performed in triplicate. As shown in Figure 3.9, the $P_{app,pig}$ of Atorvastatin after a 2 h experiment with no excipient was added to the donor circuit was consistently low; with the highest $P_{app,pig}$ being 0.0518 x 10^{-6} cm/s. When 0.4% v/v Polysorbate-80 was added to the donor circuit, there was a slight increase in the $P_{app,pig}$ of Atorvastatin. There was, however, one experiment that yielded an extremely high $P_{app,pig}$ that was more than 80 times higher than the average $P_{app,pig}$ value of the other two replicate experiments.

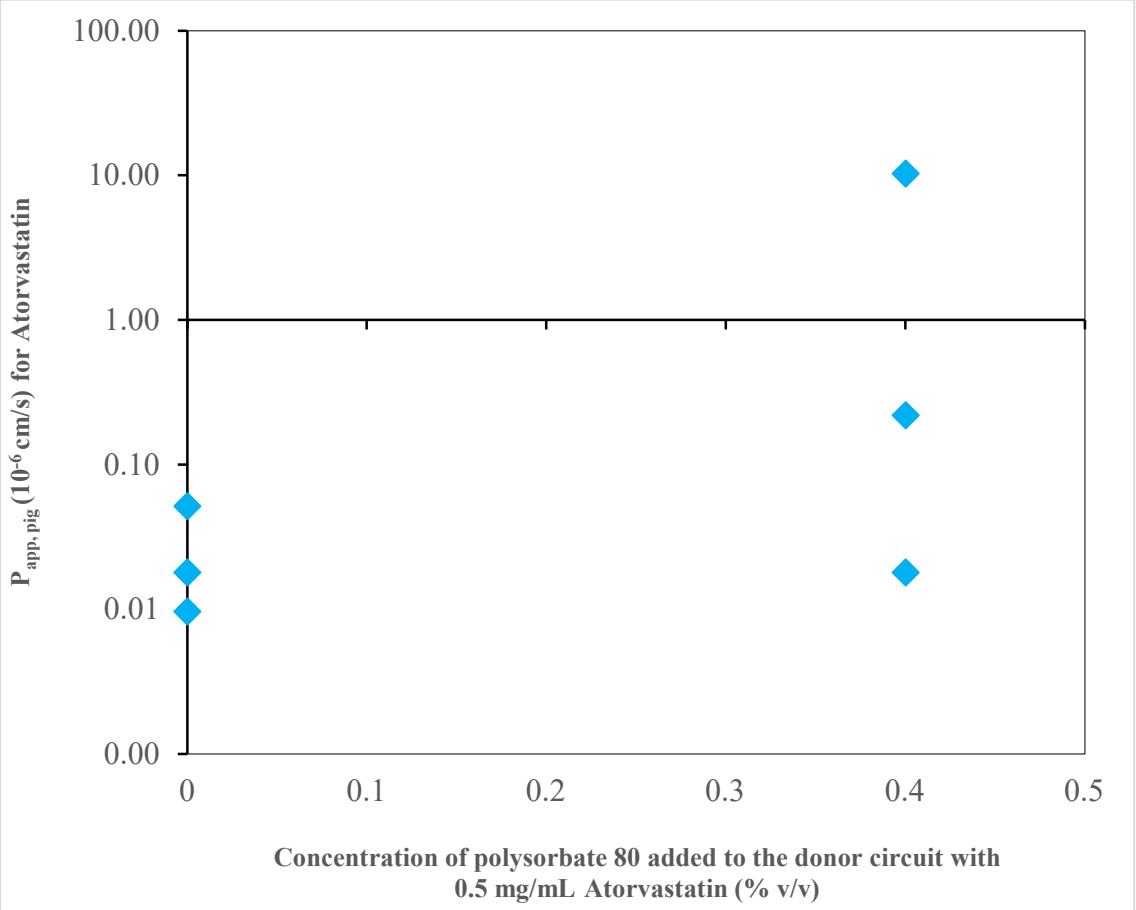

Figure 3.9: *A graph to show the $P_{app,pig}$ of Atorvastatin after a 2 h absorption experiment at pump setting 120/58; three experiments were performed with Polysorbate-80 and three without (n=3).*

When compared to experimental data from the same Biopharmaceutical Classification System (BCS) published by (Arnold et al., 2019), the apparent outlier was found to be most similar to that of other reported data. Although the paper does not report the $P_{app,pig}$ for Atorvastatin, the $P_{app,pig}$ of other drugs from the same BCS group were reported from Ussing chamber studies using porcine intestine. The experimental $P_{app,pig}$ values for each drug were reported in 10^{-6} cm/s and ranged over 1-2 significant figures. Additionally, the mass balance for each experiment was calculated to ensure that all the drug was accounted for and that the calculations were appropriate. As shown in Table 3.1, all mass balances were within the allowed tolerance, 85-115%, as stipulated in Chapter 1 and 2.

Table 3.1: *A summary of the $P_{app,pig}$ values and mass balances for all experiment replicates performed using the 120/58 pump setting.*

Experiment Type	0.5 mg/mL Atorvastatin			0.5 mg/mL Atorvastatin with 0.4% v/v Polysorbate-80		
Replicate	1	2	3	1	2	3
$P_{app,pig}$ value (10^{-6} cm/s)	0.0097	0.018	0.0518	0.018	10.3	0.22
Mass Balance (%)	109.3	102.1	106.6	95.2	95.2	109.6

With the exception of the outlier, the $P_{app,pig}$ of Atorvastatin was approximately two orders of magnitude lower than that of the published data for oral drugs from the same BCS group. With the fluctuations in pressure experienced during the set-up optimisation experiments due to bubbles and reservoir positioning, it was decided that the donor circuit flow rate would be increased to guarantee a positive pressure gradient that should promote Atorvastatin movement in the correct direction. For the second set of experiments, the donor circuit was set to be ten times that of the acceptor circuit. The pump setting for the donor circuit was increased from 120 to 580 au. Using the calibration graph and equation shown in Figure 3.8, this gave a theoretical flow rate of 1 mL/min.

The $P_{app,pig}$ of Atorvastatin from the experiments with a higher pump setting are shown in Figure 3.10. It was consistently observed that with the addition of 0.4% v/v Polysorbate-80 to the donor circuit, there was a significant rise in the $P_{app,pig}$ of Atorvastatin; this was supported by a P value of 0.005 showing a statistically significant difference between the two experiment types. The finding suggests that the presence of

the excipient improved the permeation of Atorvastatin through the tissue disc and into the acceptor circuit. The solubilising abilities of Polysorbate-80 could be an explanation of the apparent increase in permeation observed.

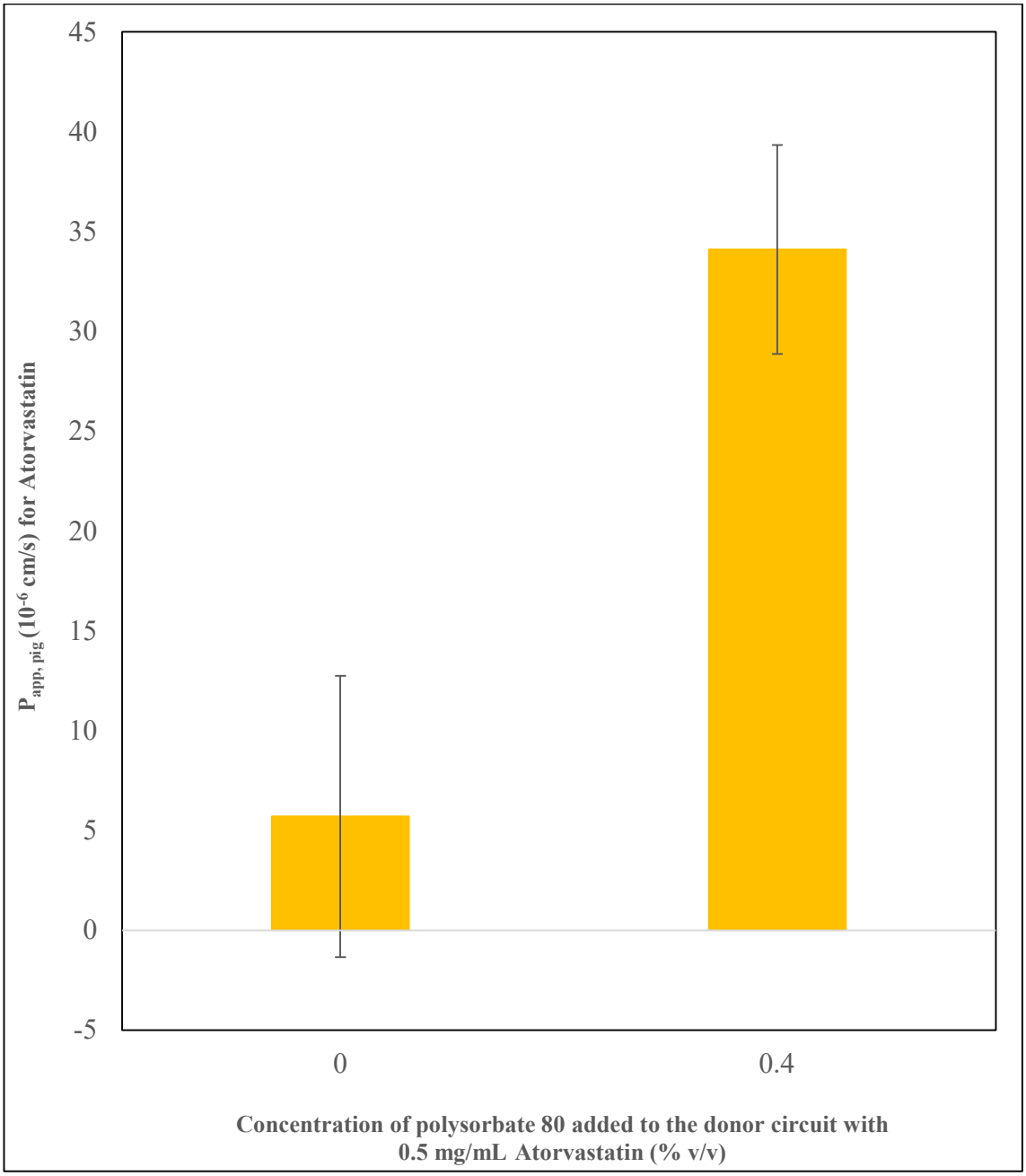

Figure 3.10: *A graph to show the $P_{app,pig}$ of Atorvastatin after a 2 h absorption experiment at pump setting 580/58; three experiments were performed with Polysorbate-80 and three without (n=3).*

When comparing the graph in Figure 3.10 to the graph in Figure 3.9, there was a clear overall increase in the $P_{app,pig}$ of Atorvastatin when a higher pump setting was used in

the donor circuit. This trend was observed with or without adding Polysorbate-80 to the donor circuit. More specifically, the $P_{app,pig}$ of Atorvastatin had exceeded that of the apparent outlier in five out of six of the experiments performed at a higher pump speed. Consequently, the $P_{app,\ pig}$ values calculated for each experiment with a higher upper flow rate were well within range of those reported by (Arnold et al., 2019) for other drugs within the same BCS group. There was one exception, in which the $P_{app,pig}$ of Atorvastatin was as low as 0.08 x 10^{-6} cm/s; this was similar to the findings from the experiment set using the 120/58 pump setting. The mass balance for each experiment was calculated and displayed in Table 3.2 along with the its corresponding $P_{app,pig}$ value; again, all mass balances were within tolerance.

Table 3.2: *A summary of the $P_{app,pig}$ values and mass balances for all experiment replicates performed using the 580/58 pump setting.*

Experiment Type	0.5 mg/mL Atorvastatin			0.5 mg/mL Atorvastatin with 0.4% v/v Polysorbate-80		
Replicate	1	2	3	1	2	3
$P_{app,pig}$ value (10^{-6} cm/s)	13.6	0.08	3.43	30.0	32.3	40.0
Mass Balance (%)	91.2	87.6	96.1	88.2	88.7	91.76

The significant improvement shown in the $P_{app,pig}$ values would imply that the increase in the flow rate of the donor circuit had improved the permeation of the drug through the tissue. It is thought that this significant improvement was due to an increase in pressure in the donor circuit that helped to secure a positive pressure gradient between the two circuits. Despite this, there remains an unexplained outlier in both experiment sets; one in which very little movement of drug was observed and another displaying the opposite. While in the development stages, it was important to attempt to identify the cause of any inconsistencies in the obtained data in order to eliminate them, if possible. With ex vivo tissue naturally comes an array of variability with factors, such as mucus thickness, that cannot be regulated. Therefore, it is crucial to remove any other factors that could cause further variability within the data. Due to the havoc that bubble formation and air displacement had on tissue placement and thus, system pressure, it

was deemed necessary to confirm that the difference in pressure between the two circuits was significant and that the gradient was in the correct direction.

3.4.4 QV600 LLI Further Modifications

As illustrated in Figure 3.3, pressure sensors were attached to each circuit of the system. The sensors were connected to a laptop that allowed real-time monitoring of the pressure in both circuits with the ability to save the data for future reference. The real-time monitoring element provided valuable information during experimental set-up; the impact that certain movements had on pressure were identified prior to the tissue discs becoming dislodged and the experiment consequently being aborted.

The most significant movement identified using the sensors was the effect of raising the reservoir. When keeping the acceptor circuit reservoir below the system while filling, there was a clear difference between the pressure in both circuits with the donor circuit having a considerably higher pressure. However, as soon as the reservoir was returned to the same level as the system, there was a sharp rise in the acceptor circuit pressure which exceeded that of the donor circuit. The pressure readings that were acquired while performing this manoeuvre were plotted in the graph shown in Figure 3.11. Annotations within the figure highlight the exact moment that the system configuration was returned to standard. It is clear to see that as a direct result of this movement, the acceptor circuit pressure exceeded that of the donor circuit which consequently meant, the experiment would continue with the pressure gradient in the wrong direction.

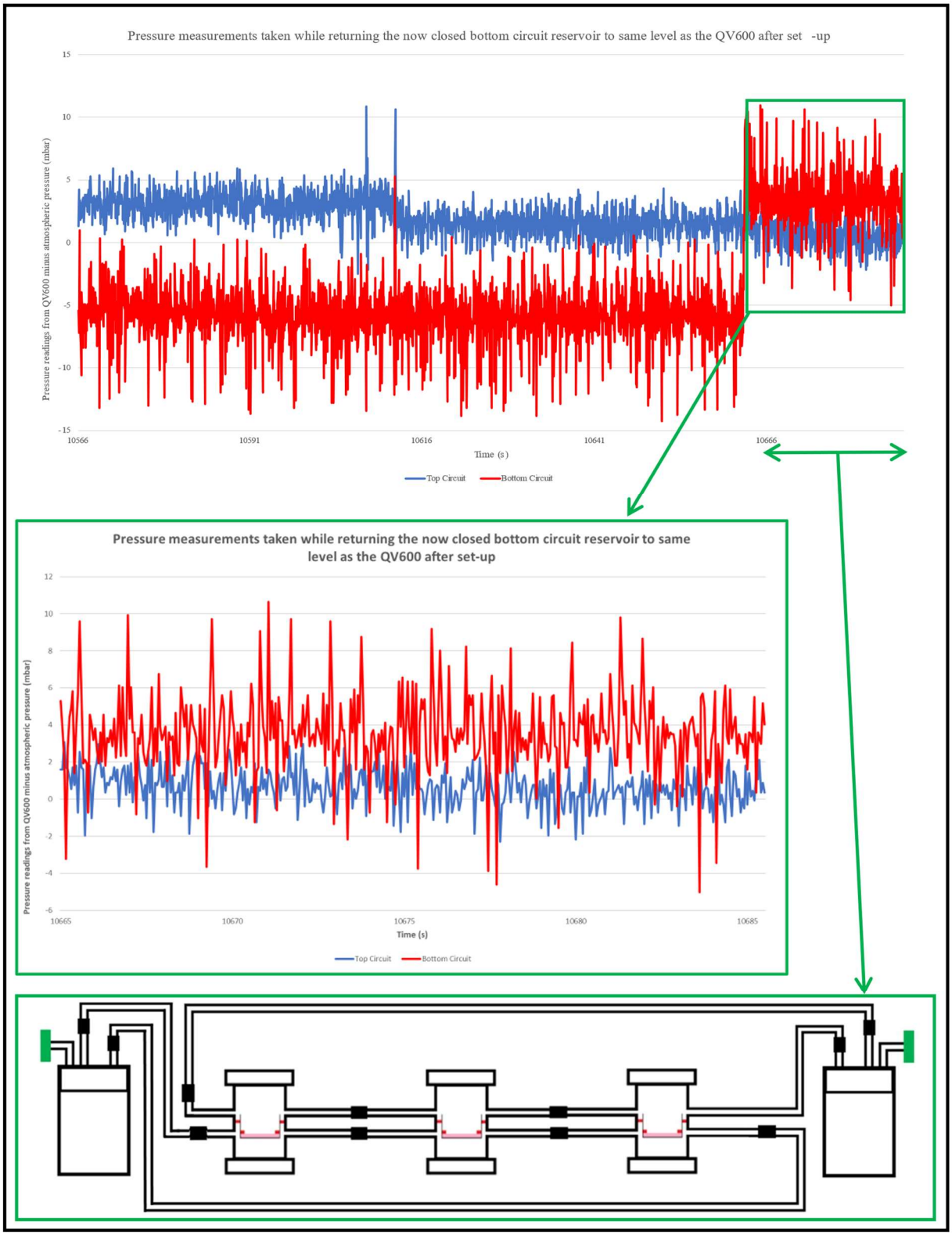

Figure 3.11: *An annotated graph showing the pressure measurements taken on both circuits while changing the system configuration. The annotations highlight the period in which the reservoir was returned to the configuration shown in the diagram as well as a close-up of the pressure measurements taken while in that configuration. (Red = donor circuit. Blue = acceptor circuit)*

Considering that the elevated pressure in the acceptor circuit occurred despite all air being expelled and bubbles removed on this occasion, this would suggest that the complete separation of the circuits creates an imbalance of pressure within the system due to its design. A closer examination of the system tubing configurations revealed that the tubing fused with the QV600 chambers had different diameters. As previously illustrated in Figure 3.2, for each chamber, there were two sets of inlets and outlets built into the chamber; one set for the donor circuit and another for the acceptor circuit. The donor circuit inlet and outlet tubing were both 2.4 mm in diameter whereas the acceptor circuit had 1.6mm inlet tubing and 2.4 mm outlet tubing. Originally, the system would have been specifically designed to counterbalance the pressure between the two circuits based on the notion that the circuit fluid can freely move between cells. However, with the adaptations made for the system to house ex vivo tissue, the circuits are now completely separated and thus, the space within the tubing available to the acceptor circuit was lesser than that in the donor circuit. Consequently, if the same pump setting was used on each of the separate circuits, different levels of pressure would be generated and therefore, different flow rates would be experienced. Hence, the suggested pump calibration method is not suited for the overall system. Additionally, the same calibration method could not be applied with the circuits separated by tissue as the discs would become dislodged once the system was opened.

With this in mind, no further studies were performed to establish the relationship between the pump setting and flow rate for each circuit but rather, more focus was placed on the information provided by the pressure sensors. It was clear from the graph shown in Figure 3.11 that lowering the acceptor circuit reservoir had a profound effect on the difference in pressures between the two circuits. Therefore, it was decided that a trial experiment would be conducted to determine whether the pressure difference would be significant and remain constant throughout an entire absorption experiment. For this trial experiment, pressure sensor monitoring was initiated while the system was at the standard configuration with fluid only in the circuit reservoirs. To maintain the distance between the system and the acceptor reservoir when lowered, a lab jack was used to raise the entire system to the maximum height that would allow the reservoir to remain flat (rather than suspended by the tubing). The system was allowed to fill using the faster filling rates and the acceptor circuit reservoir was moved to the lower position prior to reaching the final chamber. The absorption experiment was allowed to run for 2

h before being stopped and disposed of; the pressure measurements acquired during the set up and duration of this experiment were plotted on the graph shown in Figure 3.12.

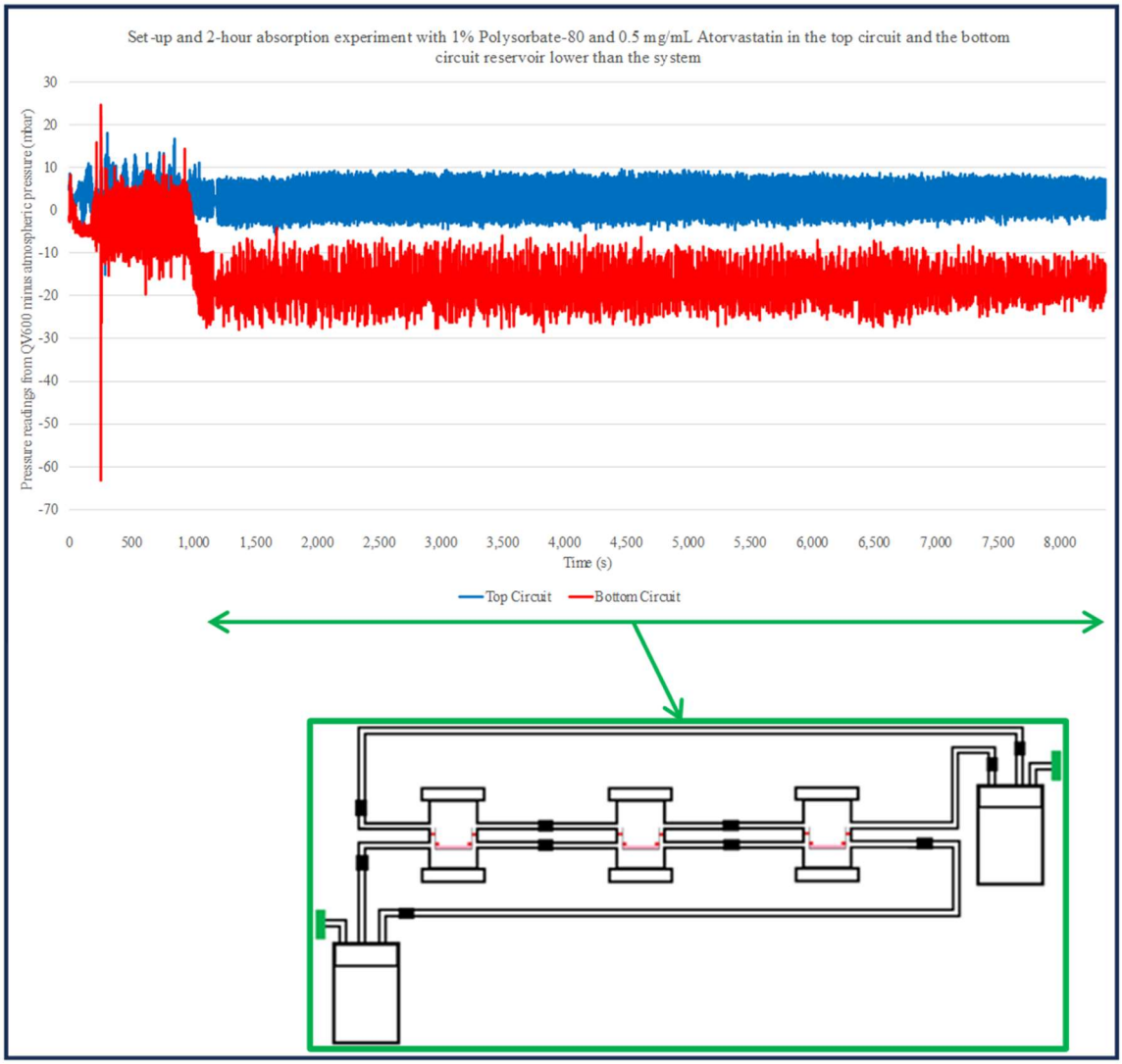

Figure 3.12: *An annotated graph showing the pressure measurements taken on both circuits while setting up the system, changing the system configuration and running an absorption experiment for 2 h. The annotations highlight the time period in which the reservoir was lowered to the new configuration pictured. (Red = donor circuit. Blue = acceptor circuit)*

From the pressure measurements shown in Figure 3.12, it was evident that the movement of the acceptor reservoir to the lower position created a significant pressure gradient between the two circuits that was maintained for the duration of the absorption experiment. The significant pressure gradient also lessened the effect of bubbles within the system tubing. In some instances, the formation of bubbles was unavoidable and

therefore, had to be carefully teased from the system. As witnessed using the live pressure monitoring feature, the removal of bubbles from the system could cause a rise in the acceptor circuit pressure. However, due to the significant pressure gradient created when the system was re-configured, the effect from the bubble formation could not exceed the pressure in the donor circuit and therefore, was no longer detrimental to the adherence of the tissue or direction of the pressure gradient.

It was not always possible to completely eradicate the bubbles from the system, as sometimes they were too large to fit between the chamber wall and the insert; this meant they became trapped within the chamber. While with the new system configuration the bubbles were no longer causing tissue discs to dislodge, there was new concern for the consistency of the conditions within the system including the pressure and the timings. As well as the fluctuations in pressure caused by the formation, presence and removal of bubbles, there was also a discrepancy in the time that would be needed to remove them; especially if this was later deemed not possible.

With the effect of lowering a reservoir bottle in mind, it was discovered that a syringe could be attached to the acceptor circuit tubing and used to draw the acceptor circuit fluid through the system and simultaneously, remove any bubbles without disrupting the tissue disc positioning. Additionally, the chambers could be angled whilst drawing the fluid to prevent bubbles from forming in the first instance. A crucial part of this new filling method was found to be the positioning of the clips on the pump tubing. To successfully draw the liquid through the circuit, it was paramount that the clip on the pump was released prior to attaching the syringe and the clip was fastened before removing the syringe. It was found that failure to do the latter, resulted in the fluid rapidly retracting back through the circuit and in some cases, caused disruption to the tissue disc placement.

With the acceptor circuit almost completely filled by the syringe, the pump was switched on. Due to the liquid in the inserts, the partially filled donor circuit could be rapidly filled within several minutes at full pump speed. With the lowering of the acceptor circuit reservoir and syringe-filling technique, the system was now able to be primed and filled more rapidly than when using the method described in Chapter 2; the lack of bubble formation also meant that the time needed to set up the experiment was more reproducible.

While the new system configuration ensured the pressure gradient was in the correct direction, it also had the potential to mask minor leaks around the edge of tissue into the acceptor circuit that might be unnoticed until much later in the experiment or not be noticed at all. In the standard configuration, the pressure gradient was so small that any ill-fitted tissue would become dislodged and forced upwards and create a clear leak within the donor circuit. Whereas any ill-fitted tissue under such a great pressure gradient, would force the donor circuit fluid down the sides of the tissue and into the acceptor circuit. While large leaks would be obvious due to the colour difference in the circuit fluids and volume recovered, small slow leaks would be difficult to recognise. By using the syringe-filling method, the force created when drawing the syringe would pull the tissue discs flat against the insert mesh and thus, highlight any potential weak areas in the tissue fitting. With the insert pre-filled with fluid, it was possible to identify flaws with the tissue fitting as this would cause a visible reduction in the donor circuit fluid when the syringe was drawn in addition to a droplet formation under the insert; thereby highlighting any ill-fitted tissue that would have slowly leaked prior to starting the experiment.

Again, the real-time pressure monitoring element was instrumental in troubleshooting the system and allowed for a more informative investigation into the reasons why this occurred than trial and error style experiments. There remained the infrequent occasion where leaks were identified when the syringe was drawn. As the previously identified causes of these problems had been eliminated with the modifications to the system configuration and a filling technique, focus was placed on the tissue discs; the same tissue preparation method was used each time and so, the only variables were with the tissue itself. The tissue preparation and adherence step were closely reviewed as there was visible variability in the tissue after each collection, namely the thickness of the tissue and the mucus.

Given the structure of a standard insert, illustrated in Figure 3.13A, the larger internal O-ring could only be pushed down as far as the recess within the insert whilst maintaining complete contact with the inside of the insert; this is shown in Figure 3.13B. For the most part, the tissue thickness exceeded the recess within the insert and thus, could be suitably clamped into place using the larger internal O-ring; see illustration in Figure 3.13C. In this scenario, tissue movement was not observed when drawing the syringe and each absorption experiment was set up successfully.

There were several instances where the tissue was considerably thinner than usual and failed to reach the recess within the insert. These experiments had to be aborted before set-up as a seal could not be established around the edge of the tissue and it was obvious that the donor circuit fluid would be able to seep down the sides of the tissue into the acceptor circuit; this is shown in Figure 3.13D.

Upon closer inspection of the tissue discs that had become dislodged when the syringe was drawn, a very thick mucus layer was present on top of the tissue which had started to migrate away at the edges where the O-ring had been fitted. When the mucus layer was scraped away, it revealed that the tissue itself was not thick enough to exceed, or sit level with, the recess on the insert. It was apparent that the true thickness of the tissue was masked with a very thick layer of mucus that could only be realised once the mucus had been removed. When fitting the internal O-ring, it was pushed into the mucus layer which gave the appearance of a tight seal created as illustrated in Figure 3.13E. However, once the syringe was drawn to fill the system, the mucus layer would loosen with continued exposure to the donor circuit fluid and the tissue disc would become dislodged. This would result in another instance where the experiment had to be aborted.

It was not possible to distinguish whether the tissue was too thin during collection at the abattoir, this only became apparent once tissue preparation had begun in the lab. Due to the abattoir having set slaughtering hours and not being located within the vicinity of the lab, an experiment aborted in the lab meant that the entire day was lost as replacement fresh tissue could not be collected that day. While these incidences were not common, it was important that the system set-up procedure was as robust as possible to reduce sample loss and time wasted. To improve this, an additional O-ring, with a diameter matching that of the recess in the insert, was fitted on top of the tissue. Therefore, any tissue that sat lower than the top of the recess was fixed into place with the edges suitably sealed. By pairing the narrower O-ring with the original O-ring, this created a secure fitting that was suitable for each scenario discussed in terms of tissue thickness; see illustrated examples in Figure 3.13F-H.

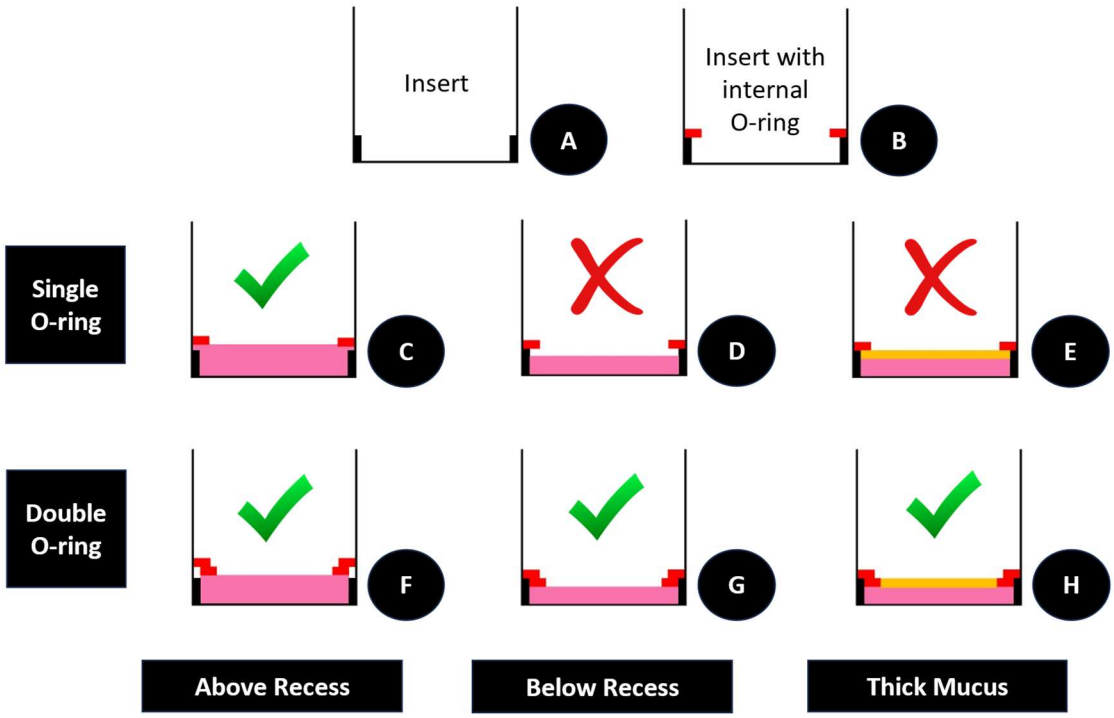

Figure 3.13: *Several diagrams illustrating the effect varying tissue and mucus thickness has on different O-ring fittings. A) A MilliCell Cell Culture insert detailing the recess at the bottom. B) An insert illustrating how far down an O-ring can be pushed before being hindered by the recess. C) A tissue disc in pink which is thick enough to sit above the recess and is successfully sealed with a single O-ring. D) A thin tissue disc in pink which sits below the recess and thus, is not sealed by the single O-ring fitted. E) A thin tissue disc reaching the recess with a thick mucus layer, shown in orange, leading to a false fitting when using a single O-ring. F) A tissue disc in pink which is thick enough to sit above the recess and is successfully sealed with a double O-ring fitting. G) A thin tissue disc sitting below the recess that has been successfully sealed by a smaller O-ring that fits inside the recess and held in place by a larger O-ring on top. H) A thin tissue disc coated in thick mucus that has been successfully sealed by a double O-ring, with the smaller O-ring pushing through the mucus and pinning the tissue disc in place within the recess.*

Although a double O-ring fitting is not essential for thicker tissue, it still needed to be implemented to maintain consistency between the amount of tissue surface directly exposed to the drug solution. The surface area available to the drug solution is known to impact permeation and thereby, the apparent permeability coefficient calculation. With these findings, a double O-ring fitting was implemented for all absorption experiments going forward. Since implementing the double O-ring fitting as well as the other

modifications discussed, the success rate of setting up the system and experiment significantly improved; with the only failed experiments being caused by human error. The absence of a leak during the syringe-filling process provided an extra level of confidence that the tissue discs were correctly fitted and secured well. With the final modifications made, the set-up of the absorption experiment was much more time-efficient than reported in Chapter 2 which was essential for fresh tissue experiments in order to maintain viability.

3.4.5 Tissue Viability

With the absorption experiment set-up time now significantly optimised, the viability of tissue was assessed at different time points before, during and after the absorption experiment had been performed.

Two absorption experiments were conducted over two days using the same time points to collect tissue for viability testing; the experiments lasted 2 h and 4 h, respectively. On the day of each experiment, three pig intestines were collected from the abattoir immediately after slaughter. Upon arrival at the laboratory, a piece of tissue was taken from each pig to assess the initial viability of the tissue. Straight after the removal of the muscle-serosal layer, another sample was taken from each pig to assess the effect of the procedure. From here, a disc from the intestine of each pig was fitted into each of the three chambers in the system and set up using the final modifications described in section 3.3.5 (Both experiments were performed as described in section 3.3.4 using 0.5 mg/mL atorvastatin with 0.4 % (v/v) Polysorbate-80). Simultaneously, a disc from each of the three intestines was set aside in PBS and incubated at the same time as the system to assess the effect that the system conditions had on viability. At the end of each experiment, all discs were collected from the system and the PBS.

On the day of the 2 h absorption experiment, a positive control tissue sample (B) was taken from each pig intestine and added to hydrogen peroxide which is a known apoptosis inducer (Xiang et al., 2016). All tissue samples were immunologically stained in three batches with a secondary control (SI) which had no primary antibody added. A full set of time points from the 2 and 4 h experiments were stained within the same batch.

The percentage of apoptotic cells measured from each tissue sample has been shown in Figure 3.14. In each staining batch, unspecific staining by the secondary antibody could

not be observed (see SI samples). Over both days, the percentage of apoptotic cells calculated from tissue that arrived at the lab were relatively very low; this ranged from 0.09-0.27% across the six pigs tested (see A/H samples). After the muscle serosal layer was removed from the tissue, the percentage of apoptotic cells detected were similar to those counted on arrival; the range fell between 0.13-0.40% (see I/C samples). Despite the overlapping ranges, a t-test considered the differences in apoptotic cells between the two sample groups to be statistically significant with a P value of 0.0144. This would suggest that, in this instance, the removal of the muscle-serosal layer had an effect on the viability of the tissue. After the 2 h absorption experiment, the percentage of apoptotic cells had increased whether the tissue had been within the system (sample = D) or kept outside of the system in PBS with the muscle left intact (sample = E). When compared to the I samples, P values of 0.0063 and 0.0201 indicated statistically significant differences to samples D and E, respectively. This was suggestive of a further reduction in viability after a 2 h experiment, enhanced under the system conditions with the muscle removed. Despite this, neither sample exceeded 0.7% apoptotic cells.

There was a significant rise in the percentage of apoptotic cells found in all tissue samples that were recovered after the 4 h absorption experiment; this was applicable whether the sample had been in the system or in PBS (see sample F & G). An unpaired t test performed on the corresponding samples collected after the 2 h experiment found statistically significant differences in the percentage of apoptotic cells with P values of 0.0402 (samples D & F) and 0.0018 (samples E & G). Unlike in the 2 h experiment, a P value of 0.4349 meant no statistically significant differences were found in the percentage of apoptotic cells between samples that had been exposed to the system with the muscle removed and in PBS with the muscle intact for 4 h. Overall, the percentage of apoptotic cells detected after the 4 h experiment were more than double that of the percentage attained when the intestines arrived at the lab. Although statistically significant differences in the samples show a decline in viability, the percentage of apoptotic cells remained relatively low and ranged from 1.31-2.33%. Thus, the tissue was still considered to be healthy and viable.

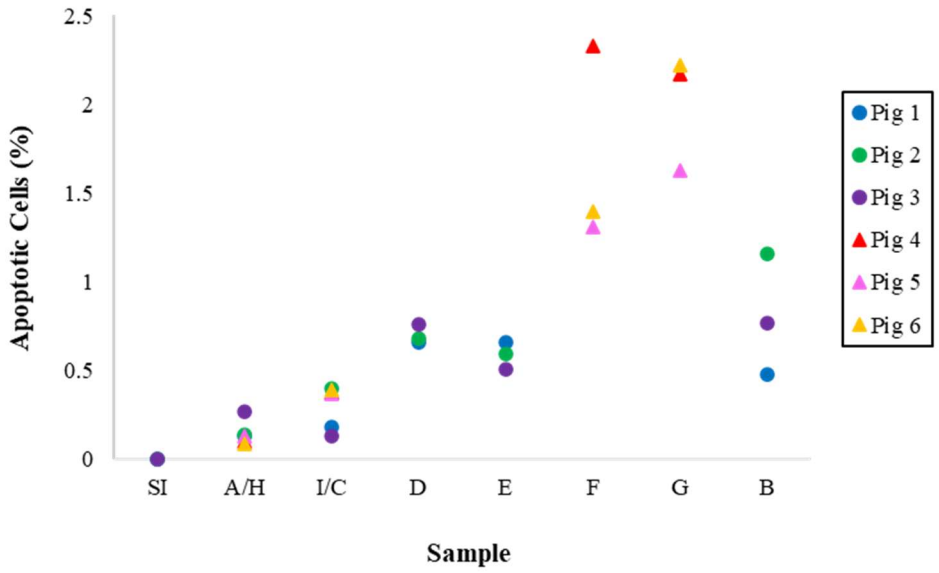

SI = Secondary control - no antibody added to I
A = On arrival at the lab with muscle intact (Day of 2 h experiment)
H = On arrival at the lab with muscle intact (Day of 4 h experiment)
I = Straight after muscle removal (Day of 2 h experiment)
C = Straight after muscle removal (Day of 4 h experiment)
D = After absorption experiment (2 h exposure in the system)
E = After absorption experiment (Kept in PBS with muscle intact)
F = After absorption experiment (4 h exposure in the system)
G = After absorption experiment (Kept in PBS with muscle intact)
B = After hydrogen peroxide treatment

Figure 3.14: *A graph showing the percentage of apoptotic cells for the different sample types collected from six pigs. The tissue samples collected from the day of the 2 h experiment are represented by circular data points i.e. pigs 1-3. The tissue samples collected from the day of the 4 h experiment are represented by triangular data points i.e. pigs 4-6 (n=3).*

The tissue samples treated with hydrogen peroxide (sample = B) were variable and shown to be a poor inducer of apoptosis for porcine intestinal tissue. When counting the apoptotic cells, areas to assess were chosen at random with one exception; random areas on the edge of the tissue were disregarded because of higher autofluorescence at the edges of the tissue. Therefore, it remains a possibility that the positive control samples were not left in the hydrogen peroxide for long enough to penetrate deeper into the tissue where counting took place.

Viability experiments such as those reported here are time-consuming and render the tissue unsuitable for LC-MS/MS and DESI MSI analysis. Thus, meaning that viability

experiments must be performed separately to absorption experiments. A consequence of this is that any sporadic environmental changes that could occur during an absorption experiment and affect viability would be missed. At a minimum, the labour-intensive viability experiment should be repeated when new excipients are introduced to the system as this could impact viability. A more ideal approach would be to modify the system further to incorporate built in probes to allow TEER measurements; this would allow for in-line viability testing to be performed throughout an absorption experiment with significantly less processing post-experiment.

As an interim solution, it would be wise to repeat the positive control with either smaller pieces of tissue or leave the tissue in hydrogen peroxide for a longer period of time. Additionally, different concentrations, and even different reagents, could be trialled to establish a suitable positive apoptosis control for this tissue type.

3.5 Conclusions

Incorporation of real-time pressure monitoring sensors into the QV600 LLI system when it was used with fresh tissue provided a valuable insight into the dynamics of the system and enabled rapid troubleshooting. This allowed the system to be successfully filled much more rapidly and reproducibly, improving the robustness of the system. With the further modifications made, the pressure sensors provided confidence that the correct pressure gradient was established and maintained throughout each absorption experiment. The improvement to the tissue preparation method to include a double O-ring fitting further increased the success rate in setting an experiment up each time. In combination with the syringe filling method, this provided great confidence that the barrier between the two circuits was intact for every absorption experiment. With the final modifications made to the system, the experimental set up was reduced to the extent that a 2 h absorption experiment could be performed (using material obtained from that day's slaughter at a local abattoir) and the ex vivo tissue remain viable throughout.

References

Arnold, Y. E., Thorens, J., Bernard, S., & Kalia, Y. N. (2019). *Drug transport across porcine intestine using an ussing chamber system: Regional differences and the effect of P-glycoprotein and CYP3A4 activity on drug absorption*. MDPI AG. 10.3390/pharmaceutics11030139

Cummings, B. S., & Schnellmann, R. G. (2013). *Measurement of cell death in mammalian cells*. Wiley. 10.1002/0471141755.ph1208s25

Dunn, J., & Grider, M. (2024). *Physiology, adenosine triphosphate*. Treasure Island (FL): StatPearls Publishing.

Giusti, S., Sbrana, T., La Marca, M., Di Patria, V., Martinucci, V., Tirella, A., Domenici, C., & Ahluwalia, A. (2014). A novel dual-flow bioreactor simulates increased fluorescein permeability in epithelial tissue barriers. *Biotechnology Journal, 9*(9), 1175-1184. 10.1002/biot.201400004

Kirkstall Ltd.*QV600 user manual - liquid / liquid*

Mukherjee, B., Satapathy, B. S., Bhattacharya, S., Chakraborty, R., & Mishra, V. P. (2017). *Pharmacokinetic and pharmacodynamic modulations of therapeutically active constituents from orally administered nanocarriers along with a glimpse of their advantages and limitations*. Elsevier. 10.1016/b978-0-323-52727-9.00019-4

Qiu, Y., Chen, Y., Zhang, G., Yu, L., & Mantri, R. (2017). *Developing solid oral dosage forms* (2nd ed.). Mica Haley.

Ripken, D., & Hendriks, H. F. J. (2015). *Porcine ex vivo intestinal segment model*. Springer International Publishing. 10.1007/978-3-319-16104-4_23

Xiang, J., Wan, C., Guo, R., & Guo, D. (2016). *Is hydrogen peroxide a suitable apoptosis inducer for all cell types?*. Hindawi Limited. 10.1155/2016/7343965

Chapter 4:

The Effect of Excipients and Other Environmental Factors on the Absorption and Permeation of Atorvastatin through Ex-Vivo Porcine Intestinal Tissue

4.1 Introduction

Oral drugs require careful formulation to overcome the many obstacles and challenges brought by the oral administration route. Improper formulation can lead to early drug delivery meaning absorption in the wrong compartment and consequently, a reduction in the amount of active ingredient (API) reaching the site of action.

In addition to the challenges detailed in Chapter 1, Atorvastatin calcium has specific issues in terms of solubility. The drug was assigned to Class II of the Biopharmaceutics Classification System (BCS) due to its poor aqueous solubility (Al-Kazemi et al., 2019). Therefore, atorvastatin calcium can be commonly found formulated with polysorbate-80 which acts as a solubilising agent (Khan & Dehghan, 2011). The excipient acts as a surfactant which in turn, would increase the solubility of an agent into another. In absence of formulation, atorvastatin acid is regarded highly soluble at pH 6. This is physiologically relevant to the small intestine as the pH rapidly changes from pH 1-3 in the stomach to pH 6 in the duodenum before slowly reaching pH 7.4 by the end of the intestinal tract. Despite this, the bioavailability of atorvastatin was reported to be as low as 14% (Lennernas, 2003). Extensive first-pass metabolism was thought to play a large role in this since the gut wall contains metabolising enzymes (CYP3A4) known to assist in the major metabolic pathway of atorvastatin; this has been thoroughly detailed in Chapter 1.

Other excipients have been advertised to increase drug permeation although, these are not commonly formulated with atorvastatin calcium. The excipient DEGEE LQ is promoted as a co-solvent that can improve delivery and bioavailability by stabilising poorly water-soluble drugs within oral formulations (*Super refined™ DEGEE* . 2024). Another excipient that acts to improve permeation is mapcho-12. This excipient is often used for membrane protein solubilisation and has been shown to improve permeability by modulating tight junctions (*Mapcho®-12.* 2024).

When replicating the GI tract to test different excipients and formulations, a few considerations should be deemed essential. To observe optimal permeation in the correct direction within a GI model, a significant pressure gradient should exist between the two compartments to encourage drug movement. In addition, suitable sink conditions should be used in accordance to the solubility-permeability relationship for the specific drug under investigation (Sugita et al., 2021).

As previously discussed in chapter 1 and 2, mass balance calculations should be performed in this kind of study. The mass balance highlights any significant drug loss from inefficient extraction and extensive metabolism as well as discrepancies caused by instrumental and human error. Upon quantification of atorvastatin from media, care should be taken during the extraction process. Atorvastatin was reported to be extremely susceptible to plasma protein binding with levels exceeding 98% (Lennernas, 2003). Therefore, the extraction method should be optimised to minimise drug loss during this process.

In order to generate further information, DESI MS imaging has promise to be the perfect tool to map the distribution of drugs and related ions in tissue along with other species such as lipids and proteins; thus providing useful spatial information. This mass spectrometry imaging technique requires little-to-no sample preparation as no matrix application is required. The lack of matrix provides the perfect opportunity for post-staining of the tissue sections due to being in the native state. This saves time in optimisation of the DESI method when compared to MALDI. Additionally, the Waters Select series MRT in DESI mode boasts a high mass resolution TOF that in turn, delivers excellent mass accuracy. The ultra-high resolving power enables confident and precise identification which is ideal for the discovery of metabolites and other native species. As discussed in Chapter 1, to achieve such an impressive resolution, the significant increase in TOF length leads to a reduction in the duty cycle and thus, sacrifices a level of instrument sensitivity. However, some of the sensitivity loss is recuperated in this instrument by the use of a specifically developed encoded frequent pushing (EFP) method (LECO Corporation, 2018).

The effect of different excipients were observed by conducting a series of studies in which the excipient levels were increased in sensible increments as well as being combined with other types of excipients. Additionally, these studies were repeated using different pH levels and acceptor circuit supplements in order to gauge its effect on permeation and the sink conditions. In addition, the plethora of studies allowed the adapted millifluidics system to undergo more thorough testing and the identification of areas for further improvement. DESI MSI was implemented to allow the distribution of atorvastatin and related compounds to be mapped on the tissue section in relation to the lipid distribution with a high level of mass accuracy and thus, certainty of assignment. The method provided high throughput data to be acquired with minimal preparation and

alteration of the tissue. The previously optimised LC-MS/MS method was utilised in order to quantify the amount of atorvastatin present in the experiment samples using newly improved instrument-friendly sample extraction techniques.

4.2 Chapter Aims

The overall aim of the following chapter was to investigate the effects of different excipients and environmental factors on drug permeation using the adapted millifluidics model. The initial objective focused on the selection of suitable excipients for atorvastatin which were then added to each experiment in increasing increments and combinations. The subsequent objective saw the repetition of these studies using the theoretically optimal pH in the donor circuit and supplements added to the acceptor circuit in an endeavour to improve permeation. A consequential objective entailed a short study which explored the partial removal of mucus from the tissue surface.

4.3 Materials and Methods

4.3.1 Materials

Gibco BenchStable DMEM/F12, phosphate-buffered saline (PBS), fetal bovine serum (FBS), bicarbonate-buffered krebs-ringer solution (KRS), 2-methylbutane 99+% extra pure, LC-Grade methanol, HPLC grade Methyl-Tert-Butyl Ether (MTBE), HPLC grade ethyl acetate, LC-Grade acetonitrile (ACN) and magnesium sulphate ($MgSO_4$) were purchased from Fisher Scientific Ltd**.** (Loughborough, UK). Sodium chloride (NaCl), Atorvastatin calcium salt and the deuterated internal standard, Atorvastatin-(anilide ring-d5) calcium salt were purchased from Merck Life Sciences (Dorset, UK). Formic acid 98% was purchased from Scientific Laboratory Supplies (Nottingham, UK). 18.2 MΩ × cm water was collected from an ELGA water purification system (Buckinghamshire, UK). Cryo-M-Bed and hydrochloric acid were purchased from VWR International Ltd**.** (Lutterworth, UK). Porcine small intestine was provided by R.B Elliott & Son (Chesterfield, UK). Super refined Polysorbate (80) LQ and DEGEE LQ was donated by CRODA (DE, USA). Mapcho-12 was purchased from Avanti Polar Lipids (AL, USA).

4.3.2 Fresh Tissue Preparation

The tissue used for the absorption experiments performed in this chapter were collected and prepared as described in section 3.3.2. The single O-ring fitting was originally used before it was later upgraded to the double O-ring fitting as described in 3.3.5.4. The choice of fitting has been specified along with other details relevant to the absorption study in Table 4.1.

4.3.3 QV600 LLI Set Up

For each absorption experiment, the QV600 LLI was set up with pressure sensors and configured as described in section 3.3.5; the syringe-filling technique was used to fill and prime the system.

4.3.4 Absorption Experiment

The standard donor circuit fluid consisted of PBS with 0.5 mg/mL of Atorvastatin calcium; varied amounts of different excipients and other compounds were added dependent on the study performed. The standard acceptor circuit fluid consisted of Gibco BenchStable DMEM/F12 with some studies including 10% FBS as an additional supplement. After both circuits in the system had been filled completely, the system was transported into an incubator set to 37 °C, 5% CO_2 for 2 h. At the end of the experiment, the circuit tubing lines were drained before removing the inserts containing tissue. Each tissue disc was rinsed thoroughly with PBS before being immediately snap-frozen by liquid nitrogen whilst submerged in 2-methylbutane. Each disc was stored separately at −80 °C. The donor and acceptor circuit reservoirs were emptied and stored at 4 °C. The entire system was flushed with 500 mL of 70% methanol in 50 mL increments. The system was subsequentially flushed with 50 mL of sterile PBS before being drained fully of all fluid using a Pasteur pipette and syringe. All solutions used for rinsing the tissue and cleaning the system were collected and stored at 4 °C.

4.3.4.1 Excipient Studies

A series of different excipient studies were performed using varying concentrations and combinations of excipients in the donor circuit. The donor circuit consisted mostly of PBS which, without interference, buffered the circuit to pH 7.4. Most studies were repeated with the donor circuit adjusted to pH 6; this was achieved by adding 0.1 M hydrochloric acid dropwise until the pH of the donor circuit was within 0.1 of pH 6.0.

The pH of the donor circuit solution was confirmed each time using a pH probe before it was added to the donor reservoir. For each experiment performed at pH 6, 30 mL of DMEM/F12 containing 10% FBS was added to the acceptor reservoir. All experiments within a study were ran in triplicate. A summary of the parameters for each of the studies conducted has been shown in Table 4.1.

Table 4.1: *A table summarising the parameters and modifications used in each excipient study. All studies were performed in triplicate.*

Study Name	Donor Circuit Modifications				10% FBS in the acceptor circuit?	O-ring fitting used?
	Varying Excipient	Excipient concentration range	Addition of 0.4 % (v/v) Polysorbate-80?	pH		
Polysorbate-80 Only	Polysorbate-80	0-2 % (v/v)	No	7.4	No	Single
DEGEE LQ Only	DEGEE LQ	0-2 % (v/v)	No	7.4	No	Single
Polysorbate-80 & DEGEE LQ	DEGEE LQ	0-2 % (v/v)	Yes	7.4	No	Double
Polysorbate-80 Only	Polysorbate-80	0-2 % (v/v)	No	6	Yes	Double
Polysorbate-80 & DEGEE LQ	DEGEE LQ	0-2 % (v/v)	Yes	6	Yes	Double
Polysorbate-80 & Mapcho-12	Mapcho-12	0-1 mM	Yes	6	Yes	Double

4.3.4.2 Study with Partial Mucus Removal

A triplicate absorption experiment with 0.4% v/v Polysorbate-80 was ran with an extra tissue preparation step. The tissue was soaked in ice-cold KRS during transportation. Once at the lab, the tissue was then flushed with fresh KRS similar to the practice detailed by (Arnold et al., 2019). The tissue was fitted using the double O-ring combination.

4.3.5 Sample Extraction and Preparation

Prior to any extraction, the volume of each solution collected was measured. To extract from the donor circuit fluid, 1 mL of the sample was added to 4 mL of MTBE:ethyl acetate (50:50 v/v) and 0.9g NaCl. The mixture was vortexed for 10 minutes before centrifuging at 3000 rpm for a further 10 minutes. The supernatant was collected and dried completely under a nitrogen stream while in a water bath set to 37 °C. The sample

was reconstituted in 1mL of 90% methanol. The donor circuit fluid was then diluted 1 in 250 with 90% methanol.

For the tissue rinse solution, 1 mL of the sample was added to 4 mL of MTBE:ethyl acetate (50:50 v/v). The mixture was vortexed for 10 minutes before centrifuging at 3000 rpm for a further 10 minutes. The supernatant was collected and dried completely under a nitrogen stream while in a water bath set to 37 °C. The sample was reconstituted in 1mL of 90% methanol. The tissue rinse solution was then diluted 1 in 10 with 90% methanol.

The final system rinse solution was extracted using the same method as above but in different proportions. 10 mL of the sample was added to 10 mL of MTBE:ethyl acetate (50:50 v/v). The mixture was vortexed for 10 minutes before centrifuging at 3000 rpm/min for a further 10 minutes. The supernatant was collected and dried completely under a nitrogen stream while in a water bath set to 37 °C. The sample was reconstituted in 100 µL of 90% methanol.

The acceptor circuit fluid required an additional extraction step. 10 mL of the sample was added to 20 mL of ACN and vortexed for 1 minute. The solution was then centrifuged at 4000 rpm for 5 minutes. The supernatant was collected and added to 20 mL of 2M $MgSO_4$. The solution was then vortexed for 1 minute before being centrifuged at 4000 rpm at 0 °C for 5 minutes. The upper layer was collected and dried completely under a nitrogen stream. The sample was reconstituted in 10 mL of PBS. This solution was added to equal amounts of MTBE:ethyl acetate (50:50 v/v). The mixture was vortexed for 10 minutes before centrifuging at 3000 rpm/min for a further 10 minutes. The supernatant was collected and dried completely under a nitrogen stream while in a water bath set to 37 °C. The sample was reconstituted in 100 µL of 90% methanol.

One tissue disc from each experiment was selected for extraction and weighed. The tissue disc was added to 30 mL of 90% methanol and homogenised. The solution was then centrifuged at 3000 xg for 5 minutes. The supernatant was collected, syringe filtered before being centrifuged again for a further 5 minutes. The solution was then syringe filtered again. This solution and the initial system rinse solution were then diluted 1 in 2 with 90% methanol. Once extracted and suitably diluted, the samples were ready for LC-MS/MS analysis.

From a 5 µg/mL Atorvastatin stock solution, nine calibration standards and a blank were prepared in 90% methanol and ranged from 0–5 µg/mL. From all prepared calibration standards and samples, 50 µL was added to a low volume LC vial along with 25 µL of 0.1 µg/mL deuterated internal standard, Atorvastatin-d5 for LC-MS/MS analysis. All standards and samples were run in triplicate.

4.3.6 LC-MS/MS Method

All LC-MS/MS experiments were performed using the Agilent 6420 triple quad mass spectrometer in negative ion mode. The analyzer was set to detect the product ion of Atorvastatin-d5 calcium salt (*m*/*z* 562 -> *m*/*z* 458) and the product ion of Atorvastatin calcium salt (*m*/*z* 557 -> *m*/*z* 453) in multiple reaction monitoring (MRM) mode. Additionally, the method was set to measure qualifier transitions at *m*/*z* 562 -> *m*/*z* 283 and *m*/*z* 557 -> *m*/*z* 278 for Atorvastatin-d5 calcium salt and Atorvastatin calcium salt, respectively. An Agilent EclipsePlusC18 RRHD 1.8 µm 2.1 × 50 mm column was used. The mobile phase consisted of water: ACN: methanol (41:19:40, *v*/*v*/*v*) with 0.005% formic acid and was used in isocratic mode at a flow rate of 0.275 mL/min.

4.3.7 Cryosectioning

Tissue discs were transferred to the Leica CM 1950 Cryostat (Leica Microsystems, Milton Keynes, UK). The discs were mounted onto a cork ring using Cryo-M-Bed embedding compound and were allowed to thermally equilibrate for 1 h. The chamber and specimen head temperature were set at −20 °C. Each tissue disc was cryosectioned into 10 µm sections and thaw mounted onto glass microscope slides. The sections were then vacuum packed and stored at −80 °C until needed.

4.3.8 DESI Imaging

Prior to DESI imaging, optical images of the selected tissue sections were acquired using the Super Coolscan 5000 ED Film Scanner. All tissue sections in this study were imaged using the Waters Select Series MRT mass spectrometer with a DESI source. The instrument was calibrated every day using polyalanine applied to a separate microscope slide. The DESI images were acquired in positive ion mode and focused on a mass range of *m/z* 0-2400. The spatial resolution was set to 30 µm. Three separate sections from the same absorption experiment were imaged within the same batch to confirm distribution. One tissue disc from each absorption experiment type was imaged.

4.3.9 Mass Balance Evaluation

Two different formulations of 500 µg/mL atorvastatin were made in PBS and buffered to pH 6; one contained 0.4% polysorbate-80 and the other did not. Each standard was made in triplicate. All standard replicates were extracted following the method detailed in section 4.3.5 for the donor circuit fluid. The amount of atorvastatin recovered from the extracts was quantified using the LC-MS/MS method detailed in section 4.3.6.

Two different formulations of 250 µg/mL atorvastatin standards were made in DMEM/F12; one with 10% FBS and the other without. Each formulation was made in triplicate. From each standard replicate, three aliquots were extracted following the method detailed in section 4.3.5 for the acceptor circuit fluid. The only exception to this method was that the final extracts were diluted rather than re-constituted. The amount of atorvastatin recovered from the extracts was quantified using the LC-MS/MS method detailed in section 4.3.6.

4.3.10 Data Analysis

The DESI MS data was lockmass corrected with polyalanine using Mass Lynx V4.2 SCN1026 Release 3 and processed using the HDI v1.7 software from Waters. For the LC-MS/MS data, the chromatographic peaks for Atorvastatin and Atorvastatin-d5 were integrated and processed using the Agilent MassHunter Quantitative Analysis Version 8.09 software. This software was also used to create the calibration graph from the standards and calculate the concentration of all the samples. The back-calculations from software generated concentrations were performed manually.

The apparent permeability coefficient for transport across porcine intestinal tissue ($P_{app,pig}$) was determined for each drug absorption experiment performed in the study (Arnold et al., 2019). The following equation was used to determine the Papp,pig value for each experiment:

$$P_{\text{app,pig}} = \frac{dc}{dt} \times \frac{V}{A \times C_0} \left(\frac{cm}{s}\right)$$

where dc/dt is the change in the acceptor concentration calculated using the final concentration in the acceptor circuit divided by the length of the experiment (2 h), V is the volume in the donor circuit (30 mL), A is the exposed surface area (single o-ring

fitting = 0.515 cm^2 & double o-ring fitting = 0.292 cm^2), and C_0 is the initial concentration of Atorvastatin in the donor circuit (500 µg/mL).

4.4 Results and Discussion

The initial study discussed here was conducted in a similar manner to the frozen tissue study reported in Chapter 2. The key differences between the two studies were the use of viable tissue and some changes to the system configuration.

4.4.1 Frozen vs Fresh Comparison

When comparing the Papp,pig values from the frozen to the fresh tissue study in Figure 4.1, it was clear that four out of the eighteen absorption experiments in the fresh study had much higher permeation coefficients in comparison to the others within the study. In addition to the exceptionality of these values, they appeared to be random and sporadic; the values belonged to three different experiment types and did not show any clear trend. It was critical to note that for this study, that the single o-ring fitting was still in use. While no obvious leaks were detected and these values did not exceed those in similar published works, minor leaks post set-up could not be confidently ruled out when using a single o-ring fitting (Iqbal et al., 2021). While the frozen tissue studies also used the single o-ring fitting, the lack of viability meant that there was ample time and tissue to carefully select from. Thus, thicker tissue was always opted for making a single o-ring fitting suitable in that scenario. Furthermore, tissue viability was of no concern in the frozen study and so, the experiments were set-up at a much lower flow rate which, significantly reduced the chance of tissue disc movement.

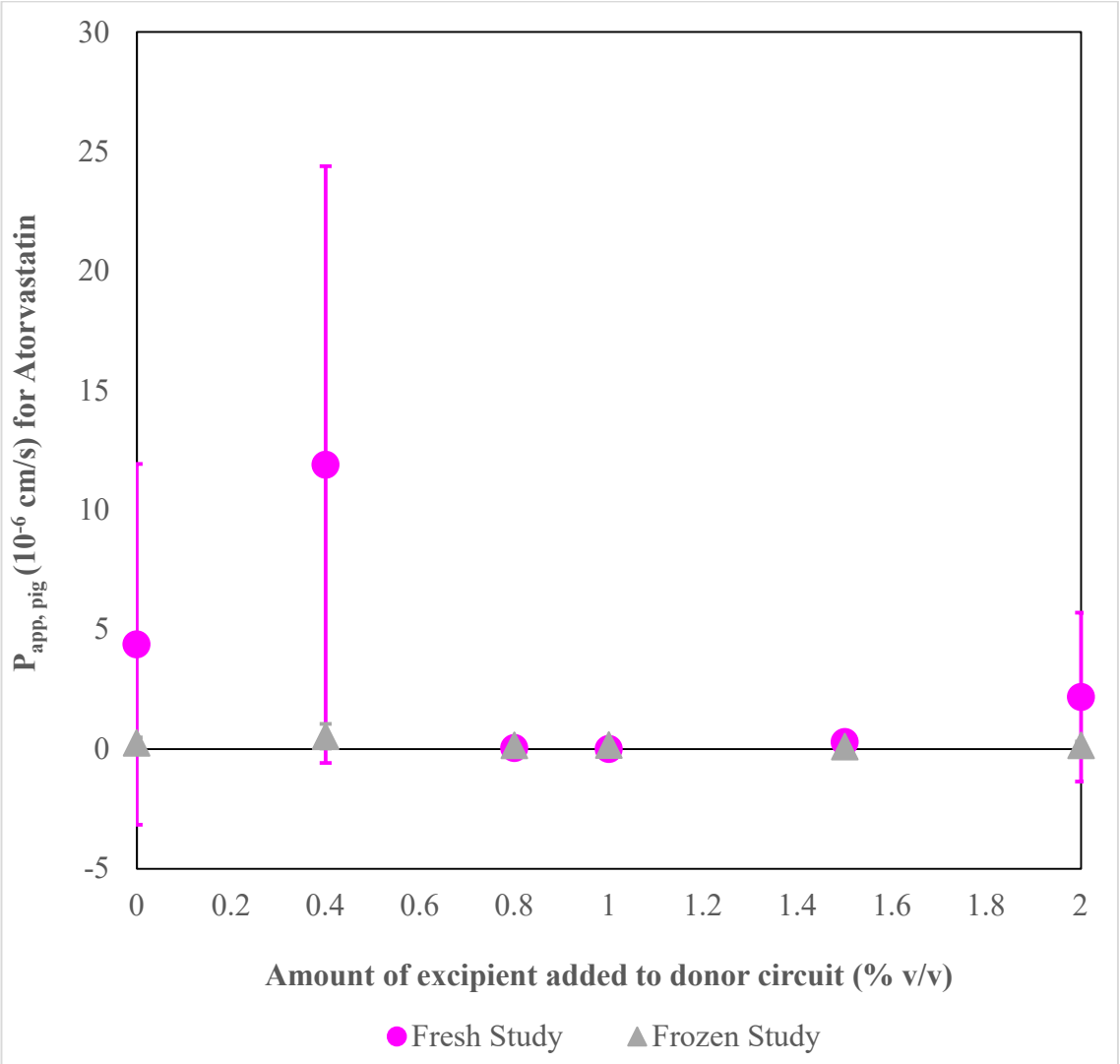

Figure 4.1: *A graph showing the $P_{app,pig}$ of Atorvastatin plotted against the concentration of Polysorbate-80 in the donor circuit of the corresponding absorption experiment. The data from two different studies have been shown together here; each experiment from the frozen study from Chapter 2 and the corresponding fresh study have been represented by grey triangles and pink circles, respectively (n=3).*

Three data points in Figure 4.1 were considered to be outliers and skewed the other data points. In order to fully interpret the other data points, the data was statistically analysed without this data point and replotted in Figure 4.2.

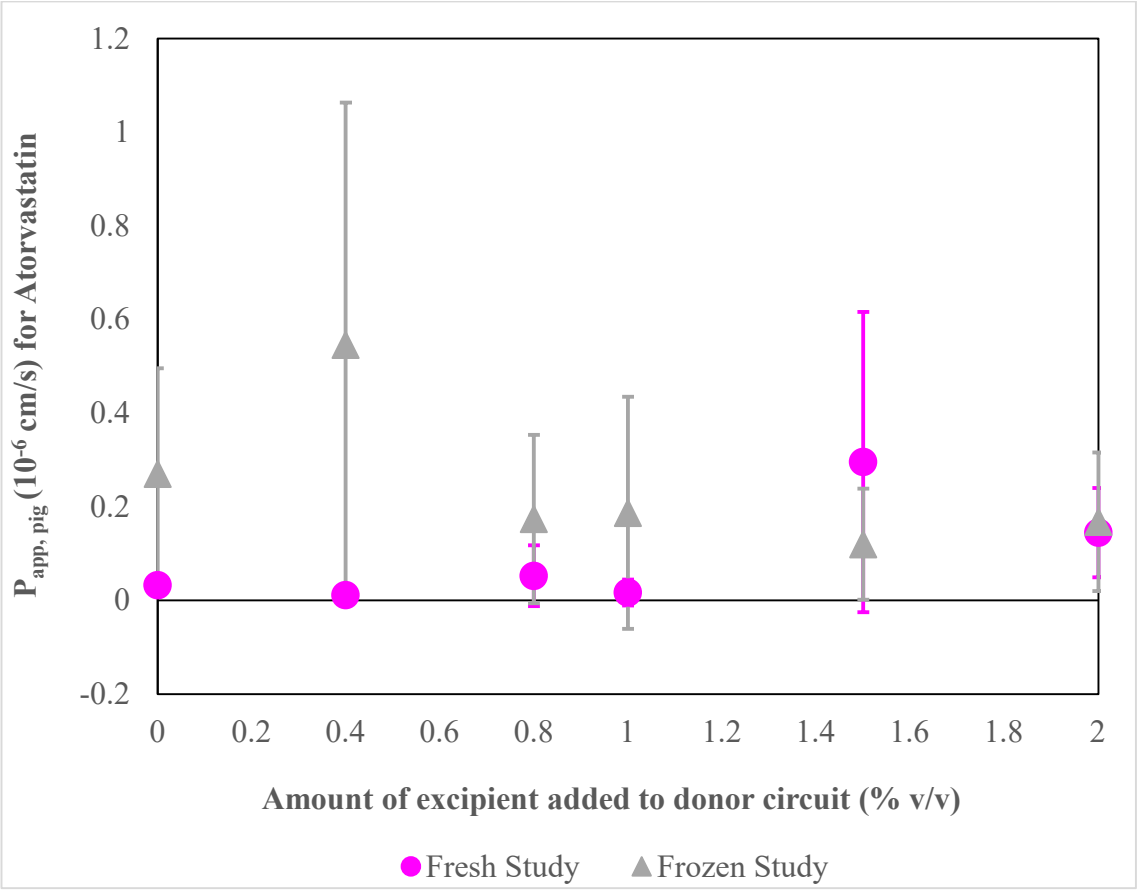

Figure 4.2: *A graph showing the dataset from Figure 4.1 with the identified outliers removed and data reanalysed (n=3).*

With the outliers temporarily excluded, it appeared that the amount of Atorvastatin which had permeated into the acceptor circuit was lower than that in the corresponding experiments in the frozen study. Despite this, an unpaired t test between the two studies gave a P value of 0.0771 which implies that statistically, the differences between the studies were not quite significant. Key differences that were considered when comparing the two studies were the time difference and the status of the tissue. The frozen study was performed over 6 h while the fresh study was limited to 2 h. To account for this, the data was presented in the form of the $P_{app,pig}$ value as the duration of the experiment was factored into the equation. Regardless of this, it has been widely reported that Atorvastatin would achieve peak plasma concentration within 2 hours of oral administration. When comparing the acceptor concentration of the datasets prior to calculating the $P_{app,pig}$ values, it was clear that even with the assumption of a linear increase, the fresh study values would be lower than those obtained in the frozen study.

As the name suggests, the frozen study had utilised tissue that had been previously frozen and thawed directly before use. This practise had the potential to pose an issue unique to this study; the possibility of micro-fracturing through the tissue. While visibly cracked or damaged tissue would not be used, small cracks were observed on a number of occasions upon the final snap-freeze of the collected tissue discs. An important observation to note was that no cracking or other damage occurred on the initial snap-freeze of the freshly collected tissue. For both snap-freezing sessions, the tissue was snap-frozen for the minimal amount of time required whilst submerged in 2-methylbutane to minimalise damage to the tissue structure while snap-freezing. With this in mind, it remains possible that micro-fractures were present in the tissue after the initial snap-freeze and were exacerbated during the second. Thus, leading to an overall increased movement of Atorvastatin through the tissue and into the acceptor circuit.

A potentially significant observation made during the preparation of the tissue for the frozen tissue study was the inadvertent removal of mucus. During the thawing process, large quantities of mucus would become visibly separated from the tissue. Mucus acts as a physical barrier between the drug and the surface of the tissue which can hinder the rate of drug absorption into the intestinal tissue. Thus, its removal would provide a more direct absorption pathway for drugs to move into the tissue. It should also be noted that between tissue collections, the amount and visual composition of mucus on the surface of the tissue was highly variable. Continuing with the previous theory, this could explain the high variability seen in the amounts of atorvastatin that had completely permeated through the fresh tissue.

Another inherent difference between the two studies was the absorption routes available to Atorvastatin. With the original study, the only absorption route available to Atorvastatin would have been passive diffusion as the tissue had been previously frozen and was no longer viable. Whereas with viable cells, a previous study has shown that Atorvastatin could be transported across the apical membrane via P-glycoprotein mediated transport (Wu et al., 2000). Additionally, Atorvastatin is now susceptible to metabolism by intestinal CYP3A4 enzymes present in the epithelium of the small intestine. Atorvastatin is extensively metabolised in the gut as well as the liver, with the oral bioavailability reported to be as little as 14%. Therefore, another possible explanation for the drastic reduction of Atorvastatin seen in the acceptor circuit of fresh tissue could be the result of extensive metabolism.

While the $P_{app,pig}$ values provided no information on the effect increasing Polysorbate-80 had on fresh tissue, more valuable information was acquired from the tissue discs. The amount of Atorvastatin recovered from the tissue extract was calculated using one tissue disc from each experiment within the fresh tissue study and displayed in Figure 4.3. Like the frozen study, a clear relationship was shown between the amount of Atorvastatin quantified in the tissue extract and the amount of Polysorbate-80 added to the donor circuit. When Polysorbate-80 was absent from the donor circuit, the amount of Atorvastatin within the tissue extract was at an optimum. As Polysorbate-80 was introduced to the donor circuit and gradually increased, it appeared that the amount of Atorvastatin in the tissue extract suffered a sharp decline before reaching a plateau. A one-way ANOVA and Tukey HSD test confirmed that only the data points with no excipient were significantly different with P values less than 0.05.

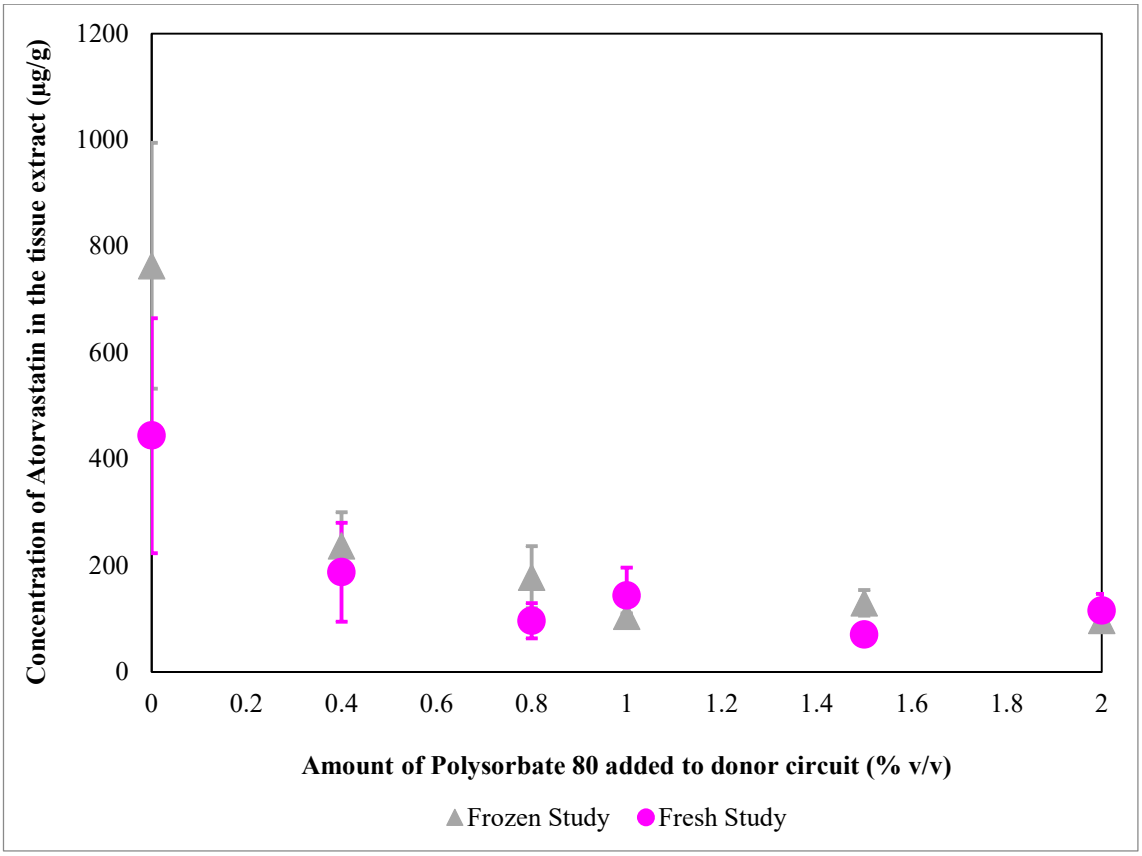

Figure 4.3: *A graph showing the concentration of Atorvastatin calculated from the tissue disc extract plotted against the corresponding amount of Polysorbate-80 that was added to the donor circuit for that absorption experiment. The data from two different studies have been shown together here; each experiment from the frozen study from Chapter 2 and the corresponding fresh study have been represented by grey triangles and pink circles, respectively (n=3).*

Interpretation of the graph alone could falsely lead to implications that the presence of Polysorbate-80 hinders the permeation of Atorvastatin into the tissue. A tissue disc from experiments in the study with 0%, 0.4%, 1% and 2% Polysorbate-80 were sectioned, scanned and imaged using DESI MS. The DESI MS images, displayed from Figure 4.4-4.9, provide further information into the spatial distribution of the drug within the tissue section. The images show the distribution of Atorvastatin in the calcium salt form in which it was originally administered as well as the various ion adducts of the active hydroxy-acid form, Atorvastatin acid.

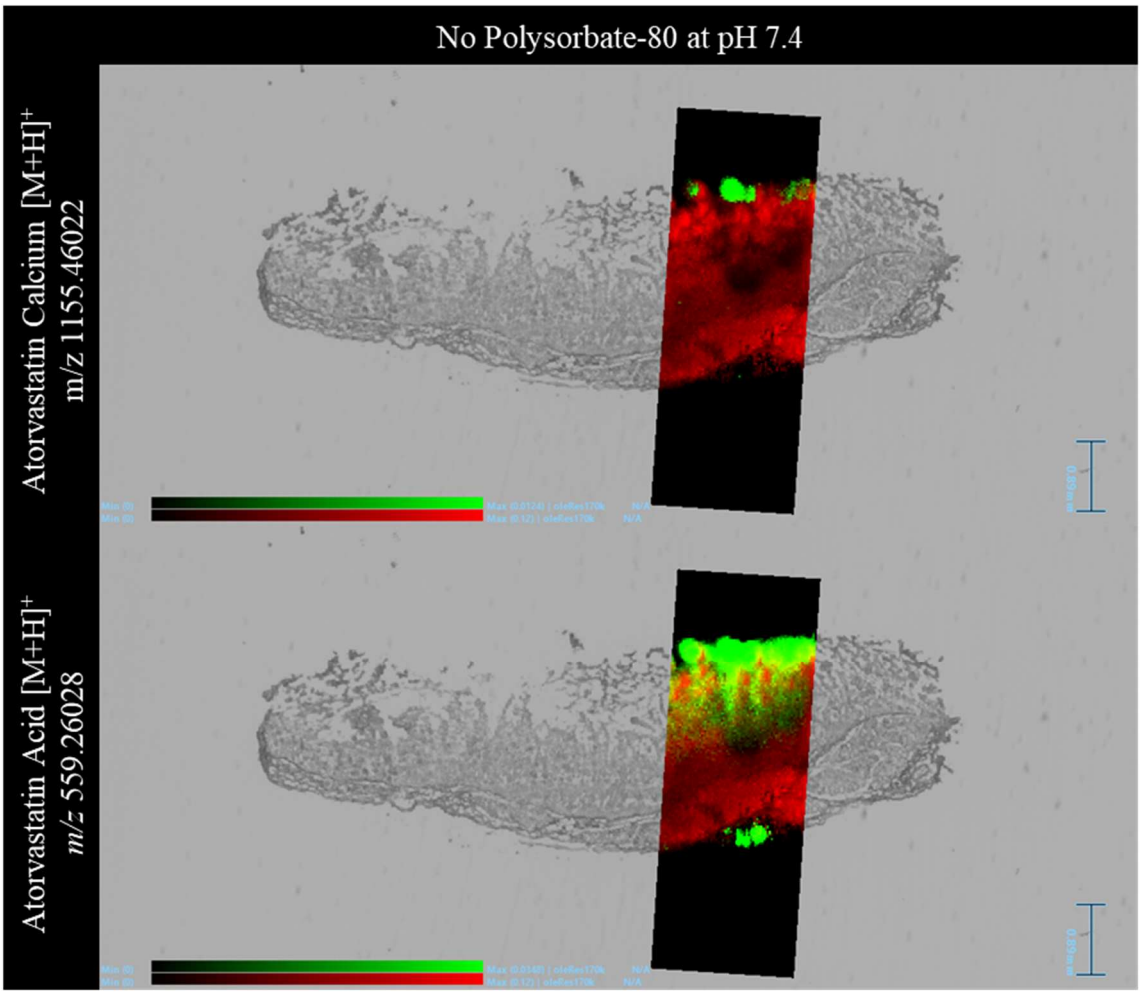

Figure 4.4: *DESI Images overlaid onto an optical image of the tissue section they were acquired from with the surface of the tissue facing upwards. The tissue section was acquired from a fresh tissue absorption experiment with no polysorbate-80 in the donor circuit which was buffered to pH 7.4. The distribution of the lipid ion m/z 780.5 has been displayed in a red colour scale. The distribution of protonated atorvastatin calcium and atorvastatin acid were shown in the top and bottom window, respectively, using a green colour scale. All identified drug related ions were well within 1ppm.*

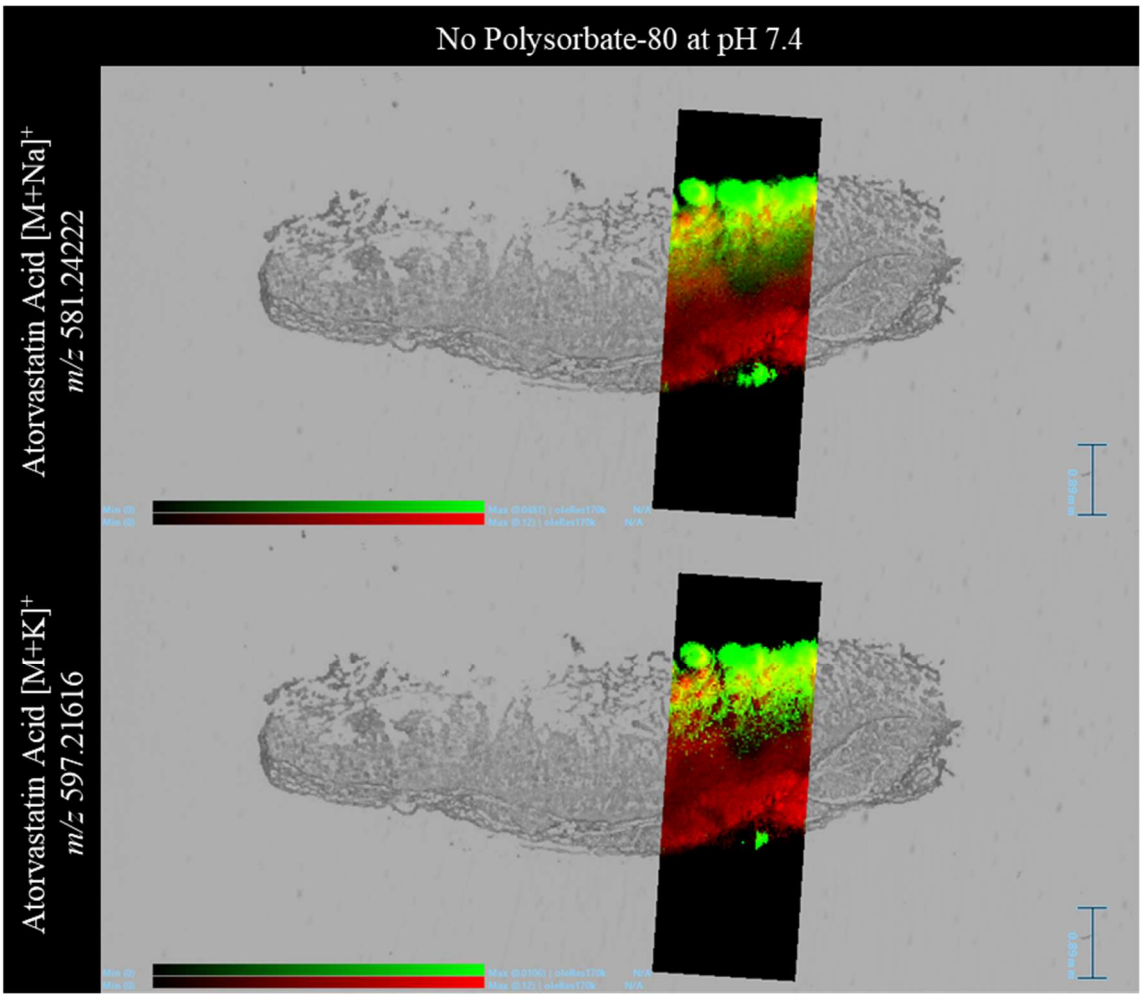

Figure 4.5: *DESI Images overlaid onto an optical image of the tissue section they were acquired from with the surface of the tissue facing upwards. The tissue section was acquired from a fresh tissue absorption experiment with no polysorbate-80 in the donor circuit which was buffered to pH 7.4. The distribution of the lipid ion m/z 780.5 has been displayed in a red colour scale. The distribution of atorvastatin acid sodium and potassium adducts were shown in the top and bottom window, respectively, using a green colour scale. All identified drug related ions were well within 1ppm.*

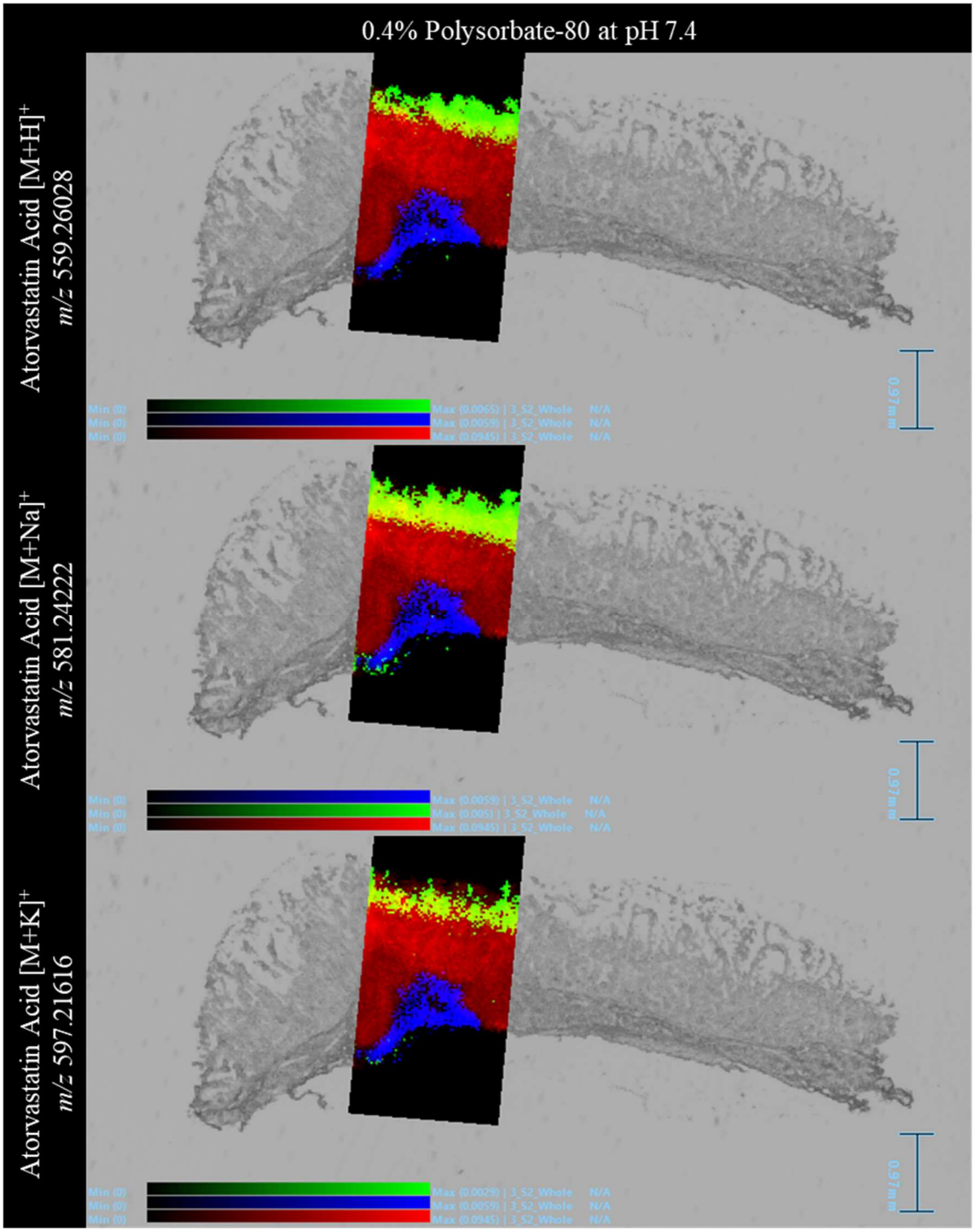

Figure 4.6: *DESI Images overlaid onto an optical image of the tissue section they were acquired from with the surface of the tissue facing upwards. The tissue section was acquired from a fresh tissue absorption experiment with 0.4% polysorbate-80 in the donor circuit which was buffered to pH 7.4. The distribution of the lipid ion m/z 780.5 was displayed in a red colour scale. The distribution of protonated atorvastatin acid as well as the sodium and potassium adducts were shown from top to bottom, respectively, using a green colour scale. All identified drug related ions were well within 1ppm.*

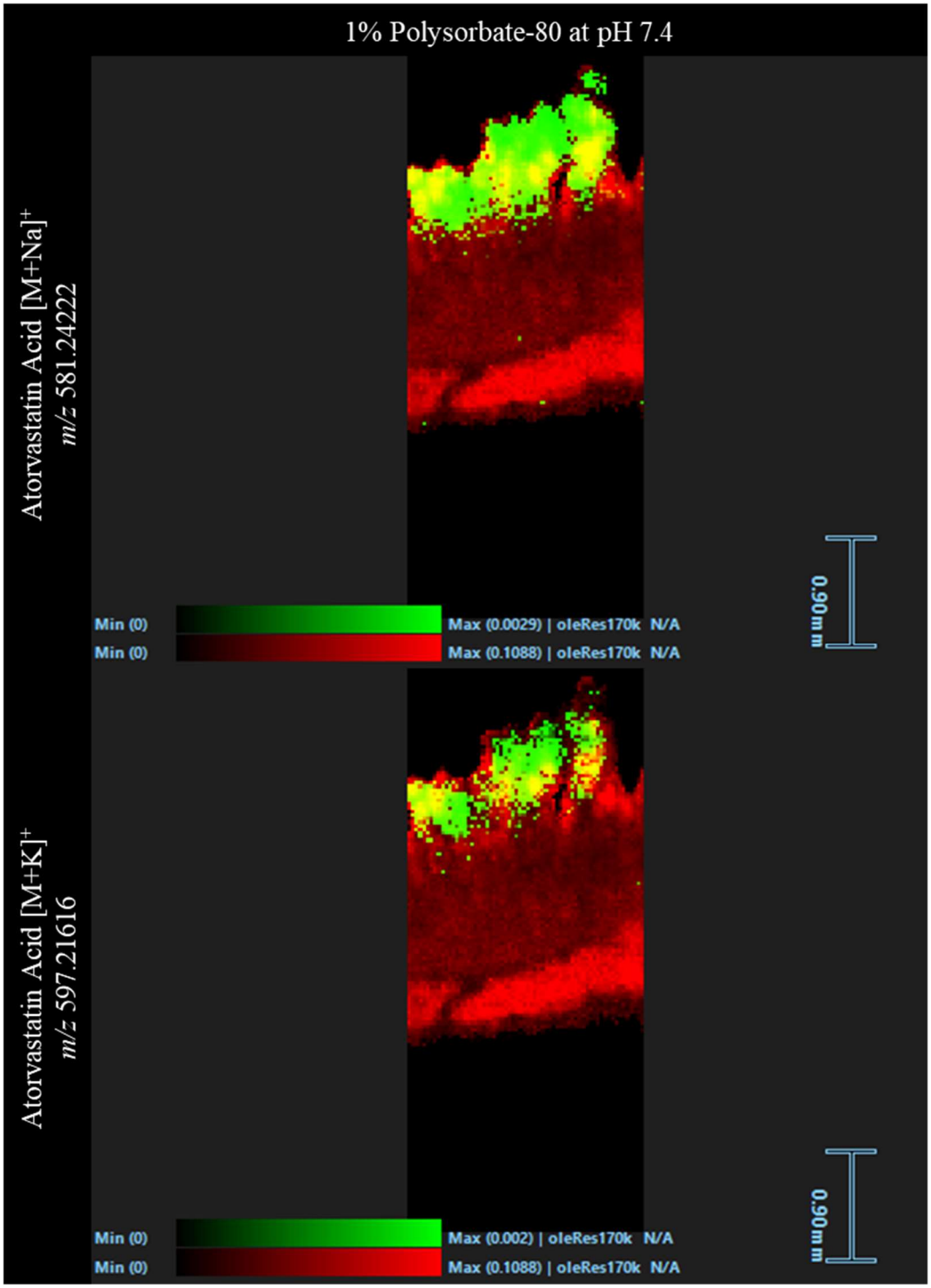

Figure 4.7: *DESI Images from a tissue section with the surface of the tissue facing upwards. The tissue section was acquired from a fresh tissue absorption experiment with 1% polysorbate-80 in the donor circuit, buffered to pH 7.4. The distribution of the lipid ion m/z 780.5 was displayed in a red colour scale. Atorvastatin acid adducts, sodium and potassium, were shown from top to bottom, respectively, using a green colour scale. All identified drug related ions were within 1ppm.*

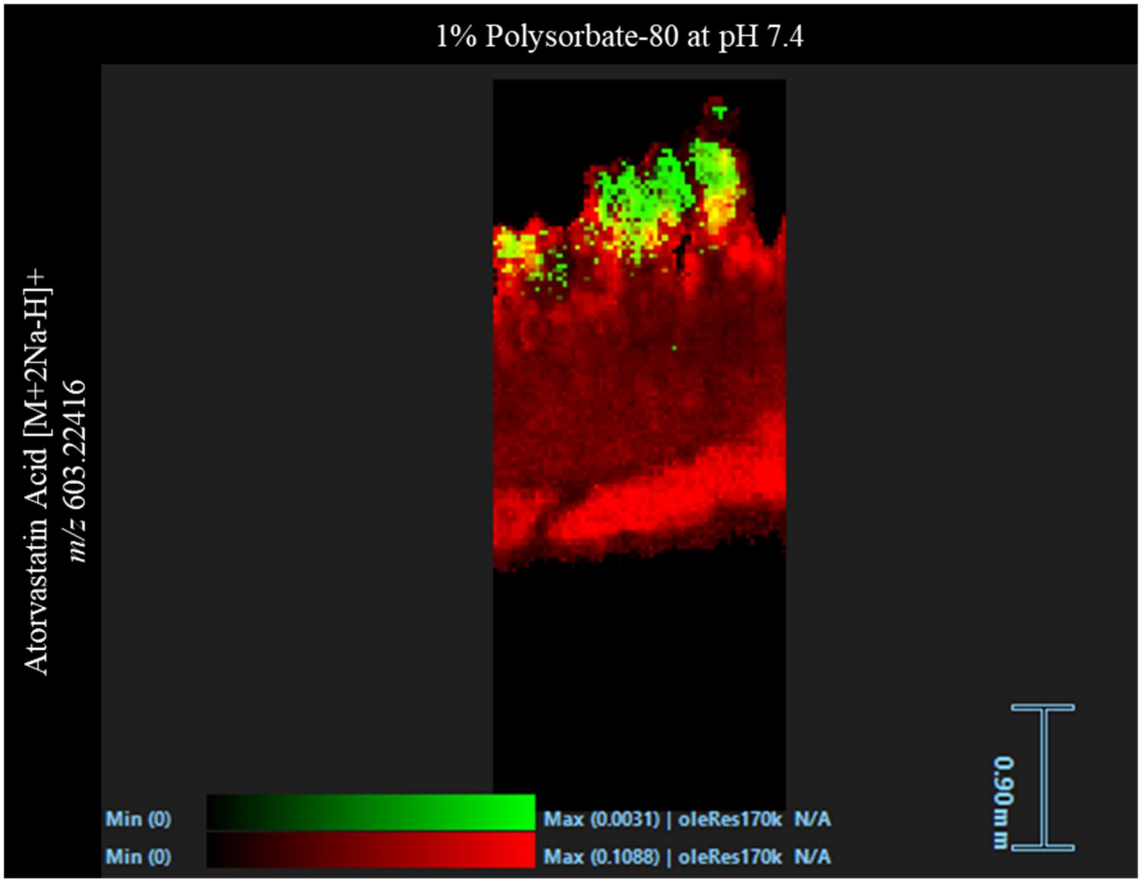

Figure 4.8: *DESI Image from a tissue section with the surface of the tissue facing upwards. The tissue section was acquired from a fresh tissue absorption experiment with 1% polysorbate-80 in the donor circuit, buffered to pH 7.4. The distribution of the lipid ion m/z 780.5 and Atorvastatin acid adduct* $[M+2Na-H]^+$ *were shown using a red and green colour scale, respectively. All identified drug related ions were within 1ppm.*

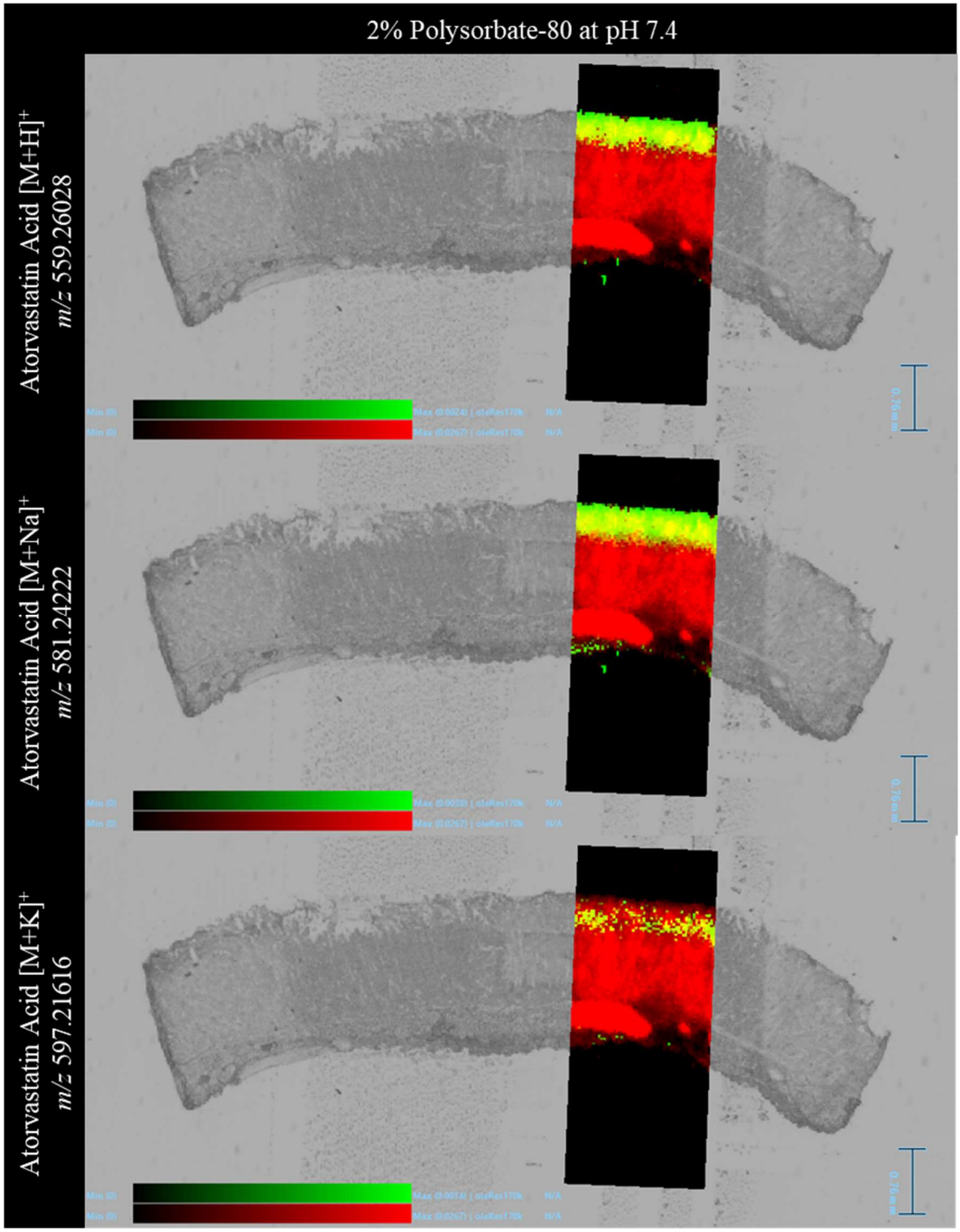

Figure 4.9: *DESI Images overlaid onto an optical image of the tissue section they were acquired from with the surface of the tissue facing upwards. The tissue section was acquired from a fresh tissue absorption experiment with 2% polysorbate-80 in the donor circuit which was buffered to pH 7.4. The distribution of the lipid ion m/z 780.5 was displayed in a red colour scale. The distribution of protonated atorvastatin acid as well as the sodium and potassium adducts were shown from top to bottom, respectively, using a green colour scale. All identified drug related ions were well within 1ppm.*

Consistently throughout all images displayed in Figures 4.4-4.9, ions related to atorvastatin acid were shown to be localised on the surface and within the upper layers of the tissue section, regardless of the amount of polysorbate-80 used in the study. From a visual observation, the ions appear to be concentrated in the villi layer and within a material coating the surface of that structure. For confirmation, the sections should be histologically stained to officially identify the different layers and structures present. Regardless of the area of distribution, it was evident that atorvastatin had not been evenly distributed throughout the tissue section. Therefore, the amount of Atorvastatin recovered from the tissue extract was more representative of the amount of drug concentrated on the tissue surface rather than a homogenous distribution across the tissue layers. Thereby the combination of mass spectrometry imaging as well as quantification was paramount in correctly interpreting the data.

From thoroughly processing the DESI images acquired for this study, tissue sections collected from an experiment without polysorbate-80 were found to be the only experiment to show a distribution of atorvastatin calcium salt. The ion was shown to be sat on the surface of the tissue in a definitive circular distribution. The rest of the ions relating to atorvastatin acid in this study incorporate the same shape but also, appear to be diffusing away from it into the tissue. The visualisation of Atorvastatin in the calcium salt form was considered unusual in this instance as typically, it would be quickly converted into atorvastatin acid when in solution. Therefore, this hints that the Atorvastatin had not fully dissolved in the donor circuit fluid and thus, stood to be plausible that a cluster of undissolved atorvastatin calcium salt had settled on the surface of the tissue.

The observation of high levels of atorvastatin settled onto the tissue surface and the inability to visualise a clear pathway of drug absorption into the tissue, led to an investigation of signal masking effects. Three regions of interest (ROIs) were extracted from each image to manually search the corresponding mass spectra for the drug signal. Of the three ROIs, the first was the whole tissue, the second was an area on the tissue away from any pixels indicating drug signal and the final region was an area away from the tissue. The results of this investigation were summarised in Table 4.2 and the specific location of each ROI have been detailed in Appendix I Figure 1-4.

Table 4.2: *A summary of whether the named atorvastatin related ions were detectable in different ROIs in the DESI image. The ROIs specified here included the whole tissue, an area on the tissue with no drug signal and an area away from the tissue. All data here relates to DESI images collected from the polysorbate-80 study performed at pH 7.4.*

Polysorbate-80 Only Study at pH 7.4					
Atorvastatin and Related Ions	ROI	Ion present in ROI? Concentration of Polysorbate-80 (% v/v)			
		0	0.4	1	2
Atorvastatin Calcium $[M+H]^+$ *m/z* 1155.46022	Whole tissue?	✓	×	×	×
	Within tissue away from drug distribution?	×	×	×	×
	Away from tissue?	×	×	×	×
Atorvastatin Acid $[M+H]^+$ *m/z* 559.26028	Whole tissue?	✓	✓	×	✓
	Within tissue away from drug distribution?	✓	×	×	×
	Away from tissue?	×	×	×	×
Atorvastatin Acid $[M+Na]^+$ *m/z* 581.24222	Whole tissue?	✓	✓	✓	✓
	Within tissue away from drug distribution?	✓	✓	×	×
	Away from tissue?	×	×	×	×
Atorvastatin Acid $[M+K]^+$ *m/z* 597.21616	Whole tissue?	✓	✓	✓	✓
	Within tissue away from drug distribution?	×	×	×	×
	Away from tissue?	×	×	×	×
Atorvastatin Acid $[M+2Na-H]^+$ *m/z* 603.22416	Whole tissue?	×	×	✓	×
	Within tissue away from drug distribution?	×	×	×	×
	Away from tissue?	×	×	×	×

While not the case for every ion, there were a few instances where the Atorvastatin related ion had been detected in the ROI away from the apparent imaged drug distribution. This finding holds an interesting standpoint in that the drug ion was present but was perhaps limited by the capabilities of the software to allow full visualisation. The DESI MRT itself utilised an algorithm that would automatically delete any signal considered to be background noise; this in turn with the extreme mass accuracy of the instrument, provided confidence that the identification of the ions was correct. In addition, an ROI analysed away from the tissue supports that the signal was not external contamination from the slide.

Knowledge of the sensitivity of the instrument (compared to LC/MS/MS) combined with visualisation of atorvastatin related ions in the final layer of the tissue in most instances, it can be assumed that the drug had moved through the tissue to some extent. Despite this, most often the amount of atorvastatin acid detected in the acceptor circuit was suspiciously low. Therefore, the DESI images acquired for this study were checked for ions relating to known atorvastatin metabolites. The images acquired have been shown in Figure 4.10.

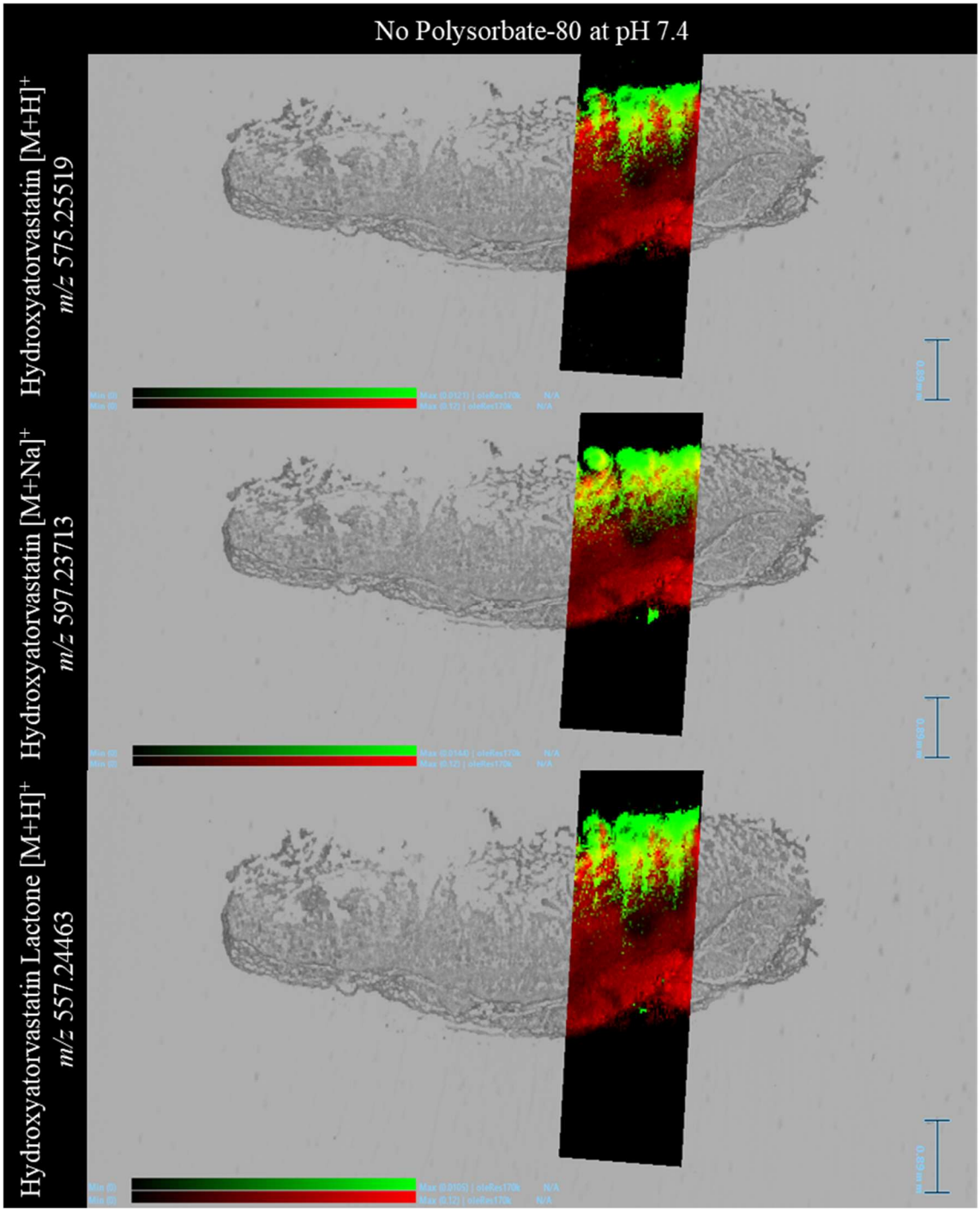

Figure 4.10: *DESI Images overlaid onto an optical image of the tissue section they were acquired from with the surface of the tissue facing upwards. The tissue section was acquired from a fresh tissue absorption experiment with no polysorbate-80 in the donor circuit buffered to pH 7.4. The distribution of the lipid ion m/z 780.5 was displayed in a red colour scale. The distribution of metabolites hydroxyatorvastatin (protonated and sodium adduct) and hydroxyatorvastatin lactone were shown from top to bottom, respectively, using a green colour scale. All metabolite ions were within 1 ppm.*

The DESI images in Figure 4.10 demonstrate the metabolite distribution in a similar area to that of atorvastatin acid. In addition, the metabolite distribution appeared to have travelled further into the tissue, with clear pixels shown fading towards the final layer. The extremely high mass accuracy of the DESI MRT provided confidence that the ions were those as identified; although MS/MS would confirm this.

Interestingly, the distribution of atorvastatin metabolites could only be visualised in the experiment with no polysorbate-80 added to the donor circuit. The possibility remains that the metabolites were not present in high enough concentrations to be detected by DESI MSI on the Waters MRT. To confirm this, it would be wise to analyse the tissue extracts for atorvastatin metabolites. With the visualisation of a clump of undissolved atorvastatin calcium salt sat on the surface of the tissue, it would be plausible that, in this instance, a higher amount of drug had settled on the surface of the tissue and been allowed to metabolise. This would be a credible scenario in this instance as the only experiment that allowed the visualisation of metabolites did not use polysorbate-80, a known solubiliser. Despite this, it must be remembered that the DESI images represent a snapshot in time and in the absence of normalisation to an internal standard, intensities cannot be directly compared (between runs) to give any real quantitative meaning. The ROIs previously analysed in Table 4.2 were also checked for metabolites of atorvastatin. The findings have been summarised in Table 4.3.

Table 4.3: *A summary of whether the named atorvastatin metabolites were detectable in different ROIs in the DESI image. The ROIs specified here included the whole tissue, an area on the tissue with no drug signal and an area away from the tissue. All data here relates to DESI images collected from the polysorbate-80 study performed at pH 7.4.*

Polysorbate-80 Only Study at pH 7.4					
Atorvastatin Metabolites	ROI	Ion present in ROI? Concentration of Polysorbate-80 (% v/v)			
		0	0.4	1	2
Hydroxyatorvastatin $[M+H]^+$ *m/z* 575.25519	Whole tissue?	✓	×	×	×
	Within tissue away from drug distribution?	×	×	×	×
	Away from tissue?	×	×	×	×
Hydroxyatorvastatin $[M+Na]^+$ *m/z* 597.23713	Whole tissue?	✓	✓	×	×
	Within tissue away from drug distribution?	×	×	×	×
	Away from tissue?	×	×	×	×
Hydroxyatorvastatin lactone $[M+H]^+$ *m/z* 557.24463	Whole tissue?	✓	✓	✓	✓
	Within tissue away from drug distribution?	×	×	✓	×
	Away from tissue?	×	×	×	×
Hydroxyatorvastatin lactone $[M+Na]^+$ *m/z* 579.22657	Whole tissue?	✓	×	×	✓
	Within tissue away from drug distribution?	×	×	×	×
	Away from tissue?	×	×	×	×

Both hydroxyatorvastatin and hydroxyatorvastatin lactone were putatively identified in the spectra of the whole tissue ROI for absorption experiments with increasing amounts of polysorbate-80 in the donor circuit. Protonated hydroxyatorvastatin lactone was identified in the whole tissue ROI of each absorption experiment, despite only being visualised in one experiment. Using the same processing parameters, the metabolite ions identified in absorption experiments with polysorbate-80 could not be visualised. For all but one experiment, atorvastatin metabolites could not be detected in regions away from the main drug distribution. The experiment without polysorbate-80 remains to be the only experiment in this study that allowed the visualisation and detection of both metabolites named above with two ions representing each.

When Polysorbate-80 was absent from the donor circuit, atorvastatin would be visibly insoluble, with almost the entirety of the material falling out of solution. The addition of Polysorbate-80 to the donor circuit solution appeared to improve the solubility of Atorvastatin in PBS as there would be visibly less precipitate after combining. With more precipitation in the system when Polysorbate-80 was absent, it can be expected that the fall-out would also coat the apical layers of the tissue disc that were exposed to the donor circuit fluid. To minimise interference from unwanted atorvastatin signals from the drug being rested on the surface of the tissue, additional sample preparation steps were taken. Prior to snap-freezing the tissue for storage, each tissue disc was rinsed to remove any excess drug solution that was rested on the surface of the tissue. As hypothesised, a much greater amount of Atorvastatin was consistently rinsed from the surface of the tissue discs when Polysorbate-80 was absent from the donor circuit; this trend can be seen in Figure 4.11. A one-way ANOVA and Tukey HSD test confirmed this; experiments with no excipient were identified as significantly different from the others with a P value less than 0.01.

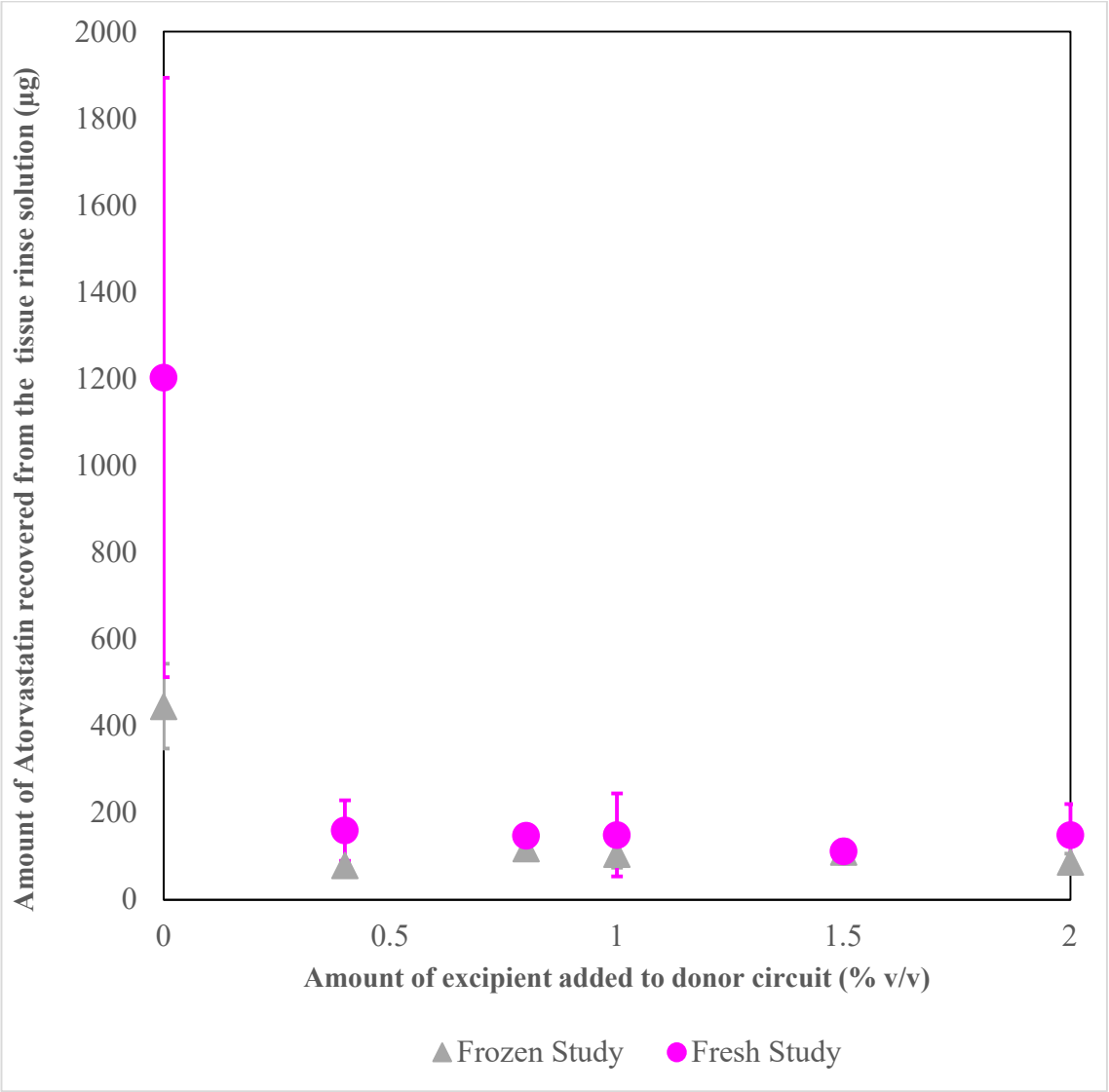

Figure 4.11: *A graph to show the amount of Atorvastatin that was rinsed from the tissues discs plotted against the concentration of Polysorbate-80 in the donor circuit of the corresponding absorption experiment. The data from two different studies have been shown together here; each experiment from the frozen study from Chapter 2 and the corresponding fresh study have been represented by grey triangles and pink circles, respectively (n=3).*

Once polysorbate-80 had been added to the donor circuit, an immediate reduction was seen in the amount of atorvastatin that was rinsed from the tissue surface. This same trend was observed in both the fresh and frozen polysorbate-80 study. While the tissue discs were rinsed to remove any substance rested on the surface of the tissue, it was apparent that the drug had become saturated on the surface of the tissue discs. From a visual examination of the tissue discs prior to and after the rinsing step, there were

instances where white particles could be seen on the surface of the tissue discs. The particulates could not be removed during the rinsing step and appeared to be embedded within the thick mucus on the surface of the tissue. This was evident in the relevant DESI images as previously discussed.

The effect of Polysorbate-80 on the solubility of Atorvastatin inferred by these findings, is confirmed by the analysis of the system rinsing solution collected post-experiment. After the system had been drained following an absorption experiment, the system was thoroughly flushed with a solution that Atorvastatin was fully soluble in. From the evaluation of the amount of Atorvastatin retrieved during the initial system rinse from each experiment in the study, the effect of Polysorbate-80 on Atorvastatin has been clearly evidenced. As shown in Figure 4.12, a clear relationship was demonstrated between the amount of Polysorbate-80 added to the system and the amount of Atorvastatin recovered during the initial system rinse. When Polysorbate-80 was absent from the donor circuit, the highest amount of Atorvastatin was recovered from the system. Once Polysorbate-80 was added to the donor circuit, there was a sharp decline in the amount of Atorvastatin recovered from the system which very quickly came to a plateau when the concentration of Polysorbate-80 was gradually increased. A one-way ANOVA and Tukey HSD test confirmed the finding and identified that only ‘no excipient’ experiments were significantly different ($P > 0.01$). When draining the system prior to the initial system rinse, any drug that was not in solution would easily be left behind in the system. Hence, providing a sensible explanation for the trend seen in both Figure 4.11 and 4.12.

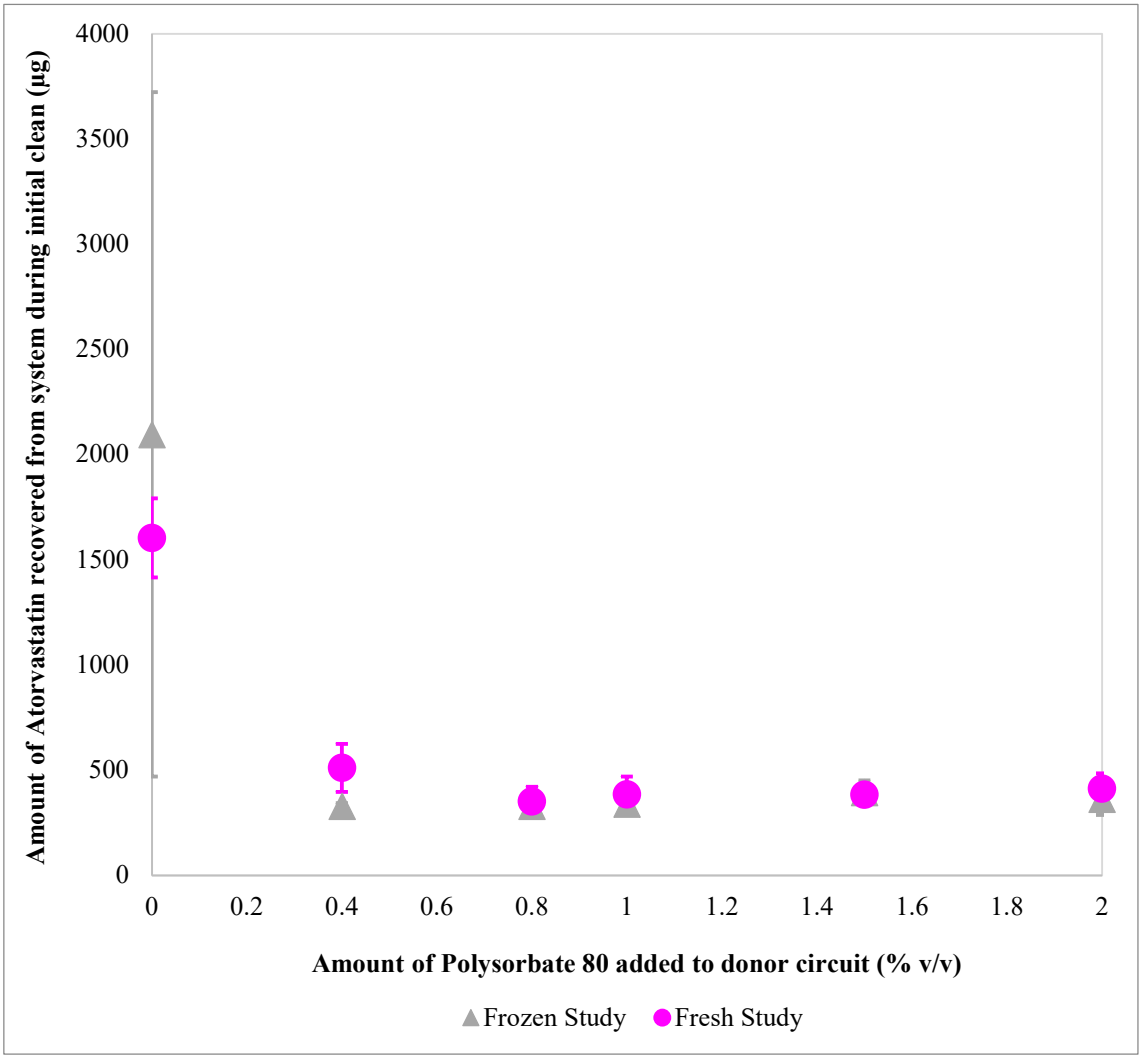

Figure 4.12: *A graph showing the amount of Atorvastatin that was recovered from the QV600 LLI after the system had been drained following an absorption experiment with varied amounts of Polysorbate-80 added to the donor circuit. The data from two different studies have been shown together here; each experiment from the frozen study from Chapter 2 and the corresponding fresh study have been represented by grey triangles and pink circles, respectively (n=3).*

While Polysorbate-80 was proven to increase the solubility of Atorvastatin within a medium, the improved solubility does not seem to have improved permeation into the tissue, or at least this was not demonstrated here. Additionally, the DESI MS images show the drug to be heavily saturated on the surface of the tissue section within the region of the mucus layer and villi. With this in mind, the next set of studies aimed to improve the permeation of Atorvastatin utilising the excipient, DEGEE, which is a known permeation enhancer.

4.4.2 Other Excipient Combinations at pH 7.4

4.4.2.1 DEGEE LQ Only

DEGEE LQ was added to the donor circuit alone with PBS buffered to pH 7.4 in the same concentrations as the previous study. All parameters were the same as the previous study. The permeation coefficients were calculated for each experiment in the study and plotted along with the data from the previous study, see Figure 4.13.

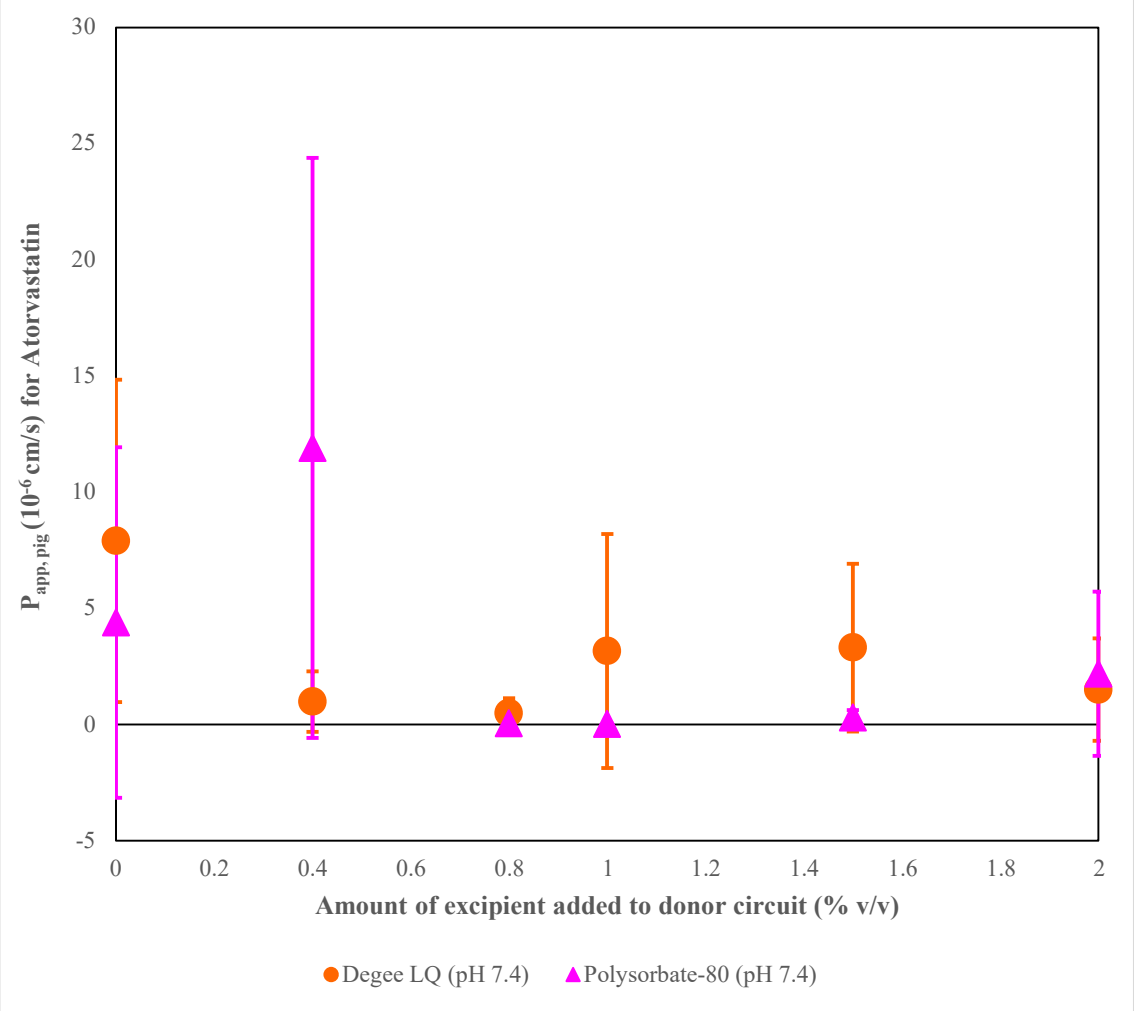

Figure 4.13: *A graph showing the Papp,pig values plotted against the concentration of excipient in the donor circuit of the corresponding absorption experiment. The data from the previous Polysorbate-80 fresh study and the Degee LQ study have been shown together here; each experiment from the Degee LQ and Polysorbate-80 study have been represented by orange circles and pink triangles, respectively (n=3).*

At first glance, a general improvement can be seen in the amount of atorvastatin that was detected in the acceptor circuit. The data points from this study were similar to the

previously identified outliers in the ‘polysorbate-80 only’ study in several instances. An unpaired t test corroborated this observation with a P value of 0.8961 meaning no statistically significant differences between the two studies. The improved $P_{app,pig}$ values were now similar to those in published works such as (Iqbal et al., 2021) and (Agrawal et al., 2015).

Although being from different studies, the first set of data points with no excipient added were essentially the same experiment, repeated six times under the same conditions. Despite this, a large variance was observed. While ex vivo studies are known to be susceptible to variance due to the variability of tissue, it was important to ensure that the model did not add further inconsistencies. It was towards the end of this study that white speckles, suspected to be atorvastatin, were noticed on the sides of the tissue that suggested that the discs were ill-fitted hence, the need for the double o-ring fitting was identified, as discussed previously in Chapter 3. While the experiments in which contamination were suspected were terminated, there remains the possibility that very fine leaks could have occurred but gone undetected post set-up. Subsequent to this discovery, all further studies yet to be discussed were performed using the double o-ring fitting.

To better understand and explore the effects of DEGEE LQ on the permeation of atorvastatin, the tissue discs were analysed by LC-MS/MS prior to DESI imaging. The concentration of atorvastatin extracted from one tissue disc of each absorption experiment in the ‘DEGEE LQ only’ study was plotted against the concentration of DEGEE LQ added to the donor circuit in Figure 4.14. When no excipient was added to the circuit, there was a similar amount of atorvastatin recovered from the extract when compared to the same set of experiments in the ‘polysorbate-80 only’ study. Contrastingly, when the amount of DEGEE LQ in the donor circuit was gradually increased, the general trend observed was that the amount of atorvastatin recovered from the tissue extract did not significantly increase nor decrease. This was confirmed with a one-way ANOVA test.

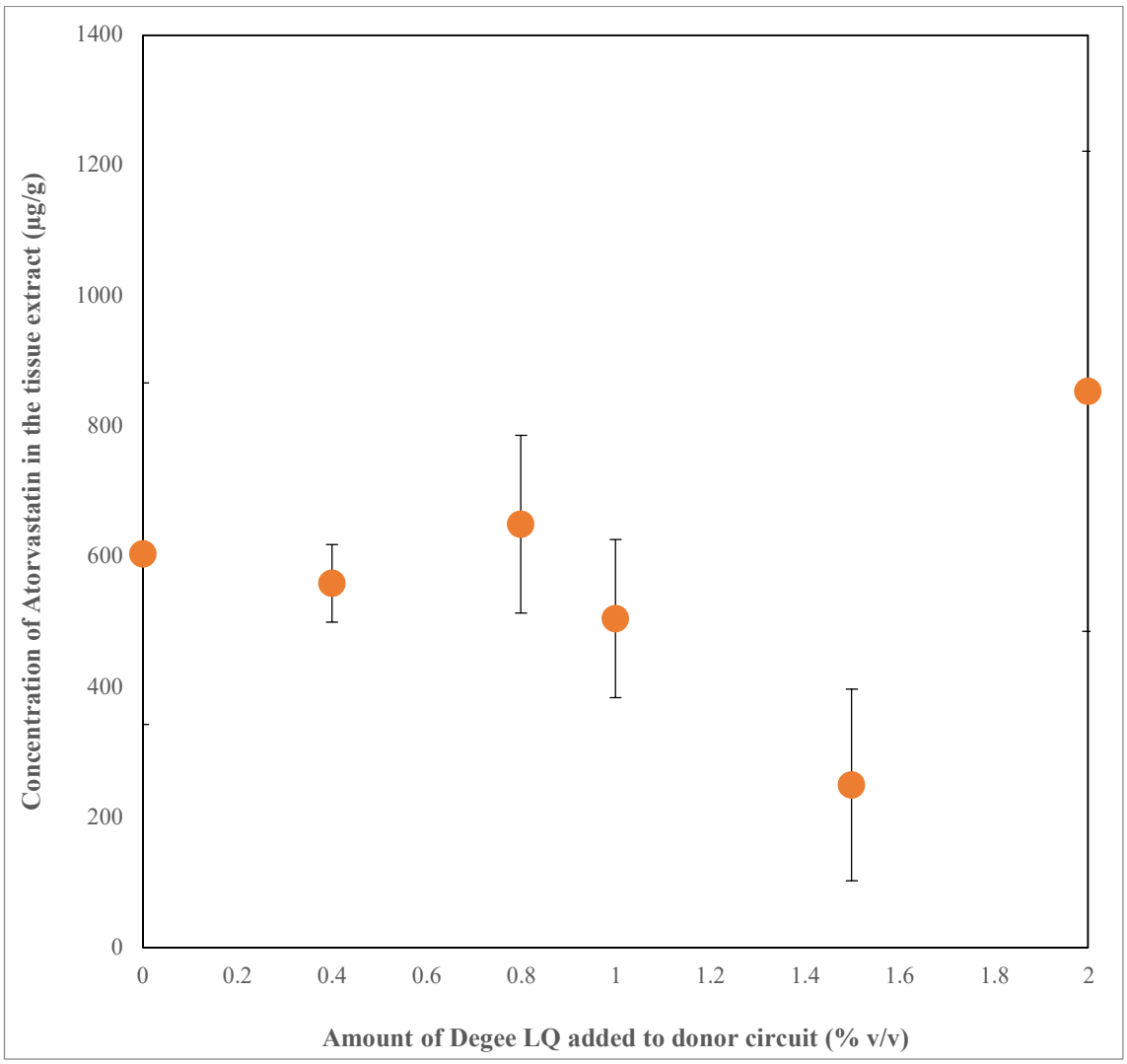

Figure 4.14: *A graph showing the concentration of Atorvastatin calculated from the tissue disc extract plotted against the corresponding amount of Degee LQ that was added to the donor circuit for that absorption experiment. The data presented here is from the DEGEE only study performed at pH 7.4 (n=3).*

While the data from the tissue extracts imply that DEGEE LQ had no significant effect on the amount of atorvastatin that had permeated into the tissue, visual observations suggest this data may be more of a reflection on drug solubility. It was consistently observed during experiments with the addition of DEGEE LQ, that atorvastatin would not stay in solution. Whereas previously, the addition of excipient polysorbate-80 had visually improved drug solubility. The amount of atorvastatin rinsed from the surface of the tissue discs was quantified with LC-MS/MS and plotted against the amount of DEGEE LQ added to the donor circuit as shown in Figure 4.15.

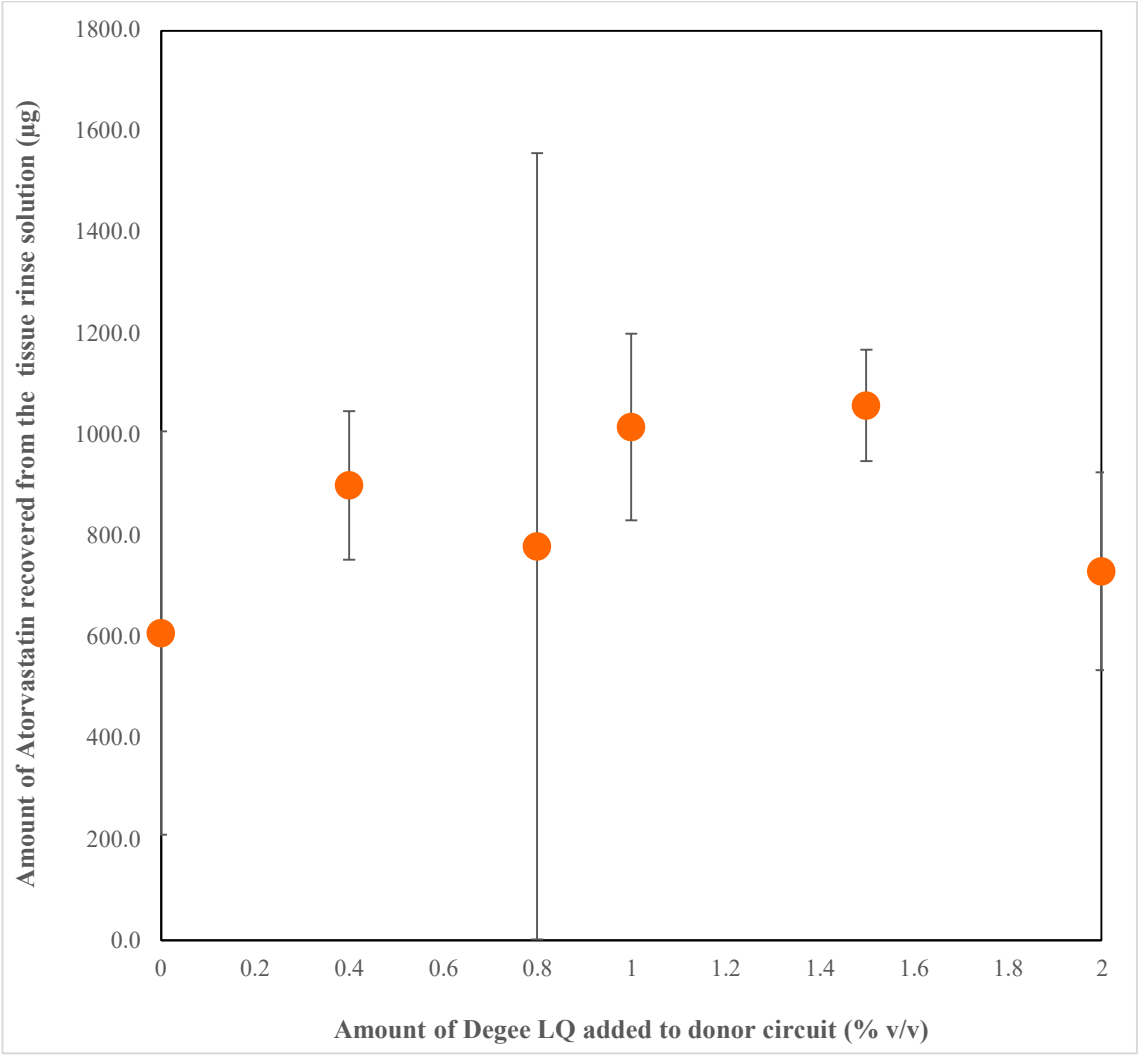

Figure 4.15: *A graph to show the amount of Atorvastatin that was rinsed from the tissues discs plotted against the concentration of Degee LQ in the donor circuit of the corresponding absorption experiment. The data presented here is from the DEGEE only study performed at pH 7.4 (n=3).*

Whether or not DEGEE LQ had been added to the donor circuit, no significant differences were identified in the amount of atorvastatin recovered from the surface of the tissue; this was confirmed by a one-way ANOVA test. As it had become known that without an excipient, atorvastatin would precipitate out of solution, it would be logical to hypothesise that DEGEE LQ provided no effect on the solubility of atorvastatin in PBS. Further analysis of the system rinsing solution, shown in Figure 4.16, demonstrated the same trend and was statistically insignificant.

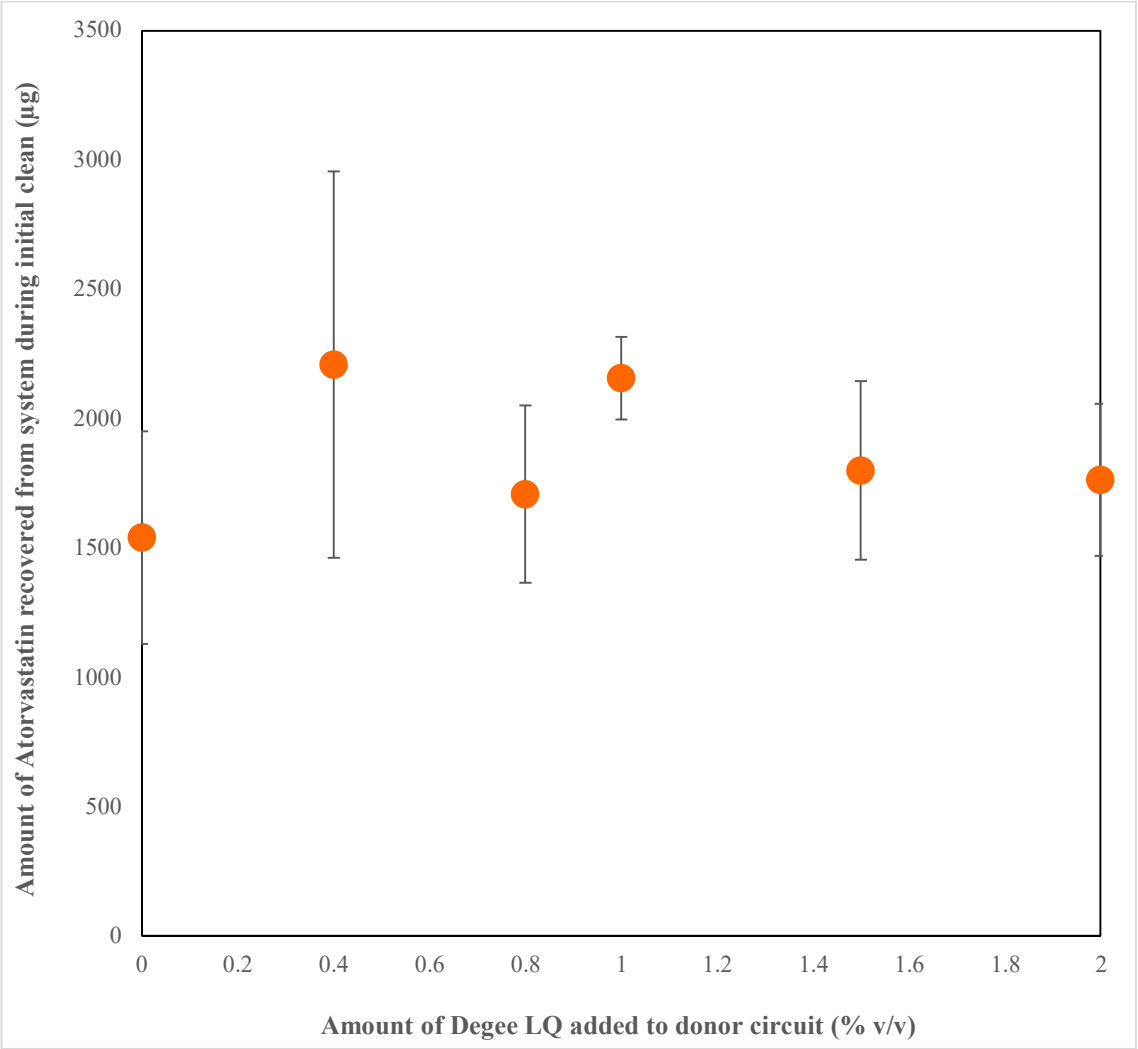

Figure 4.16: *A graph showing the amount of Atorvastatin that was recovered from the QV600 LLI after the system had been drained following an absorption experiment with varied amounts of Degee LQ added to the donor circuit. The data presented here is from the DEGEE only study performed at pH 7.4 (n=3).*

The amount of atorvastatin that was recovered from the drained system remained relatively the same as increasing amounts of DEGEE LQ were added to the donor circuit. This finding would be consistent with the drug remaining poorly soluble. The precipitation of the drug from the solution would be sporadic meaning that the amount of drug that would fall out of solution and settle on the surface of a tissue disc would be inconsistent and unpredictable. This would also lead to the significant variation that was observed in the amount of drug that had settled on the tissue surface. Therefore, it would be difficult to identify the effect of DEGEE LQ on the permeation of atorvastatin through the tissue unless it was significant. To better understand the effect of DEGEE LQ on the permeation of atorvastatin through the tissue, a tissue disc from experiments

in the study with 0%, 0.4%, 1% and 2% DEGEE LQ were sectioned, scanned and imaged using DESI MS. The DESI MS images, displayed from Figure 4.17-4.24, provided further information on the spatial distribution of the drug within the tissue section. The images revealed the distribution of various ion adducts of the active hydroxy-acid form, Atorvastatin acid as well as the occasional atorvastatin calcium in the salt form it was originally administered.

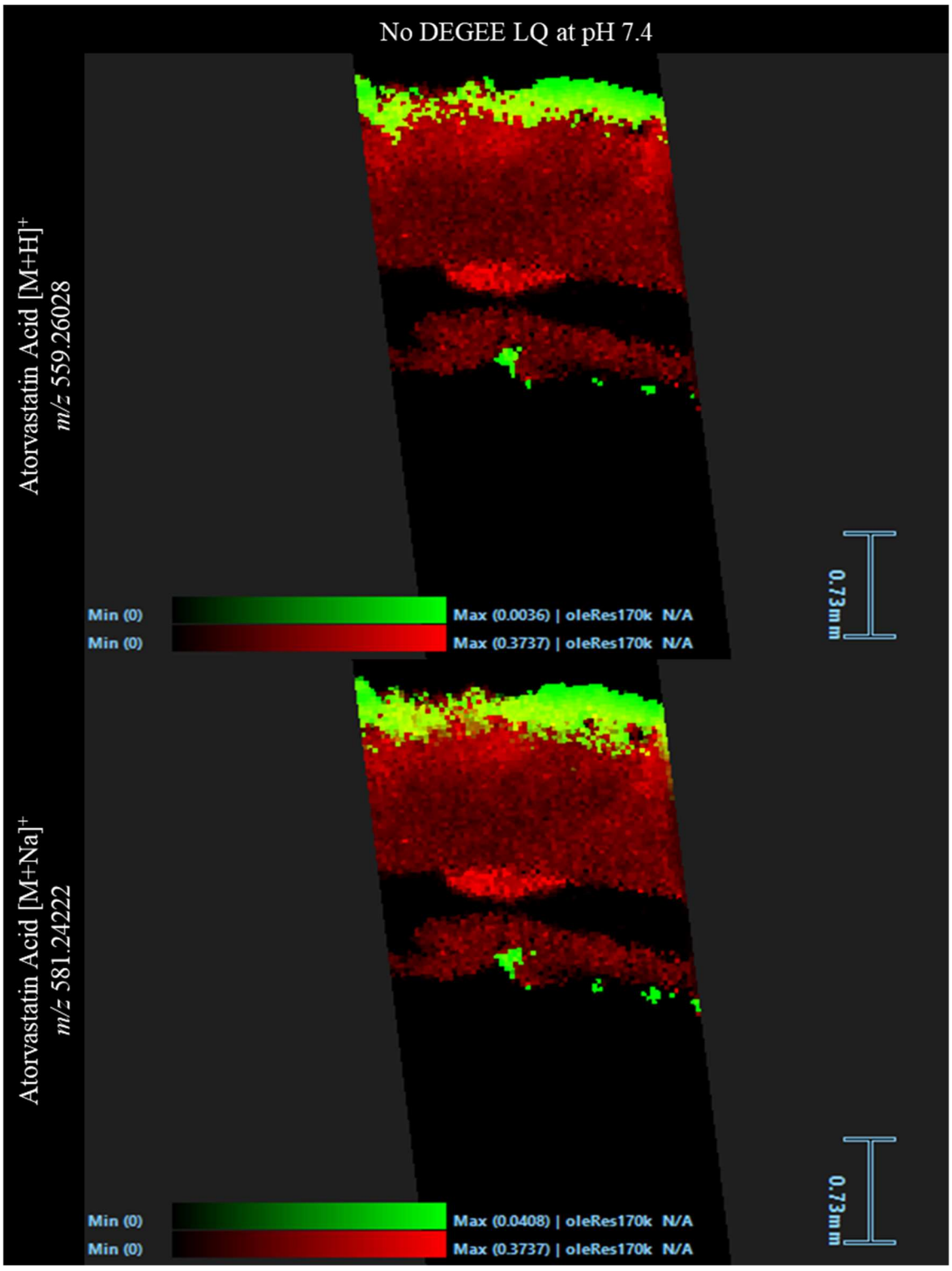

Figure 4.17: *DESI Images from a tissue section with the surface of the tissue facing upwards. The tissue section was acquired from a fresh tissue absorption experiment with no DEGEE LQ in the donor circuit, buffered to pH 7.4. The distribution of the lipid ion m/z 780.5 was displayed in a red colour scale. Protonated atorvastatin acid and its sodium adduct were shown in the top and bottom window, respectively, using a green colour scale. All identified drug related ions were within 1ppm.*

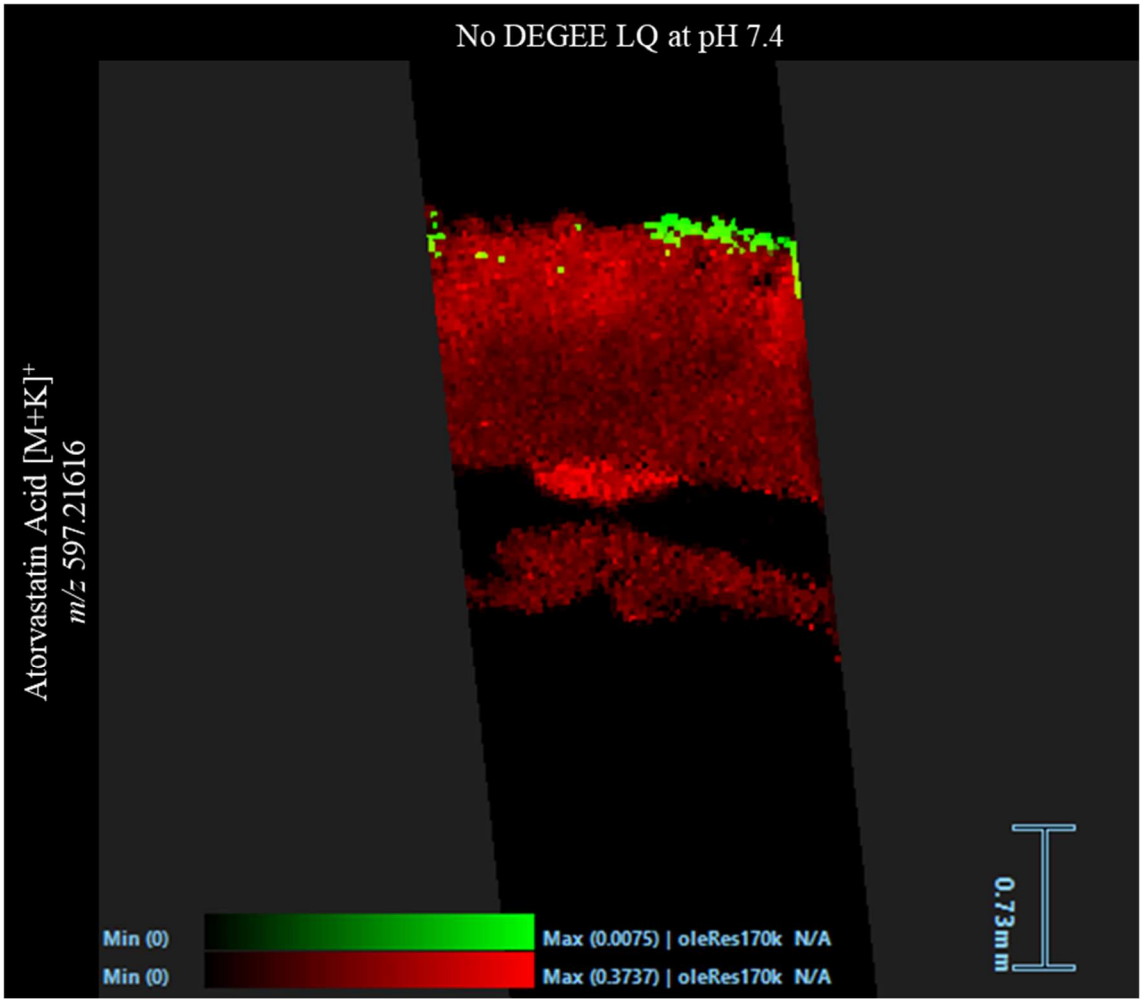

Figure 4.18: *DESI Images from a tissue section with the surface of the tissue facing upwards. The tissue section was acquired from a fresh tissue absorption experiment with no DEGEE LQ in the donor circuit, buffered to pH 7.4. The distribution of the lipid ion m/z 780.5 was displayed in a red colour scale. The potassium adduct of atorvastatin acid was shown using a green colour scale. The identified drug related ion was within 1ppm.*

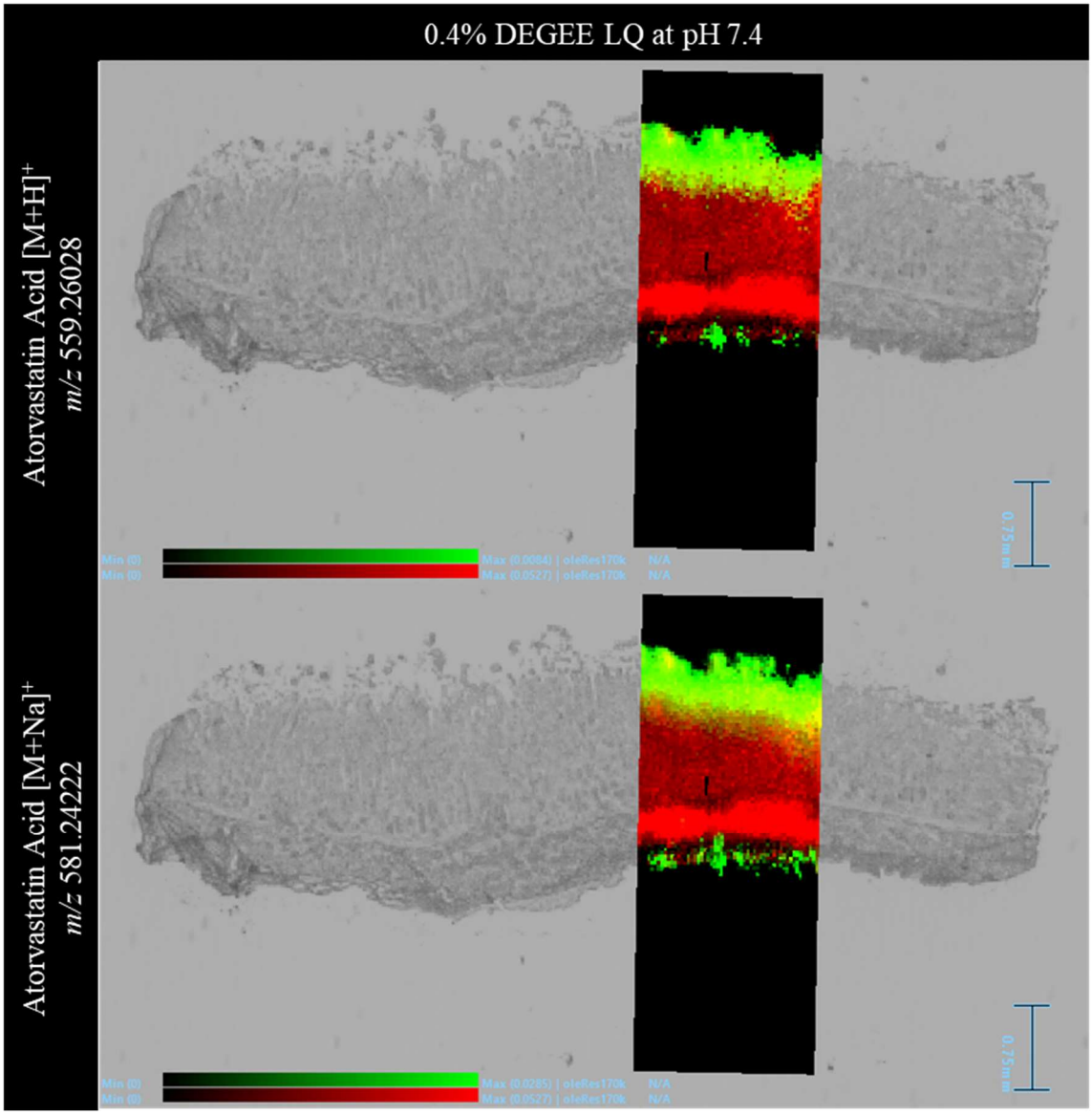

Figure 4.19: *DESI Images overlaid onto an optical image of the tissue section they were acquired from with the surface of the tissue facing upwards. The tissue section was acquired from a fresh tissue absorption experiment with 0.4% DEGEE LQ in the donor circuit which was buffered to pH 7.4. The distribution of the lipid ion m/z 780.5 was displayed in a red colour scale. The distribution of protonated atorvastatin acid as well as the sodium and potassium adducts were shown in the top and bottom window, respectively, using a green colour scale. All identified drug related ions were well within 1ppm.*

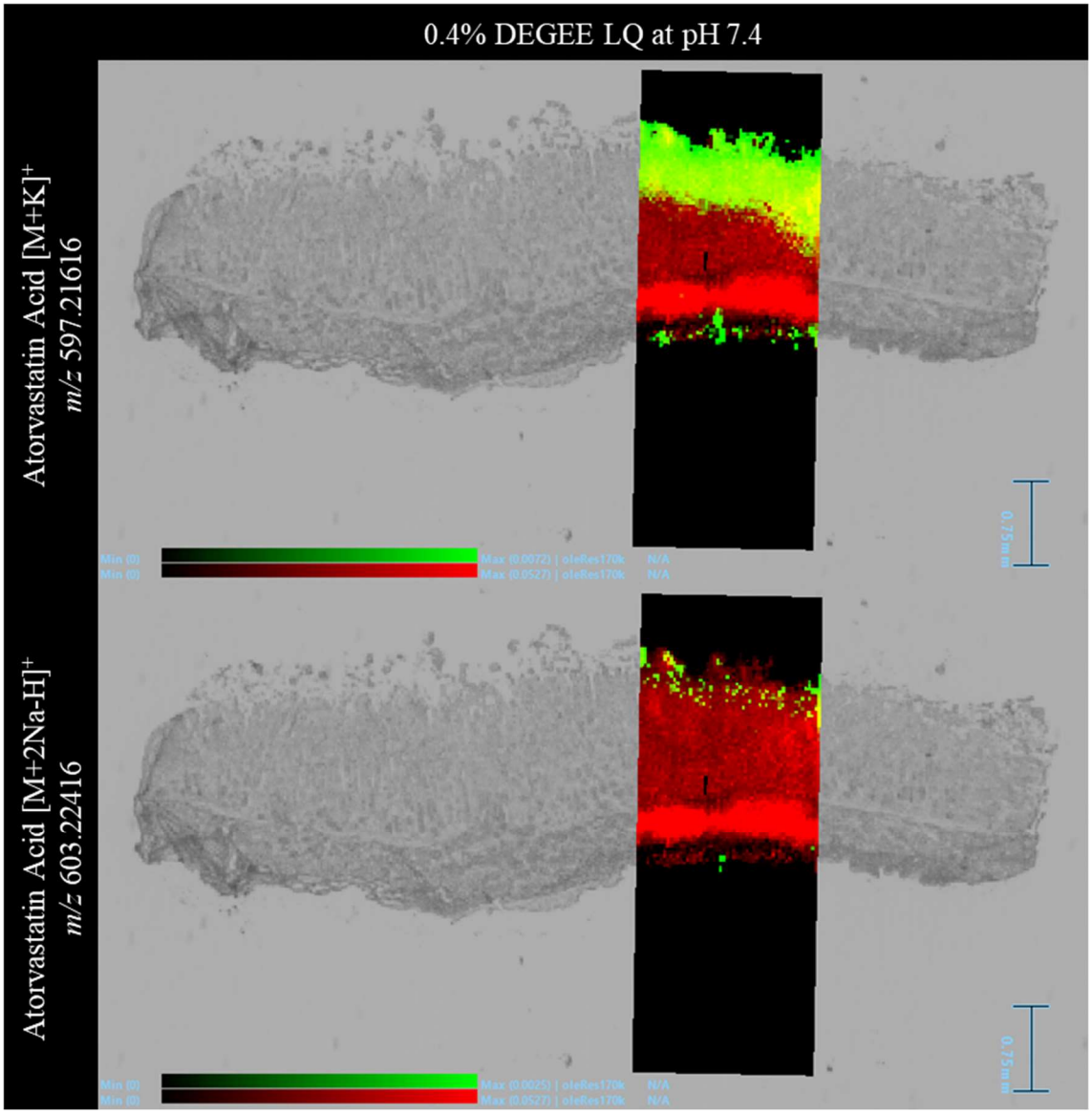

Figure 4.20: *DESI Images overlaid onto an optical image of the tissue section they were acquired from with the surface of the tissue facing upwards. The tissue section was acquired from a fresh tissue absorption experiment with 0.4% DEGEE LQ in the donor circuit which was buffered to pH 7.4. The distribution of the lipid ion m/z 780.5 was displayed in a red colour scale. The distribution of atorvastatin acid potassium and* $[M+2Na-H]^+$ *adduct were shown in the top and bottom window, respectively, using a green colour scale. All identified drug related ions were well within 1ppm.*

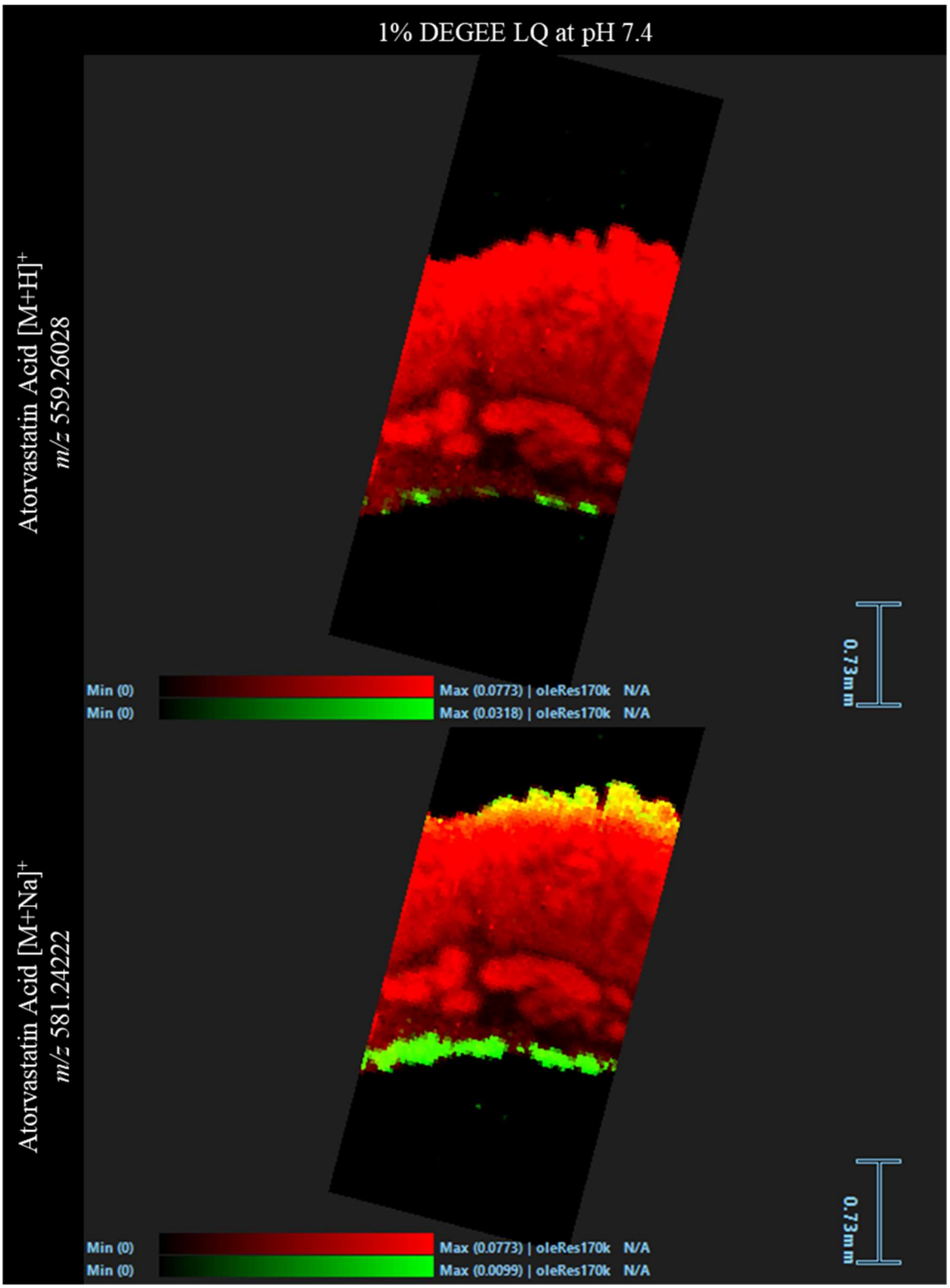

Figure 4.21: *DESI Images from a tissue section with the surface of the tissue facing upwards. The tissue section was acquired from a fresh tissue absorption experiment with 1% DEGEE LQ in the donor circuit, buffered to pH 7.4. The distribution of the lipid ion m/z 780.5 was displayed in a red colour scale. Protonated atorvastatin acid and its sodium adduct were shown in the top and bottom window, respectively, using a green colour scale. All identified drug related ions were within 1ppm.*

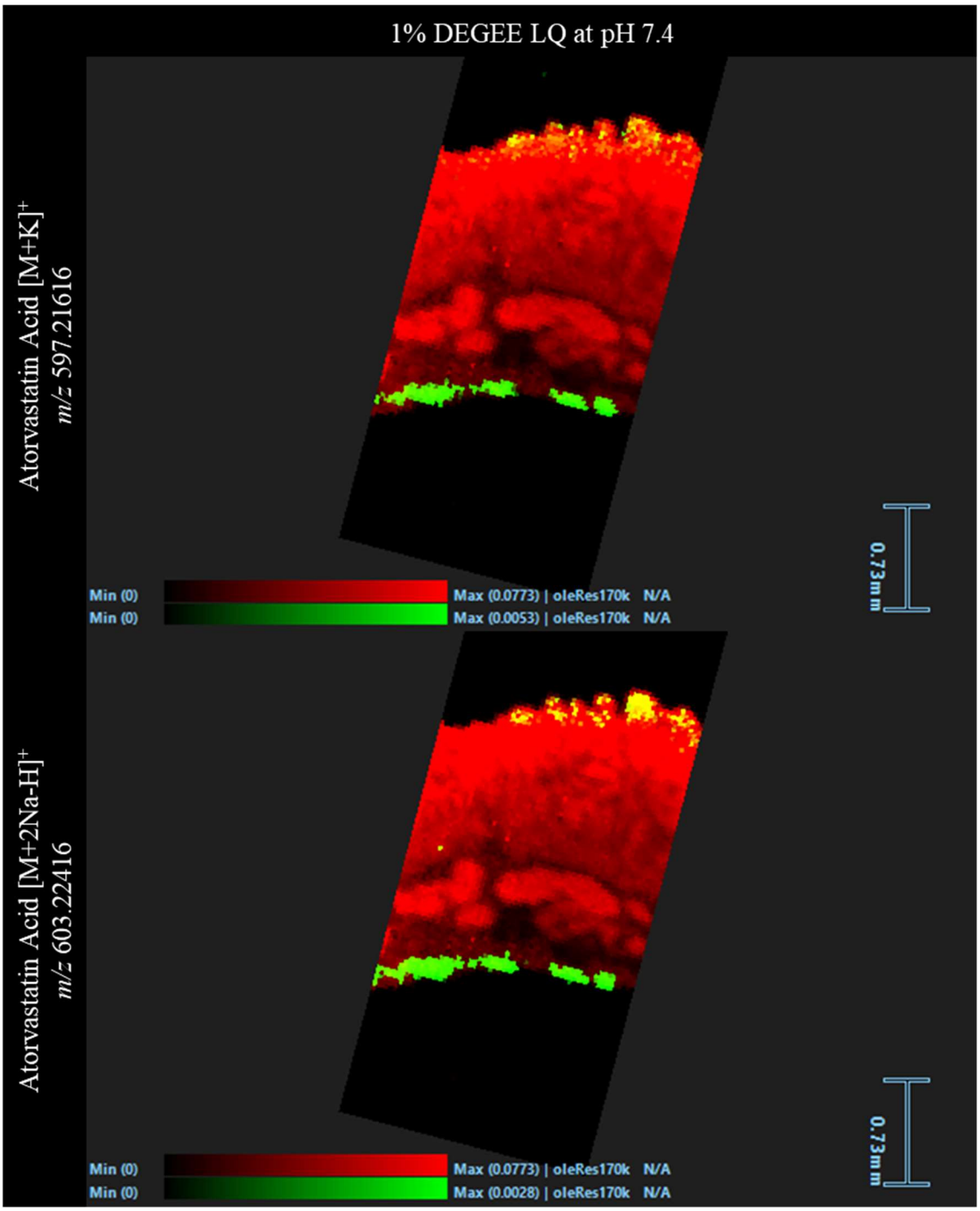

Figure 4.22: *DESI Images from a tissue section with the surface of the tissue facing upwards. The tissue section was acquired from a fresh tissue absorption experiment with 1% DEGEE LQ in the donor circuit, buffered to pH 7.4. The distribution of the lipid ion m/z 780.5 was displayed in a red colour scale. The distribution of atorvastatin acid potassium and $[M+2Na-H]^+$ adduct were shown in the top and bottom window, respectively, using a green colour scale. All identified drug related ions were well within 1ppm.*

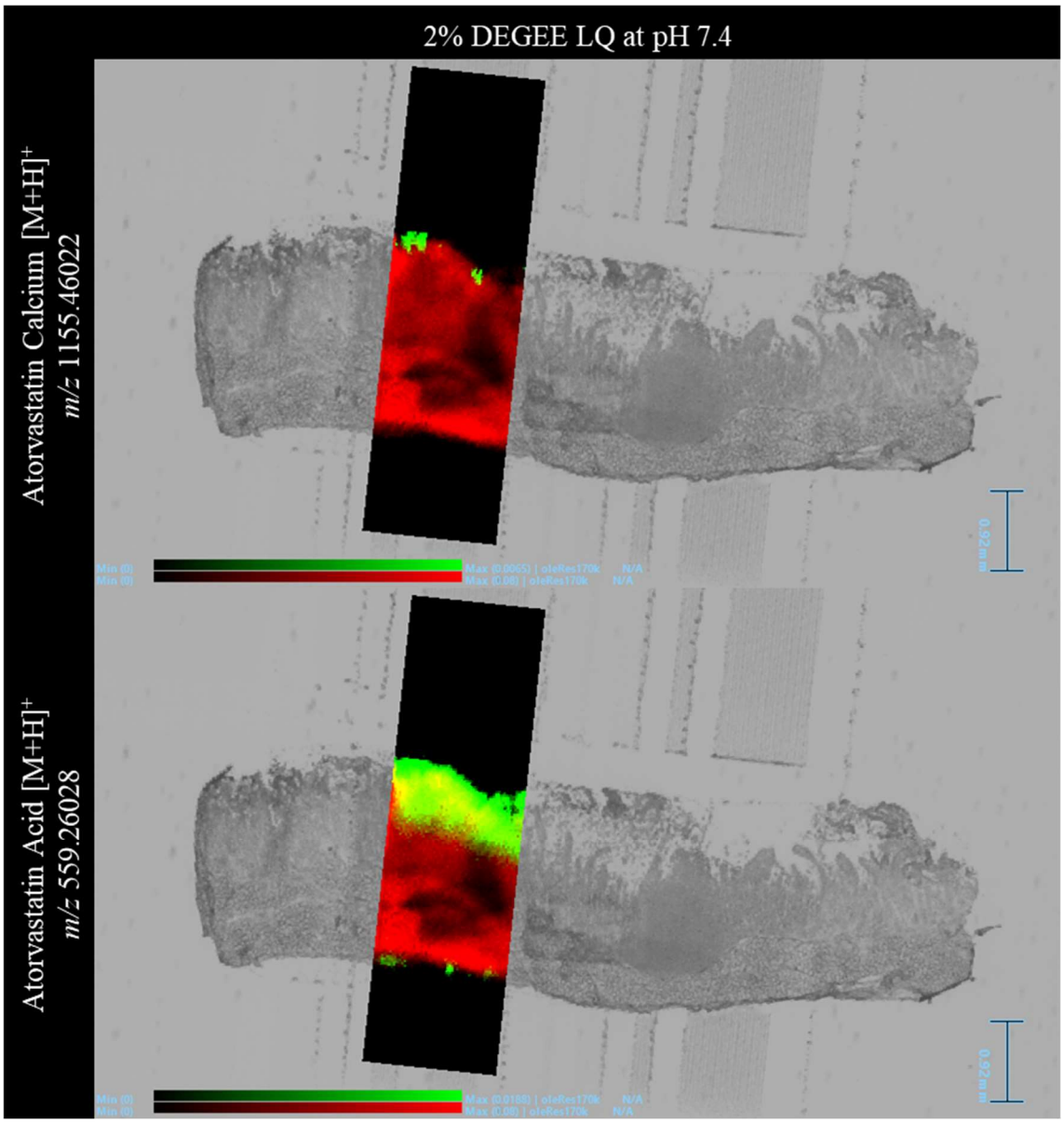

Figure 4.23: *DESI Images overlaid onto an optical image of the tissue section they were acquired from with the surface of the tissue facing upwards. The tissue section was acquired from a fresh tissue absorption experiment with 2% DEGEE LQ in the donor circuit which was buffered to pH 7.4. The distribution of the lipid ion m/z 780.5 has been displayed in a red colour scale. The distribution of protonated atorvastatin calcium and atorvastatin acid were shown in the top and bottom window, respectively, using a green colour scale. All identified drug related ions were well within 1 ppm.*

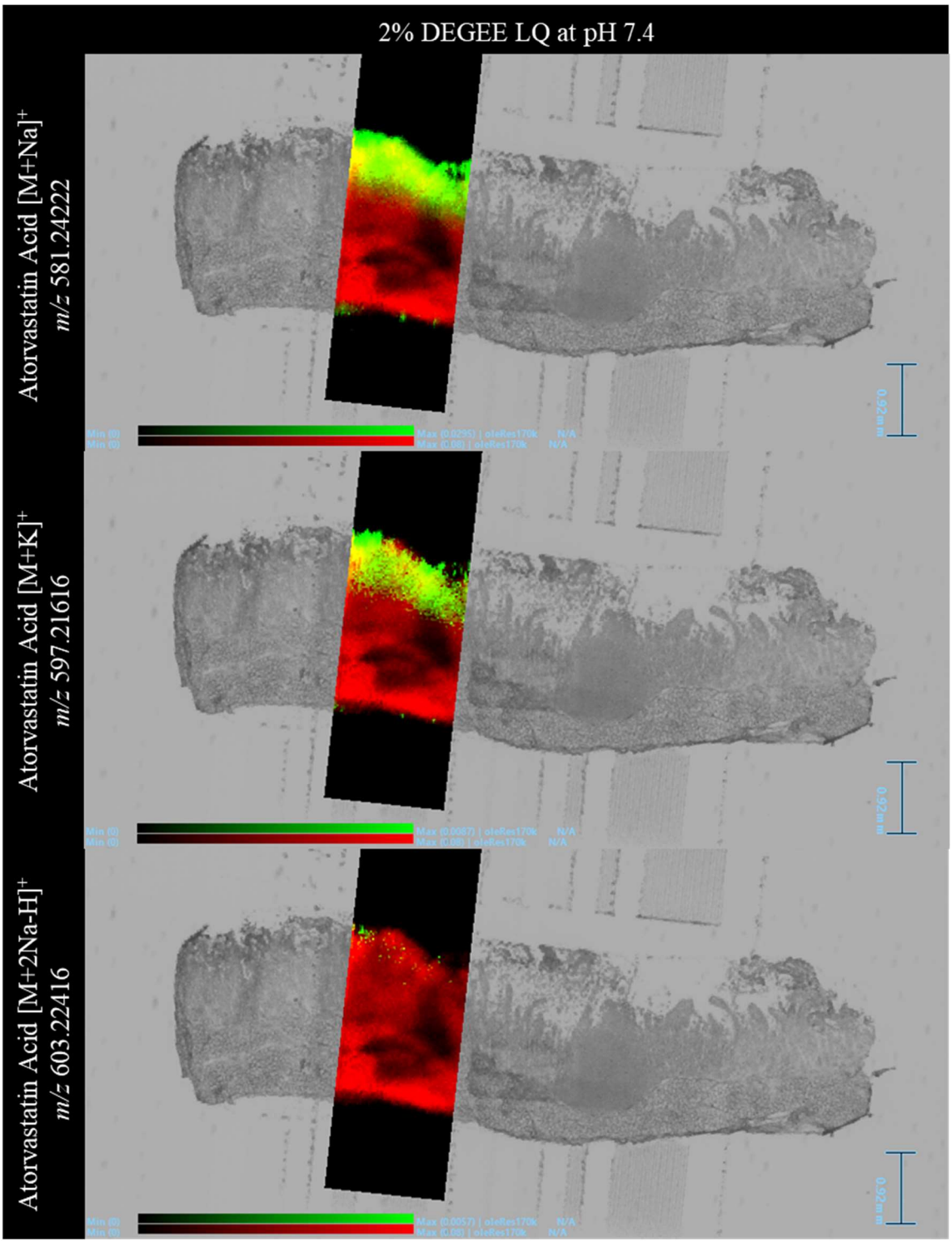

Figure 4.24: *DESI Images overlaid onto an optical image of the tissue section they were acquired from with the surface of the tissue facing upwards. The tissue section was acquired from a fresh tissue absorption experiment with 2% DEGEE LQ in the donor circuit which was buffered to pH 7.4. The distribution of the lipid ion m/z 780.5 was displayed in a red colour scale. The distribution of sodium, potassium and [M+2Na-H]$^+$ adducts of atorvastatin acid were shown from top to bottom, respectively, using a green colour scale. All identified drug related ions were well within 1ppm.*

The ion for atorvastatin calcium salt, which was the original form upon administration, was visualised solely on the surface of the tissue taken from a 2% DEGEE LQ experiment, shown in Figure 4.23. The distribution of this ion was different from all the other atorvastatin related ions that were identified; the calcium salt was shown in a very defined irregular, isolated shape that did not coat the entire surface. As previously observed and discussed, this suggested that there was a clump of undissolved atorvastatin calcium embedded onto the surface tissue. In most instances, the various adducts of atorvastatin acid were distributed in the lowest layer of the tissue in addition to its surface. This indicated that atorvastatin had permeated through the tissue. Despite this, there remained a lack of pixels in between the two distributions that would have highlighted the absorption pathway. As previously explained, three ROIs were drawn on each DESI image and extracted into mass spectra to establish whether lower levels of atorvastatin related ions were detectable. The results of this investigation have been summarised in Table 4.4 and the specific location of each ROI have been detailed in Appendix I Figure 5-8.

Table 4.4: *A summary of whether the named atorvastatin related ions were detectable in different ROIs in the DESI image. The ROIs specified here included the whole tissue, an area on the tissue with no drug signal and an area away from the tissue. All data here relates to DESI images collected from the DEGEE LQ study performed at pH 7.4.*

DEGEE LQ Only Study at pH 7.4					
Atorvastatin and Related Ions	ROI	Ion present in ROI? Concentration of DEGEE LQ (% v/v)			
		0	0.4	1	2
Atorvastatin Calcium $[M+H]^+$ *m/z* 1155.46022	Whole tissue?	×	×	✓	✓
	Within tissue away from drug distribution?	×	×	×	×
	Away from tissue?	×	×	×	×
Atorvastatin Acid $[M+H]^+$ *m/z* 559.26028	Whole tissue?	✓	✓	✓	✓
	Within tissue away from drug distribution?	×	×	×	×
	Away from tissue?	×	×	×	×
Atorvastatin Acid $[M+Na]^+$ *m/z* 581.24222	Whole tissue?	✓	✓	✓	✓
	Within tissue away from drug distribution?	×	✓	×	✓
	Away from tissue?	×	×	×	×
Atorvastatin Acid $[M+K]^+$ *m/z* 597.21616	Whole tissue?	✓	✓	✓	✓
	Within tissue away from drug distribution?	×	✓	×	×
	Away from tissue?	×	×	×	×
Atorvastatin Acid $[M+2Na-H]^+$ *m/z* 603.22416	Whole tissue?	×	✓	✓	✓
	Within tissue away from drug distribution?	×	×	×	×
	Away from tissue?	×	×	×	×

On a few instances, atorvastatin acid ions were detected in the ROI in which no atorvastatin signal was indicated by the DESI image. In addition, atorvastatin calcium salt was detected in the whole tissue ROI taken from the 1% DEGEE LQ experiment as well as the 2% DEGEE LQ experiment which allowed visualisation of said ion. This begs the question as to whether the drug in between the main distributions was genuinely absent or present in such little concentrations that it could not be detected using this instrument or when in the presence of a significant concentration gradient.

Although the DESI images do not show a full permeation pathway through the tissue, the majority of the $P_{app,pig}$ values acquired in this study were sensible and similar to those published. Therefore, the DESI images from the entire study were checked for all known atorvastatin metabolites using the same processing parameters. The images acquired have been shown in Figure 4.25 and 4.26.

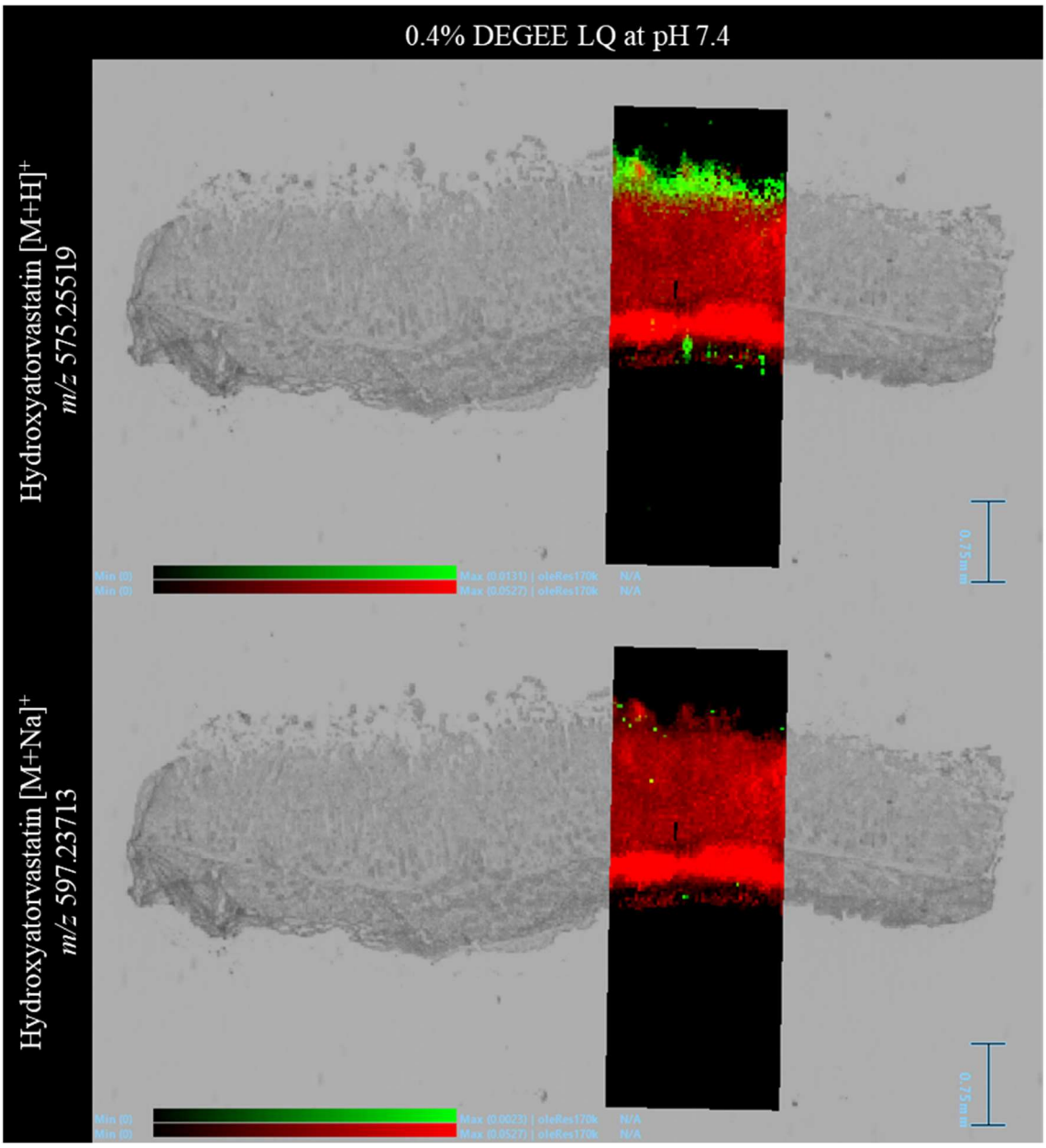

Figure 4.25: *DESI Images overlaid onto an optical image of the tissue section they were acquired from with the surface of the tissue facing upwards. The tissue section was acquired from a fresh tissue absorption experiment with 0.4% DEGEE LQ in the donor circuit buffered to pH 7.4. The distribution of the lipid ion m/z 780.5 was displayed in a red colour scale. The distribution of metabolite hydroxyatorvastatin (protonated and sodium adducts) were shown from top to bottom, respectively, using a green colour scale. All metabolite ions were within 1 ppm.*

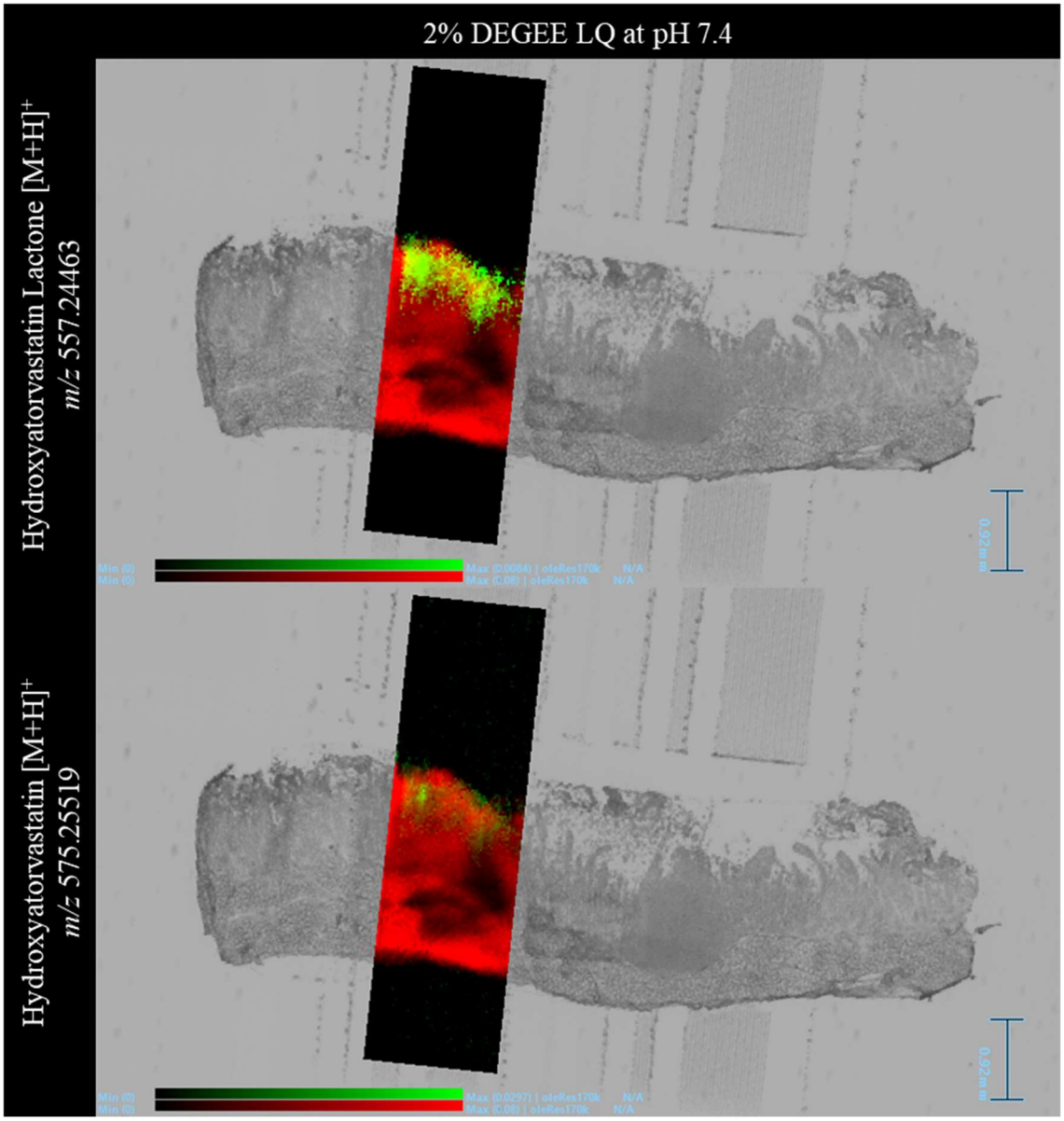

Figure 4.26: *DESI Images overlaid onto an optical image of the tissue section they were acquired from with the surface of the tissue facing upwards. The tissue section was acquired from a fresh tissue absorption experiment with 2% DEGEE LQ in the donor circuit buffered to pH 7.4. The distribution of the lipid ion m/z 780.5 was displayed in a red colour scale. The distribution of metabolites hydroxyatorvastatin lactone and hydroxyatorvastatin (both protonated ions) were shown from top to bottom, respectively, using a green colour scale. All metabolite ions were within 1 ppm.*

Some atorvastatin metabolites were visualised in the tissue sections taken from 0.4% and 2% DEGEE LQ experiments. The distribution of these metabolites were extremely similar to the atorvastatin acid adducts previously visualised. The exceptional mass accuracy and similar distribution led to the putative identification of these metabolites. In the 0.4% DEGEE LQ experiment, the metabolite ions can be seen in the final tissue layer; this was also demonstrated by the atorvastatin acid adducts. Similarly, there were no pixels relating to any atorvastatin metabolites in between the two distributions and thus, a clear drug absorption pathway was not seen. Using the ROIs in the same location as for the atorvastatin acid ions, the mass spectra were searched for all known atorvastatin metabolite ions; the results have been summarised in Table 4.5.

Table 4.5: *A summary of whether the named atorvastatin metabolites were detectable in different ROIs in the DESI image. The ROIs specified here included the whole tissue, an area on the tissue with no drug signal and an area away from the tissue. All data here relates to DESI images collected from the DEGEE LQ study performed at pH 7.4.*

DEGEE LQ Study at pH 7.4					
Atorvastatin Metabolites	ROI	Ion present in ROI? Concentration of DEGEE LQ (% v/v)			
		0	0.4	1	2
Hydroxyatorvastatin $[M+H]^+$ *m/z* 575.25519	Whole tissue?	✓	✓	×	✓
	Within tissue away from drug distribution?	×	✓	×	×
	Away from tissue?	×	×	×	×
Hydroxyatorvastatin $[M+Na]^+$ *m/z* 597.23713	Whole tissue?	×	✓	×	✓
	Within tissue away from drug distribution?	×	×	×	×
	Away from tissue?	×	×	×	×
Hydroxyatorvastatin lactone $[M+H]^+$ *m/z* 557.24463	Whole tissue?	✓	✓	×	✓
	Within tissue away from drug distribution?	×	✓	×	×
	Away from tissue?	×	×	×	×
Hydroxyatorvastatin lactone $[M+Na]^+$ *m/z* 579.22657	Whole tissue?	×	✓	×	×
	Within tissue away from drug distribution?	×	×	×	×
	Away from tissue?	×	×	×	×

No atorvastatin metabolites were detected in the tissue section taken from the 1% DEGEE LQ experiment. This finding was in keeping with the lack of atorvastatin metabolites that could be imaged for this study. Contrastingly, hydroxyatorvastatin and hydroxyatorvastatin lactone metabolites were detected in the whole tissue ROI from a no DEGEE LQ experiment but were not present in the DESI image. Furthermore, different adducts of the metabolites that were visualised in the DESI images from the 0.4% and 2% DEGEE LQ experiments were found to be present in the whole tissue ROI but not visible in the image. There were also a couple of instances in which metabolite signals were detected in the ROI on the tissue away from the visual drug distribution shown in the DESI image.

Overall, for the 'DEGEE LQ only' study performed at pH 7.4, significant amounts of atorvastatin acid were detectable in the acceptor circuits in addition to the DESI images showing the drug-related ions in the final tissue layer. The lack of signal from the atorvastatin throughout the entirety of the tissue section, teamed with the intense signal focused across the surface and final tissue layer insinuated an accumulation of atorvastatin. A further study was then performed with a combination of 0.4% polysorbate-80 and varying amounts of DEGEE LQ. The theory here was that polysorbate-80 would increase the solubility of atorvastatin and when combined with DEGEE, permeation levels would increase.

4.4.2.2 DEGEE LQ Combined with 0.4% Polysorbate-80

DEGEE LQ was added to the donor circuit in final concentrations of 0%, 0.4%, 1% and 2% along with 0.4% polysorbate-80 in PBS, buffered to pH 7.4. All parameters were the same as the previous studies, except a double o-ring fitting was used hereinafter.

To evaluate how the combination of polysorbate-80 and DEGEE LQ affected solubility, the amount of atorvastatin rinsed from the drained system after each experiment in the study was plotted against the concentration of DEGEE LQ in the presence of 0.4% polysorbate-80; see Figure 4.27.

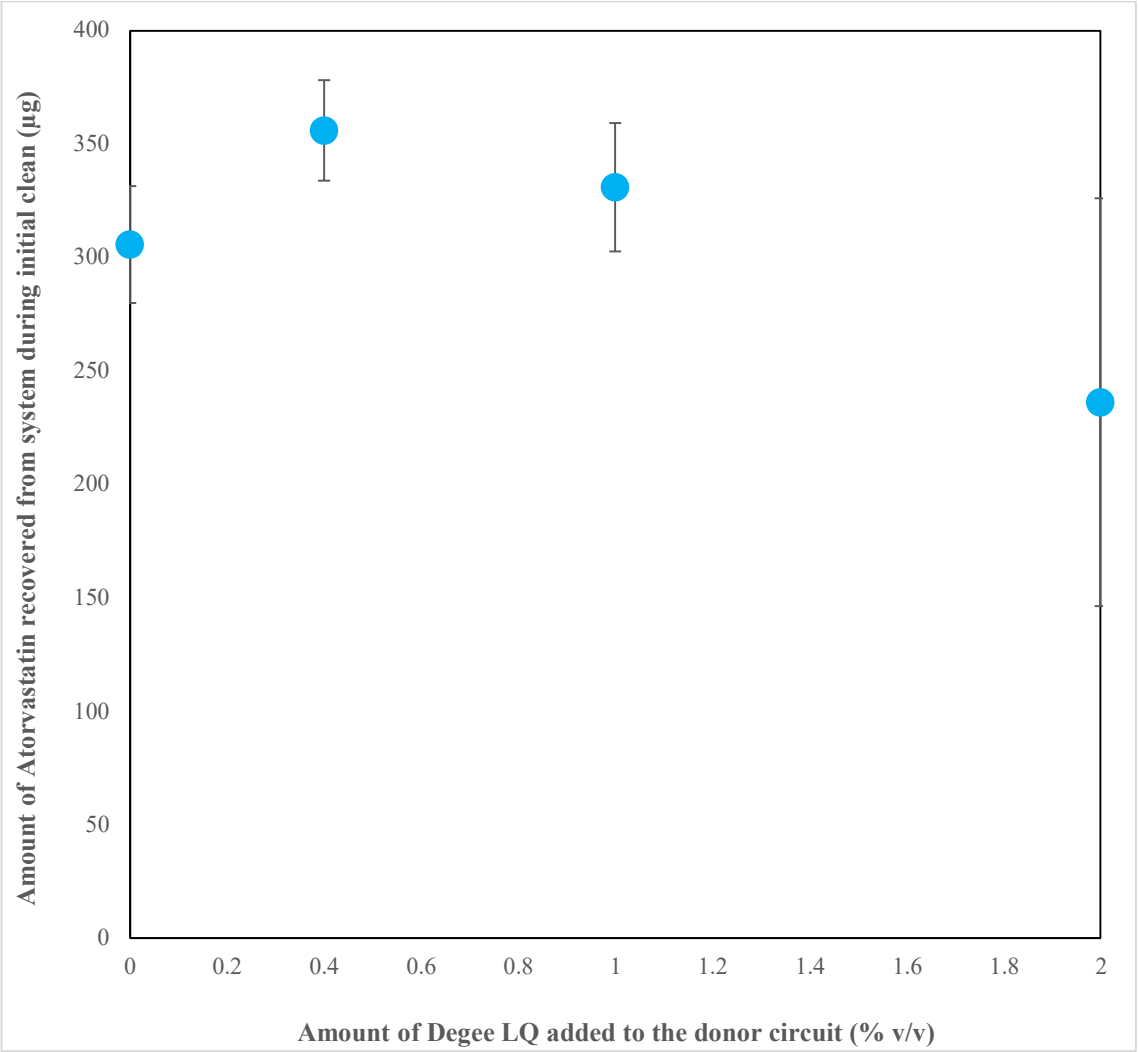

Figure 4.27: *A graph showing the amount of Atorvastatin that was recovered from the QV600 LLI after the system had been drained following an absorption experiment with varied amounts of Degee LQ added to the donor circuit along with 0.4% Polysorbate-80. The data presented here is from the DEGEE mixed with 0.4% (v/v) Polysorbate-80 study performed at pH 7.4 (n=3).*

When 0.4% polysorbate-80 was in the donor circuit alone, the amount of atorvastatin rinsed from the system was similar to that from other studies using polysorbate-80. When any amount of DEGEE LQ was added to 0.4% polysorbate-80 in the donor circuit, there was no significant differences in the amount of atorvastatin recovered from the drained system as confirmed by a one-way ANOVA and post-hoc Tukey HSD Test. These findings indicated that in the presence of 0.4% polysorbate-80, DEGEE LQ could be added to atorvastatin and have little-to-no effect on its solubility in PBS throughout the course of this study. The analysis of the tissue rinse solution strengthened this hypothesis. In Figure 4.28, the amount of atorvastatin rinsed from the surface of the

tissue disc was plotted against the concentration of DEGEE LQ that was present in the donor circuit along with 0.4% polysorbate-80.

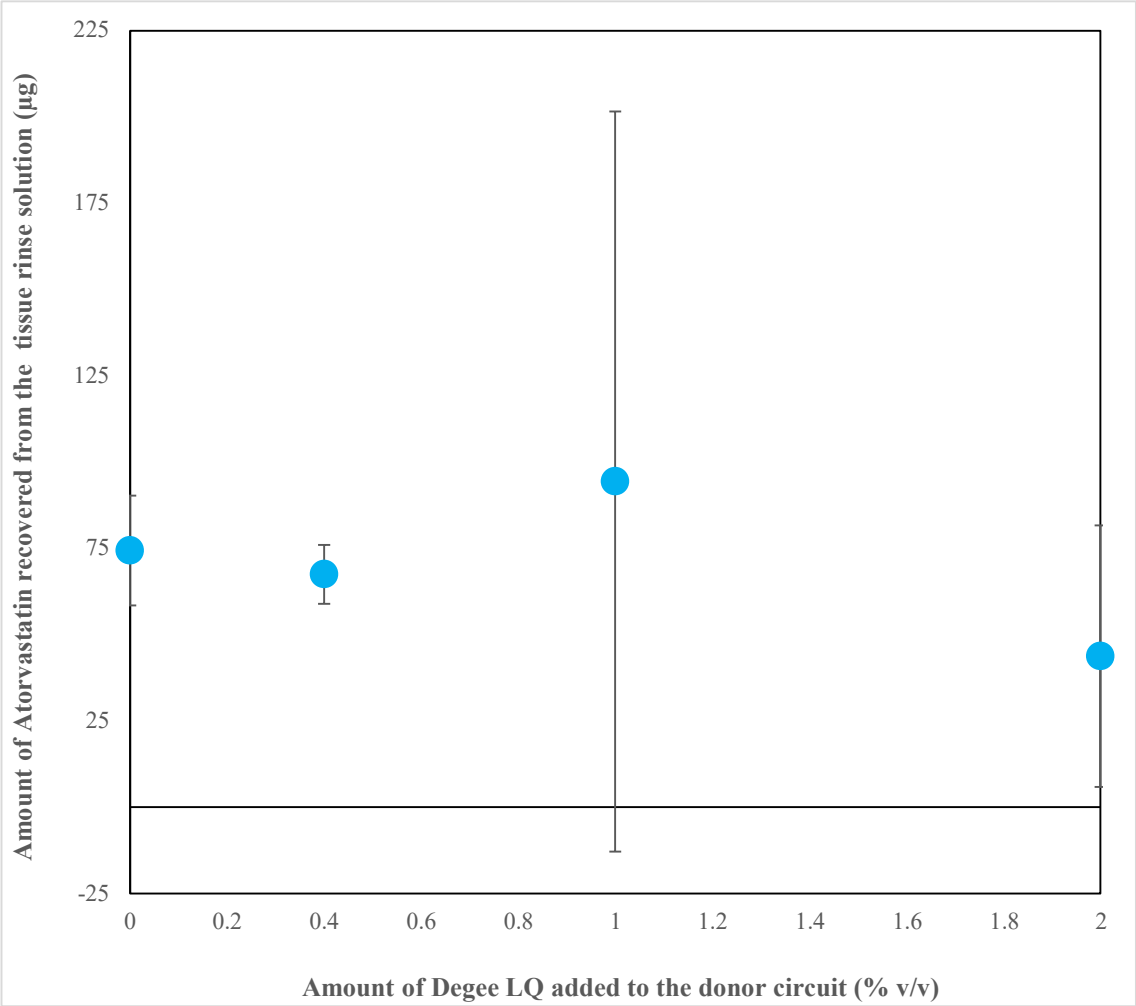

Figure 4.28: *A graph to show the amount of Atorvastatin that was rinsed from the tissue discs plotted against the concentration of Degee LQ added to 0.4% Polysorbate-80 in the donor circuit of the corresponding absorption experiment. The data presented here is from the DEGEE mixed with 0.4% (v/v) Polysorbate-80 study performed at pH 7.4 (n=3).*

When increasing amounts of DEGEE LQ were added to 0.4% polysorbate-80 in the donor circuit, a one-way ANOVA test found that there were no significant differences in the amount of atorvastatin that was rinsed from the surface of the tissue. Overall, when polysorbate-80 was present in the donor circuit alone, the amount of atorvastatin rinsed from the tissue surface was similar to that shown in other studies using polysorbate-80. Presumably, with minimal interference from solid atorvastatin calcium settled into the mucus on the surface of the tissue, the information provided from the tissue extracts in

Figure 4.29 gives more information on the drug residing within the tissue rather than on its surface.

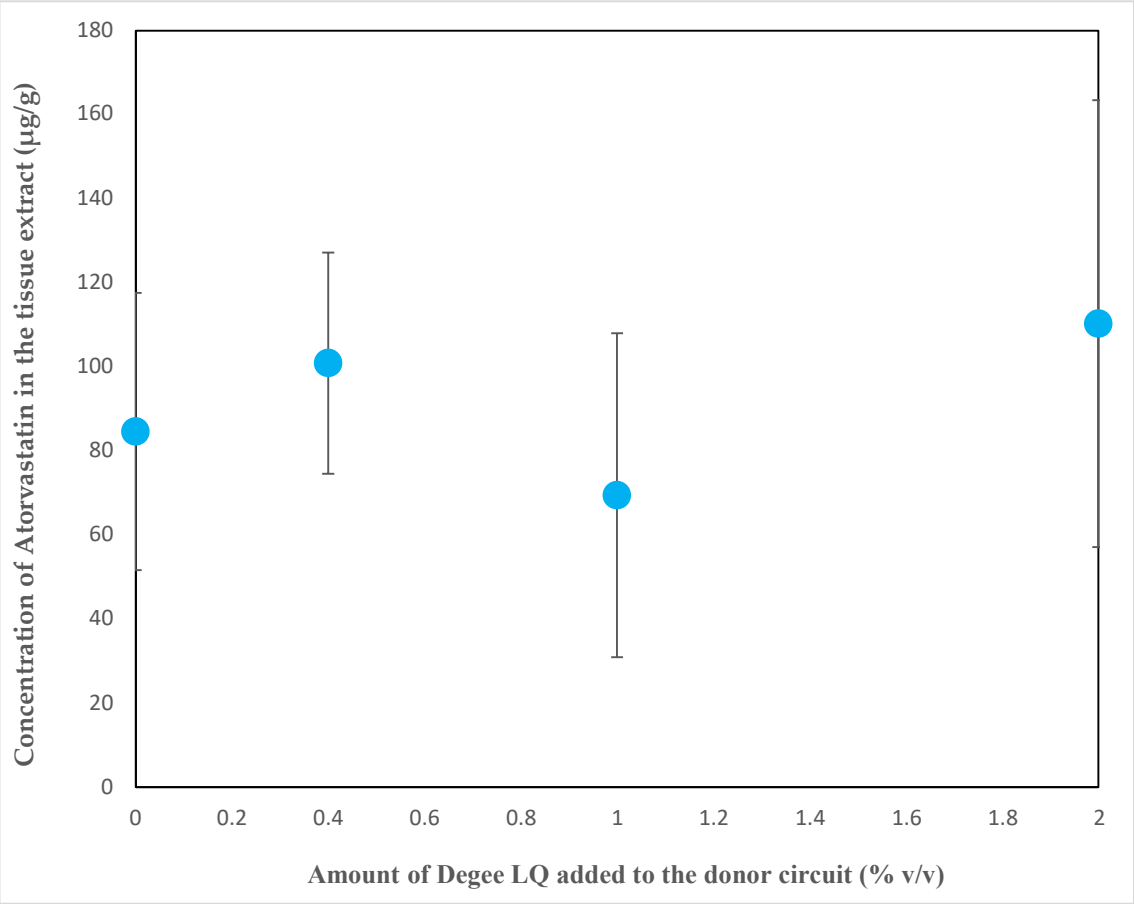

Figure 4.29: *A graph showing the concentration of Atorvastatin calculated from the tissue disc extract plotted against the corresponding amount of Degee LQ that was added to the donor circuit along with 0.4% Polysorbate-80 for that absorption experiment. The data presented here is from the DEGEE mixed with 0.4% (v/v) Polysorbate-80 study performed at pH 7.4 (n=3).*

It was determined by a one-way ANOVA test that, in the presence of 0.4% polysorbate-80, there were no statistically significant differences in the amount of atorvastatin that was recovered from the tissue extract when DEGEE LQ was added to the donor circuit. The DESI images acquired from the study were reviewed to better understand the effect of increasing the amount of DEGEE LQ in the presence of 0.4% polysorbate-80. The DESI images of atorvastatin acid detected in several tissue sections from the study were displayed in Figure 4.30-4.37.

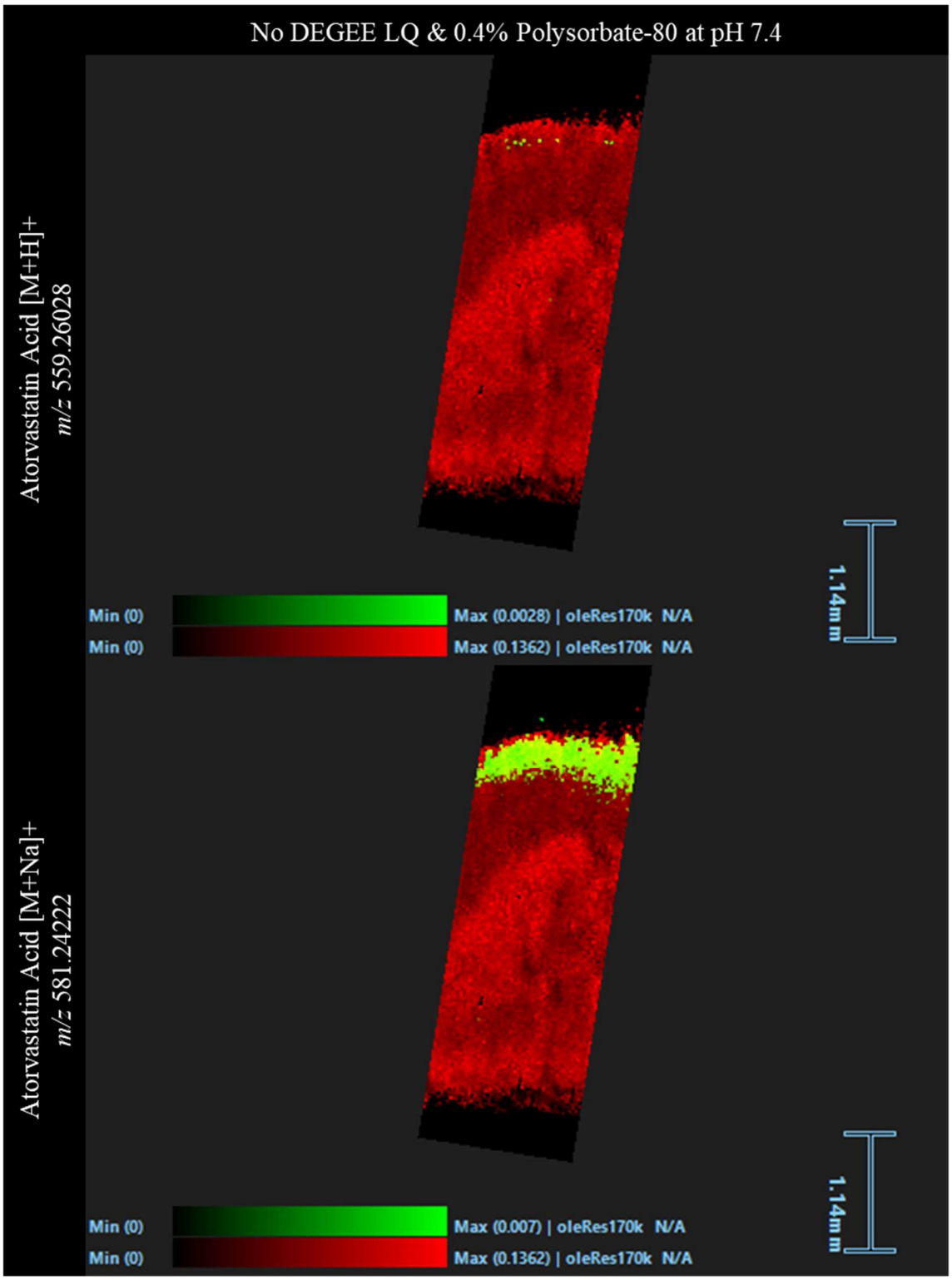

Figure 4.30: *DESI Images from a tissue section with the surface of the tissue facing upwards. The tissue section was acquired from a fresh tissue absorption experiment with 0.4% polysorbate-80 in the donor circuit, buffered to pH 7.4. The distribution of the lipid ion m/z 780.5 was displayed in a red colour scale. Protonated atorvastatin acid and its sodium adduct were shown from top to bottom, respectively, using a green colour scale. All identified drug related ions were within 1 ppm.*

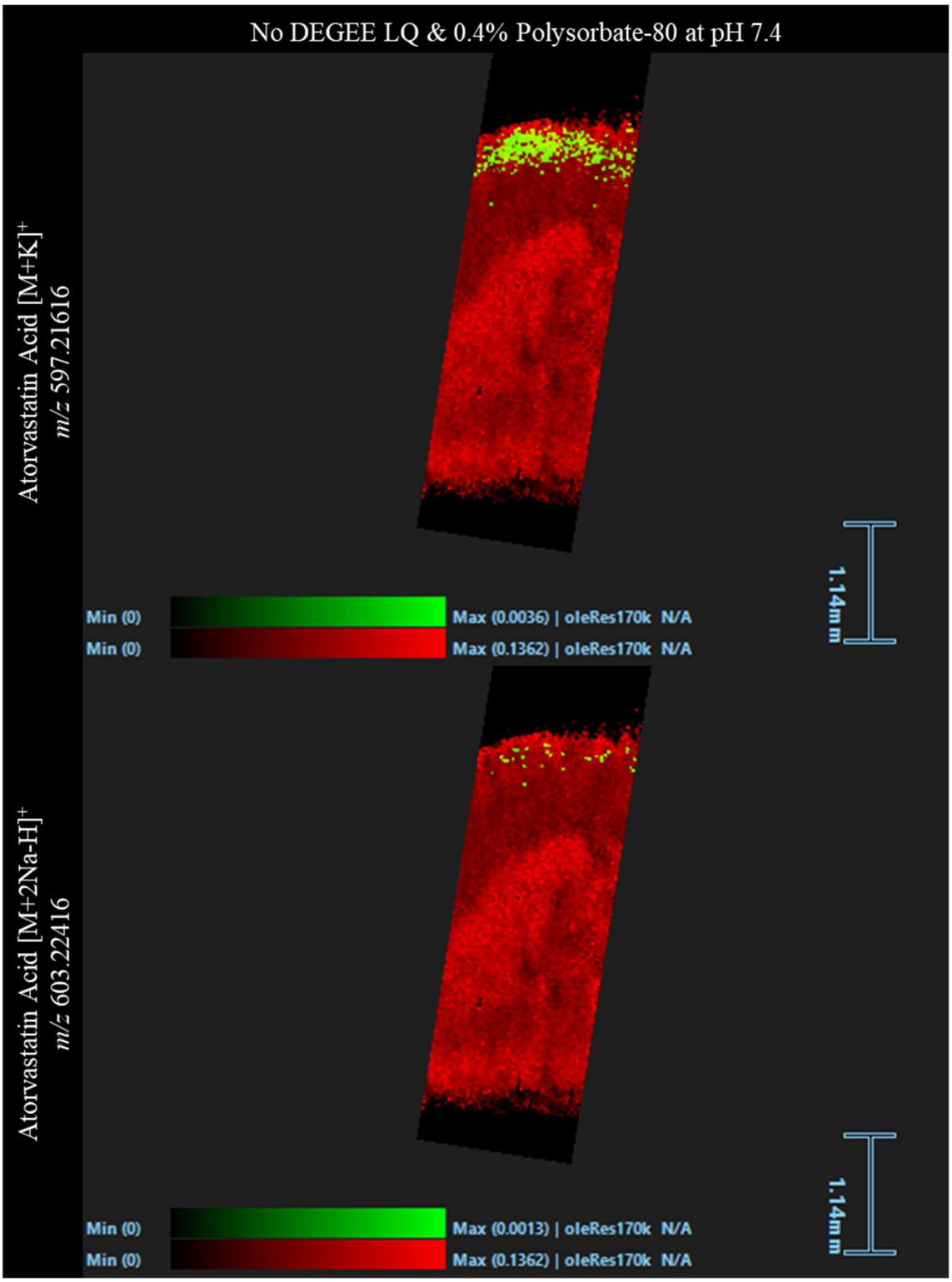

Figure 4.31: *DESI Images from a tissue section with the surface of the tissue facing upwards. The tissue section was acquired from a fresh tissue absorption experiment with 0.4% polysorbate-80 in the donor circuit, buffered to pH 7.4. The distribution of the lipid ion m/z 780.5 was displayed in a red colour scale. Atorvastatin acid sodium and $[M+2Na-H]^+$ adducts were shown from top to bottom, respectively, using a green colour scale. All identified drug related ions were within 1 ppm.*

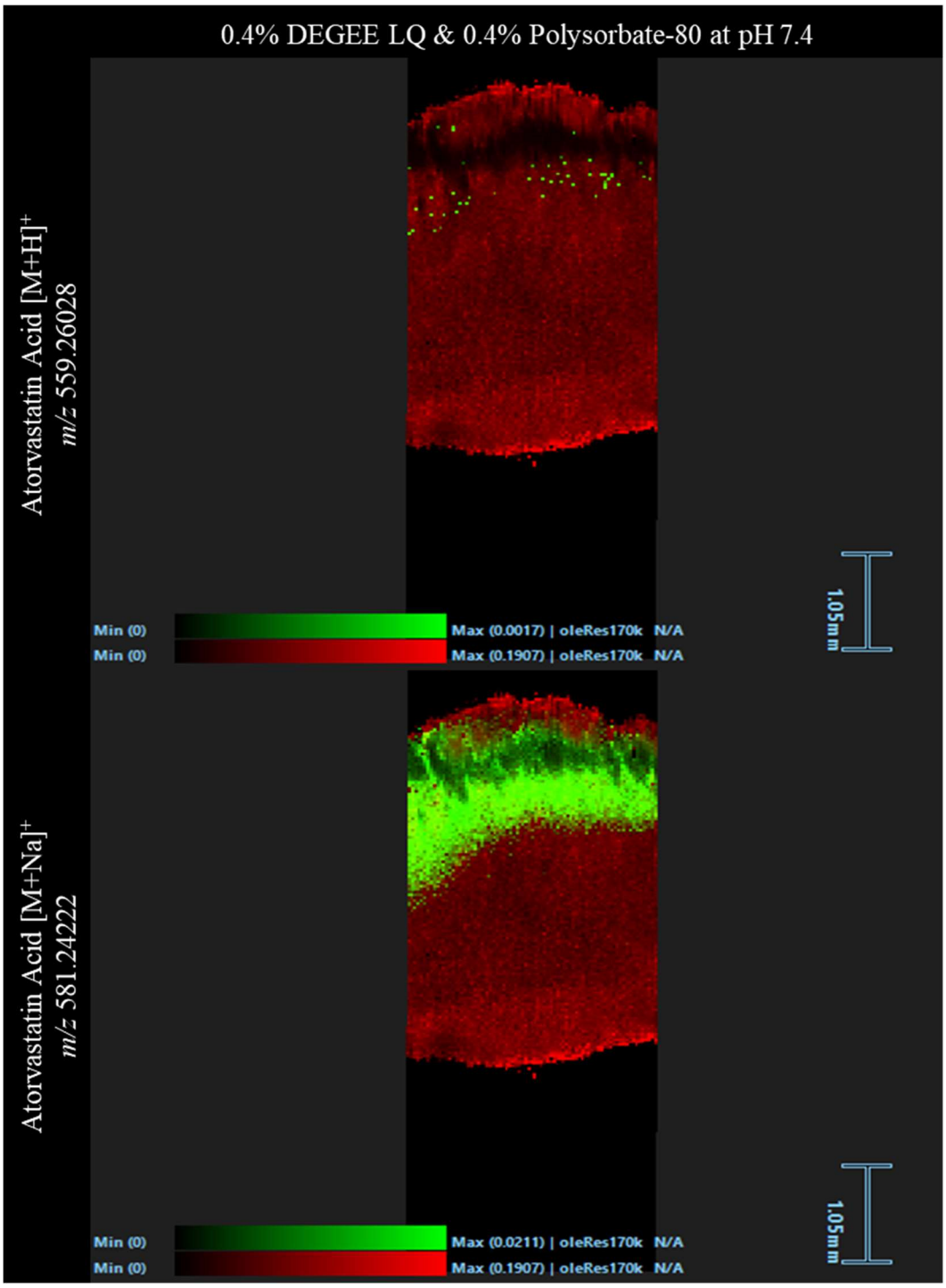

Figure 4.32: *DESI Images from a tissue section with the surface of the tissue facing upwards. The tissue section was acquired from a fresh tissue absorption experiment with 0.4% DEGEE LQ and 0.4% polysorbate-80 in the donor circuit, buffered to pH 7.4. The distribution of the lipid ion m/z 780.5 was displayed in a red colour scale. Protonated atorvastatin acid and its sodium adduct were shown from top to bottom, respectively, using a green colour scale. All identified drug related ions were within 1 ppm.*

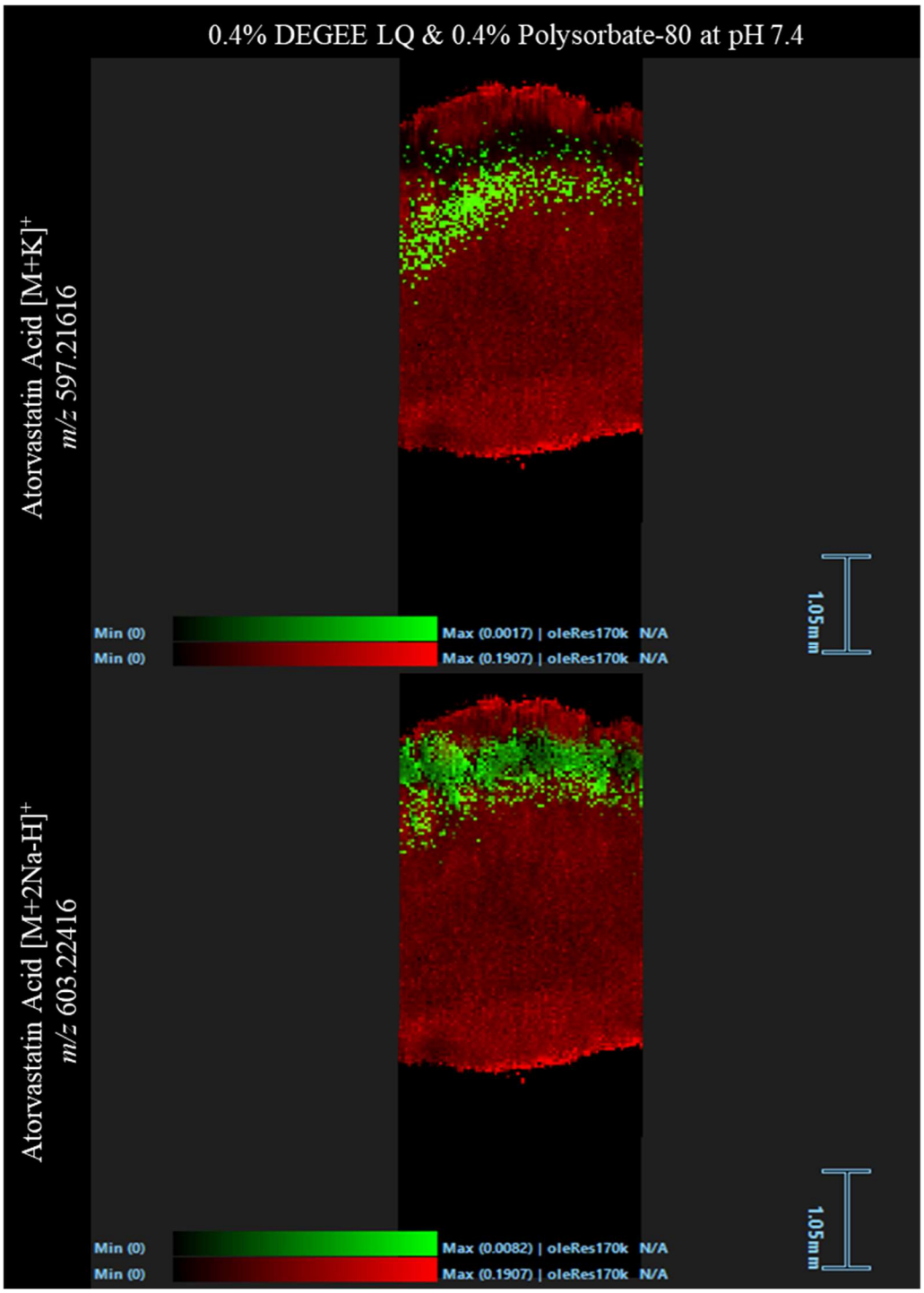

Figure 4.33: *DESI Images from a tissue section with the surface of the tissue facing upwards. The tissue section was acquired from a fresh tissue absorption experiment with 0.4% DEGEE LQ and 0.4% polysorbate-80 in the donor circuit, buffered to pH 7.4. The distribution of the lipid ion m/z 780.5 was displayed in a red colour scale. Atorvastatin acid sodium and $[M+2Na-H]^+$ adducts were shown from top to bottom, respectively, using a green colour scale. All identified drug related ions were within 1 ppm.*

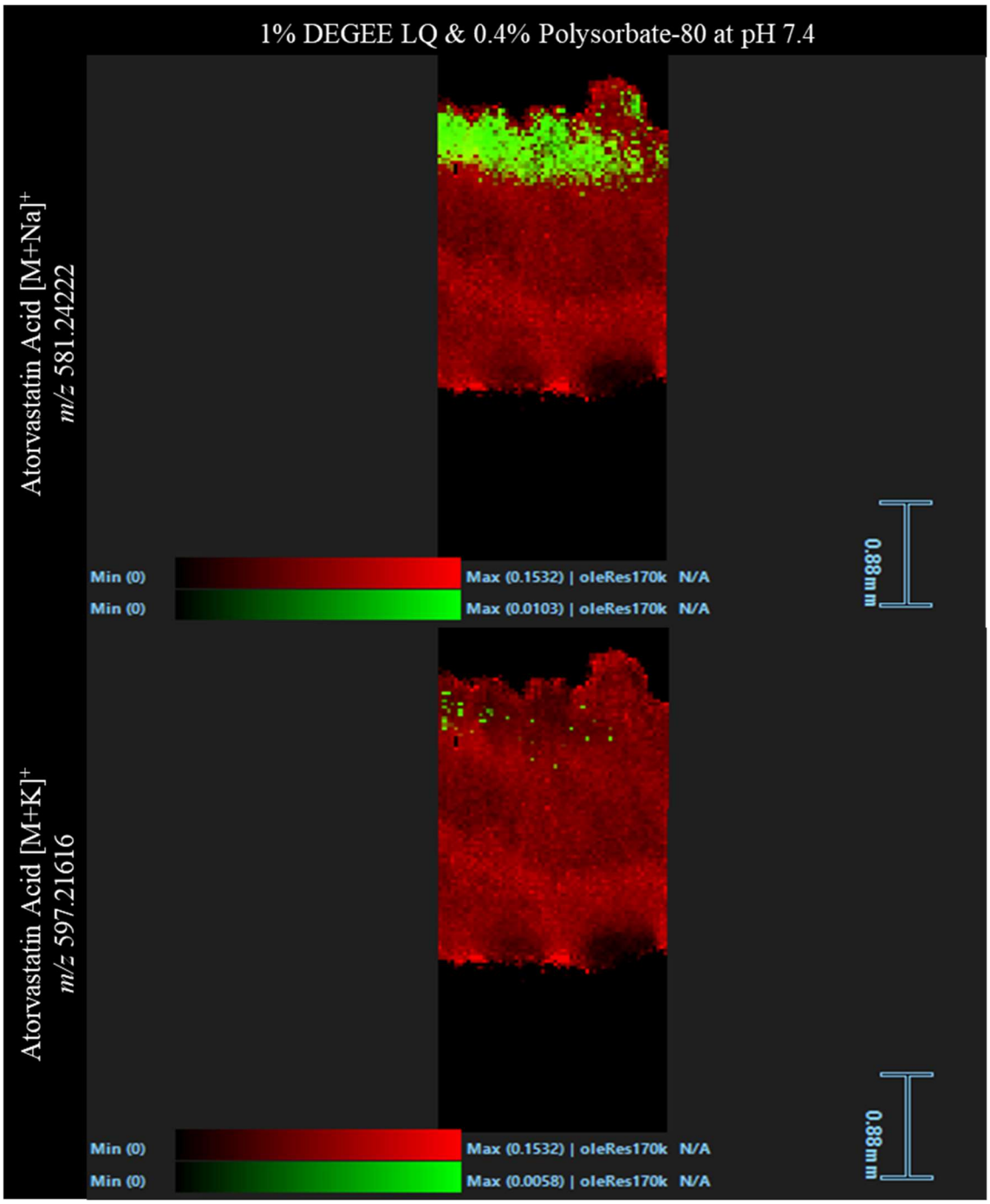

Figure 4.34: *DESI Images from a tissue section with the surface of the tissue facing upwards. The tissue section was acquired from a fresh tissue absorption experiment with 1% DEGEE LQ and 0.4% polysorbate-80 in the donor circuit, which was buffered to pH 7.4. The distribution of the lipid ion m/z 780.5 was displayed in a red colour scale. Sodium and potassium adducts of atorvastatin acid were shown from top to bottom, respectively, using a green colour scale. All identified drug related ions were within 1 ppm.*

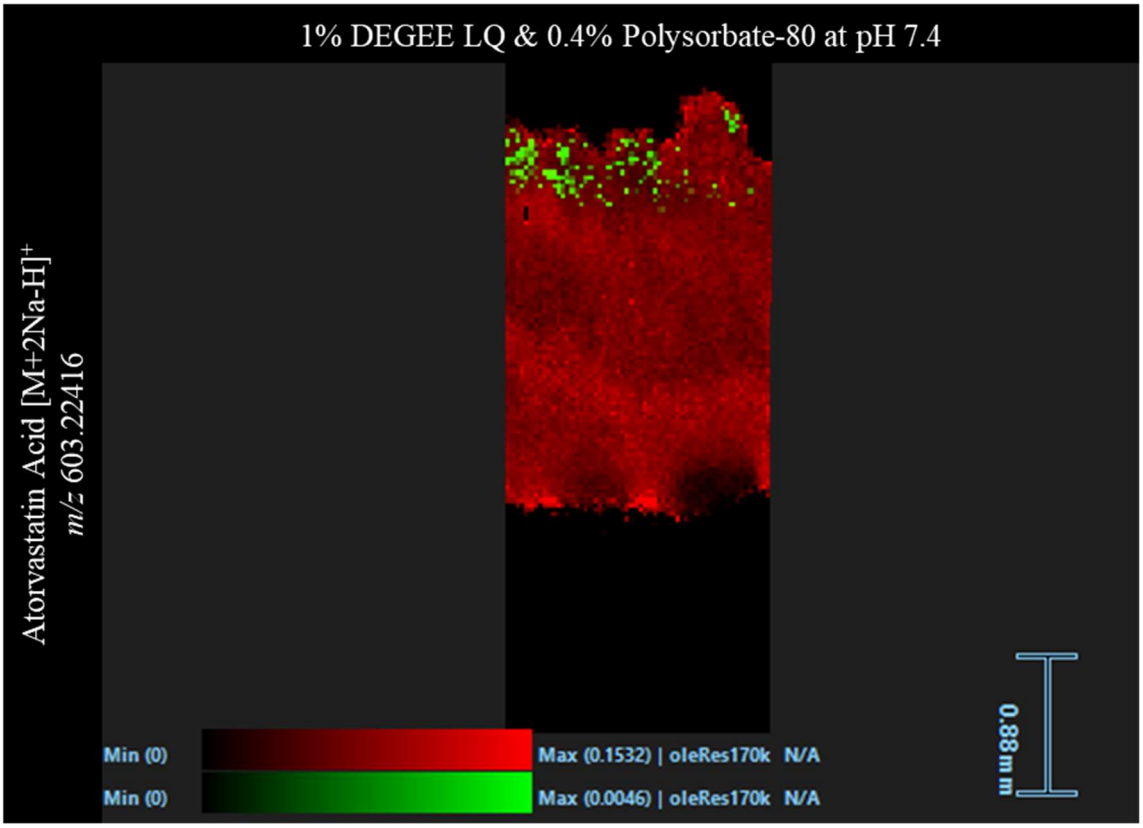

Figure 4.35: *DESI Image from a tissue section with the surface of the tissue facing upwards. The tissue section was acquired from a fresh tissue absorption experiment with 1% DEGEE LQ and 0.4% polysorbate-80 in the donor circuit, buffered to pH 7.4. The distribution of the lipid ion m/z 780.5 and atorvastatin acid adduct $[M+2Na-H]^+$ were displayed in a red and green colour scale, respectively. All identified drug related ions were within 1 ppm.*

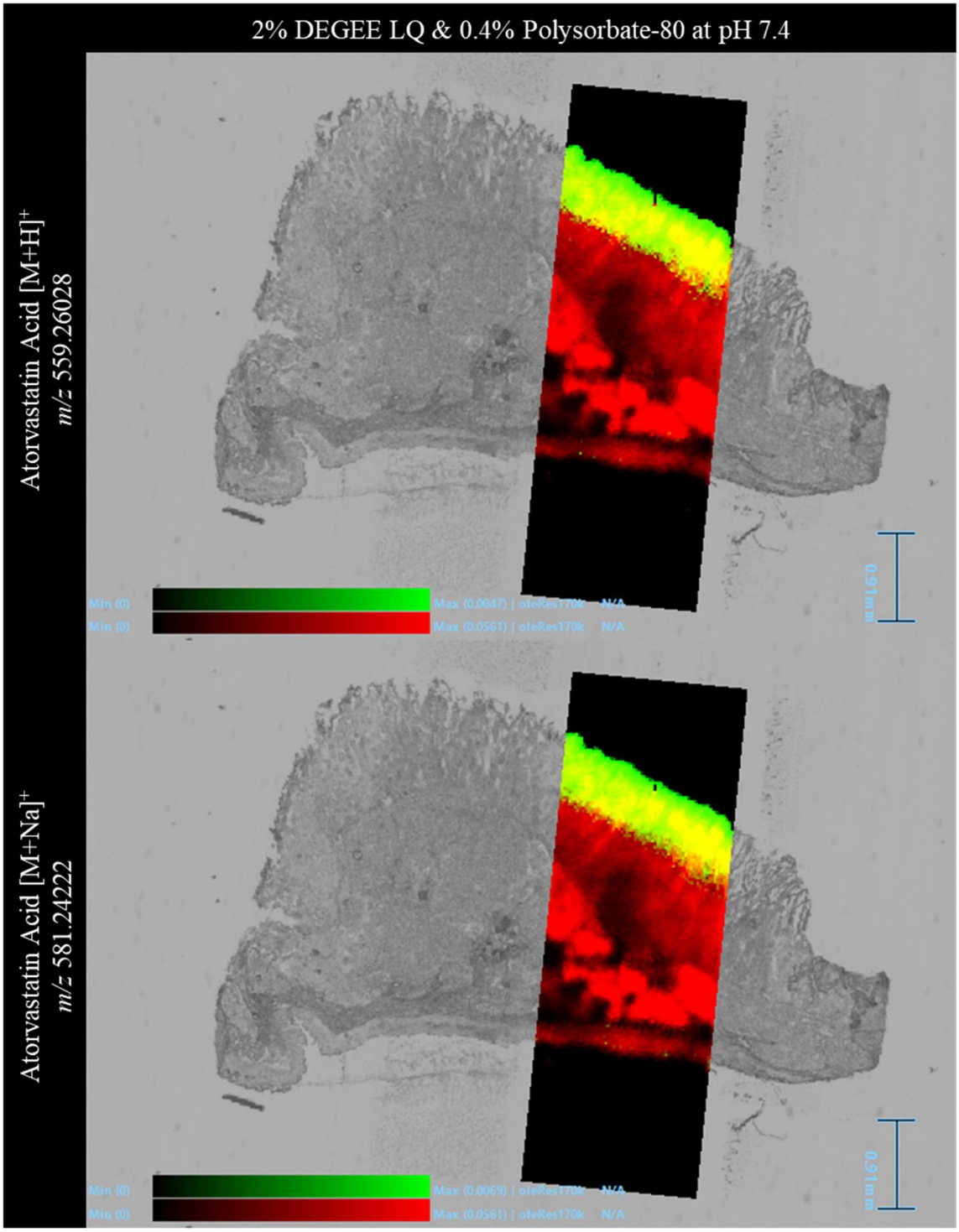

Figure 4.36: *DESI Images overlaid onto an optical image of the tissue section they were acquired from with the surface of the tissue facing upwards. The tissue section was acquired from a fresh tissue absorption experiment with 2% DEGEE LQ and 0.4% polysorbate-80 in the donor circuit, buffered to pH 7.4. The distribution of the lipid ion m/z 780.5 was displayed in a red colour scale. The distribution of protonated atorvastatin acid and its sodium adduct were shown from top to bottom, respectively, using a green colour scale. All identified drug related ions were within 1 ppm.*

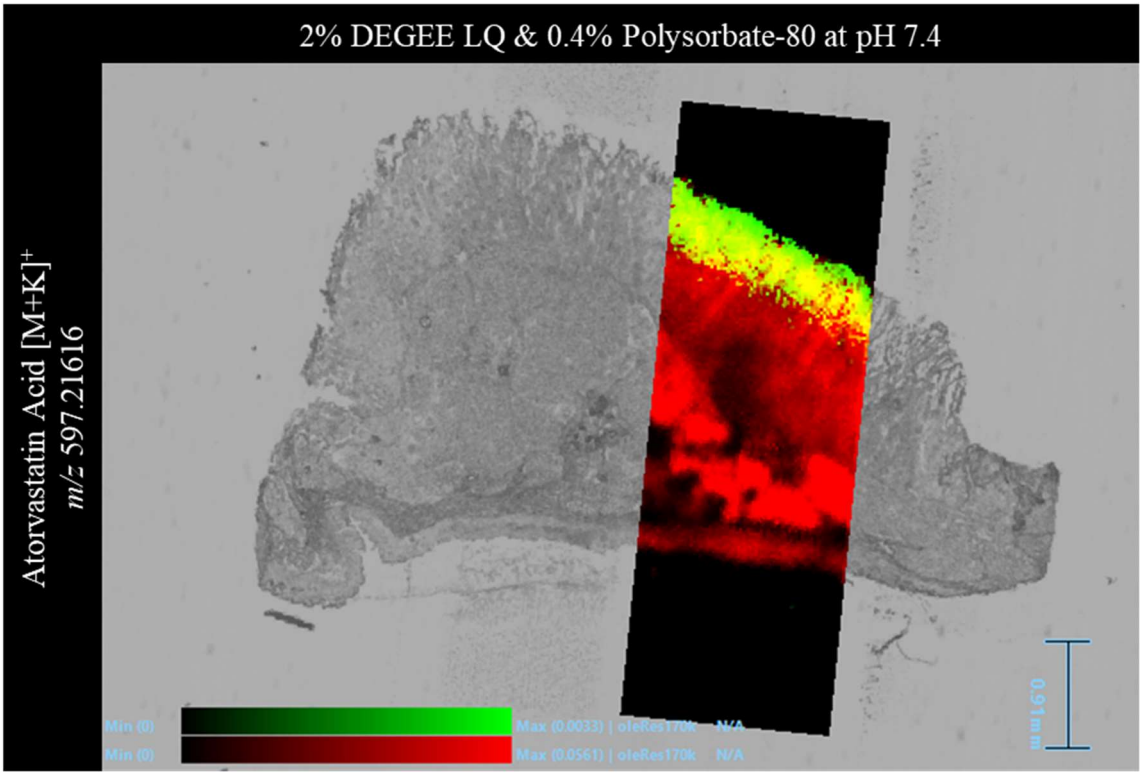

Figure 4.37: *DESI Image overlaid onto an optical image of the tissue section it was acquired from with the surface of the tissue facing upwards. The tissue section was acquired from a fresh tissue absorption experiment with 2% DEGEE LQ and 0.4% polysorbate-80 in the donor circuit, buffered to pH 7.4. The distribution of the lipid ion m/z 780.5 and the potassium adduct of atorvastatin acid were displayed in a red and green colour scale, respectively. All identified drug related ions were within 1 ppm.*

A different pattern was observed here in the DESI images for this combined study. Consistently, for the first three experiments in the study, the distribution of atorvastatin acid adducts were shown to be slightly below the surface of the tissue. The distribution suggested that the drug had permeated through the tissue to a certain extent, but it was unusual that the direction of entry was not always clear. A possible theory to explain this phenomenon would be that the drug was saturated in that area so much so that other drug signals were masked. A concerning factor here was that such level of saturation would imply the atorvastatin had stopped permeating through the tissue. Nevertheless, the drug must have moved through the tissue to reach that area but was undetected, thus it remains possible that the drug could have also moved through to the opposite side of the tissue undetected.

The findings here were different from previous studies which had demonstrated atorvastatin acid ions saturated on the surface of the tissue which then progressed deeper into the apparent villi layer. Once the concentration of DEGEE LQ had reached 2%, the DESI images reflected the same pattern as previously observed. A possible theory may be that the now-soluble atorvastatin acid was able to permeate through the tissue more easily with increasing amounts of DEGEE LQ present, causing an accumulation further into the tissue. Following this theory, it would then be possible that when 2% DEGEE LQ was reached, the rate at which atorvastatin was permeating into the tissue was much faster than the rate in which it was moving into the acceptor circuit, leading to a build up in drug on the surface layer. Another possible theory would be that the drug had begun to accumulate in the tissue because it had not fully permeated through the tissue. ROIs were drawn in areas below the drug distribution and compared to other ROIs showing the whole tissue and areas without tissue to establish whether low levels of drug could be detected in the deeper layers of the tissue. The results of this investigation were summarised in Table 4.6 and the specific location of each ROI have been detailed in Appendix I Figure 9-12.

Table 4.6: *A summary of whether the named atorvastatin related ions were detectable in different ROIs in the DESI image. The ROIs specified here included the whole tissue, an area on the tissue with no drug signal and an area away from the tissue. All data here relates to DESI images collected from the DEGEE LQ with 0.4% polysorbate-80 study performed at pH 7.4.*

DEGEE LQ with 0.4% Polysorbate-80 Study at pH 7.4					
Atorvastatin and Related Ions	ROI	Ion present in ROI? Concentration of DEGEE LQ (% v/v)			
		0	0.4	1	2
Atorvastatin Acid $[M+H]^+$ *m/z* 559.26028	Whole tissue?	✓	✓	✓	✓
	Within tissue away from drug distribution?	×	×	×	×
	Away from tissue?	×	×	×	×
Atorvastatin Acid $[M+Na]^+$ *m/z* 581.24222	Whole tissue?	✓	✓	✓	✓
	Within tissue away from drug distribution?	×	×	×	×
	Away from tissue?	×	×	×	×
Atorvastatin Acid $[M+K]^+$ *m/z* 597.21616	Whole tissue?	✓	✓	✓	✓
	Within tissue away from drug distribution?	×	×	×	×
	Away from tissue?	×	×	×	×
Atorvastatin Acid $[M+2Na-H]^+$ *m/z* 603.22416	Whole tissue?	✓	✓	✓	✓
	Within tissue away from drug distribution?	×	×	×	×
	Away from tissue?	×	×	×	×

Of all the atorvastatin acid adducts detected in the whole tissue ROIs, none were detected in the ROI away from the visible drug distribution. Interestingly, the $[M+2Na-H]^+$ adduct of atorvastatin acid was detected in all whole tissue ROIs, however was not present in the images. The DESI images from this study were then checked for any

known atorvastatin metabolites. Only one atorvastatin metabolite was able to be visualised from the entire study; this has been displayed in Figure 4.38.

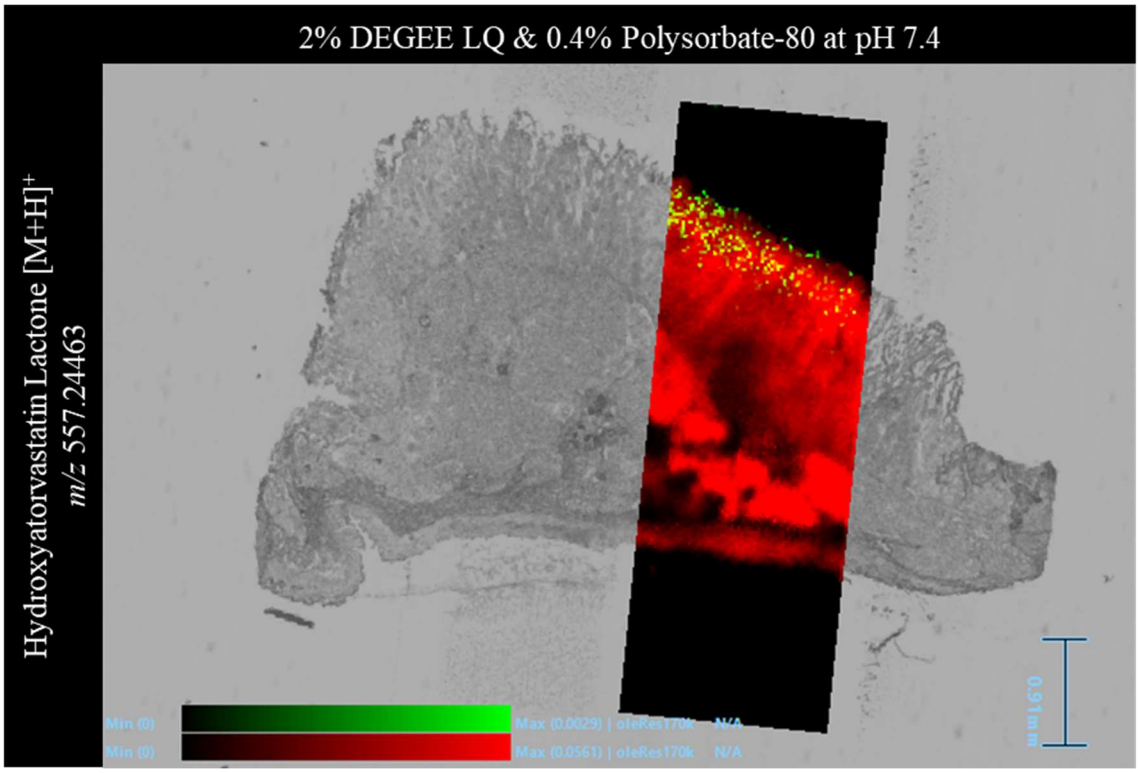

Figure 4.38: *DESI Image overlaid onto an optical image of the tissue section it was acquired from with the surface of the tissue facing upwards. The tissue section was acquired from a fresh tissue absorption experiment with 2% DEGEE LQ and 0.4% polysorbate-80 in the donor circuit buffered to pH 7.4. The distribution of the lipid ion m/z 780.5 and protonated metabolite Hydroxyatorvastatin lactone was displayed in a red and green colour scale, respectively. The metabolite ion was within 1 ppm.*

Coincidently, the only experiment in which any metabolite could be visualised was the experiment that used 2% DEGEE LQ with 0.4% polysorbate-80. The metabolite Hydroxyatorvastatin lactone was localised on the surface layer of the tissue, a similar distribution to that seen with all atorvastatin acid adducts albeit covering a significantly lower surface area. The DESI images were checked for lower levels of metabolite by exporting the mass spectra from the same ROIs as previously used for atorvastatin acid. The findings were tabulated and summarised in Table 4.7.

Table 4.7: *A summary of whether the named atorvastatin metabolites were detectable in different ROIs in the DESI image. The ROIs specified here included the whole tissue, an area on the tissue with no drug signal and an area away from the tissue. All data here relates to DESI images collected from the DEGEE LQ with 0.4% polysorbate-80 study performed at pH 7.4.*

DEGEE LQ with 0.4% Polysorbate-80 Study at pH 7.4					
Atorvastatin Metabolites	ROI	Ion present in ROI? Concentration of DEGEE LQ (% v/v)			
		0	0.4	1	2
Hydroxyatorvastatin $[M+Na]^+$ *m/z* 597.23713	Whole tissue?	×	×	×	✓
	Within tissue away from drug distribution?	×	×	×	×
	Away from tissue?	×	×	×	×
Hydroxyatorvastatin lactone $[M+H]^+$ *m/z* 557.24463	Whole tissue?	×	×	×	✓
	Within tissue away from drug distribution?	×	×	×	×
	Away from tissue?	×	×	×	×

Atorvastatin metabolites were not detected in the ROI for any other experiment. Hydroxyatorvastatin and hydroxyatorvastatin lactone were detected in the whole tissue ROI taken from the 2% DEGEE LQ with 0.4% polysorbate-80 experiment but not in the other two ROIs. A suspicious lack of metabolites in the whole tissue ROIs, with exception to the final experiment, brings the sensitivity of the instrument into question. With the presence of 0.4% polysorbate-80 throughout the study, a significant amount of the atorvastatin remains in solution. Therefore, less atorvastatin would be in contact with the surface of the tissue disc at one time. Similarly reflected in the tissue extract data, a lower amount of atorvastatin was recovered from the disc. It therefore can be reasonably expected that a lesser concentration of atorvastatin would be saturated on the surface and perhaps, display a more even distribution that draws even closer to the imaging capabilities of this particular instrument.

For such theories to bear significant weight, further work would be essential to prove the limit of detection for this particular drug in addition to potential masking effects. Although mass spectrometry imaging was used as a qualitative technique, the implementation of internal standards by way of a quantitative spotter, would enable quantitative data to be acquired from the DESI images. Meanwhile, with less interaction between the drug and the tissue surface in addition to the accumulation of drug below the surface of the tissue, a reduced permeation can be reasonably expected.

Permeation coefficients were calculated for each experiment in the combined study and presented in Figure 4.39. Overall, the $P_{app,pig}$ values were significantly lower than the data acquired from the 'DEGEE LQ only' study, with a P value of 0.0247 determined by an unpaired t test. There was much variability between replicate experiments which makes identifying and understanding a trend here particularly difficult. A one-way ANOVA with Tukey's Post HSD test determined that the differences in the $P_{app,pig}$ values as the DEGEE LQ concentration increased were not statistically significant.

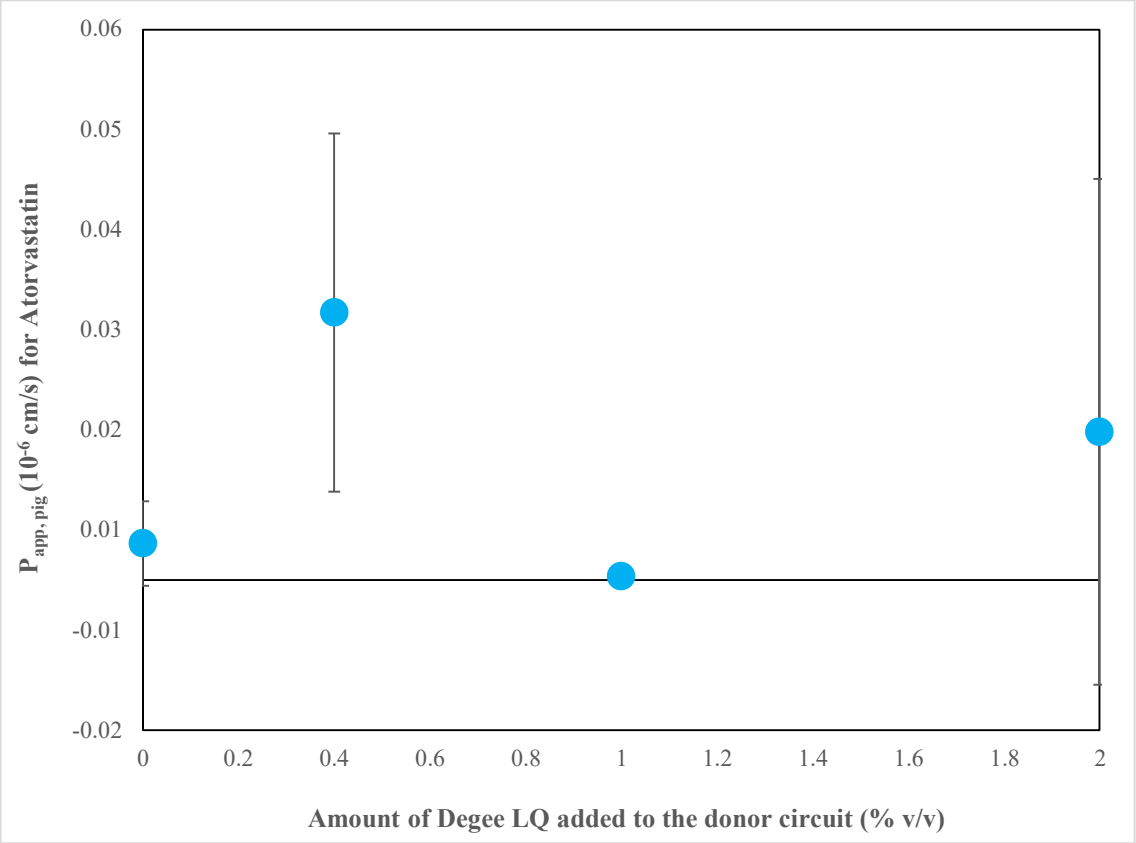

Figure 4.39: *A graph showing the $P_{app,pig}$ values plotted against the concentration of Degee LQ in the donor circuit along with 0.4% Polysorbate-80 of the corresponding absorption experiment. The data presented here is from the DEGEE mixed with 0.4% (v/v) Polysorbate-80 study performed at pH 7.4 (n=3).*

Referring back to the DESI images acquired for this particular study, a likely theory was that the Atorvastatin ion maps were showing drug accumulation within the tissue.

4.4.3 Repeated Studies at pH 6

To create a closer to real-life scenario, the pH of the donor circuit was buffered to pH 6. This pH was more relevant to the duodenum portion of the small intestine, but an unintended benefit was that atorvastatin calcium was reported to be readily soluble in tissue when in this environment. Furthermore, FBS was added to the acceptor circuit to create a closer resemblance to the contents of the blood vessels and in turn, attempt to improve the movement of atorvastatin from the tissue into the acceptor circuit. These changes were kept for future studies yet to be discussed.

4.4.3.1 Polysorbate-80 Only

The 'polysorbate-80 only' study discussed in section 4.4.1 was repeated under the conditions stated above with a key difference being the pH, acceptor circuit supplement and the double o-ring fitting. The $P_{app,pig}$ values for this study were calculated and displayed in Figure 4.40.

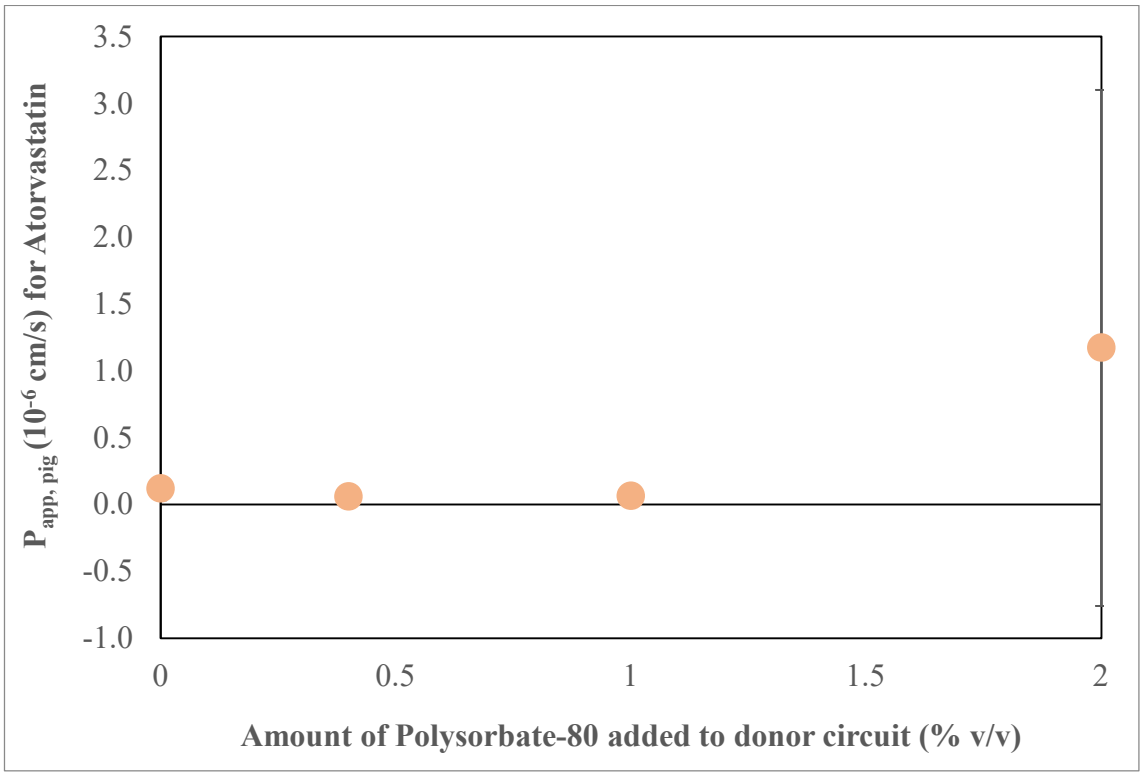

Figure 4.40: *A graph showing the Papp,pig values plotted against the concentration of Polysorbate-80 in the donor circuit (pH 6) of the corresponding absorption experiment. The data presented here is from the Polysorbate-80 only study performed at pH 6 (n=3).*

All of the data points shown here do not exceed those published by similar studies so was not considered to be an obvious leak in the system. However, the exceptionally high data point was considered an outlier and excluded in Figure 4.41.

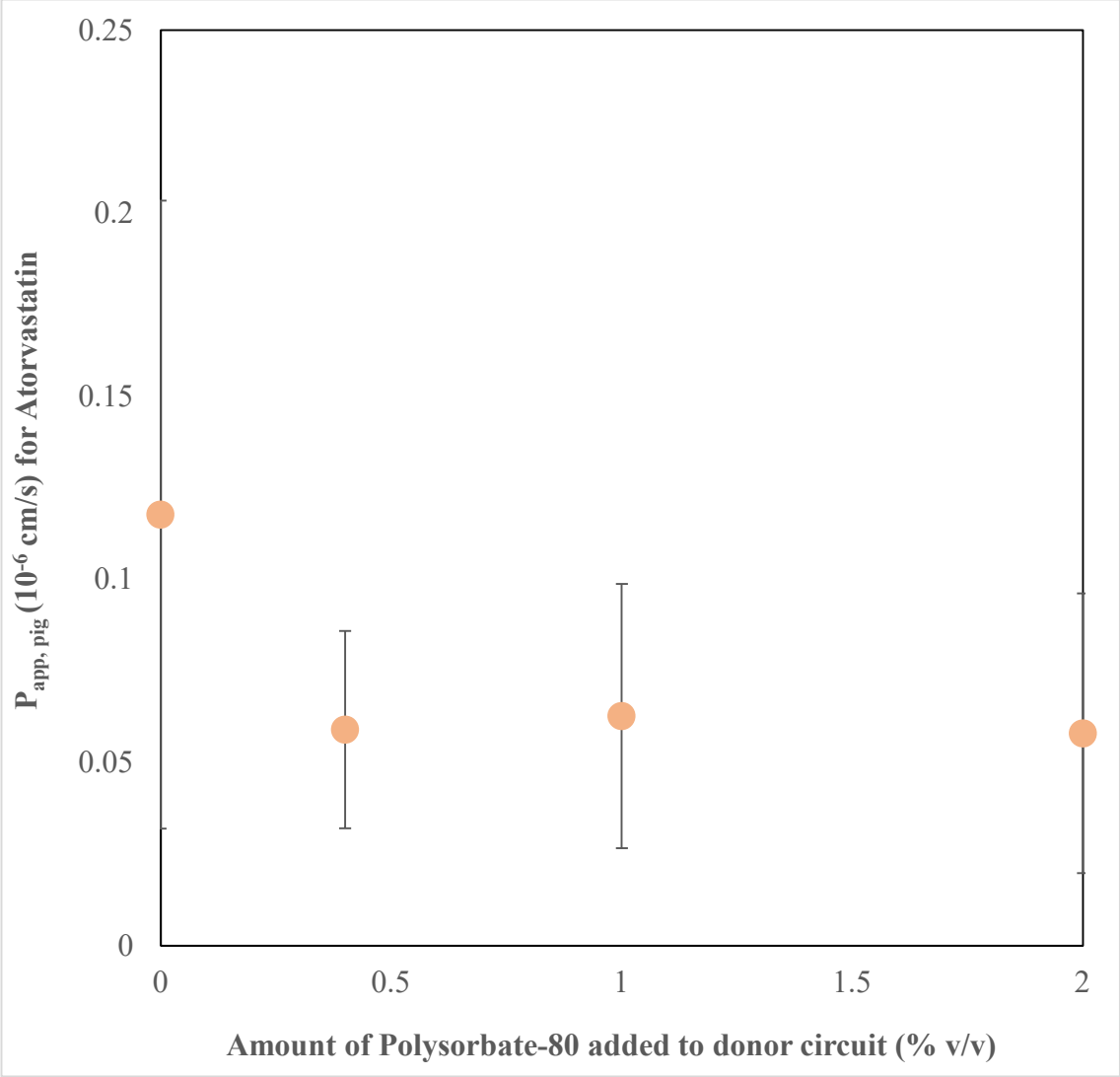

Figure 4.41: *A graph showing the data set from Figure 4.40 replotted without the outlier (n=3).*

A one-way ANOVA with post-hoc Tukey HSD test found that the differences in the amount of atorvastatin acid that had permeated into the acceptor circuit as the amount of polysorbate-80 increased were not statistically significant. Interestingly, the permeation coefficients calculated for experiments with no excipient were significantly higher than those in the comparative study performed at pH 7.4 without an FBS supplement. Once the concentration of polysorbate-80 had increased further, the findings from the comparative study at pH 7.4 were similar.

The pH and presence of an FBS supplement were the key differences between these studies. Although, due to implementing both changes at once, it would be difficult to pinpoint the individual contributions from each factor. Evaluation of the tissue and system rinse solutions would provide a better understanding on the effect of pH on the solubility of atorvastatin in the system. The amount of atorvastatin rinsed from the surface of the tissue disc was plotted against the amount of polysorbate-80 added to the donor circuit and displayed in Figure 4.42.

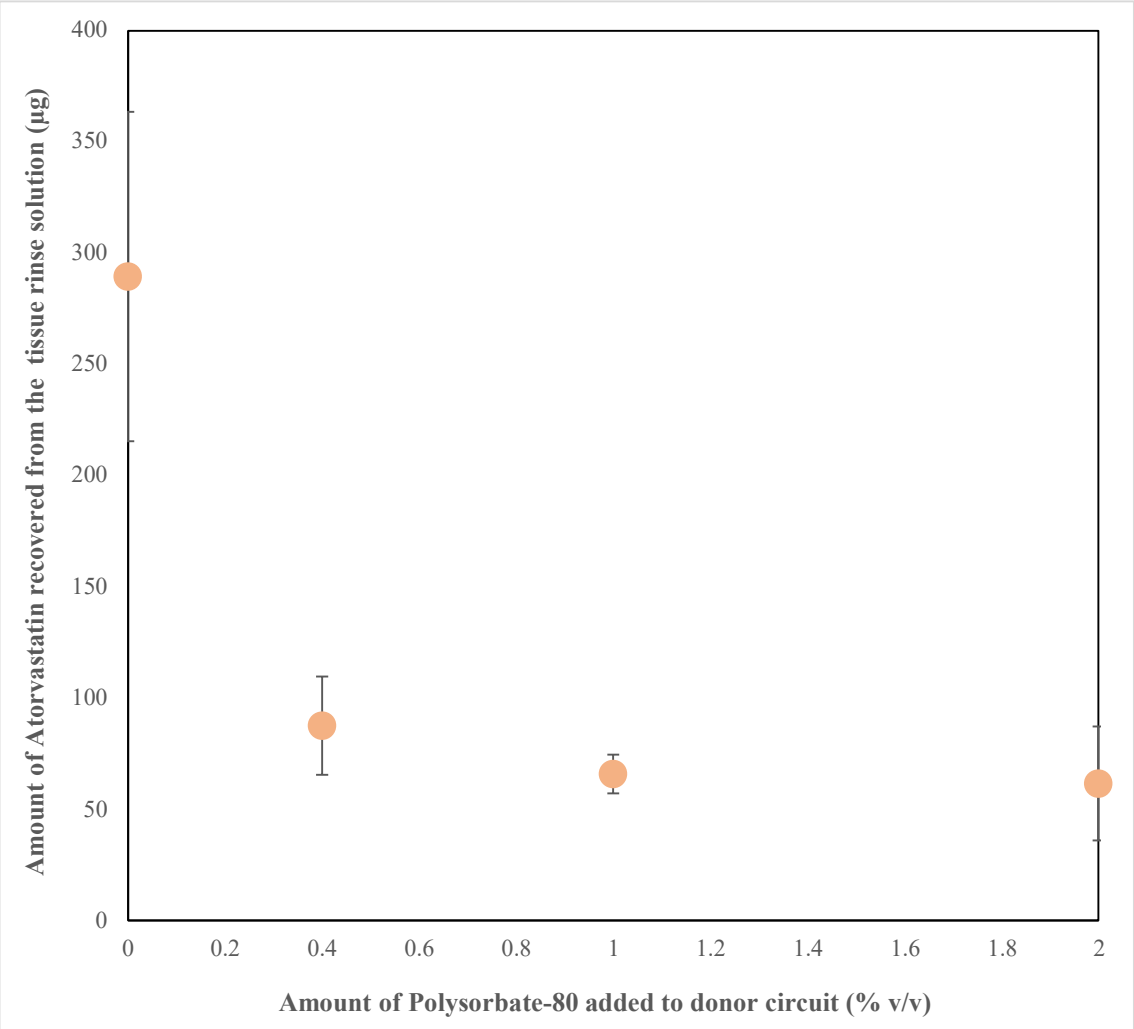

Figure 4.42: *A graph to show the amount of Atorvastatin that was rinsed from the tissue discs plotted against the concentration of Polysorbate-80 in the donor circuit (pH 6) of the corresponding absorption experiment. The data presented here is from the Polysorbate-80 only study performed at pH 6 (n=3).*

The general trend demonstrated here was that once polysorbate-80 was added to the system, the amount of atorvastatin that could be rinsed from the surface of the tissue

sharply declined. As the amount of polysorbate-80 was increased, an almost immediate plateau was reached. A one-way ANOVA with post-hoc Tukey HSD test corroborated this interpretation, identifying the data points with no excipient being significantly different to the others with a P value consistently less than 0.01. The trend and values given here were very similar to those acquired by the corresponding study performed at pH 7.4.

The effect of pH on the solubility of the atorvastatin within the system was explored further by plotting the amount of atorvastatin recovered from the drained system after each experiment against the corresponding amount of polysorbate-80 that was added to the donor circuit, see Figure 4.43.

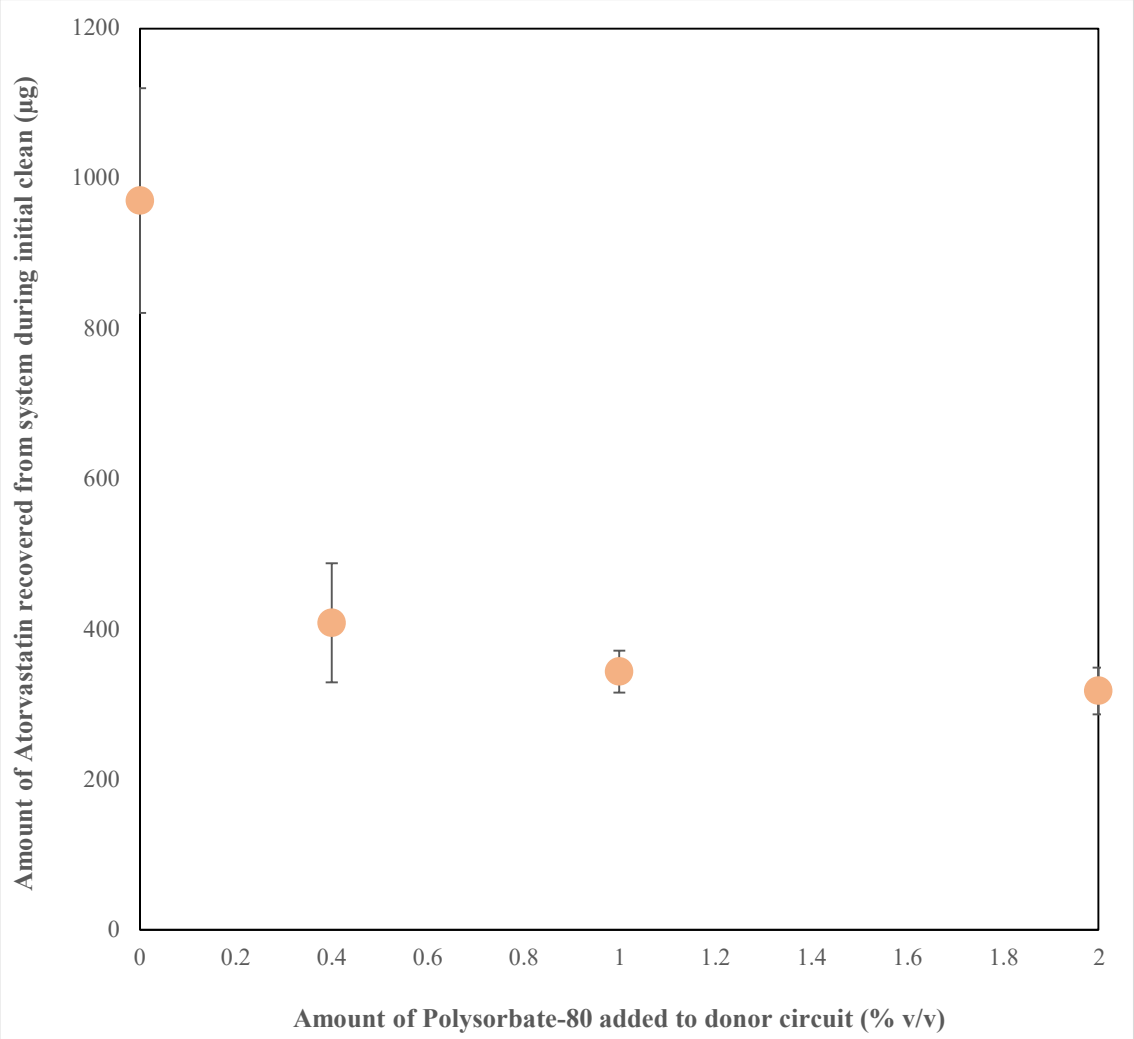

Figure 4.43: *A graph showing the amount of Atorvastatin that was recovered from the QV600 LLI after the system had been drained following an absorption experiment with varied amounts of Polysorbate-80 added to the donor circuit (buffered to pH 6). The data presented here is from the Polysorbate-80 only study performed at pH 6 (n=3).*

Similar trends were observed between the data acquired from the tissue and system rinse solutions. As polysorbate-80 was added to the donor circuit, there was a sharp decline in the amount of atorvastatin that was recovered from the system. As the concentration of polysorbate-80 was increased, the amount of atorvastatin that was recovered from the system continued to decline before quickly reaching a plateau. Again, this was corroborated by the one-way ANOVA with post-hoc Tukey HSD test with P values less 0.01. The trend shown was the same as that in the corresponding study performed at pH 7.4 and also, shared very similar data values. Therefore, in this instance, the change in pH 6 appeared to have an insignificant effect on the solubility of atorvastatin in the PBS.

The amount of atorvastatin acid that was recovered from the tissue extracts were plotted against the concentration of polysorbate-80 in the donor circuit and displayed below in Figure 4.44.

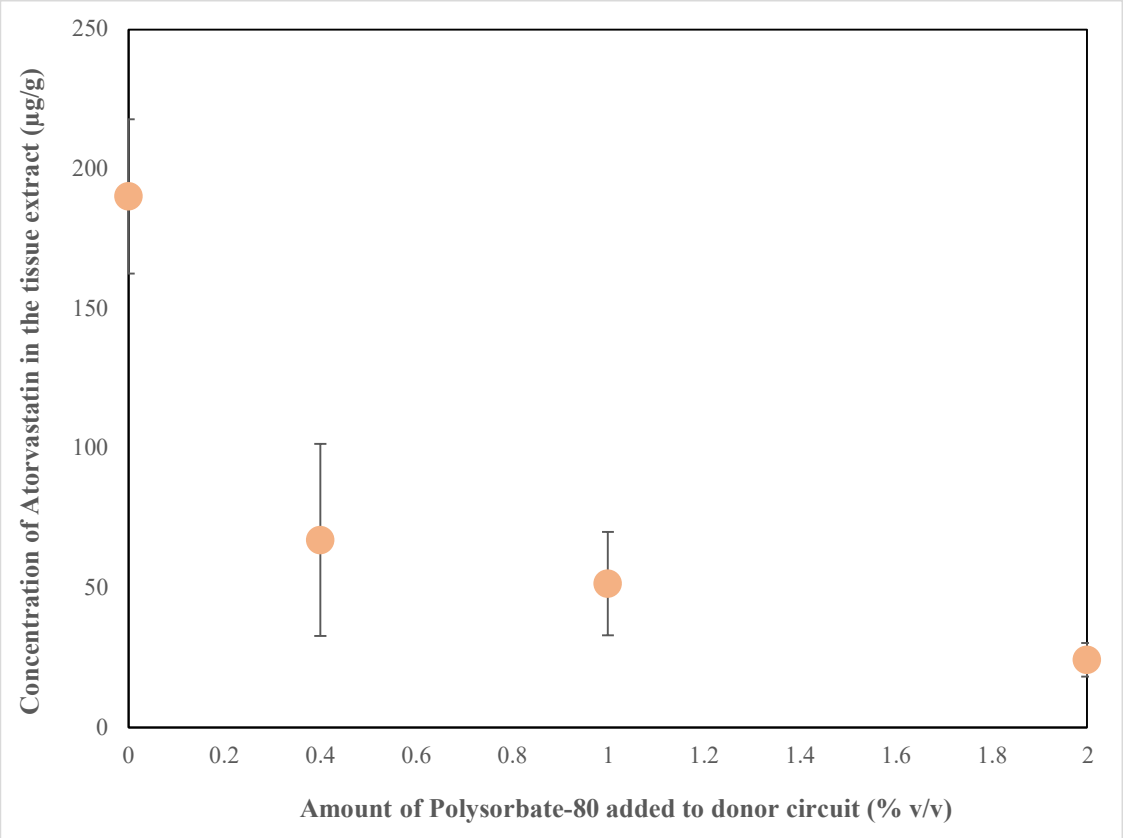

Figure 4.44: *A graph showing the concentration of Atorvastatin calculated from the tissue disc extract plotted against the corresponding amount of Polysorbate-80 that was added to the donor circuit (pH 6) for that absorption experiment. The data presented here is from the Polysorbate-80 only study performed at pH 6 (n=3).*

Once polysorbate-80 was added to the donor circuit, there was a significant reduction in the amount of atorvastatin acid that was recovered from the tissue extracts. As the concentration of polysorbate-80 was increased, the amount of atorvastatin acid detected in the tissue extract continued to steadily decline. A one-way ANOVA with post-hoc Tukey HSD test found that only the data points without polysorbate-80 were significantly different from the others with a P value less than 0.01. The trend described here was very similar to that of the comparative study performed at pH 7.4. Nevertheless, when no excipient was present in the donor circuit, less atorvastatin acid was recovered from the tissue extract during the pH 6 study when compared directly back to the pH 7.4 study. As the concentration of polysorbate-80 increased, the average amount of atorvastatin recovered from the tissue extract was slightly less than that shown in the comparative pH 7.4 study. A possible theory, given that the permeation was shown to be increased, was that the reduction of atorvastatin acid in the tissue relates to a reduction in the amount of atorvastatin acid accumulated in the tissue.

For further evaluation on the effects of pH, DESI images of atorvastatin acid and its common adducts were acquired from one of each replicate experiment in the study; see Figures 4.45-4.52.

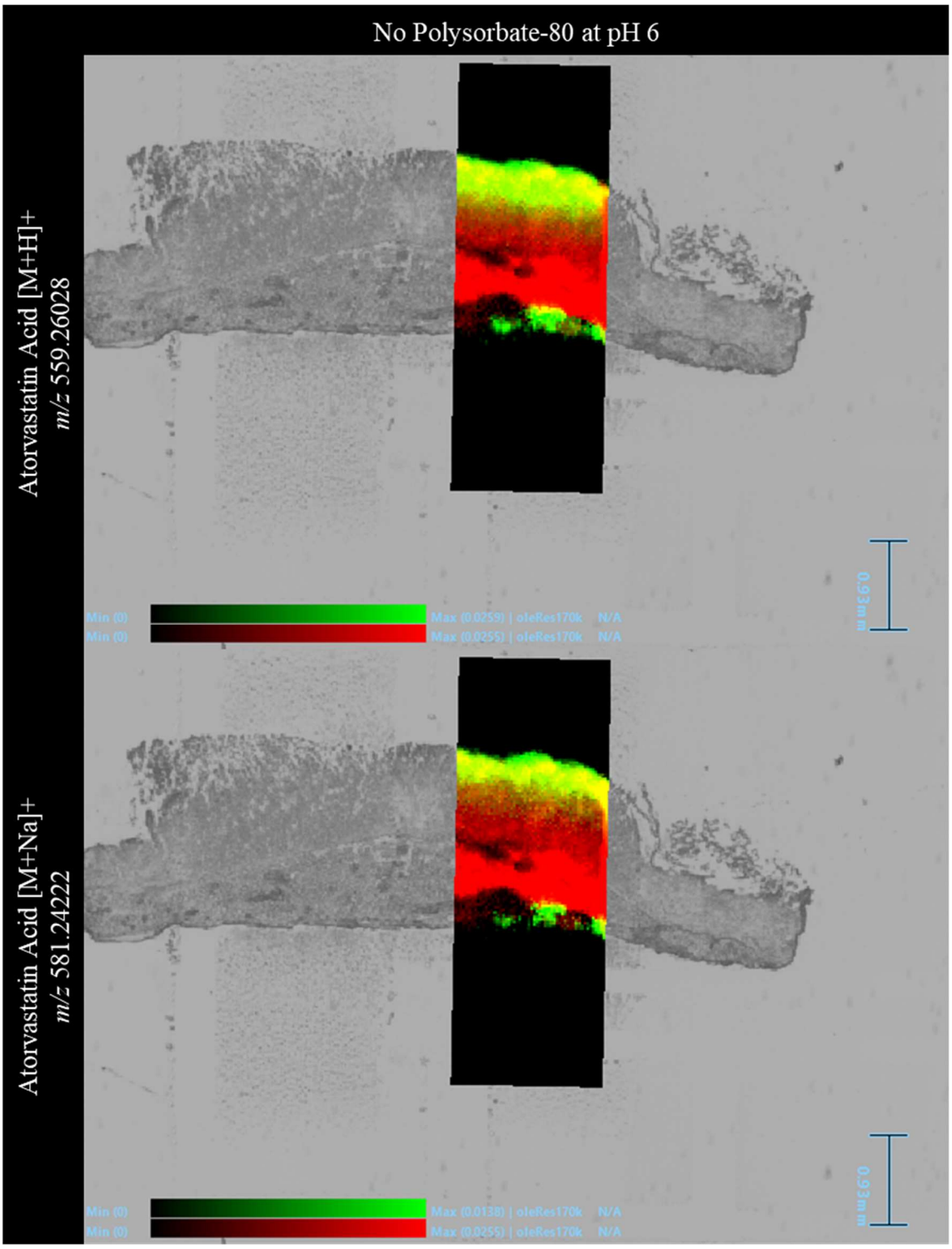

Figure 4.45: *DESI images overlaid onto an optical image of the tissue section they were acquired from with the surface of the tissue facing upwards. The tissue section was acquired from a fresh tissue absorption experiment with no polysorbate-80 in the donor circuit buffered to pH 6 and 10% FBS in the acceptor circuit. The distribution of the lipid ion m/z 780.5 has been displayed in a red colour scale. The distribution of protonated atorvastatin acid and its sodium adduct were shown in the top and bottom window, respectively, using a green colour scale. All identified drug related ions were well within 1ppm.*

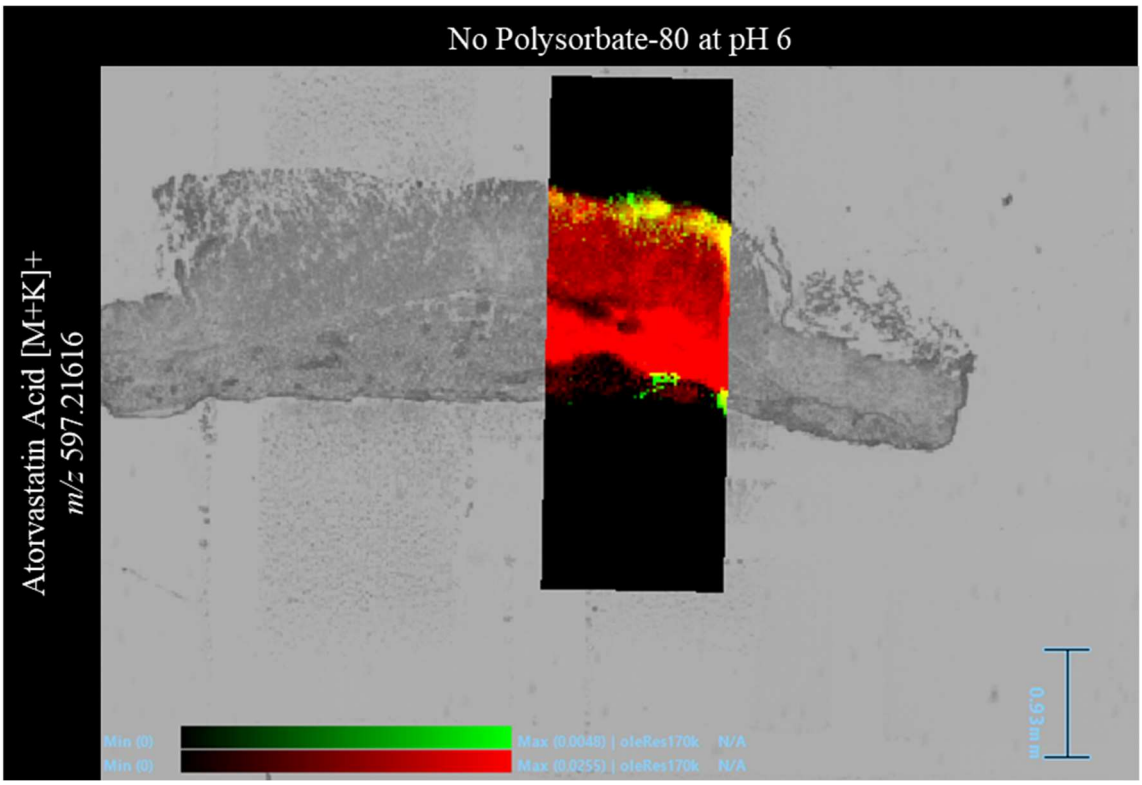

Figure 4.46: *A DESI image overlaid onto an optical image of the tissue section it was acquired from with the surface of the tissue facing upwards. The tissue section was acquired from a fresh tissue absorption experiment with no polysorbate-80 in the donor circuit buffered to pH 6 and 10% FBS in the acceptor circuit. The distribution of the lipid ion m/z 780.5 and the potassium adduct of atorvastatin acid were shown using a red and green colour scale, respectively. The drug related ion was within 1 ppm.*

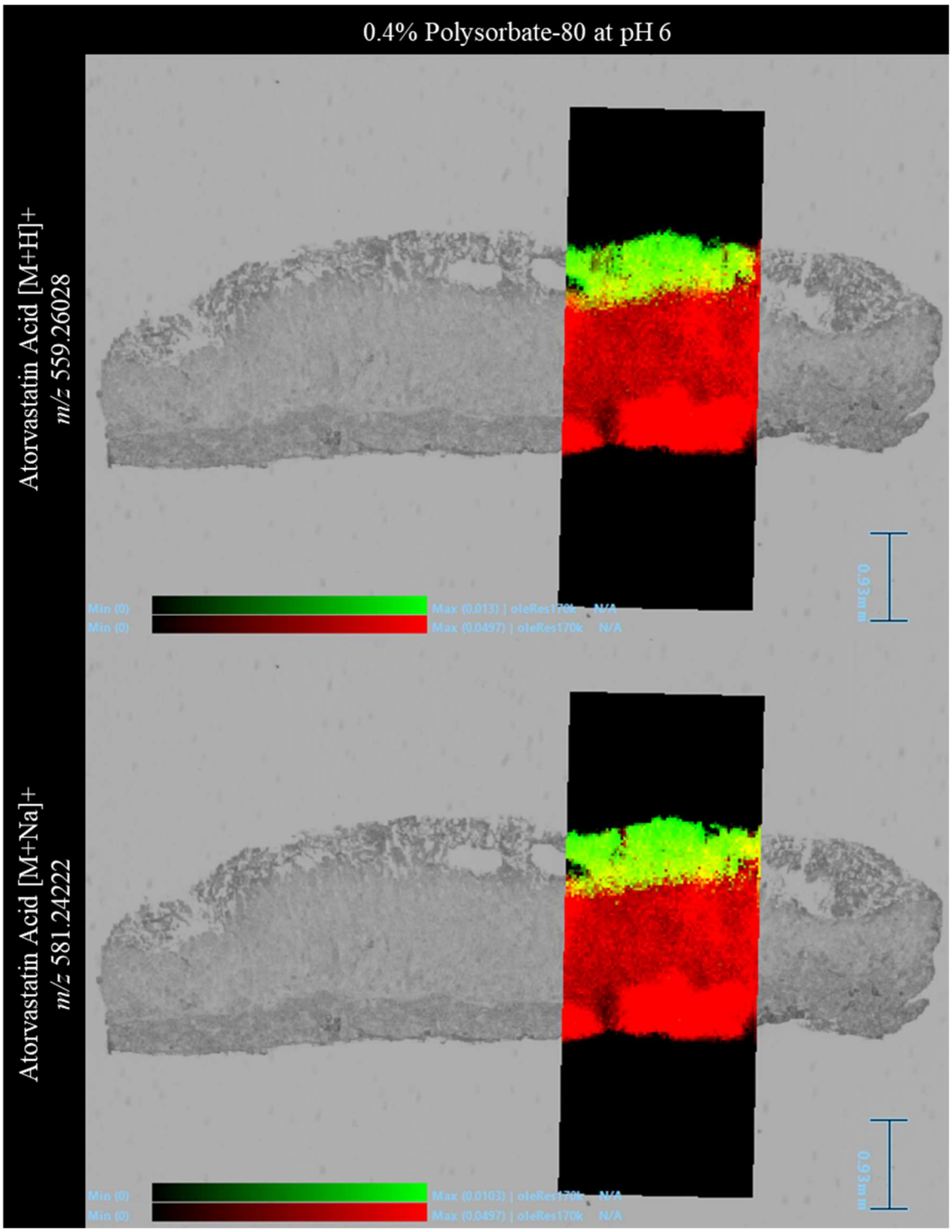

Figure 4.47: *DESI images overlaid onto an optical image of the tissue section they were acquired from with the surface of the tissue facing upwards. The tissue section was acquired from a fresh tissue absorption experiment with 0.4% polysorbate-80 in the donor circuit buffered to pH 6 and 10% FBS in the acceptor circuit. The distribution of the lipid ion m/z 780.5 has been displayed in a red colour scale. The distribution of protonated atorvastatin acid and its sodium adduct were shown in the top and bottom window, respectively, using a green colour scale. All identified drug related ions were within 1ppm.*

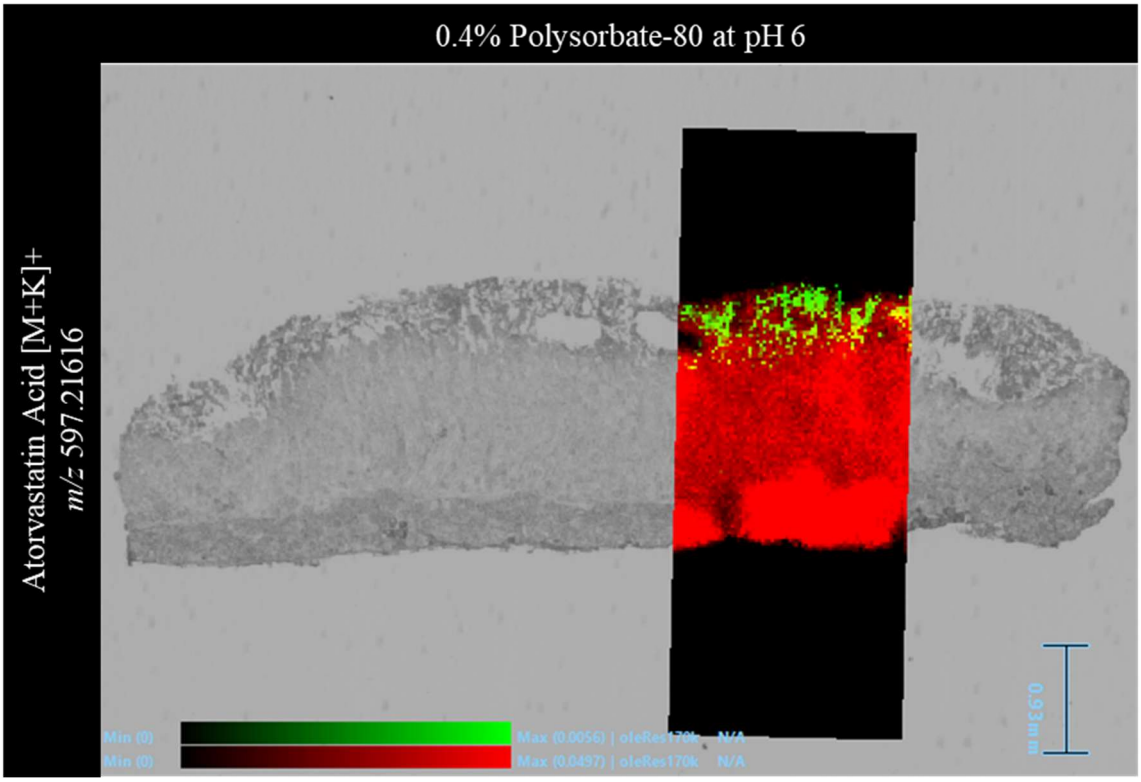

Figure 4.48: *A DESI image overlaid onto an optical image of the tissue section it was acquired from with the surface of the tissue facing upwards. The tissue section was acquired from a fresh tissue absorption experiment with 0.4% polysorbate-80 in the donor circuit buffered to pH 6 and 10% FBS in the acceptor circuit. The distribution of the lipid ion m/z 780.5 and the potassium adduct of atorvastatin acid were shown using a red and green colour scale, respectively. The drug related ion was within 1 ppm.*

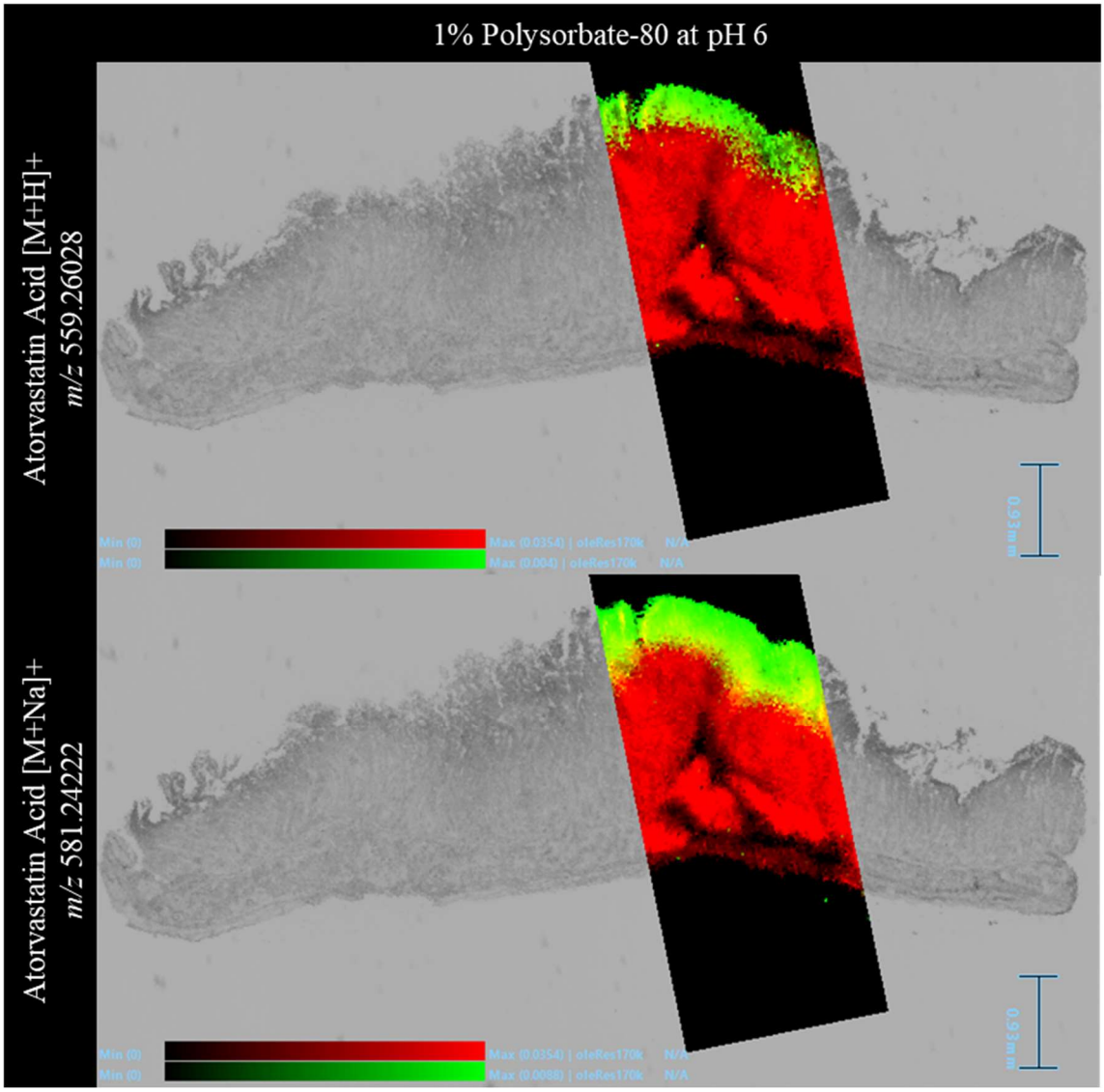

Figure 4.49: *DESI images overlaid onto an optical image of the tissue section they were acquired from with the surface of the tissue facing upwards. The tissue section was acquired from a fresh tissue absorption experiment with 1% polysorbate-80 in the donor circuit buffered to pH 6 and 10% FBS in the acceptor circuit. The distribution of the lipid ion m/z 780.5 has been displayed in a red colour scale. The distribution of protonated atorvastatin acid and its sodium adduct were shown in the top and bottom window, respectively, using a green colour scale. All identified drug related ions were within 1ppm.*

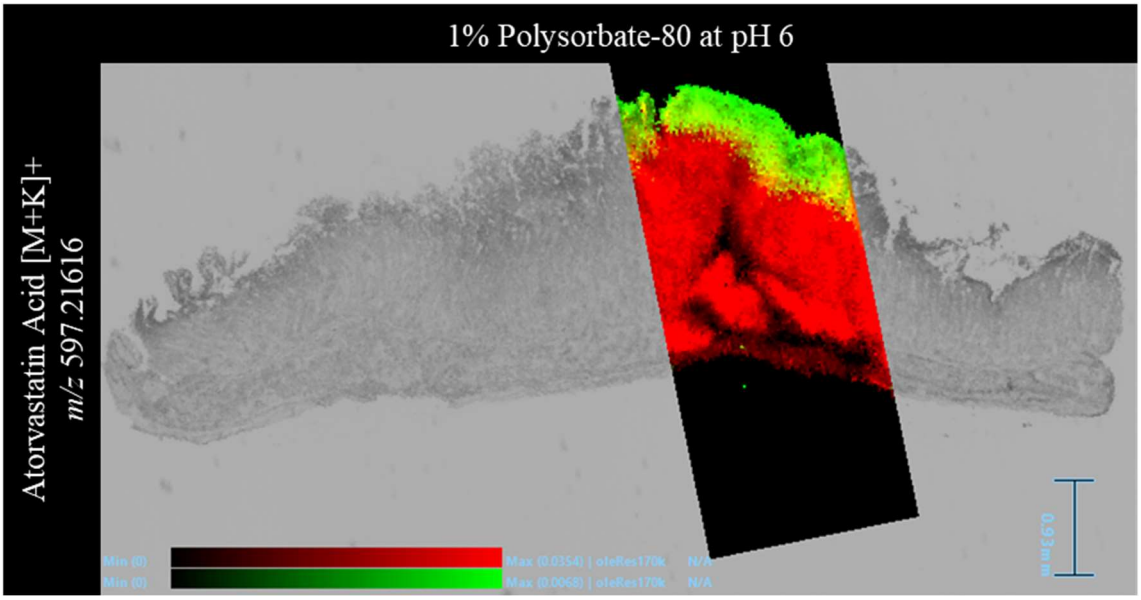

Figure 4.50: *A DESI image overlaid onto an optical image of the tissue section it was acquired from with the surface of the tissue facing upwards. The tissue section was acquired from a fresh tissue absorption experiment with 1% polysorbate-80 in the donor circuit buffered to pH 6 and 10% FBS in the acceptor circuit. The distribution of the lipid ion m/z 780.5 and the potassium adduct of atorvastatin acid were shown using a red and green colour scale, respectively. The drug related ion was within 1 ppm.*

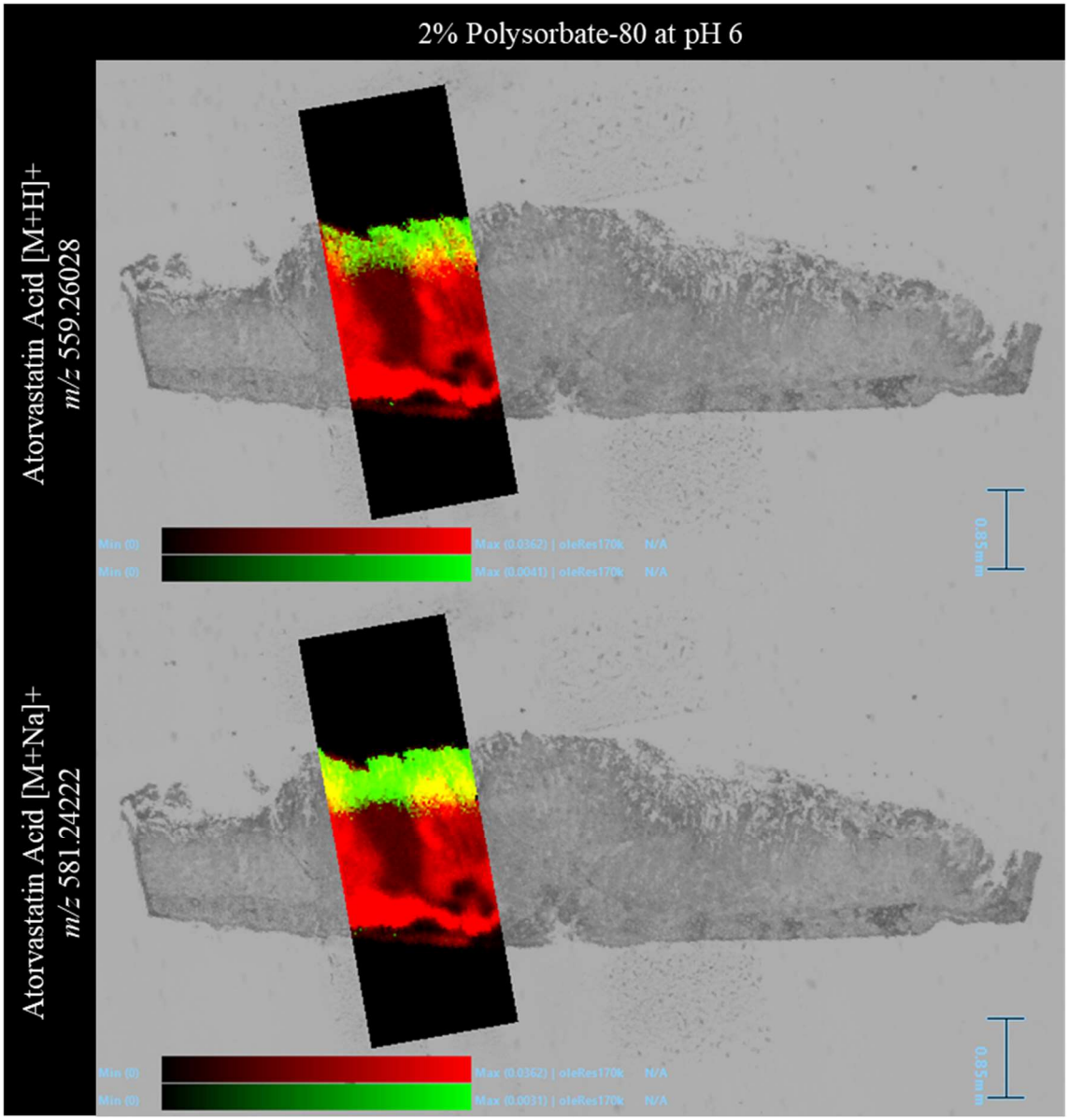

Figure 4.51: *DESI images overlaid onto an optical image of the tissue section they were acquired from with the surface of the tissue facing upwards. The tissue section was acquired from a fresh tissue absorption experiment with 2% polysorbate-80 in the donor circuit buffered to pH 6 and 10% FBS in the acceptor circuit. The distribution of the lipid ion m/z 780.5 has been displayed in a red colour scale. The distribution of protonated atorvastatin acid and its sodium adduct were shown in the top and bottom window, respectively, using a green colour scale. All identified drug related ions were within 1ppm.*

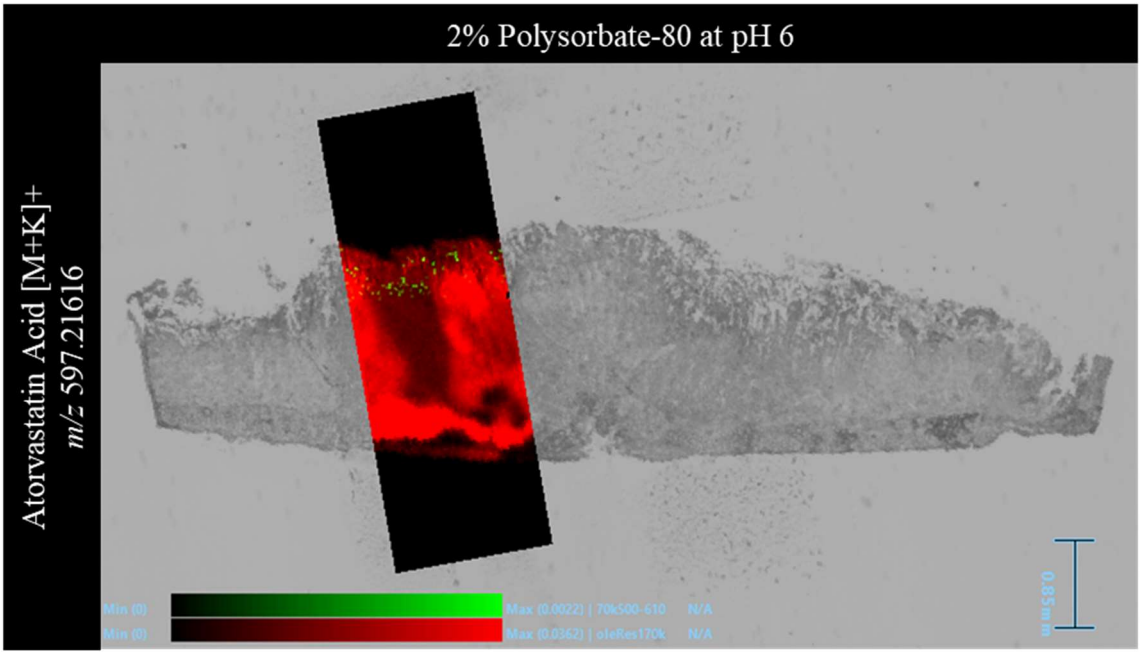

Figure 4.52: *A DESI image overlaid onto an optical image of the tissue section it was acquired from with the surface of the tissue facing upwards. The tissue section was acquired from a fresh tissue absorption experiment with 2% polysorbate-80 in the donor circuit buffered to pH 6 and 10% FBS in the acceptor circuit. The distribution of the lipid ion m/z 780.5 and the potassium adduct of atorvastatin acid were shown using a red and green colour scale, respectively. The drug related ion was within 1 ppm.*

The three most common atorvastatin acid adducts were all visible in the DESI images acquired from each experiment type in the study. The most intense signal throughout was the sodium adduct of atorvastatin acid. For this particular ion, the distribution spanned the entire surface of the tissue consistently and extended through a relatively small amount of the overall tissue thickness. In addition to this distribution, the experiment with no excipient showed a further localisation, sporadically positioned along the final layer of the tissue. This finding, combined with the knowledge of a more significant permeation coefficient compared to the others, suggested that the drug had permeated through the tissue. Nevertheless, the same could not be said for the rest of the DESI images collected from this study although their permeation coefficient values were not too dissimilar.

With reference back to the tissue extract values acquired for this study, the tissue discs from experiments with no added excipient consistently contained the highest amount of atorvastatin acid per gram of tissue. This could be linked back to the theory that limits of sensitivity were being tested for this particular instrument. While the occasional

sparse pixel representing atorvastatin acid were seen deep within the tissue section, this was not the case for the DESI image with the drug distributed on the surface and final tissue layers. Several ROIs were drawn on the DESI images to determine whether any atorvastatin acid adducts could be detected away from the main drug distribution. The results of this investigation were summarised in Table 4.8 and the specific location of each ROI have been detailed in Appendix I Figure 13-16.

Table 4.8: *A summary of whether the named atorvastatin related ions were detectable in different ROIs in the DESI image. The ROIs specified here included the whole tissue, an area on the tissue with no drug signal and an area away from the tissue. All data here relates to DESI images collected from the polysorbate-80 study performed at pH 6.*

Polysorbate-80 Only Study at pH 6					
Atorvastatin and Related Ions	ROI	Ion present in ROI? Concentration of Polysorbate-80 (% v/v)			
		0	0.4	1	2
Atorvastatin Acid $[M+H]^+$ *m/z* 559.26028	Whole tissue?	✓	✓	✓	✓
	Within tissue away from drug distribution?	✓	×	×	×
	Away from tissue?	×	×	×	×
Atorvastatin Acid $[M+Na]^+$ *m/z* 581.24222	Whole tissue?	✓	✓	✓	✓
	Within tissue away from drug distribution?	✓	×	×	×
	Away from tissue?	×	×	×	×
Atorvastatin Acid $[M+K]^+$ *m/z* 597.21616	Whole tissue?	✓	✓	✓	✓
	Within tissue away from drug distribution?	✓	×	×	×
	Away from tissue?	×	×	×	×
Atorvastatin Acid $[M+2Na-H]^+$ *m/z* 603.22416	Whole tissue?	×	✓	✓	×
	Within tissue away from drug distribution?	×	×	×	×
	Away from tissue?	×	×	×	×

The three main adducts of atorvastatin were successfully detected in the ROI which was drawn away from the pixels indicative of atorvastatin acid. The presence of these ions was confirmed by the high mass accuracy of the instrument, which allowed the mass error to be kept consistently under 1 ppm. In addition to this, an ROI taken on an area away from the tissue section corroborated that these ions were not present on the slide and were therefore, unlikely to be contaminants or background.

No atorvastatin acid ions were detected in the ROI away from the main drug distribution for the experiments that had polysorbate-80 added to the donor circuit. The concentration of atorvastatin acid per gram of tissue from these experiments was significantly lower than those that were detectable. This supports the theory that sensitivity limits of the instrument were exceeded in this environment. Further work would be recommended to establish the limits for this scenario as well as confirm this hypothesis.

The DESI images from this study were checked for all known atorvastatin metabolites. The metabolites that were able to be visualised using the same processing parameters have been displayed in Figure 4.53-4.55.

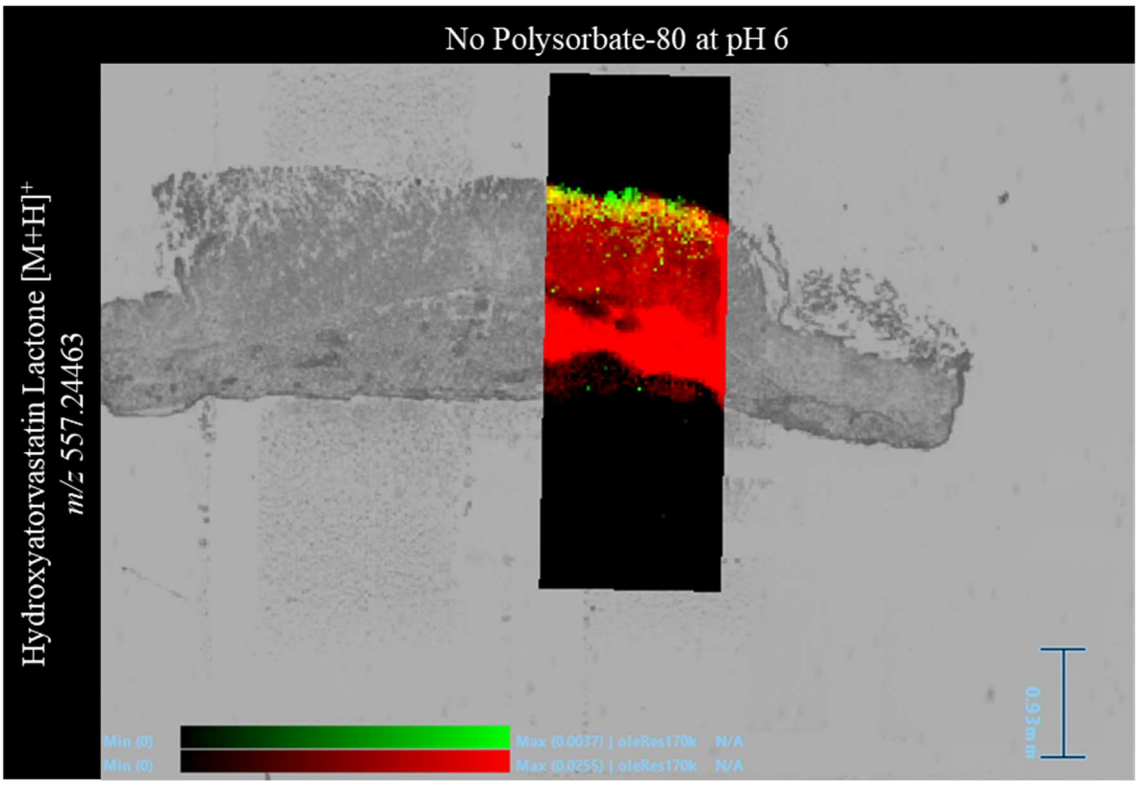

Figure 4.53: *DESI image overlaid onto an optical image of the tissue section it was acquired from with the surface of the tissue facing upwards. The tissue section was acquired from a fresh tissue absorption experiment with no polysorbate-80 in the donor circuit buffered to pH 6 and 10% FBS in the acceptor circuit. The distribution of the lipid ion m/z 780.5 and protonated metabolite Hydroxyatorvastatin lactone was displayed in a red and green colour scale, respectively. The metabolite ion was within 1 ppm.*

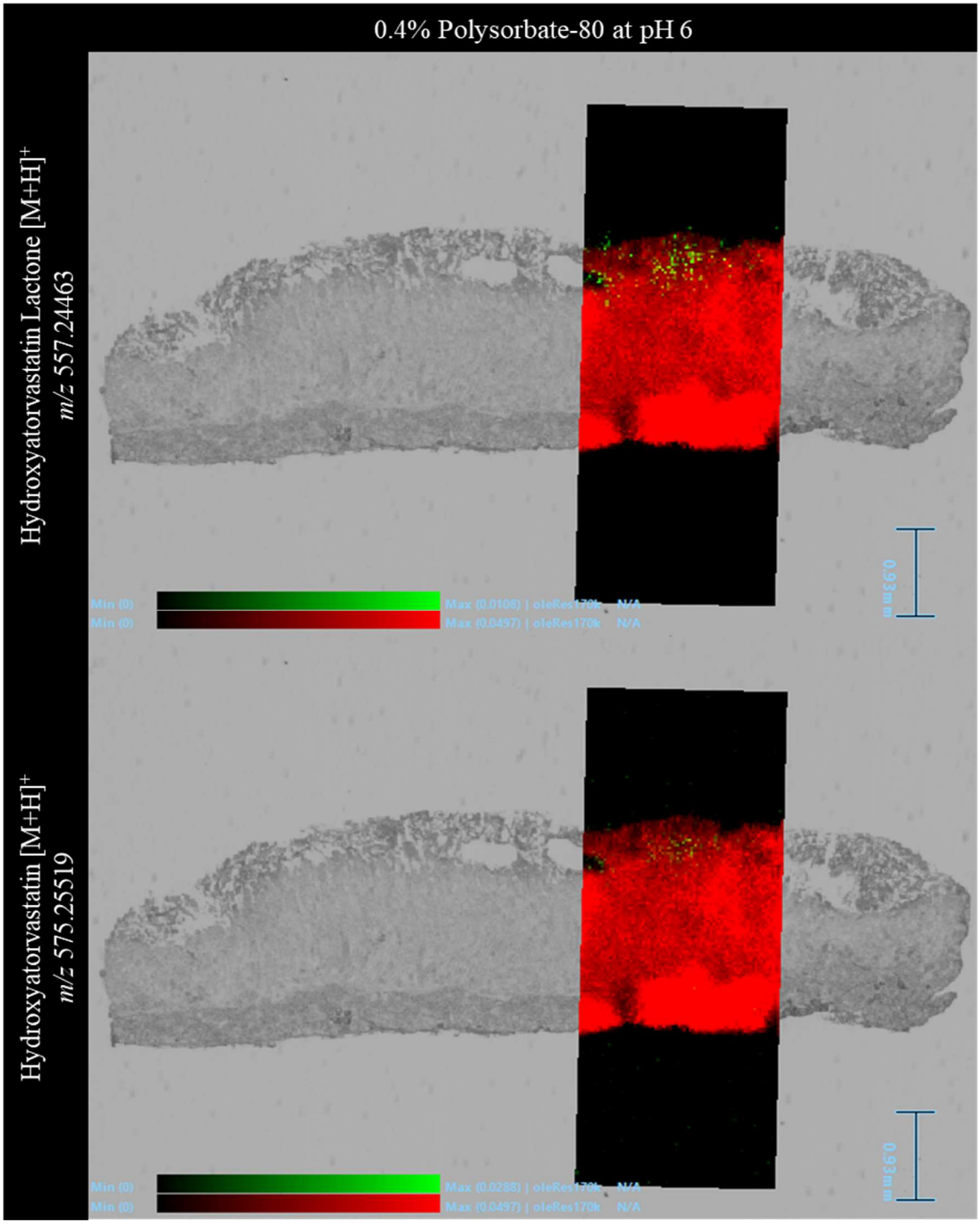

Figure 4.54: *DESI images overlaid onto an optical image of the tissue section they were acquired from with the surface of the tissue facing upwards. The tissue section was acquired from a fresh tissue absorption experiment with 0.4% polysorbate-80 in the donor circuit buffered to pH 6 and 10% FBS in the acceptor circuit. The distribution of the lipid ion m/z 780.5 has been displayed in a red colour scale. The distribution of protonated metabolites Hydroxyatorvastatin lactone and hydroxyatorvastatin were shown in the top and bottom window, respectively, using a green colour scale. The metabolite ion was within 1 ppm.*

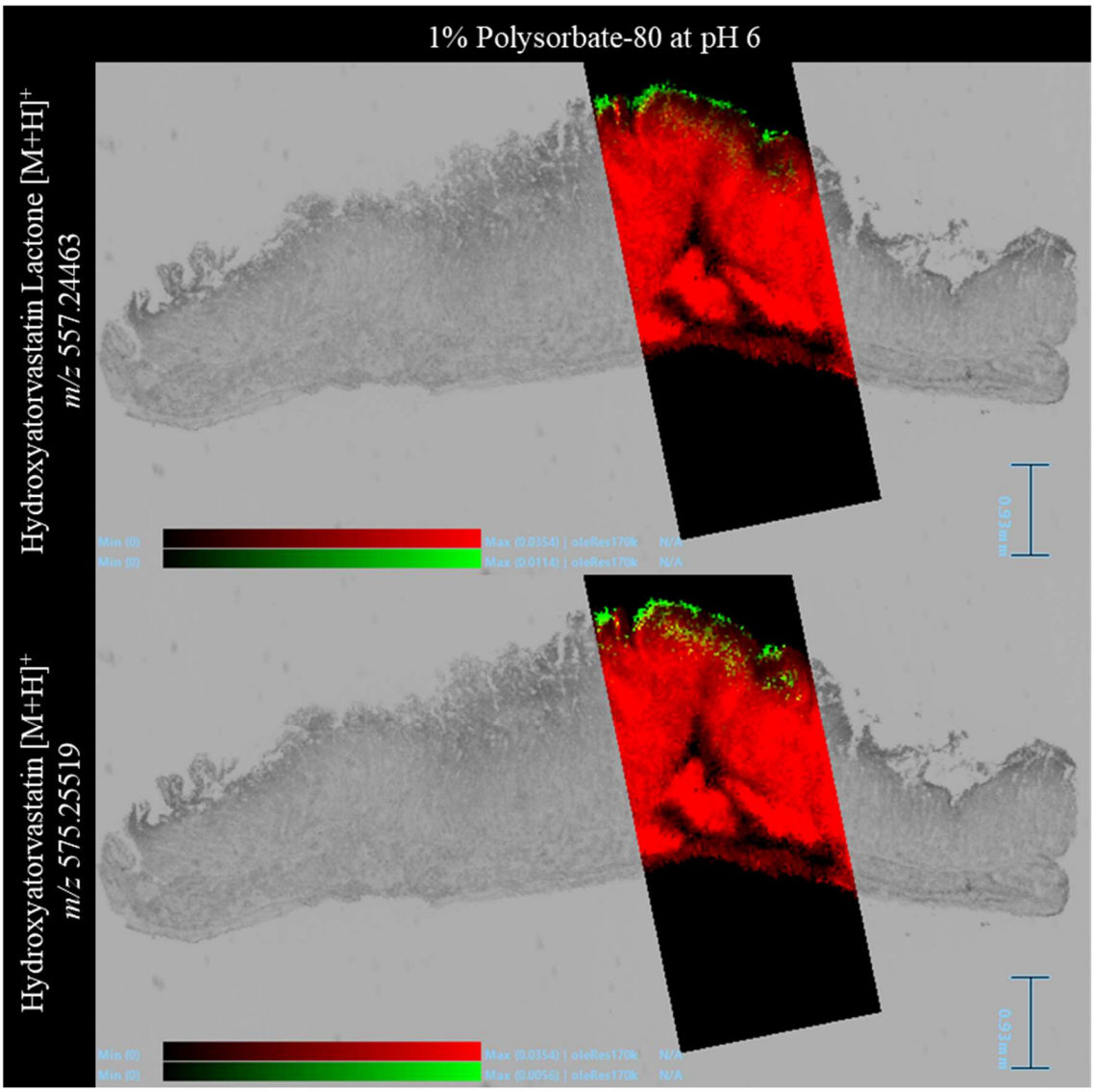

Figure 4.55: *DESI images overlaid onto an optical image of the tissue section they were acquired from with the surface of the tissue facing upwards. The tissue section was acquired from a fresh tissue absorption experiment with 1% polysorbate-80 in the donor circuit buffered to pH 6 and 10% FBS in the acceptor circuit. The distribution of the lipid ion m/z 780.5 has been displayed in a red colour scale. The distribution of protonated metabolites hydroxyatorvastatin lactone and hydroxyatorvastatin were shown in the top and bottom window, respectively, using a green colour scale. The metabolite ion was within 1 ppm.*

The metabolite hydroxyatorvastatin lactone was visualised consistently in the tissue sections from experiments with 0-1% polysorbate-80 in the donor circuit. For experiments with 0.4% and 1% polysorbate-80, both Hydroxyatorvastatin and Hydroxyatorvastatin lactone distribution could be seen. In comparison to the relative

distributions of atorvastatin acid, the metabolites were present in a similar area but much more sparsely, spanning a smaller surface area. Interestingly, in the experiment with no excipient added, hydroxyatorvastatin lactone was shown to permeate deeper into the tissue than the atorvastatin acid. This pattern was not seen with any of the other metabolite images.

ROIs were drawn on the tissue in areas away from pixels indicating atorvastatin metabolites were present. These were compared to other ROIs representing the whole tissue and areas away from the visual drug distribution to determine whether lower levels could be detected in the spectra. The results of this investigation were summarised in Table 4.9 and the specific location of each ROI have been detailed in Appendix I Figure 13-16. There were a few instances in which metabolites were detectable and successfully identified in the ROIs away from the visual drug distribution. While hydroxyatorvastatin lactone was a commonly identified metabolite in this and previous studies, its predecessor, atorvastatin lactone, was detectable for the first time. The protonated ion was detected in the whole tissue ROI in addition to the area away from the obvious drug distribution. In hindsight, quantification of all metabolites in tissue extracts by LC-MS/MS would have provided valuable information on the presence of less abundant metabolites in which perhaps the DESI MS imaging method, cannot.

Table 4.9: *A summary of whether the named atorvastatin metabolites were detectable in different ROIs in the DESI image. The ROIs specified here included the whole tissue, an area on the tissue with no drug signal and an area away from the tissue. All data here relates to DESI images collected from the polysorbate-80 study performed at pH 6.*

Polysorbate-80 Only Study at pH 6					
Atorvastatin Metabolites	ROI	Ion present in ROI? Concentration of Polysorbate-80 (% v/v)			
		0	0.4	1	2
Hydroxyatorvastatin $[M+H]^+$ *m/z* 575.25519	Whole tissue?	×	✓	✓	×
	Within tissue away from drug distribution?	×	×	×	×
	Away from tissue?	×	×	×	×
Hydroxyatorvastatin $[M+Na]^+$ *m/z* 597.23713	Whole tissue?	✓	✓	×	×
	Within tissue away from drug distribution?	×	✓	×	×
	Away from tissue?	×	×	×	×
Atorvastatin Lactone $[M+H]^+$ *m/z* 541.249712	Whole tissue?	✓	×	×	✓
	Within tissue away from drug distribution?	×	×	×	✓
	Away from tissue?	×	×	×	×
Atorvastatin Lactone $[M+Na]^+$ *m/z* 563.231654	Whole tissue?	×	×	✓	×
	Within tissue away from drug distribution?	×	×	×	×
	Away from tissue?	×	×	×	×
Hydroxyatorvastatin Lactone $[M+H]^+$ *m/z* 557.24463	Whole tissue?	✓	✓	✓	✓
	Within tissue away from drug distribution?	✓	×	×	×
	Away from tissue?	×	×	×	×

4.4.3.2 DEGEE LQ Combined with 0.4% Polysorbate-80

With improvements seen in the permeation coefficient values for non-formulated atorvastatin in the previous study (when changes were made to the pH and acceptor circuit composition) the DEGEE LQ study with 0.4% polysorbate-80 was repeated implementing these changes. The permeation coefficient values for this study were plotted against the concentration of DEGEE LQ added to the donor circuit with 0.4% polysorbate-80, see Figure 4.56.

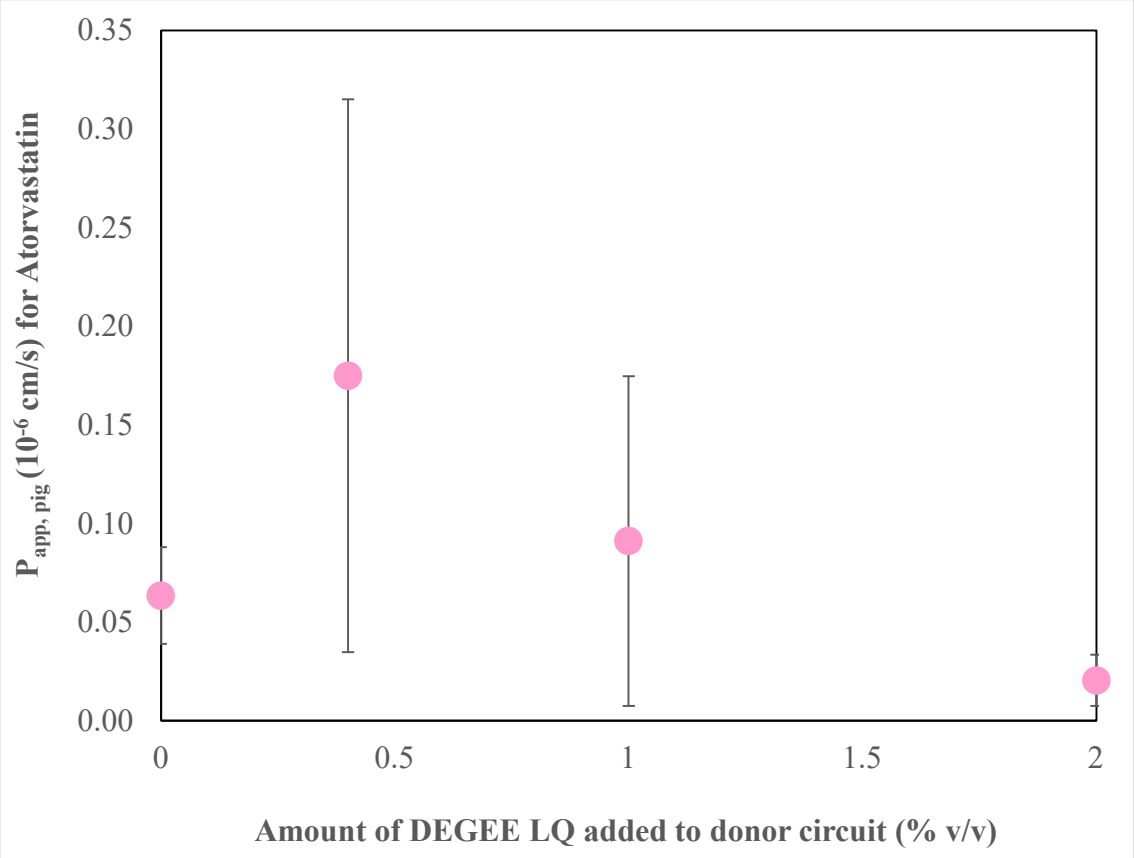

Figure 4.56: *A graph showing the $P_{app,pig}$ values plotted against the concentration of DEGEE LQ added to 0.4% Polysorbate-80 in the donor circuit (pH 6) of the corresponding absorption experiment. The data presented here is from the DEGEE with 0.4 % (v/v) Polysorbate-80 study performed at pH 6 (n=3).*

Once 0.4% DEGEE LQ was added to the donor circuit in the presence of polysorbate-80, there was a general rise in the amount of atorvastatin acid that had relatively permeated into the acceptor circuit. With increasing concentrations of DEGEE LQ, the amount of atorvastatin acid that had permeated into the acceptor circuit began to decline. Despite this visual trend, a one-way ANOVA test found no statistically

significant differences. A similar pattern was seen in the comparative study performed at pH 7.4 (with exception to the apparent outlier). However, the permeation coefficients of atorvastatin acid calculated in the pH 6 study, as a collective, were significantly higher than those reported in the pH 7.4 study. This finding strongly suggests that for this formulation, the changes made to pH 6 and the addition of supplements to the acceptor circuit had improved the permeation of atorvastatin acid through the duodenum tissue.

Furthermore, the trend seen with the Papp,pig values ascertained for the pH 6 study were seemingly reflected in the tissue extracts from that same study. The concentration of atorvastatin acid calculated per gram of tissue from the tissue extractions were plotted against the concentration of DEGEE LQ that was present in the donor circuit along with 0.4% polysorbate-80; shown in Figure 4.57.

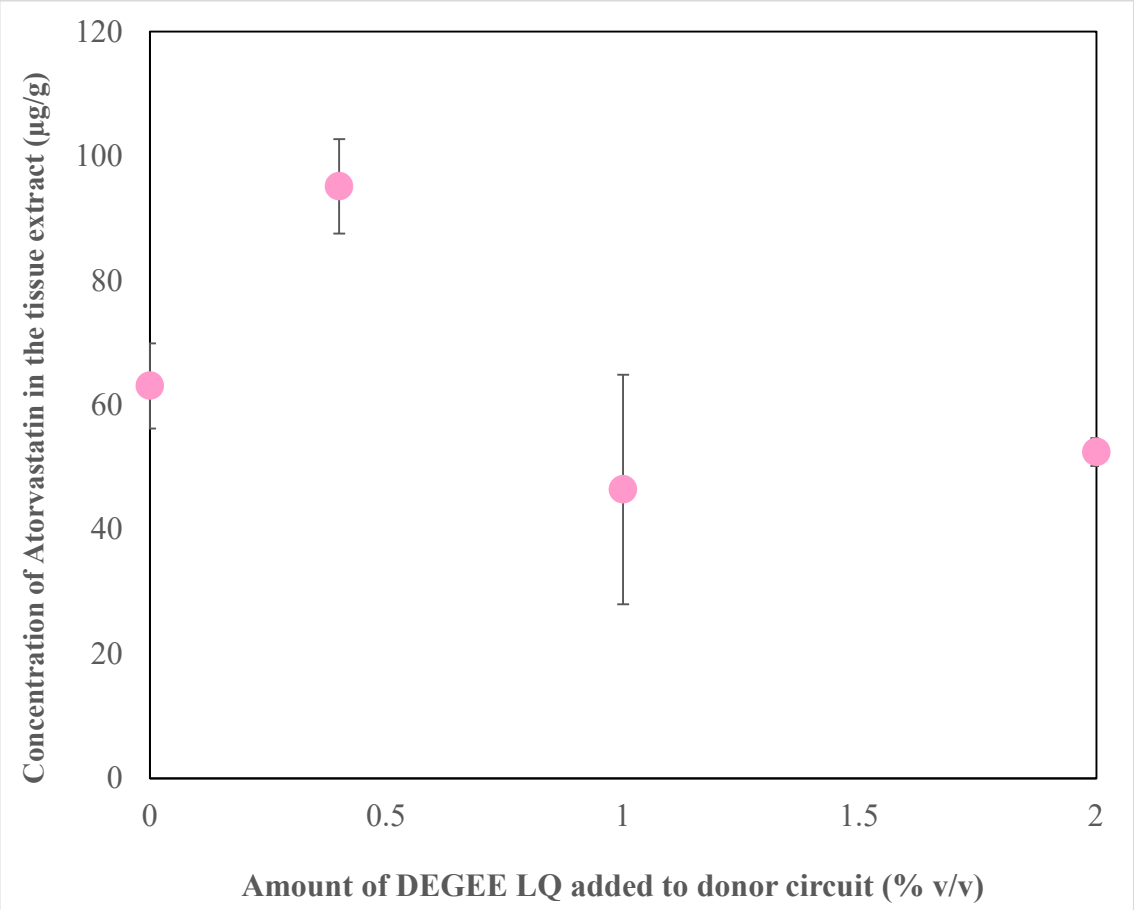

Figure 4.57: *A graph showing the concentration of Atorvastatin calculated from the tissue disc extract plotted against the corresponding amount of DEGEE LQ that was added to the donor circuit (pH 6) for that absorption experiment. The data presented here is from the DEGEE with 0.4 % (v/v) Polysorbate-80 study performed at pH 6 (n=3).*

When 0.4% DEGEE LQ was added to the donor circuit with polysorbate-80 present, there was increase in the amount of atorvastatin acid that was recovered from the tissue extracts. As the concentration of DEGEE LQ was increased, the amount of atorvastatin acid recovered from the tissue extracts reduced and appeared to have quickly reached a plateau. A one-way ANOVA with post-hoc Tukey HSD test found that 0.4% DEGEE was significantly different from the others with a P value less than 0.05. From the analysis of both the acceptor circuit fluid and the tissue extracts, it would appear that 0.4% DEGEE LQ and 0.4% polysorbate-80 at pH 6 was optimal for drug permeation. Despite this, the same trend was not reflected in the DESI images collected for the study. The most common adducts of atorvastatin acid were visualised in the tissue sections from each experiment type in the study using the same processing parameters; the DESI images acquired were collated in Figures 4.58-4.65.

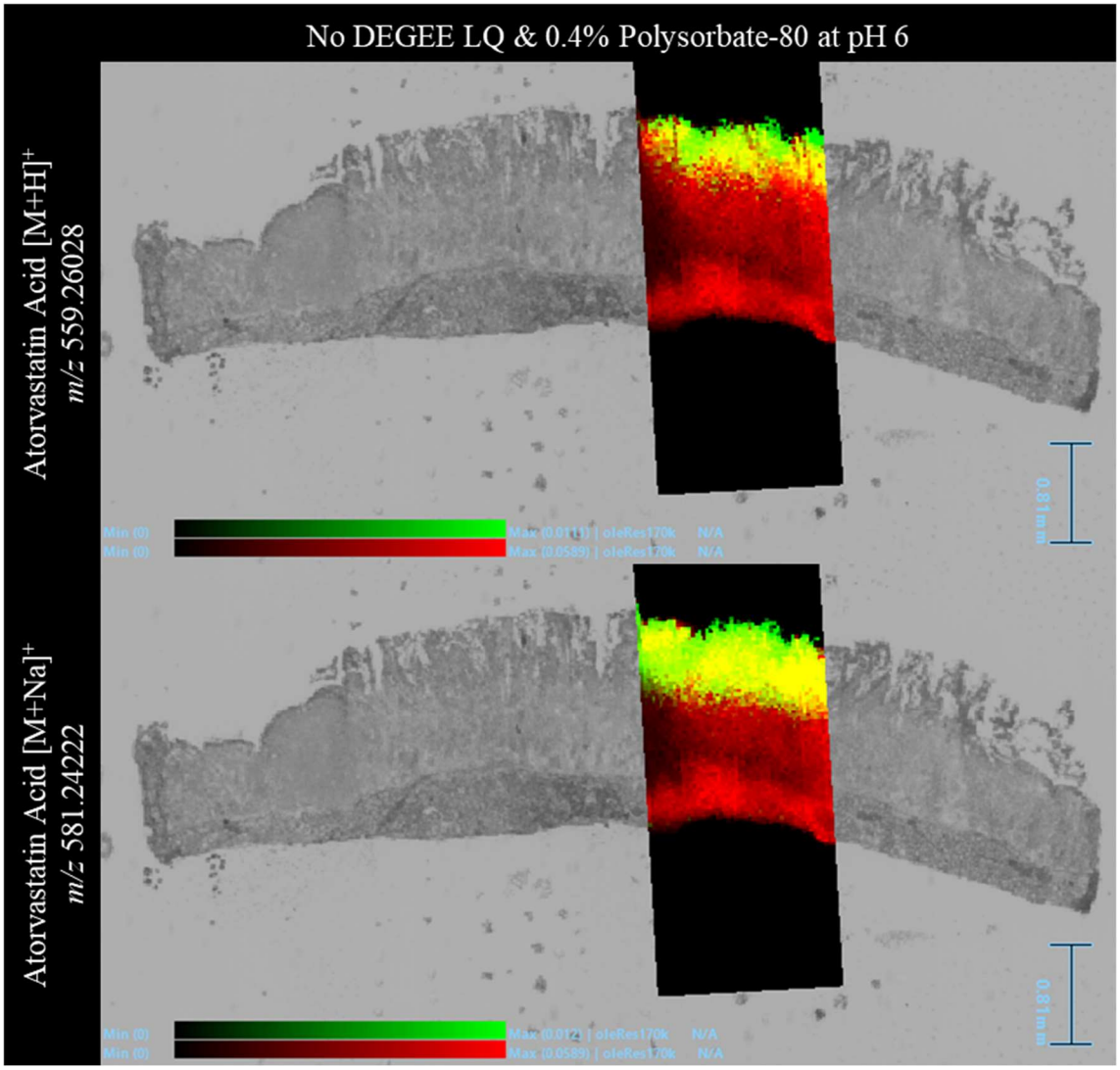

Figure 4.58: *DESI images overlaid onto an optical image of the tissue section they were acquired from with the surface of the tissue facing upwards. The tissue section was acquired from a fresh tissue absorption experiment with 0.4% polysorbate-80 in the donor circuit buffered to pH 6 and 10% FBS in the acceptor circuit. The distribution of the lipid ion m/z 780.5 has been displayed in a red colour scale. The distribution of protonated atorvastatin acid and its sodium adduct were shown in the top and bottom window, respectively, using a green colour scale. All identified drug related ions were within 1ppm.*

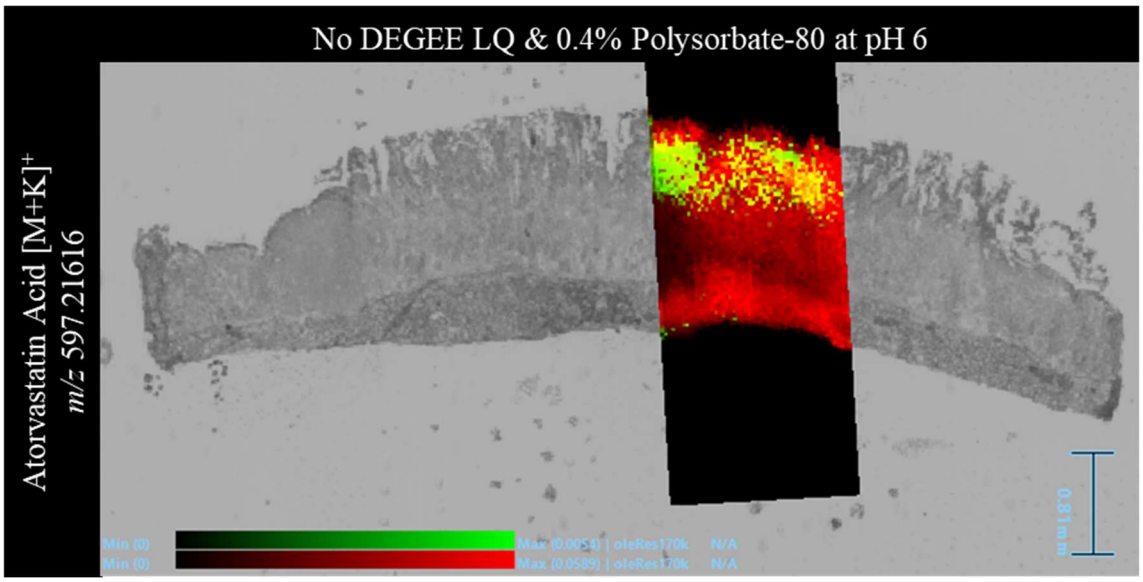

Figure 4.59: *DESI image overlaid onto an optical image of the tissue section it was acquired from with the surface of the tissue facing upwards. The tissue section was acquired from a fresh tissue absorption experiment with 0.4% polysorbate-80 in the donor circuit buffered to pH 6 and 10% FBS in the acceptor circuit. The distribution of the lipid ion m/z 780.5 and the potassium adduct of atorvastatin acid were displayed in a red and green colour scale, respectively. The identified drug ion was within 1 ppm.*

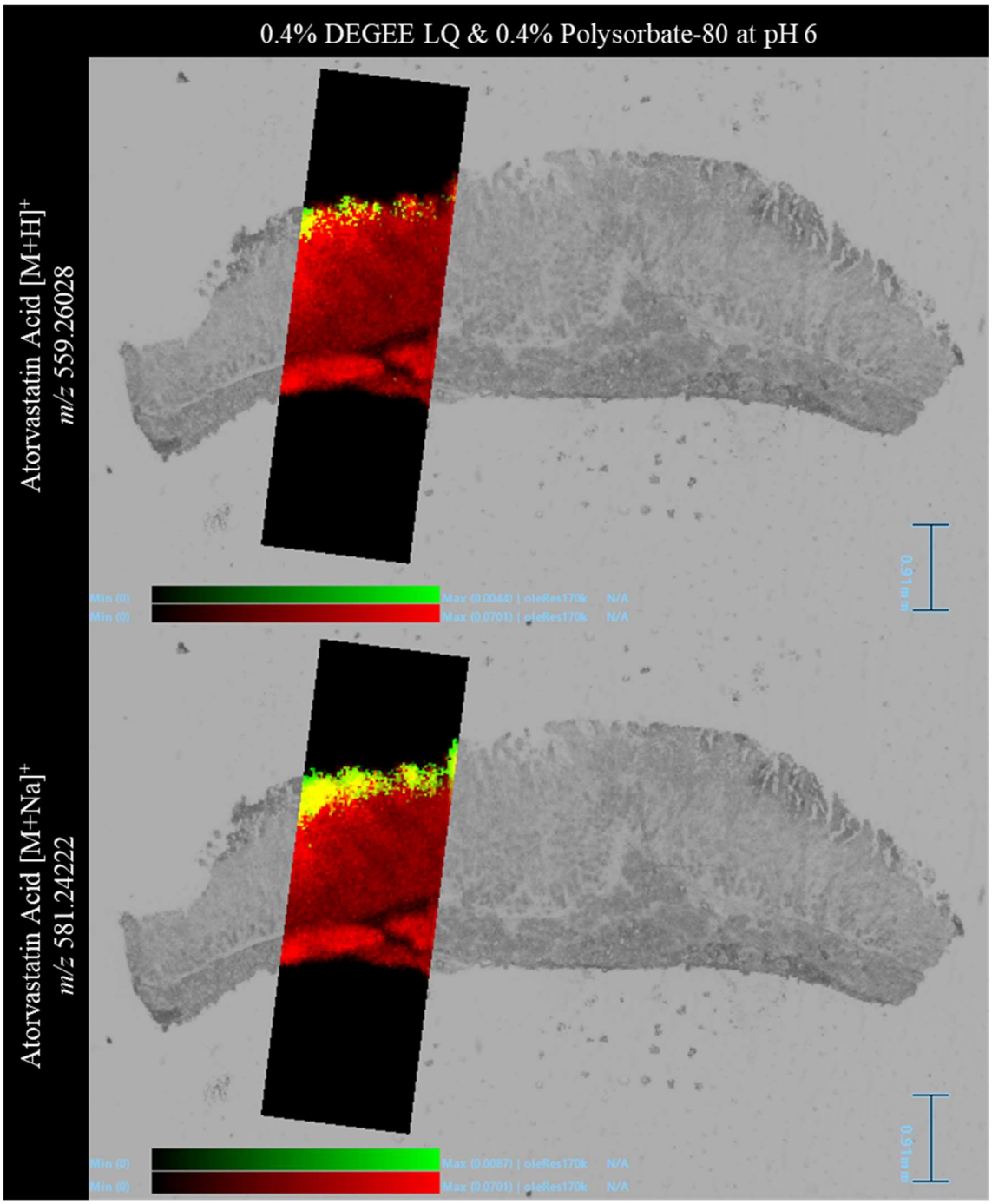

Figure 4.60: *DESI images overlaid onto an optical image of the tissue section they were acquired from with the surface of the tissue facing upwards. The tissue section was acquired from a fresh tissue absorption experiment with 0.4% DEGEE LQ and 0.4% polysorbate-80 in the donor circuit buffered to pH 6 and 10% FBS in the acceptor circuit. The distribution of the lipid ion m/z 780.5 has been displayed in a red colour scale. The distribution of protonated atorvastatin acid and its sodium adduct were shown in the top and bottom window, respectively, using a green colour scale. All identified drug related ions were within 1ppm.*

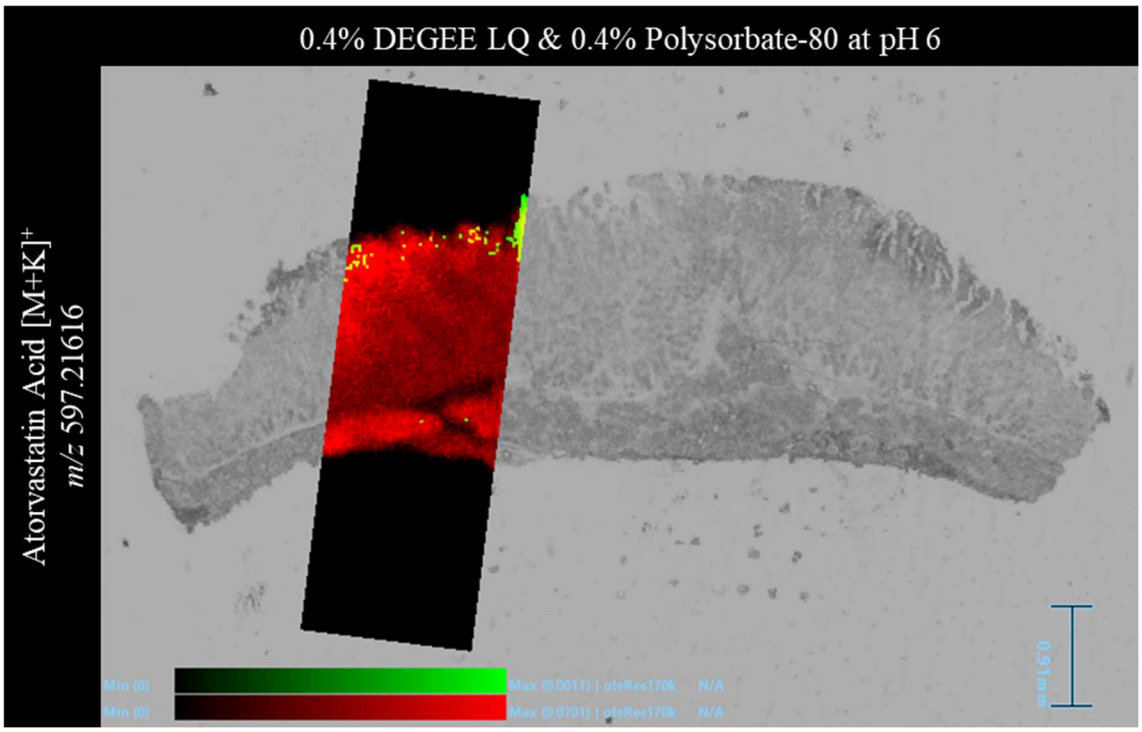

Figure 4.61: *DESI image overlaid onto an optical image of the tissue section it was acquired from with the surface of the tissue facing upwards. The tissue section was acquired from a fresh tissue absorption experiment with 0.4% DEGEE LQ and 0.4% polysorbate-80 in the donor circuit buffered to pH 6 and 10% FBS in the acceptor circuit. The distribution of the lipid ion m/z 780.5 and the potassium adduct of atorvastatin acid were displayed in a red and green colour scale, respectively. The identified drug ion was within 1 ppm.*

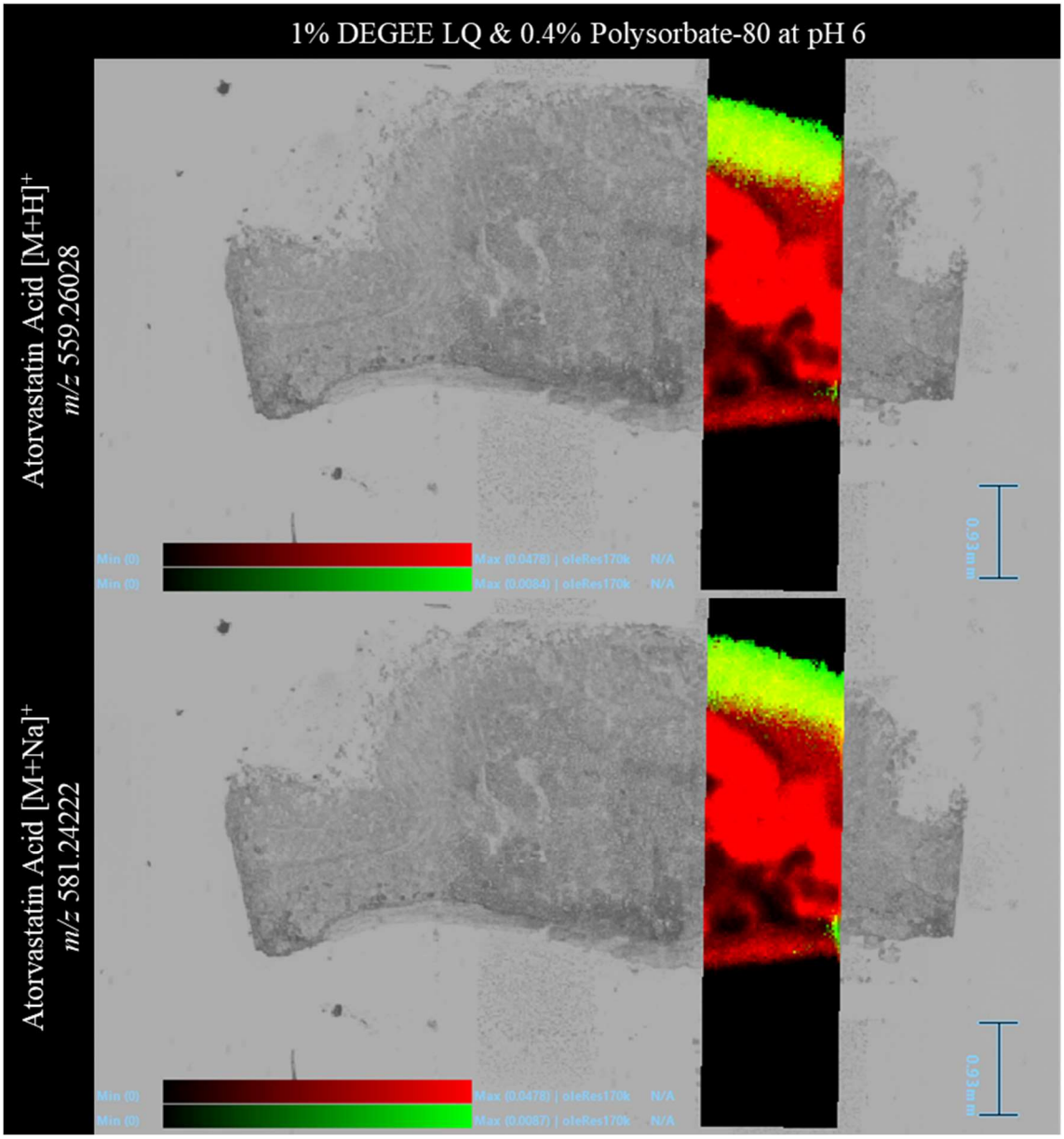

Figure 4.62: *DESI images overlaid onto an optical image of the tissue section they were acquired from with the surface of the tissue facing upwards. The tissue section was acquired from a fresh tissue absorption experiment with 1% DEGEE LQ and 0.4% polysorbate-80 in the donor circuit buffered to pH 6 and 10% FBS in the acceptor circuit. The distribution of the lipid ion m/z 780.5 has been displayed in a red colour scale. The distribution of protonated atorvastatin acid and its sodium adduct were shown in the top and bottom window, respectively, using a green colour scale. All identified drug related ions were within 1ppm.*

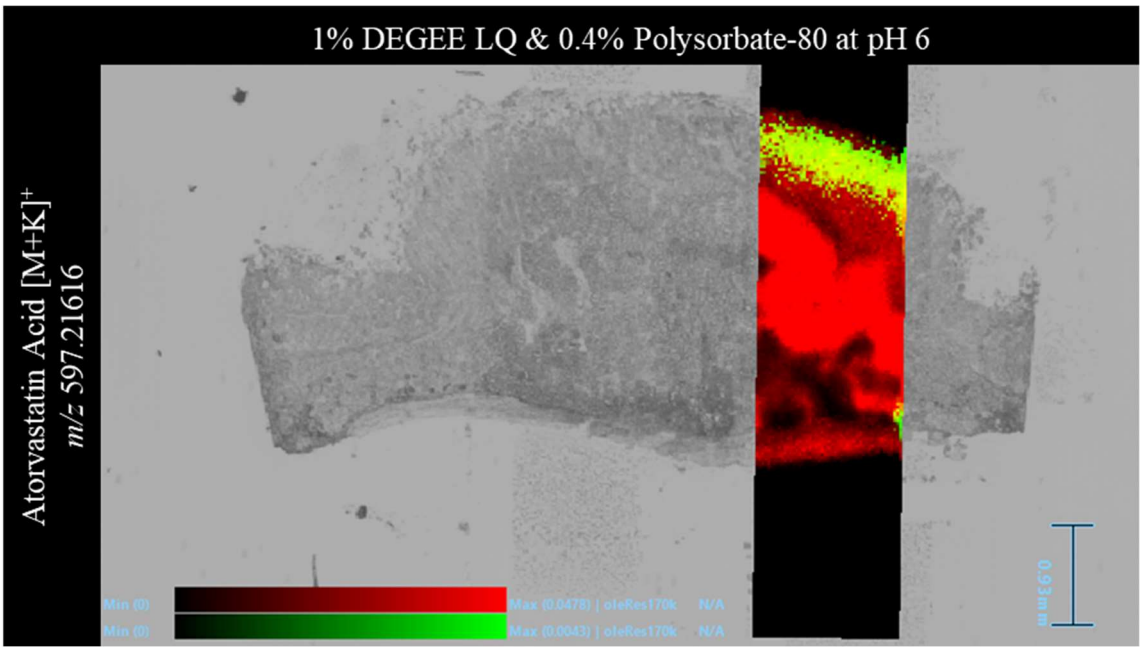

Figure 4.63: *DESI image overlaid onto an optical image of the tissue section it was acquired from with the surface of the tissue facing upwards. The tissue section was acquired from a fresh tissue absorption experiment with 1% DEGEE LQ and 0.4% polysorbate-80 in the donor circuit buffered to pH 6 and 10% FBS in the acceptor circuit. The distribution of the lipid ion m/z 780.5 and the potassium adduct of atorvastatin acid were displayed in a red and green colour scale, respectively. The identified drug ion was within 1 ppm.*

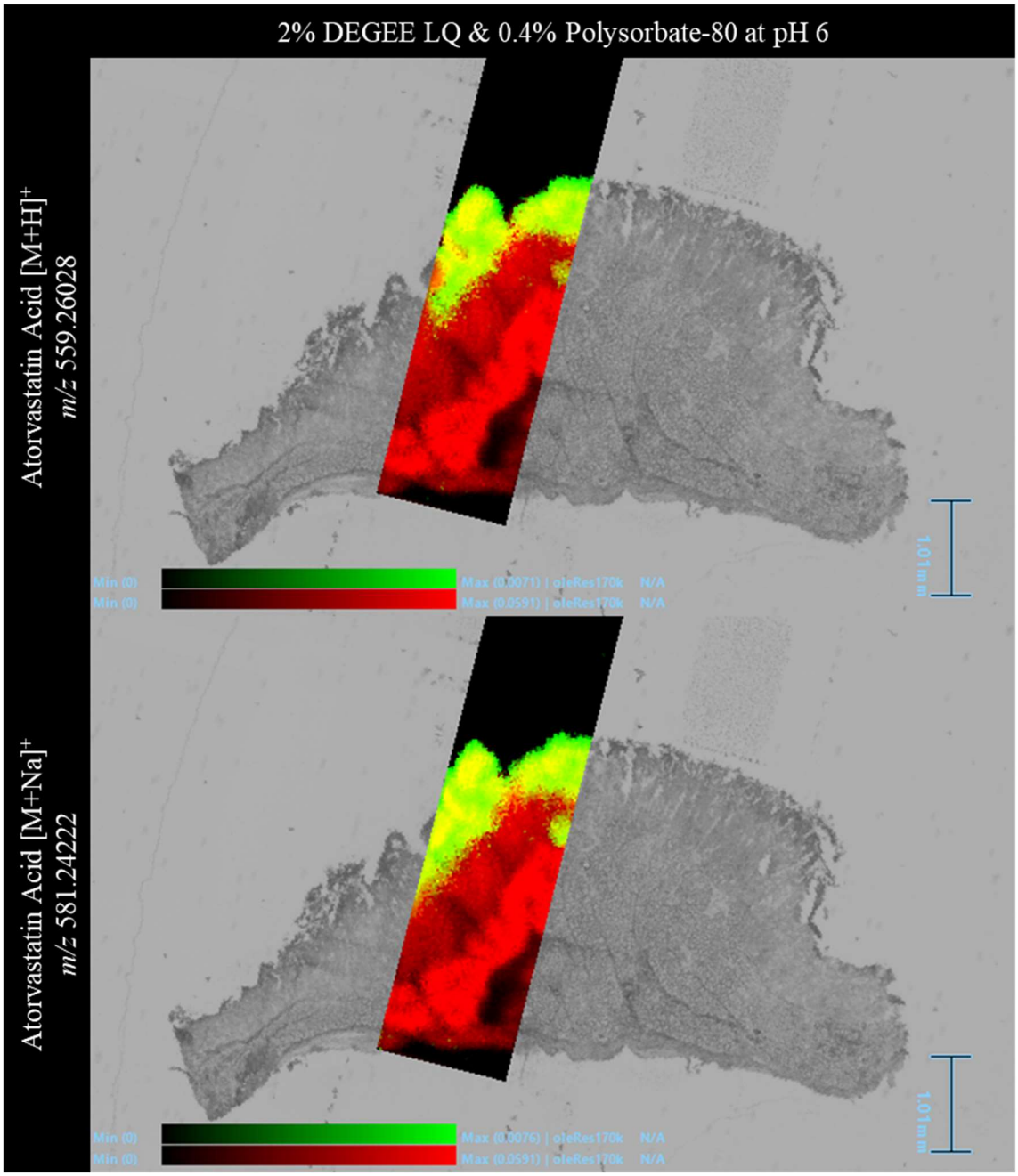

Figure 4.64: *DESI images overlaid onto an optical image of the tissue section they were acquired from with the surface of the tissue facing upwards. The tissue section was acquired from a fresh tissue absorption experiment with 2% DEGEE LQ and 0.4% polysorbate-80 in the donor circuit buffered to pH 6 and 10% FBS in the acceptor circuit. The distribution of the lipid ion m/z 780.5 has been displayed in a red colour scale. The distribution of protonated atorvastatin acid and its sodium adduct were shown in the top and bottom window, respectively, using a green colour scale. All identified drug related ions were within 1ppm.*

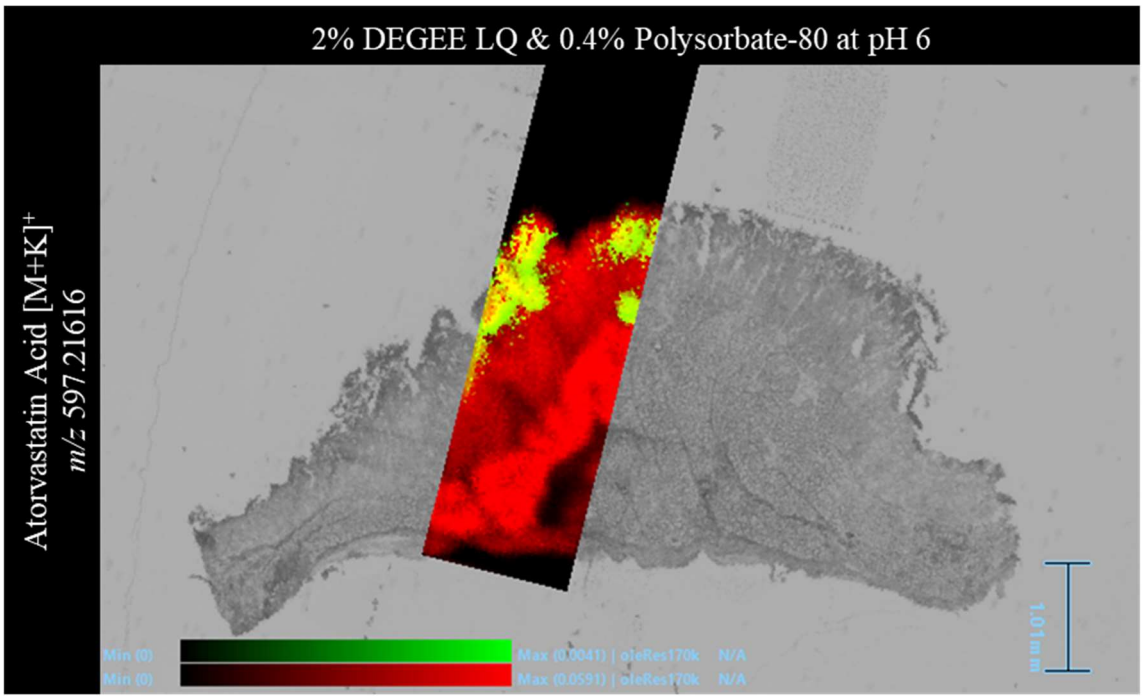

Figure 4.65: *DESI image overlaid onto an optical image of the tissue section it was acquired from with the surface of the tissue facing upwards. The tissue section was acquired from a fresh tissue absorption experiment with 2% DEGEE LQ and 0.4% polysorbate-80 in the donor circuit buffered to pH 6 and 10% FBS in the acceptor circuit. The distribution of the lipid ion m/z 780.5 and the potassium adduct of atorvastatin acid were displayed in a red and green colour scale, respectively. The identified drug ion was within 1 ppm.*

Of the three adducts of atorvastatin acid that have been shown in the previous figures, the most intense remains the sodium adduct. Throughout all images in the study, the signal from the sodium adduct of atorvastatin acid could be detected solidly spanning the entire surface of the tissue, penetrating a portion of the upper layer. In contrast, the adduct shown from the 0.4% DEGEE LQ (with 0.4% polysorbate-80) experiment appeared to cover significantly less depth and surface area when compared to the others within the study. Peculiarly, it was this study in which the most significant amount of atorvastatin acid was recovered from the tissue extract. There remain a few explanations for this finding. A common misconception would be that the distribution across each section of the tissue disc throughout would be comparable. However, changes and irregularities throughout the tissue make this highly unlikely. Additionally, DESI images of this sort only show a small snapshot in time. Since the DESI imaging experiments were not performed quantitatively, it would be unwise to closely compare the intensities of ions across different images, at least without the use of proper standards.

In DESI images acquired from experiments with 1% DEGEE and without, there was a small collection of pixels indicative of atorvastatin acid in the final layer of the tissue section. These would suggest that the drug had permeated through the tissue to reach this area of the tissue. Despite this, again no pathway or trail of atorvastatin acid through the tissue could be seen to highlight the route taken. For the DESI images from the other experiments, no atorvastatin acid was localised on the lower layers of the tissue. In order to study this further, ROIs were drawn in areas on the tissue section in which no drug distribution was visualised; the mass spectra were extracted and searched for signals from atorvastatin acid adducts. ROIs were also drawn on the whole tissue and areas away from tissue for comparison. The results of this investigation were summarised in Table 4.10 and the specific location of each ROI have been detailed in Appendix I Figure 17-20.

Table 4.10: *A summary of whether the named atorvastatin related ions were detectable in different ROIs in the DESI image. The ROIs specified here included the whole tissue, an area on the tissue with no drug signal and an area away from the tissue. All data here relates to DESI images collected from the polysorbate-80 study performed at pH 6.*

DEGEE LQ with 0.4% Polysorbate-80 Study at pH 6					
Atorvastatin and Related Ions	ROI	Ion present in ROI? Concentration of DEGEE LQ (% v/v)			
		0	0.4	1	2
Atorvastatin Acid [M+H]+ m/z 559.26028	Whole tissue?	✓	✓	✓	✓
	Within tissue away from drug distribution?	×	×	×	✓
	Away from tissue?	×	×	×	×
Atorvastatin Acid [M+Na]+ m/z 581.24222	Whole tissue?	✓	✓	✓	✓
	Within tissue away from drug distribution?	×	×	✓	×
	Away from tissue?	×	×	×	×
Atorvastatin Acid [M+K]+ m/z 597.21616	Whole tissue?	✓	✓	✓	✓
	Within tissue away from drug distribution?	×	×	✓	×
	Away from tissue?	×	×	×	×
Atorvastatin Acid [M+2Na-H]+ m/z 603.22416	Whole tissue?	✓	×	✓	✓
	Within tissue away from drug distribution?	×	×	×	×
	Away from tissue?	×	×	×	×

There were only a few instances in which atorvastatin acid adducts were successfully detected in the ROIs away from the visual drug distribution. The identity of these ions were confidently assigned by keeping within 1 ppm of error and eliminating any signals that were also present away from the tissue. The DESI data was then checked for all known atorvastatin metabolites; these data are displayed in Figure 4.66-4.70.

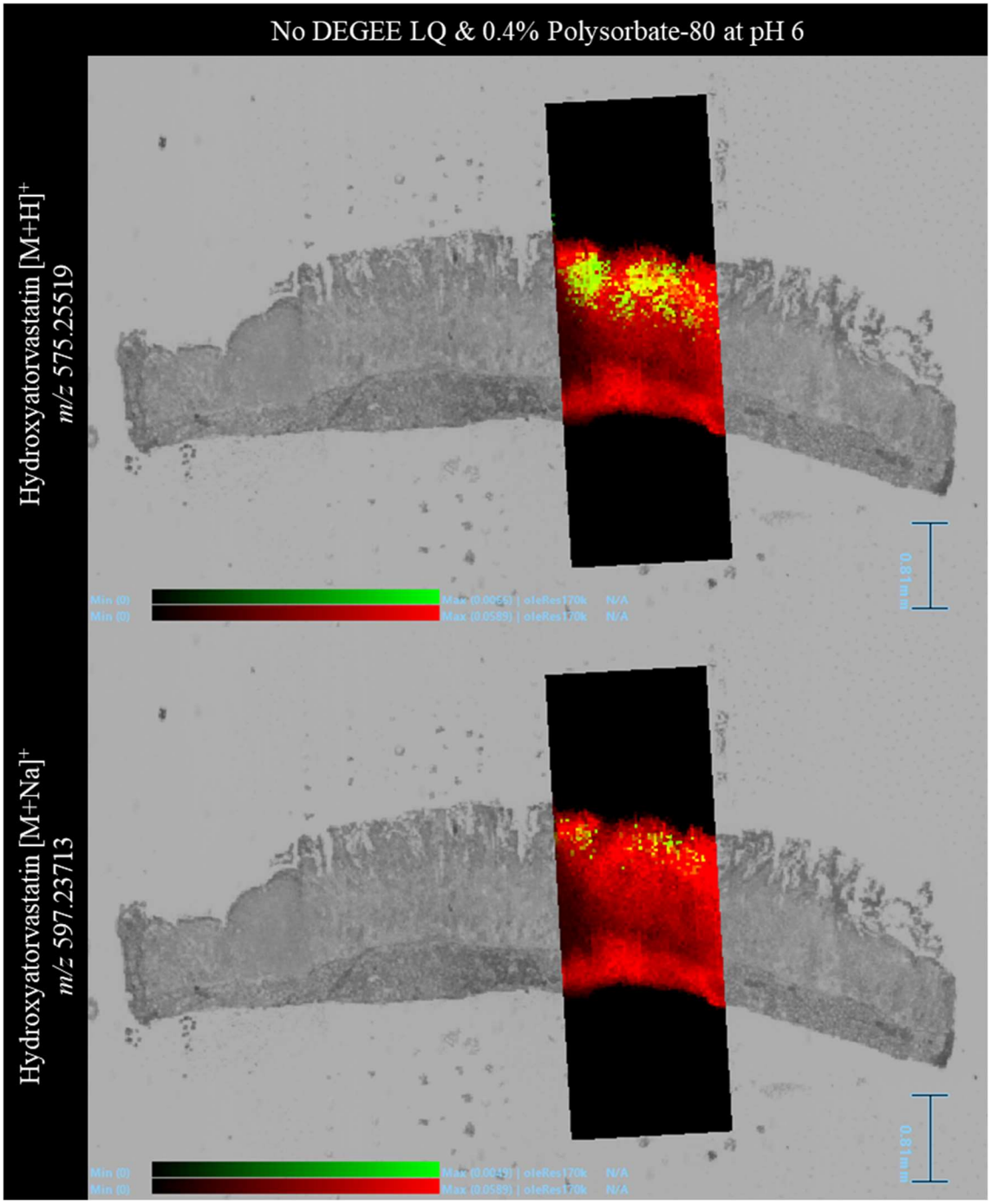

Figure 4.66: *DESI images overlaid onto an optical image of the tissue section they were acquired from with the surface of the tissue facing upwards. The tissue section was acquired from a fresh tissue absorption experiment with 0.4% polysorbate-80 in the donor circuit buffered to pH 6 and 10% FBS in the acceptor circuit. The distribution of the lipid ion m/z 780.5 has been displayed in a red colour scale. The distribution of protonated metabolites Hydroxyatorvastatin and its sodium adduct were shown in the top and bottom window, respectively, using a green colour scale. The metabolite ions were within 1 ppm.*

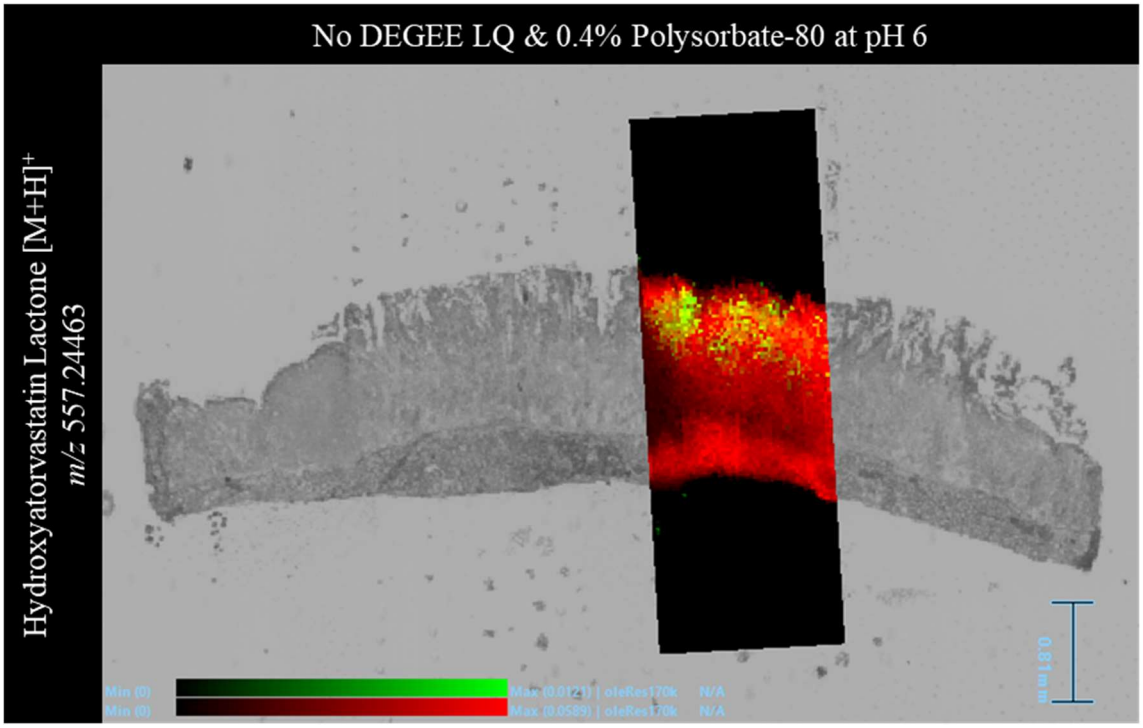

Figure 4.67: *DESI image overlaid onto an optical image of the tissue section it was acquired from with the surface of the tissue facing upwards. The tissue section was acquired from a fresh tissue absorption experiment with 0.4% polysorbate-80 in the donor circuit buffered to pH 6 and 10% FBS in the acceptor circuit. The distribution of the lipid ion m/z 780.5 and protonated metabolite, Hydroxyatorvastatin lactone, was displayed in a red and green colour scale, respectively. The metabolite ion was within 1 ppm.*

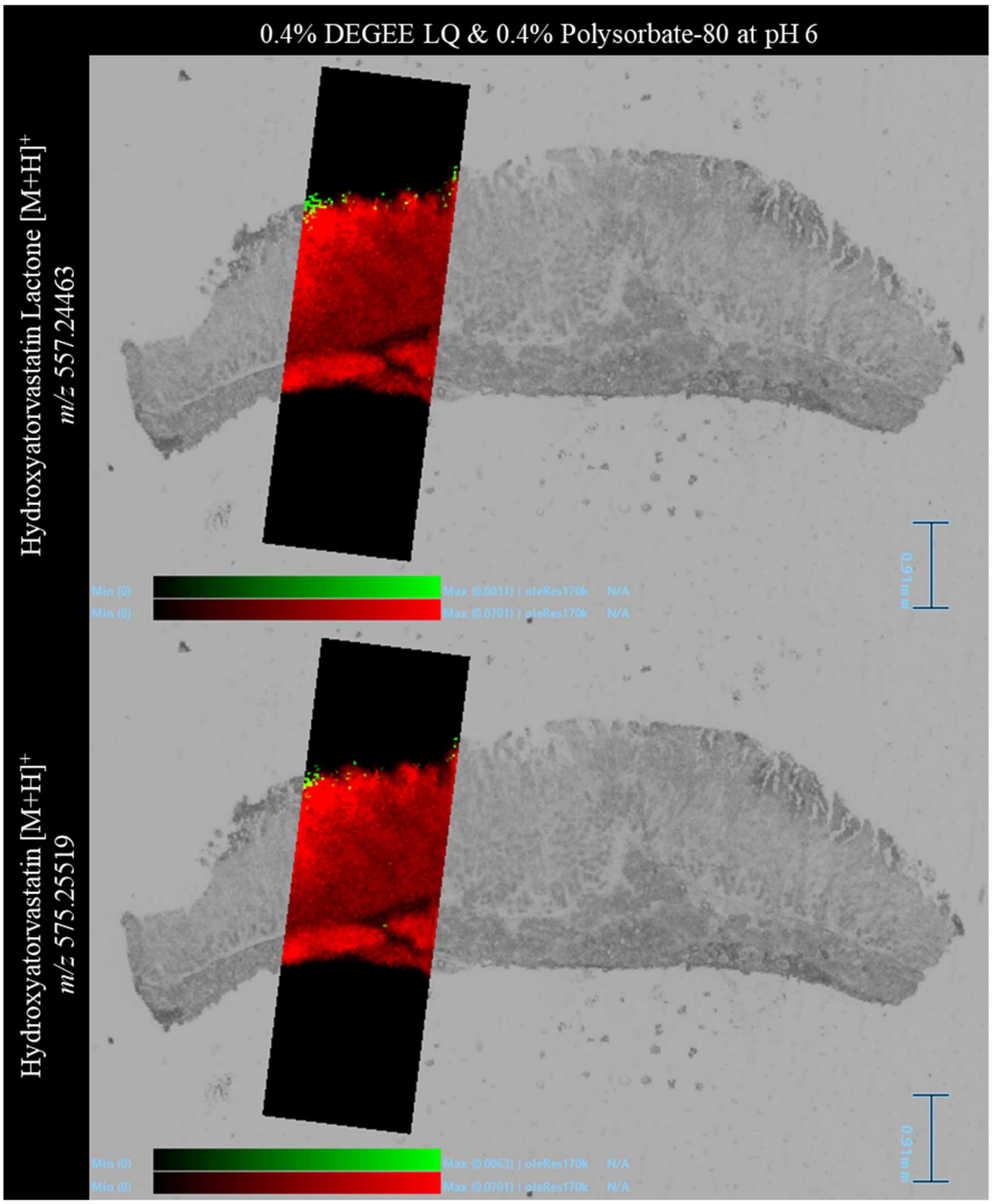

Figure 4.68: *DESI images overlaid onto an optical image of the tissue section they were acquired from with the surface of the tissue facing upwards. The tissue section was acquired from a fresh tissue absorption experiment with 0.4% DEGEE LQ and 0.4% polysorbate-80 in the donor circuit buffered to pH 6 and 10% FBS in the acceptor circuit. The distribution of the lipid ion m/z 780.5 has been displayed in a red colour scale. The distribution of protonated metabolites hydroxyatorvastatin lactone and hydroyatorvastatin were shown in the top and bottom window, respectively, using a green colour scale. The metabolite ions were within 1 ppm.*

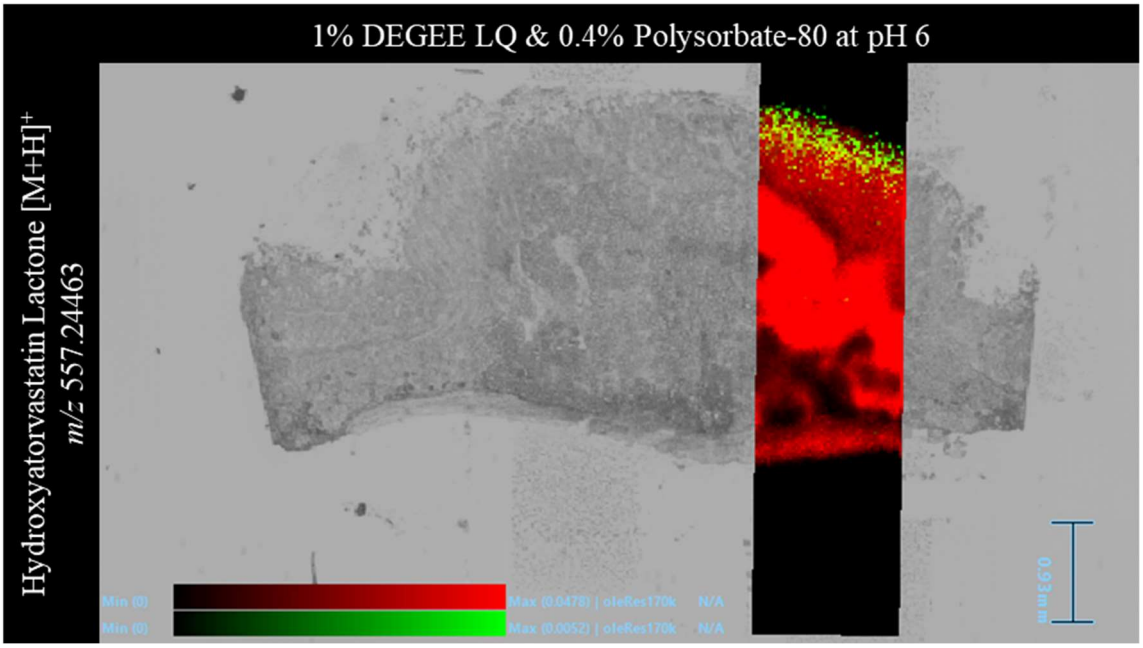

Figure 4.69: *DESI image overlaid onto an optical image of the tissue section it was acquired from with the surface of the tissue facing upwards. The tissue section was acquired from a fresh tissue absorption experiment with 1% DEGEE LQ and 0.4% polysorbate-80 in the donor circuit buffered to pH 6 and 10% FBS in the acceptor circuit. The distribution of the lipid ion m/z 780.5 and protonated metabolite, Hydroxyatorvastatin lactone, was displayed in a red and green colour scale, respectively. The metabolite ion was within 1 ppm.*

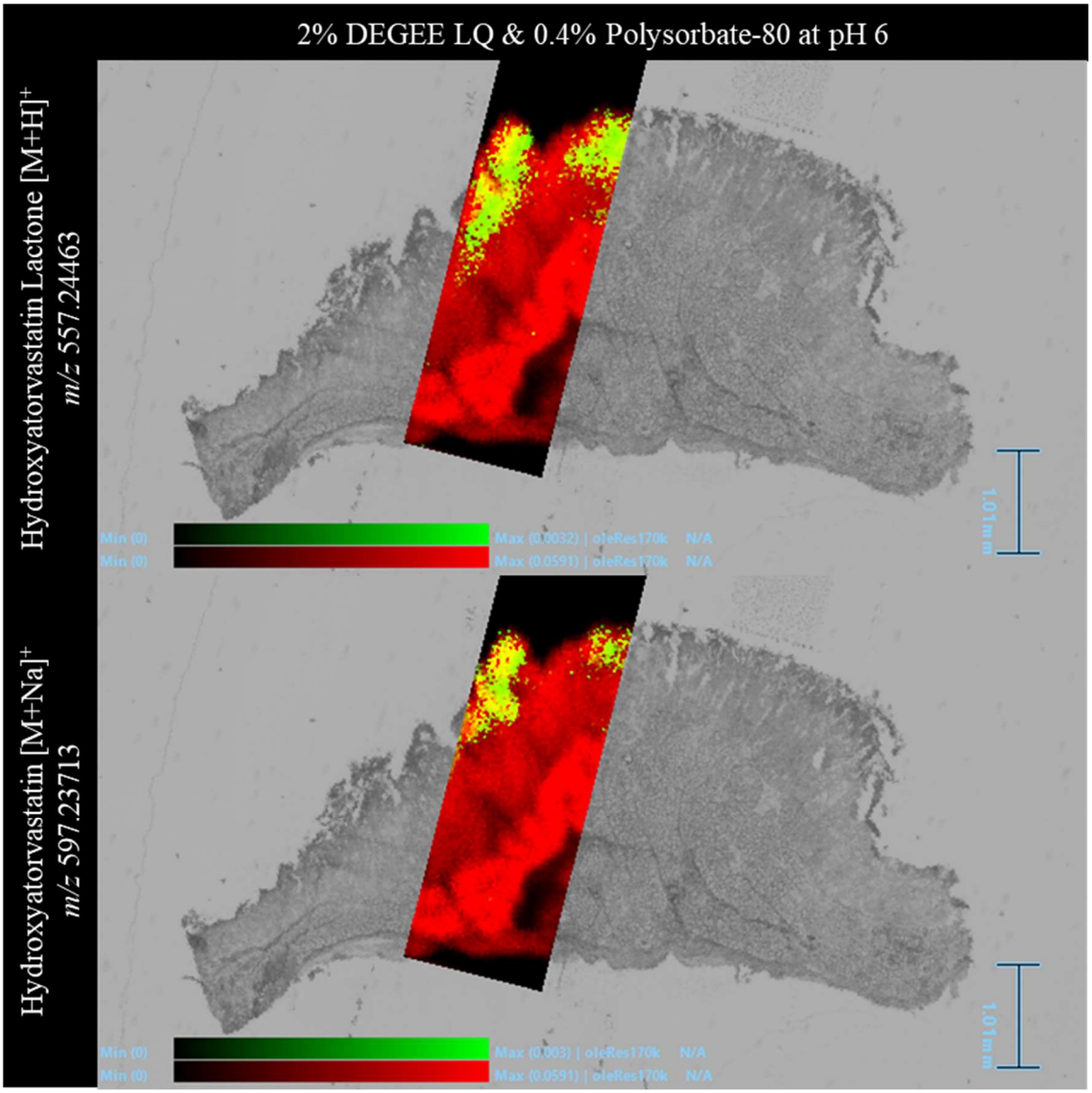

Figure 4.70: *DESI images overlaid onto an optical image of the tissue section they were acquired from with the surface of the tissue facing upwards. The tissue section was acquired from a fresh tissue absorption experiment with 2% DEGEE LQ and 0.4% polysorbate-80 in the donor circuit buffered to pH 6 and 10% FBS in the acceptor circuit. The distribution of the lipid ion m/z 780.5 has been displayed in a red colour scale. The distribution of protonated metabolites hydroxyatorvastatin lactone and the sodium adduct of hydroxyatorvastatin were shown in the top and bottom window, respectively, using a green colour scale. The metabolite ions were within 1 ppm.*

The metabolite, hydroxyatorvastatin lactone, was successfully visualised in all of the tissue sections imaged. In each instance, the metabolite was shown to be localised in a similar area to atorvastatin acid albeit, at lower abundance. Another metabolite,

hydroxyatorvastatin, was shown in all DESI images except for those acquired from one of the ‘1% DEGEE LQ with polysorbate-80’ experiments. As before, the identified metabolite ion was distributed in the same area as the ions related to atorvastatin acid. For all metabolite ion images, no signals were obtained from deep into the tissue or within the final layer. The same ROIs as used in atorvastatin acid images from this study, were analysed for all known atorvastatin metabolites. The findings are summarised in Table 4.11.

Table 4.11: *A summary of whether the named atorvastatin metabolites were detectable in different ROIs in the DESI image. The ROIs specified here included the whole tissue, an area on the tissue with no drug signal and an area away from the tissue. All data here relates to DESI images collected from the DEGEE LQ with polysorbate-80 study performed at pH 6.*

DEGEE LQ with 0.4% Polysorbate-80 Study at pH 6					
Atorvastatin Metabolites	ROI	Ion present in ROI? Concentration of DEGEE LQ (% v/v)			
		0	0.4	1	2
Hydroxyatorvastatin $[M+H]^+$ *m/z* 575.25519	Whole tissue?	✓	✓	×	✓
	Within tissue away from drug distribution?	×	×	×	×
	Away from tissue?	×	×	×	×
Hydroxyatorvastatin $[M+Na]^+$ *m/z* 597.23713	Whole tissue?	✓	✓	✓	✓
	Within tissue away from drug distribution?	×	×	×	×
	Away from tissue?	×	×	×	×
Atorvastatin Lactone $[M+H]^+$ *m/z* 541.249712	Whole tissue?	×	×	×	✓
	Within tissue away from drug distribution?	×	×	×	×
	Away from tissue?	×	×	×	×
Atorvastatin Lactone $[M+Na]^+$ *m/z* 563.231654	Whole tissue?	×	×	✓	×
	Within tissue away from drug distribution?	×	×	×	×
	Away from tissue?	×	×	×	×
Hydroxyatorvastatin Lactone $[M+H]^+$ *m/z* 557.24463	Whole tissue?	✓	✓	✓	✓
	Within tissue away from drug distribution?	×	×	×	×
	Away from tissue?	×	×	×	×
Hydroxyatorvastatin Lactone $[M+Na]^+$ *m/z* 579.22657	Whole tissue?	✓	×	✓	✓
	Within tissue away from drug distribution?	×	×	×	×
	Away from tissue?	×	×	×	×

No further signals for any of the identified metabolites were detected in the ROIs drawn away from the visual drug distribution. Despite this, as a collective, all of the known atorvastatin metabolites were detectable in the mass spectra at low levels throughout the whole tissue ROIs taken from this study. The lack of parent drug or metabolite distribution throughout the entire thickness of the tissue with saturation on the surface would imply that there had been little movement through the tissue. However, the permeation coefficients calculated for this study suggest otherwise.

Data in this study were acquired with the MRT "threshold feature" enabled which gives high mass accuracy and reduces background/low abundance signals. Therefore, it is a plausible hypothesis that atorvastatin acid was present in the tissue but the signals were not of sufficient intensity to be visualised, especially in the presence of a saturated surface layer. It could be reasonably theorised that the amount of atorvastatin acid that became settled on the surface of the tissue would impact the concentration of the drug that would become saturated in the sticky mucus layer on the surface of the tissue, even after rinsing. This would enlarge the concentration gradient between the tissue surface and deeper layers and thus, increase the risk of ion masking within the DESI images.

In this particular study, the amount of atorvastatin acid that was rinsed from the surface of the tissue discs was minimal. The amount of atorvastatin recovered from the tissue rinse solutions was plotted against the amount of DEGEE LQ added to the circuit with 0.4% polysorbate-80 and displayed in Figure 4.71. With the consistent presence of 0.4% polysorbate-80 and the donor circuit buffered to pH 6, no statistically significant changes were seen in the amount of atorvastatin that could be rinsed from the surface of the tissue; even as the concentration of DEGEE LQ was increased. This would imply that atorvastatin acid had reached its optimal level of solubility in this formulation; especially since a comparable amount of the drug had been retrieved from the tissue surface in a previous study using the maximum concentration of known solubiliser, polysorbate-80.

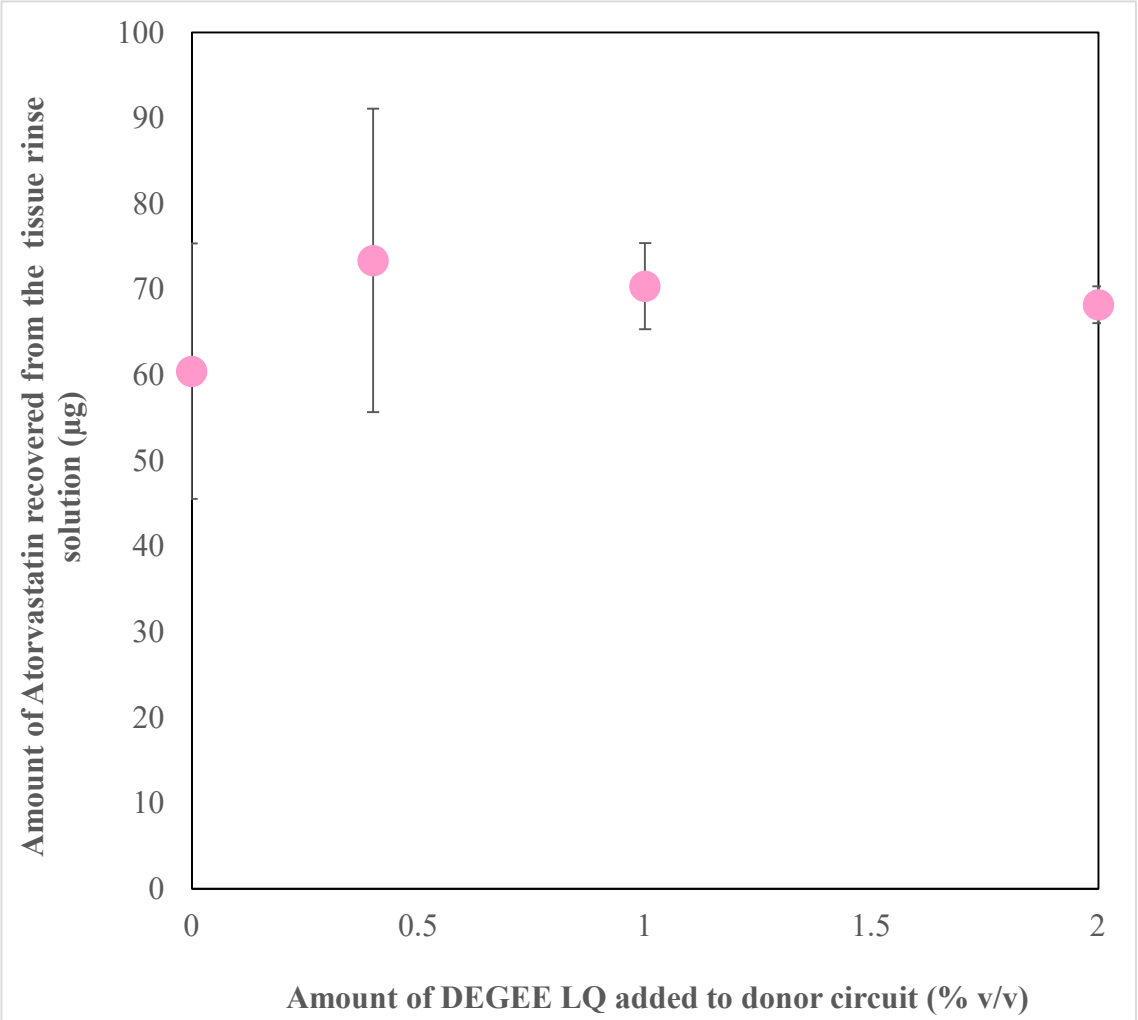

Figure 4.71: *A graph to show the amount of Atorvastatin that was rinsed from the tissue discs plotted against the concentration of DEGEE LQ added to 0.4% Polysorbate-80 in the donor circuit (pH 6) of the corresponding absorption experiment. The data presented here is from the DEGEE with 0.4 % (v/v) Polysorbate-80 study performed at pH 6 (n=3).*

The amount of atorvastatin acid recovered from the system after draining was plotted against the varying amount of DEGEE LQ added to the circuit with 0.4% polysorbate-80 and shown in Figure 4.72. The trend shown was similar to that of the tissue rinsing solution. There were no statistically significant changes to the amount of atorvastatin acid recovered from the system, despite increasing the concentration of DEGEE LQ. The amount of drug recovered from the system did not exceed the amount that was recovered when the maximum amount of polysorbate-80 was added to the donor circuit at pH 6. This supports the proposal that with the combination of 0.4% polysorbate-80

and acidity buffered to pH 6 in the donor circuit, atorvastatin acid had reached its optimal level of solubility in this scenario.

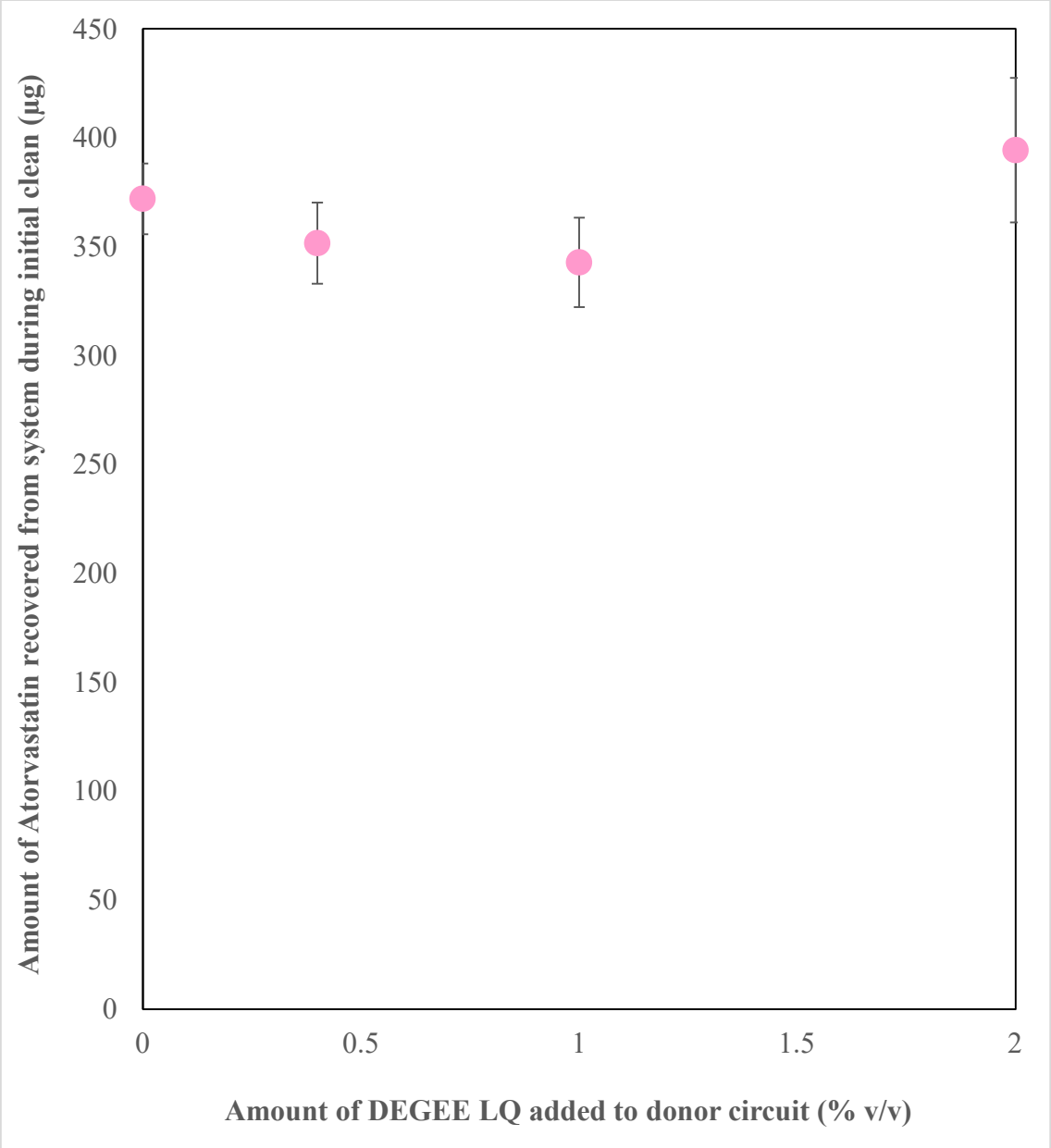

Figure 4.72: *A graph showing the amount of Atorvastatin that was recovered from the QV600 LLI after the system had been drained following an absorption experiment with varied amounts of DEGEE LQ added to 0.4% Polysorbate-80 in the donor circuit (pH 6) of the corresponding absorption experiment. The data presented here is from the DEGEE with 0.4 % (v/v) Polysorbate-80 study performed at pH 6 (n=3).*

Following the improvements in drug absorption observed when the composition of the acceptor circuit was changed, all subsequent studies were performed with the donor circuit buffered to pH 6 and with the incorporation of the FBS supplement.

4.4.4 Mapcho-12 Study

Mapcho-12 has been reported to be useful as an excipient in drug absorption since it improves permeability by modifying tight junctions. The following study was performed in combination with 0.4% polysorbate-80 buffered to pH 6 in the donor circuit and with a 10% FBS supplement added to the acceptor circuit. The permeation coefficient values for this study were calculated and are displayed in Figure 4.73. The full data set acquired contained one high value at 1mM Mapcho-12 added which was considered to be an outlier and skewed the other data points. In order to fully interpret the other data points, the data was statistically analysed without this data point and replotted in Figure 4.74.

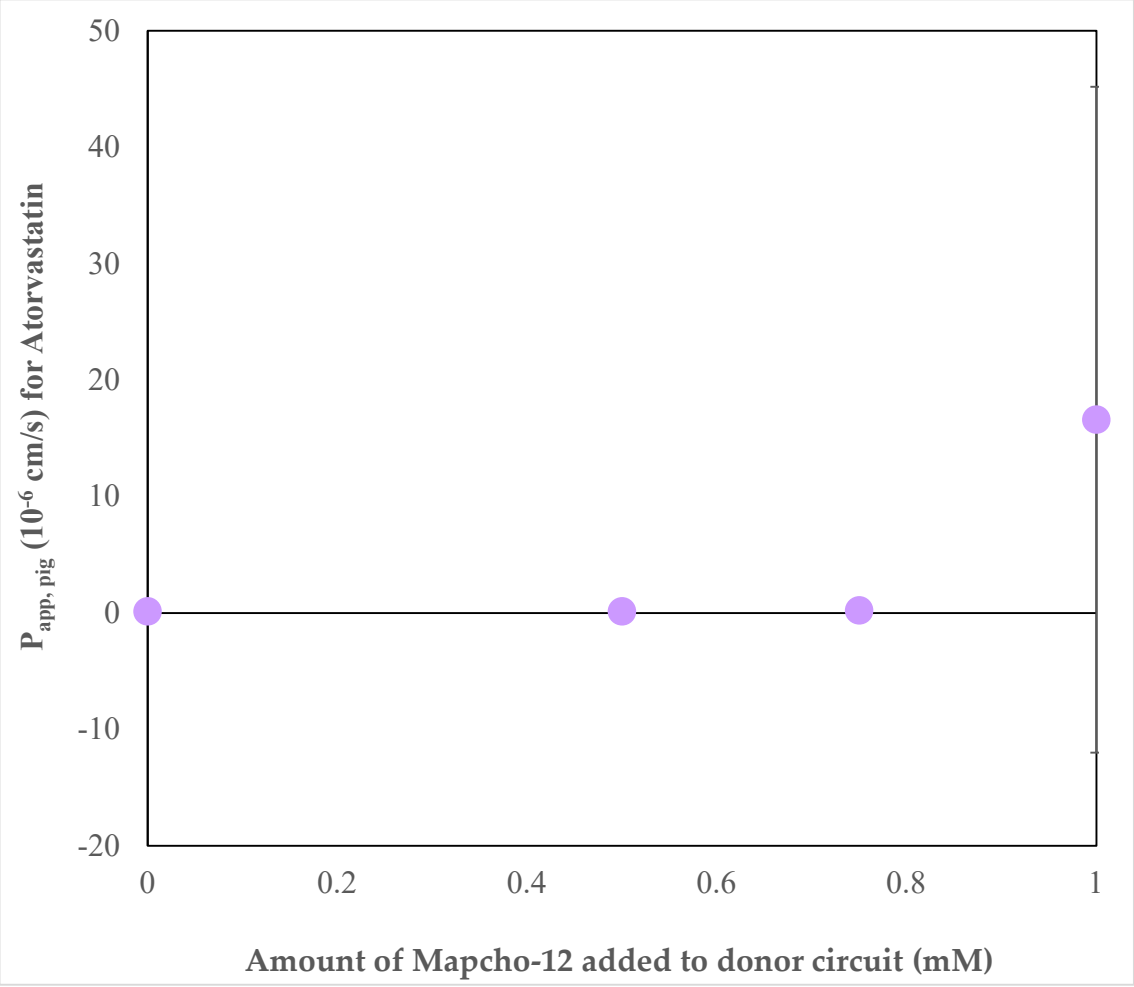

Figure 4.73: *A graph showing the $P_{app,pig}$ values plotted against the concentration of Mapcho-12 added to 0.4% Polysorbate-80 in the donor circuit (pH 6) of the corresponding absorption experiment. The data presented here is from the Mapcho-12 with 0.4 % (v/v) Polysorbate-80 study performed at pH 6 (n=3).*

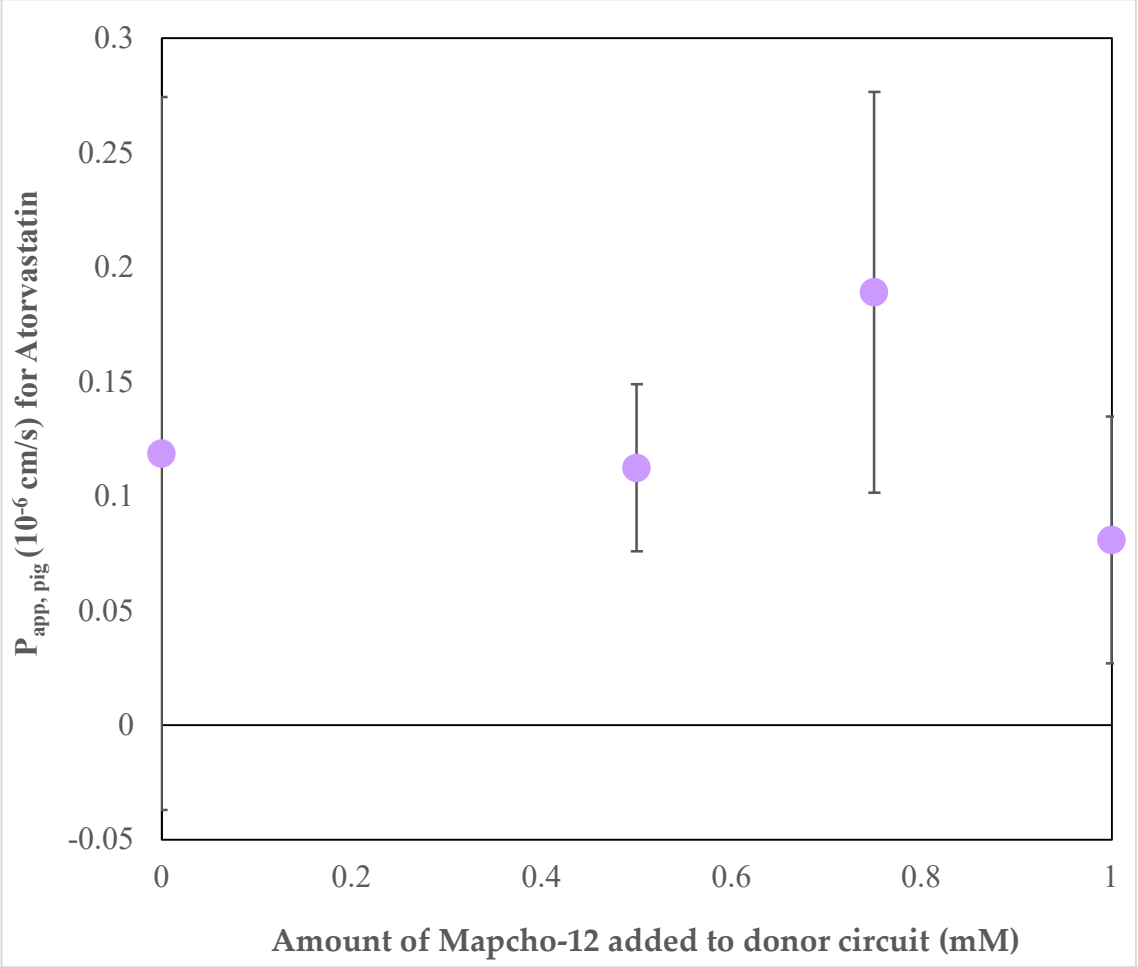

Figure 4.74: *A graph showing the data from Figure 4.73, reanalysed without the outlier.*

Figure 4.74 shows that when mapcho-12 was introduced to the circuit, the average amount of atorvastatin acid that had permeated into the acceptor circuit increased. The $P_{app,pig}$ value generally increased until it reached a maximum at 0.75 mM of mapcho-12. After this concentration, the average permeation coefficient value began to decline. Despite the visual trend with outliers excluded, a one-way ANOVA test on all data points deemed the differences between them to be statistically insignificant. (Liu et al., 1999) had performed a study using the same concentrations of mapcho-12. The study found that the optimal balance between cell viability and increased Papp value was concurrent with 0.75mM of mapcho-12 present. At 1mM and above, it was reported that irreversible damage was caused to the cell membrane. While this visual pattern would match that expected from the literature, the individual values from each experiment should be taken into account, as for some experiments, a greater amount of variability was shown which threw off the average trend.

A tissue disc from each of these experiments underwent extraction to give the concentration of atorvastatin acid per gram of tissue. These values were plotted against the concentration of mapcho-12 in the donor circuit along with 0.4% polysorbate-80 and displayed in Figure 4.75.

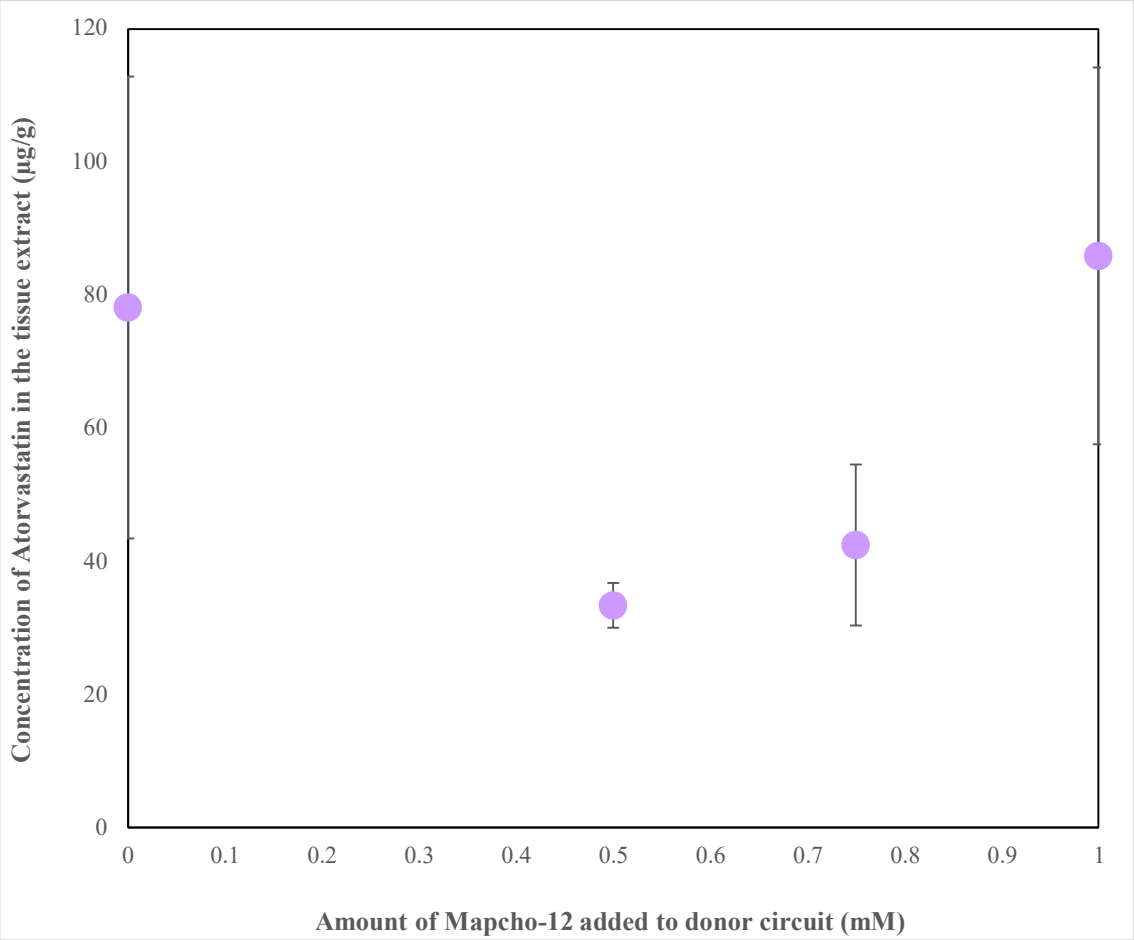

Figure 4.75: *A graph showing the concentration of Atorvastatin calculated from the tissue disc extract plotted against the corresponding concentration of mapcho-12 that was present in the donor circuit (pH 6) for that absorption experiment. The data presented here is from the Mapcho-12 with 0.4 % (v/v) Polysorbate-80 study performed at pH 6 (n=3).*

It was observed that when mapcho-12 was first introduced into the donor circuit, the amount of atorvastatin acid that was recovered from tissue extracts appeared to reduce. As the concentration of mapcho-12 in the circuit increased, the amount of atorvastatin acid recovered steadily rose. Despite the visual trend, a one-way ANOVA test deemed the difference between all data points to be statistically insignificant. The tissue discs were analysed by DESI MSI to provide additional information. Images were acquired

from a tissue disc from one of each experiment type in the study. DESI images found in each tissue section relating to atorvastatin acid and its main adducts were shown in Figures 4.76-4.83.

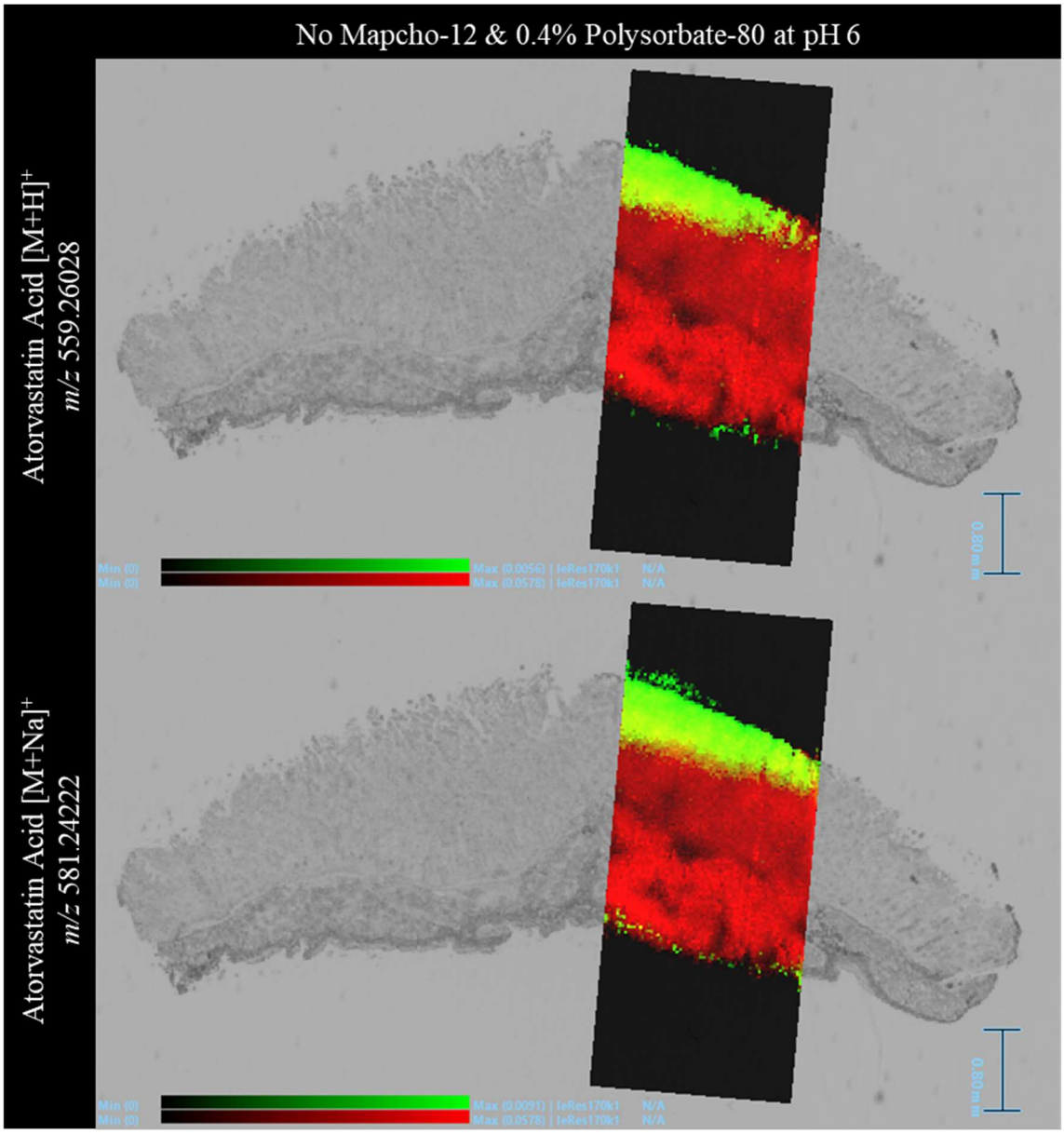

Figure 4.76: *DESI images overlaid onto an optical image of the tissue section they were acquired from with the surface of the tissue facing upwards. The tissue section was acquired from a fresh tissue absorption experiment with 0.4% polysorbate-80 in the donor circuit buffered to pH 6 and 10% FBS in the acceptor circuit. The distribution of the lipid ion m/z 780.5 has been displayed in a red colour scale. The distribution of protonated atorvastatin acid and its sodium adduct were shown in the top and bottom window, respectively, using a green colour scale. All identified drug related ions were within 1ppm.*

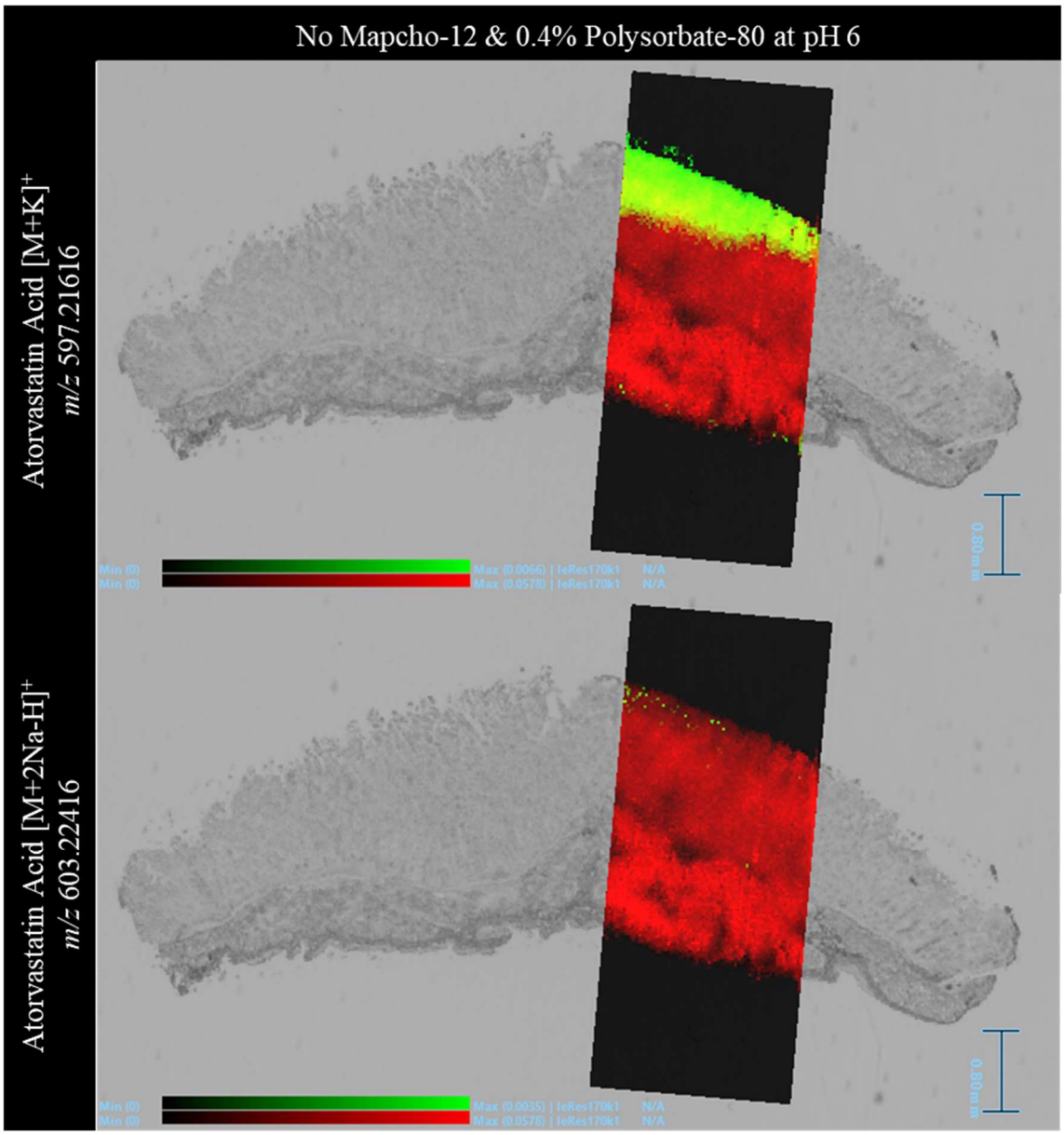

Figure 4.77: *DESI images overlaid onto an optical image of the tissue section they were acquired from with the surface of the tissue facing upwards. The tissue section was acquired from a fresh tissue absorption experiment with 0.4% polysorbate-80 in the donor circuit, buffered to pH 6. The distribution of the lipid ion m/z 780.5 was displayed in a red colour scale. Potassium and $[M+2Na-H]^+$ adducts of atorvastatin acid were shown from top to bottom, respectively, using a green colour scale. All identified drug related ions were within 1 ppm.*

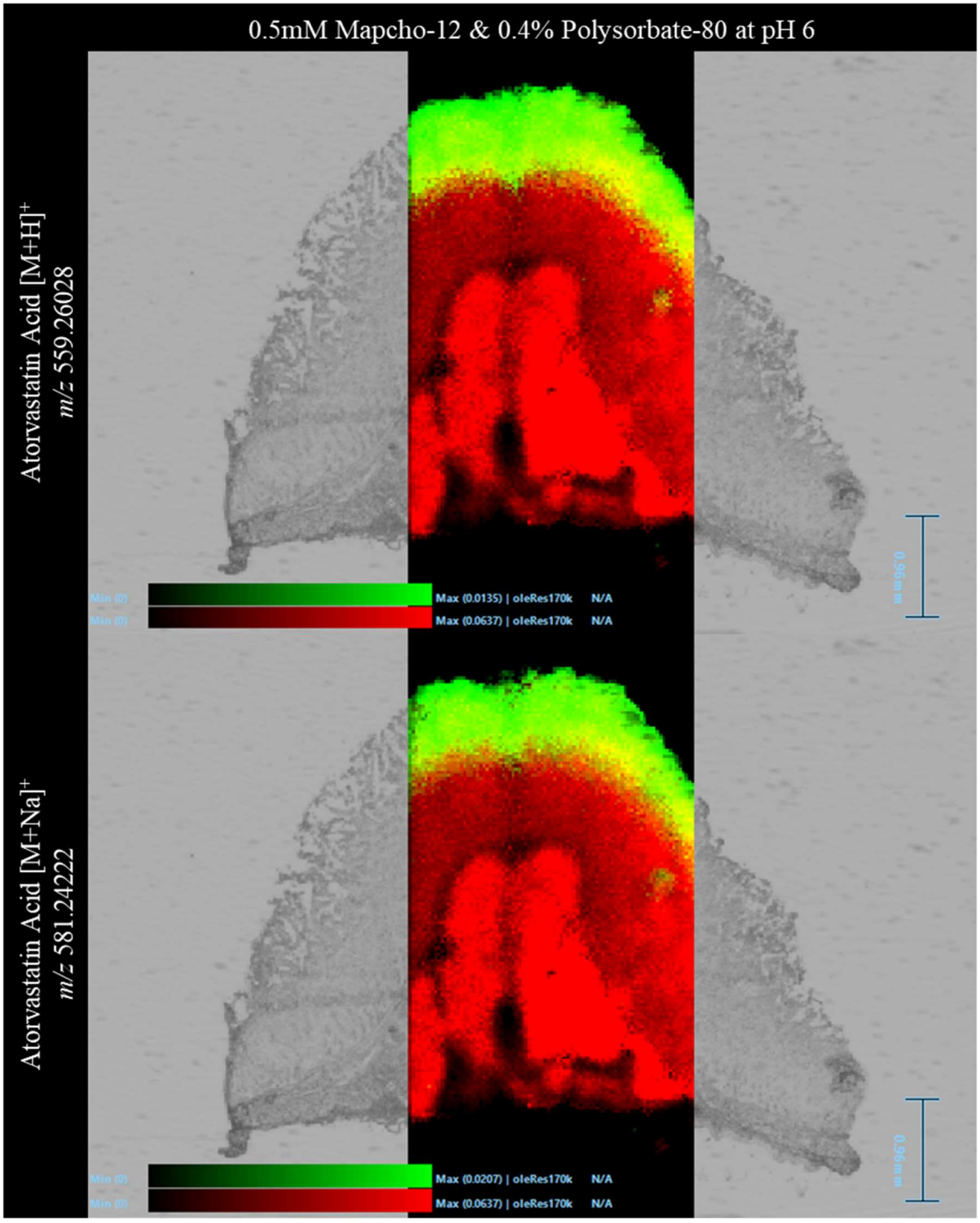

Figure 4.78: *DESI images overlaid onto an optical image of the tissue section they were acquired from with the surface of the tissue facing upwards. The tissue section was acquired from a fresh tissue absorption experiment with 0.5 mM mapcho-12 and 0.4% polysorbate-80 in the donor circuit buffered to pH 6 and 10% FBS in the acceptor circuit. The distribution of the lipid ion m/z 780.5 has been displayed in a red colour scale. The distribution of protonated atorvastatin acid and its sodium adduct were shown in the top and bottom window, respectively, using a green colour scale. All identified drug related ions were within 1ppm.*

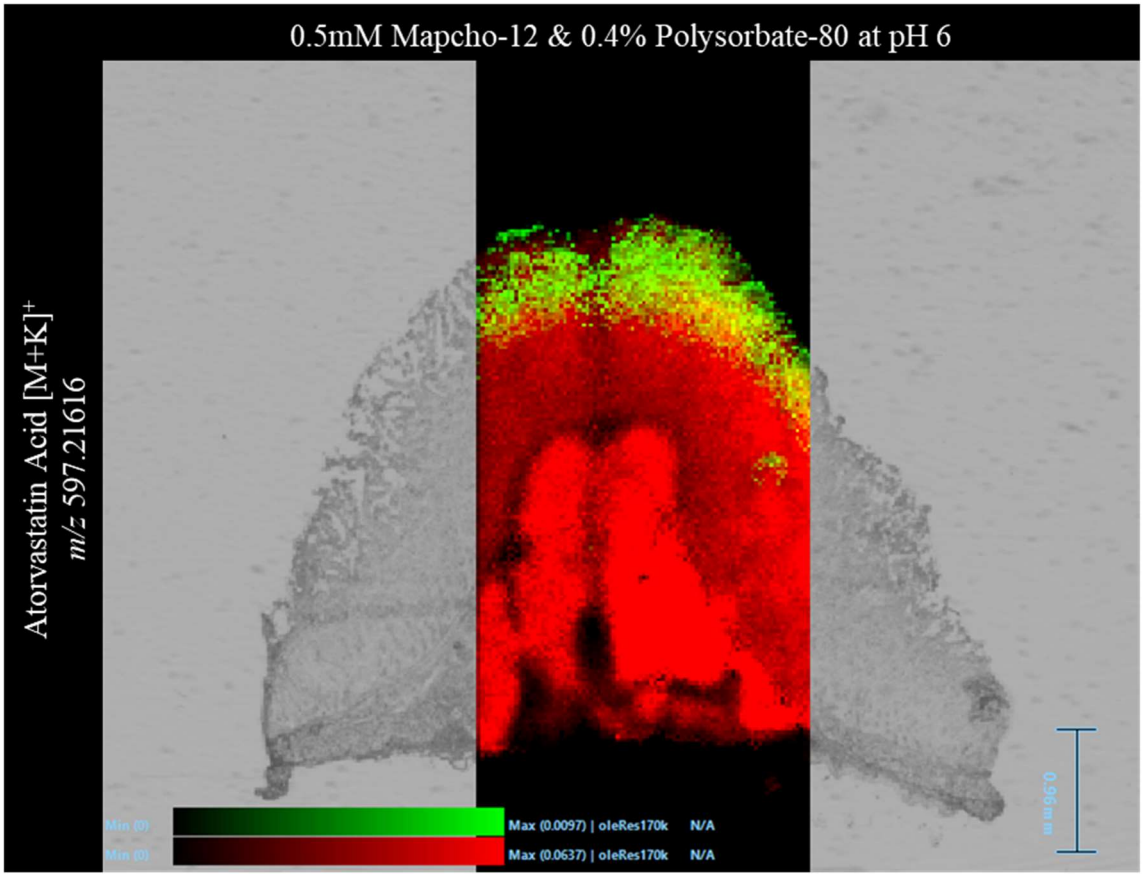

Figure 4.79: *A DESI image overlaid onto an optical image of the tissue section it was acquired from with the surface of the tissue facing upwards. The tissue section was acquired from a fresh tissue absorption experiment with 0.5 mM mapcho-12 and 0.4% polysorbate-80 in the donor circuit, buffered to pH 6. The distribution of the lipid ion m/z 780.5 and the potassium adduct of atorvastatin acid were shown using a red and green colour scale. The identified drug related ion was within 1 ppm.*

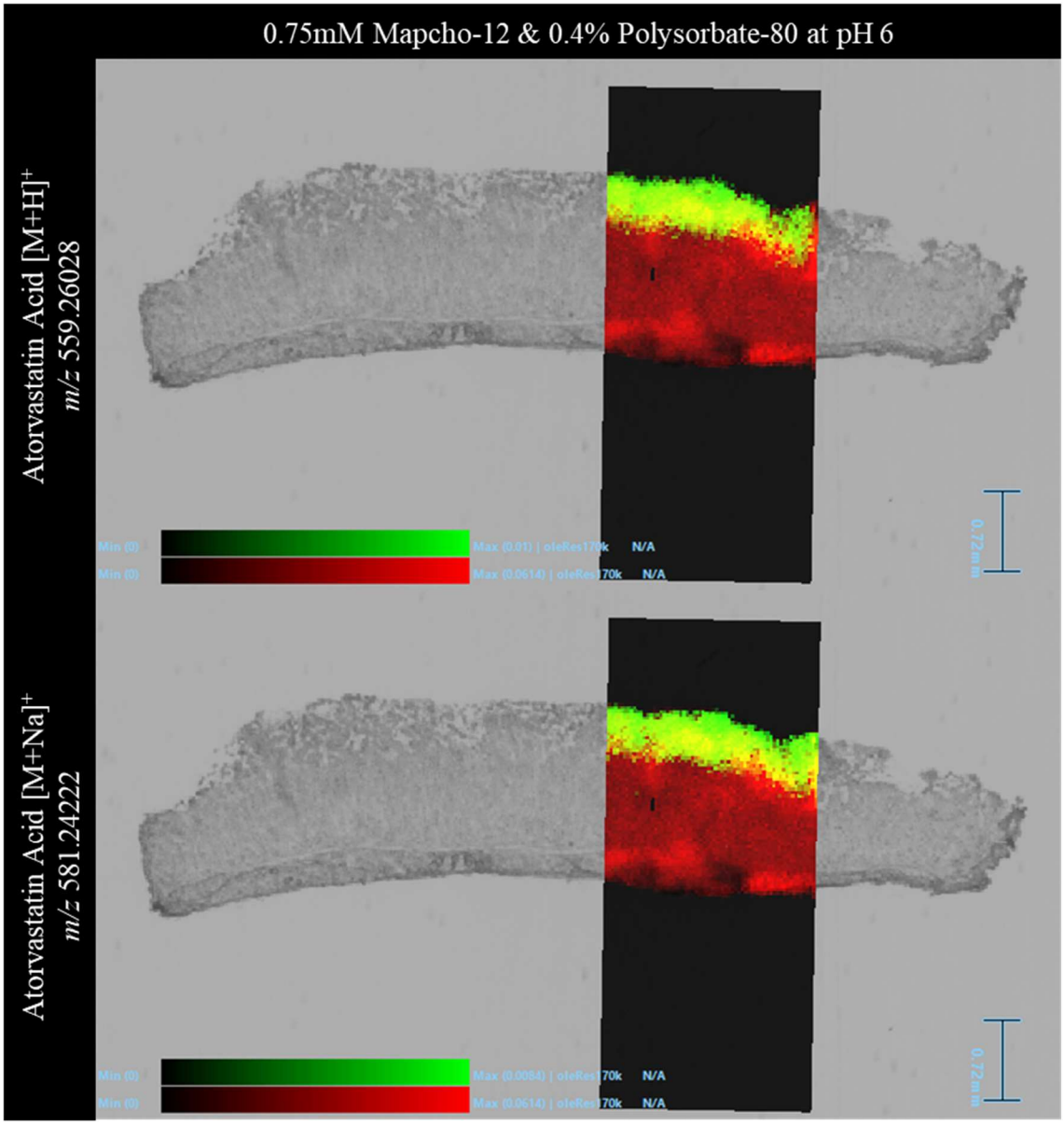

Figure 4.80: *DESI images overlaid onto an optical image of the tissue section they were acquired from with the surface of the tissue facing upwards. The tissue section was acquired from a fresh tissue absorption experiment with 0.75 mM mapcho-12 and 0.4% polysorbate-80 in the donor circuit buffered to pH 6 and 10% FBS in the acceptor circuit. The distribution of the lipid ion m/z 780.5 has been displayed in a red colour scale. The distribution of protonated atorvastatin acid and its sodium adduct were shown in the top and bottom window, respectively, using a green colour scale. All identified drug related ions were within 1ppm.*

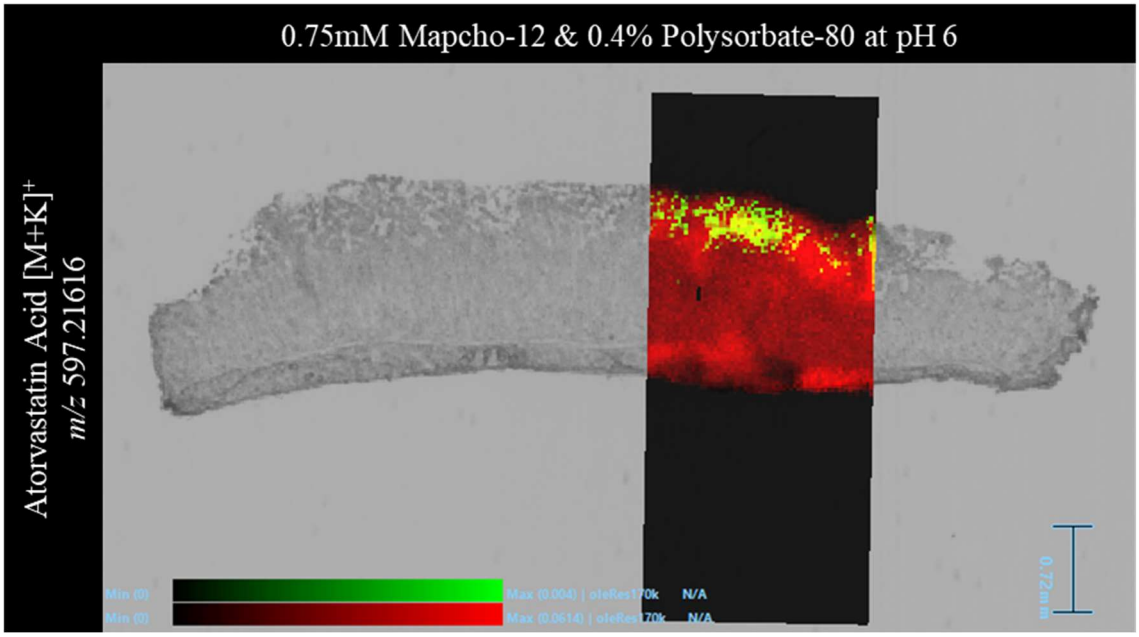

Figure 4.81: *A DESI image overlaid onto an optical image of the tissue section it was acquired from with the surface of the tissue facing upwards. The tissue section was acquired from a fresh tissue absorption experiment with 0.75 mM mapcho-12 and 0.4% polysorbate-80 in the donor circuit, buffered to pH 6. The distribution of the lipid ion m/z 780.5 and the potassium adduct of atorvastatin acid were shown using a red and green colour scale. The identified drug related ion was within 1 ppm.*

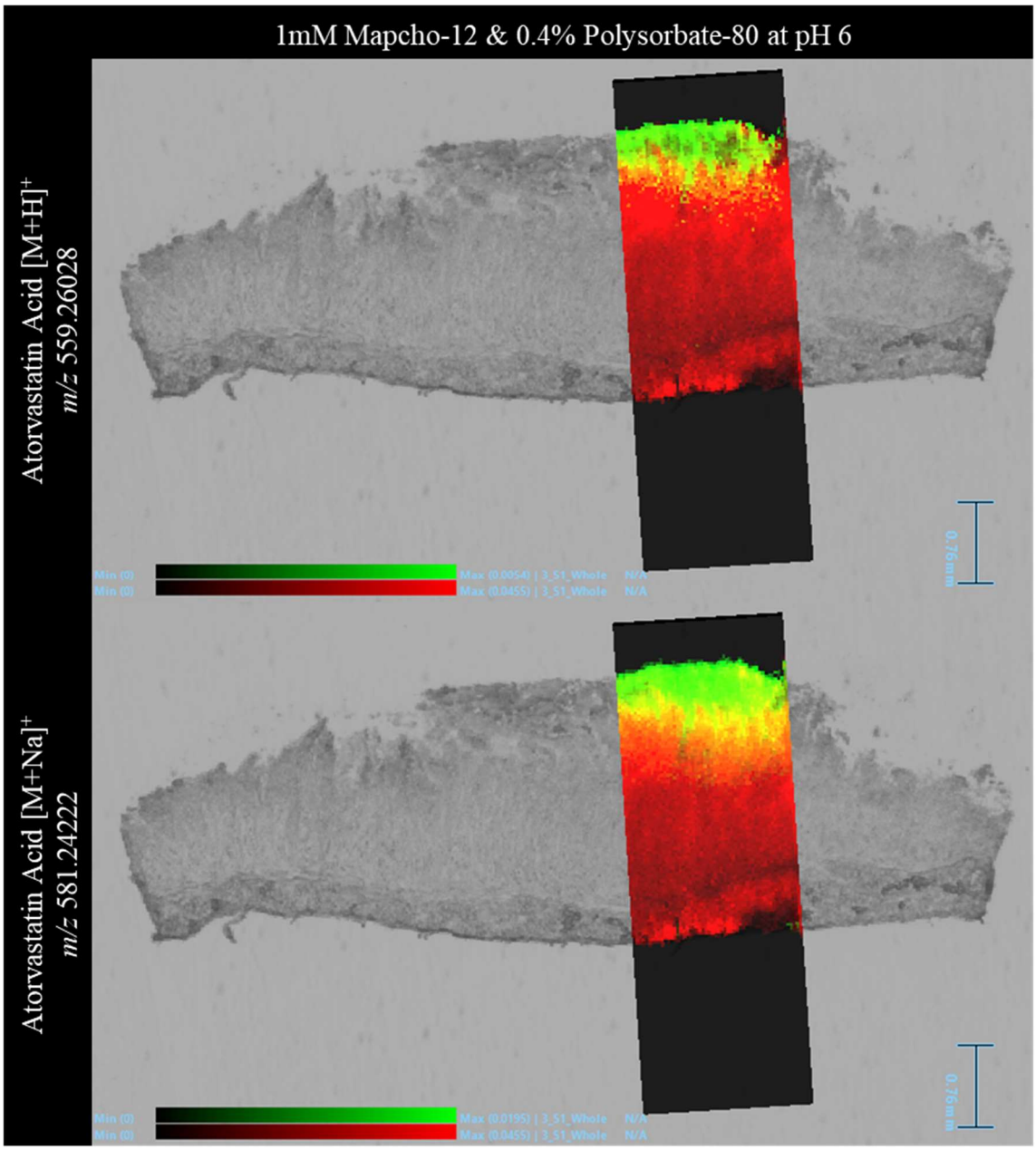

Figure 4.82: *DESI images overlaid onto an optical image of the tissue section they were acquired from with the surface of the tissue facing upwards. The tissue section was acquired from a fresh tissue absorption experiment with 1 mM mapcho-12 and 0.4% polysorbate-80 in the donor circuit buffered to pH 6 and 10% FBS in the acceptor circuit. The distribution of the lipid ion m/z 780.5 has been displayed in a red colour scale. The distribution of protonated atorvastatin acid and its sodium adduct were shown in the top and bottom window, respectively, using a green colour scale. All identified drug related ions were within 1ppm.*

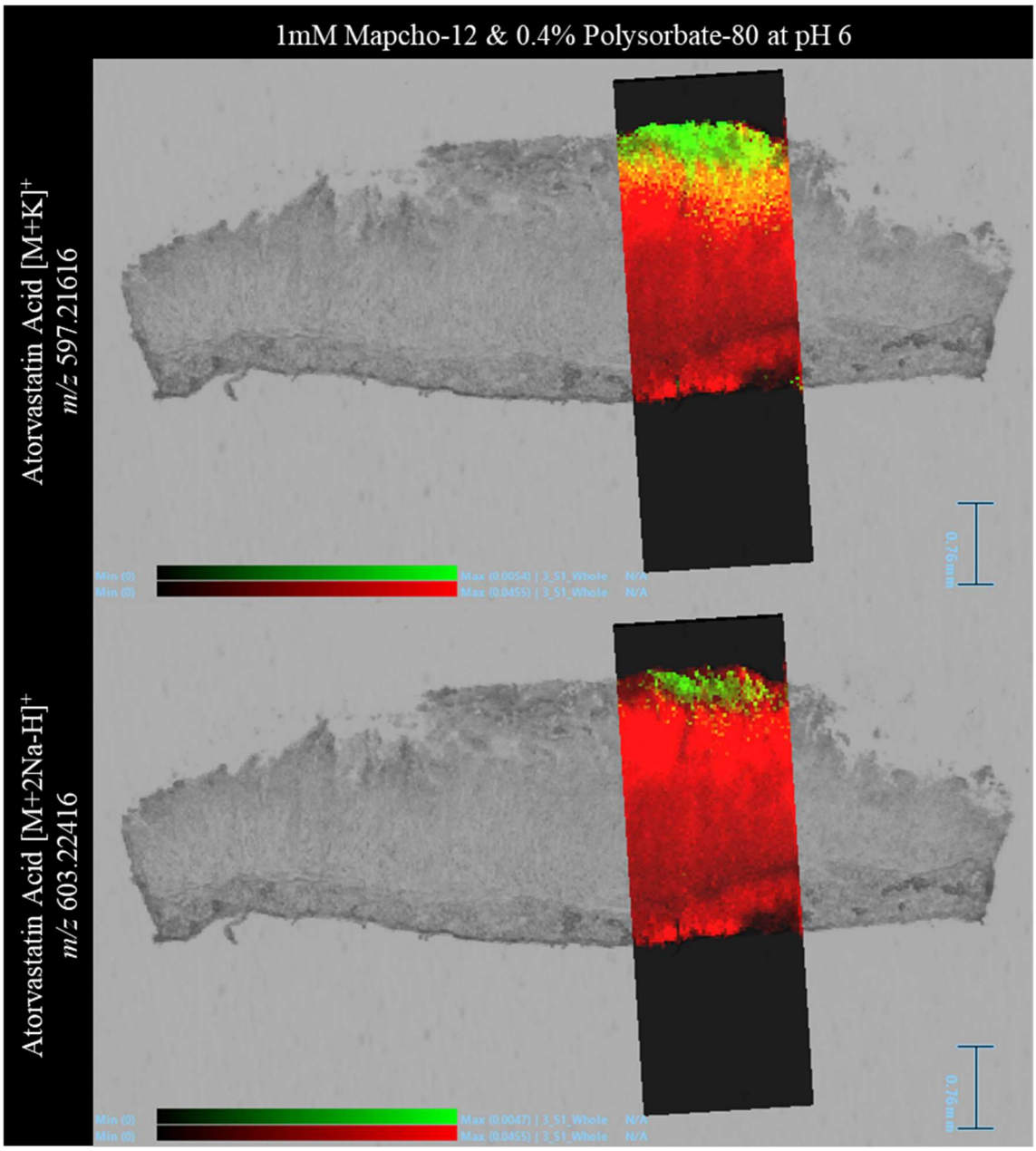

Figure 4.83: *DESI images overlaid onto an optical image of the tissue section they were acquired from with the surface of the tissue facing upwards. The tissue section was acquired from a fresh tissue absorption experiment with 1 mM mapcho-12 and 0.4% polysorbate-80 in the donor circuit, buffered to pH 6. The distribution of the lipid ion m/z 780.5 was displayed in a red colour scale. Potassium and $[M+2Na-H]^+$ adducts of atorvastatin acid were shown from top to bottom, respectively, using a green colour scale. All identified drug related ions were within 1 ppm.*

Protonated atorvastatin acid along with its sodium and potassium adducts were visible in DESI images from each experiment. Amongst these ions, the most prominent distributions resulted from the sodium adduct of atorvastatin. In each DESI image, the ion was heavily localised along the entire surface of the tissue, extending through a portion of the upper tissue layer. Additional distributions of the sodium adduct were shown in DESI images acquired from experiments with 1 mM mapcho-12 and without. When no mapcho-12 was present in the circuit, atorvastatin acid was shown to be sparsely distributed along the length of the final tissue layer. Furthermore, a similar distribution was observed in the 1 mM mapcho-12 experiment although, this was isolated to a small area in the final layer which covered a significantly lower surface area. Intriguingly, these experiments were also shown to have the highest concentrations of atorvastatin acid in the tissue extracts.

As previously seen and discussed, there was no signal shown in between the two distributions or, in the lower layers of the tissue section for some experiments. For this study there was a significant amount of atorvastatin acid shown to have permeated into the acceptor circuit and so, the sections were further analysed. ROIs were drawn on several areas of the tissue and the mass spectra extracted in attempt to detect lower levels of atorvastatin acid related ions. The results of this investigation were summarised in Table 4.12 and the specific location of each ROI have been detailed in Appendix I Figure 21-24.

Table 4.12: *A summary of whether the named atorvastatin related ions were detectable in different ROIs in the DESI image. The ROIs specified here included the whole tissue, an area on the tissue with no drug signal and an area away from the tissue. All data here relates to DESI images collected from the mapcho-12 and polysorbate-80 study performed at pH 6.*

Mapcho-12 with 0.4% Polysorbate-80 Study at pH 6					
Atorvastatin and Related Ions	ROI	Ion present in ROI? Concentration of Mapcho-12 (mM)			
		0	0.5	0.75	1
Atorvastatin Acid $[M+H]^+$ *m/z* 559.26028	Whole tissue?	✓	✓	✓	✓
	Within tissue away from drug distribution?	✓	✓	×	×
	Away from tissue?	×	×	×	×
Atorvastatin Acid $[M+Na]^+$ *m/z* 581.24222	Whole tissue?	✓	✓	✓	✓
	Within tissue away from drug distribution?	×	✓	×	×
	Away from tissue?	×	×	×	×
Atorvastatin Acid $[M+K]^+$ *m/z* 597.21616	Whole tissue?	✓	✓	✓	✓
	Within tissue away from drug distribution?	×	×	×	×
	Away from tissue?	×	×	×	×
Atorvastatin Acid $[M+2Na-H]^+$ *m/z* 603.22416	Whole tissue?	✓	✓	×	✓
	Within tissue away from drug distribution?	×	×	×	×
	Away from tissue?	×	×	×	×

In some of the ROIs drawn away from the visualised drug distribution, atorvastatin acid ions were successfully detected in low levels. Thus, proving that the software does not allow the full visualisation of all detectable amounts of the same ion. The DESI MS data from this study were also checked for the presence of atorvastatin metabolites. The DESI images collected were shown in Figures 4.84-4.88.

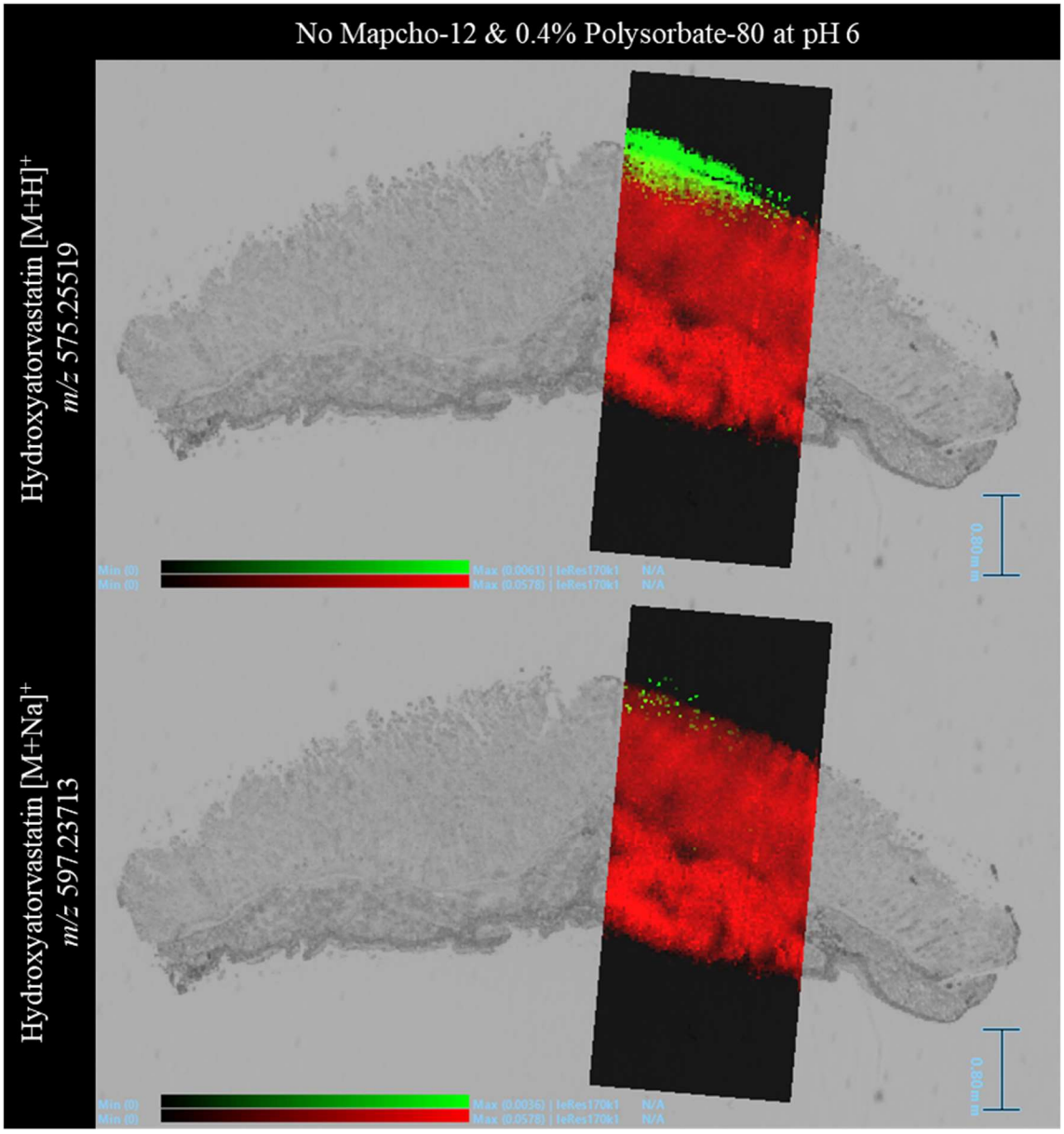

Figure 4.84: *DESI images overlaid onto an optical image of the tissue section they were acquired from with the surface of the tissue facing upwards. The tissue section was acquired from a fresh tissue absorption experiment with 0.4% polysorbate-80 in the donor circuit buffered to pH 6 and 10% FBS in the acceptor circuit. The distribution of the lipid ion m/z 780.5 has been displayed in a red colour scale. The distribution of the protonated metabolite, hydroxyatorvastatin, and its sodium adduct were shown in the top and bottom window, respectively, using a green colour scale. The metabolite ions were within 1 ppm.*

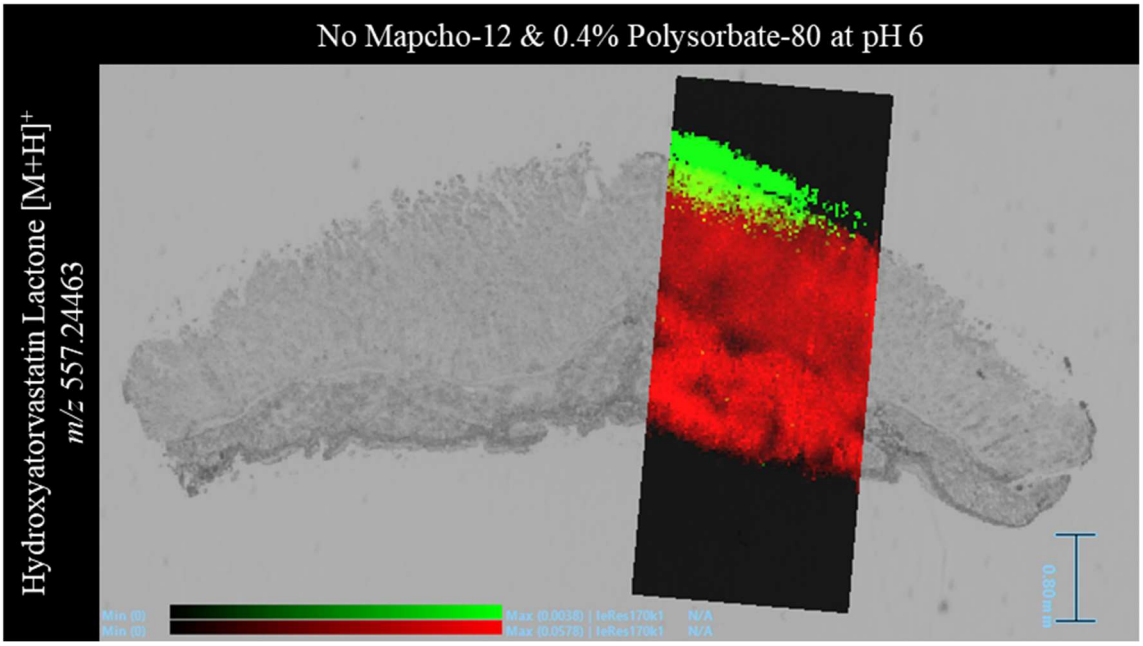

Figure 4.85: *DESI image overlaid onto an optical image of the tissue section it was acquired from with the surface of the tissue facing upwards. The tissue section was acquired from a fresh tissue absorption experiment with 0.4% polysorbate-80 in the donor circuit buffered to pH 6 and 10% FBS in the acceptor circuit. The distribution of the lipid ion m/z 780.5 and the protonated metabolite hydroxyatorvastatin lactone was displayed in a red and green colour scale, respectively. The metabolite ion was within 1 ppm.*

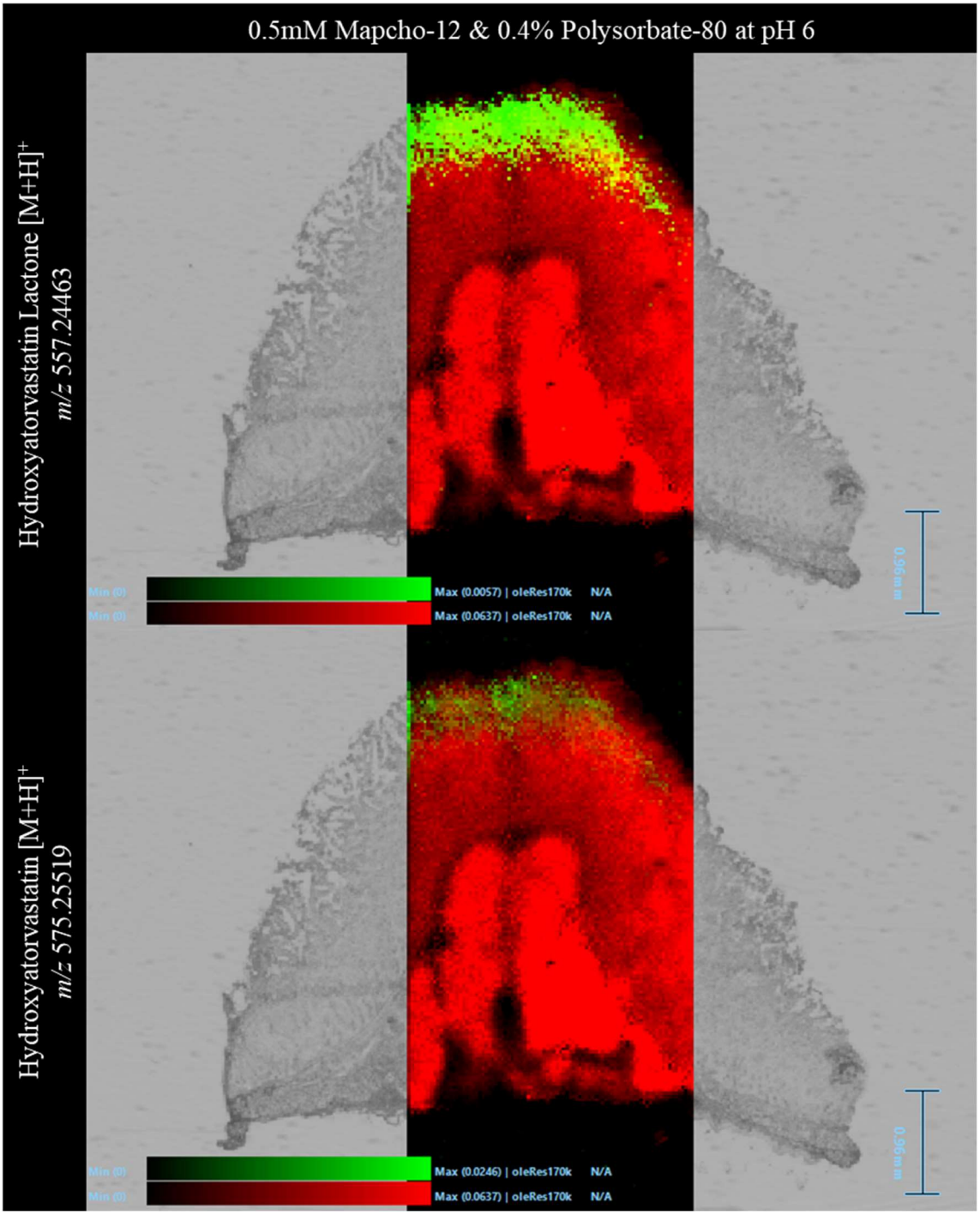

Figure 4.86: *DESI images overlaid onto an optical image of the tissue section they were acquired from with the surface of the tissue facing upwards. The tissue section was acquired from a fresh tissue absorption experiment with 0.5 mM mapcho-12 and 0.4% polysorbate-80 in the donor circuit buffered to pH 6 and 10% FBS in the acceptor circuit. The distribution of the lipid ion m/z 780.5 has been displayed in a red colour scale. The distribution of the protonated metabolites, hydroxyatorvastatin lactone and hydroxyatorvastatin were shown in the top and bottom window, respectively, using a green colour scale. The metabolite ions were within 1 ppm.*

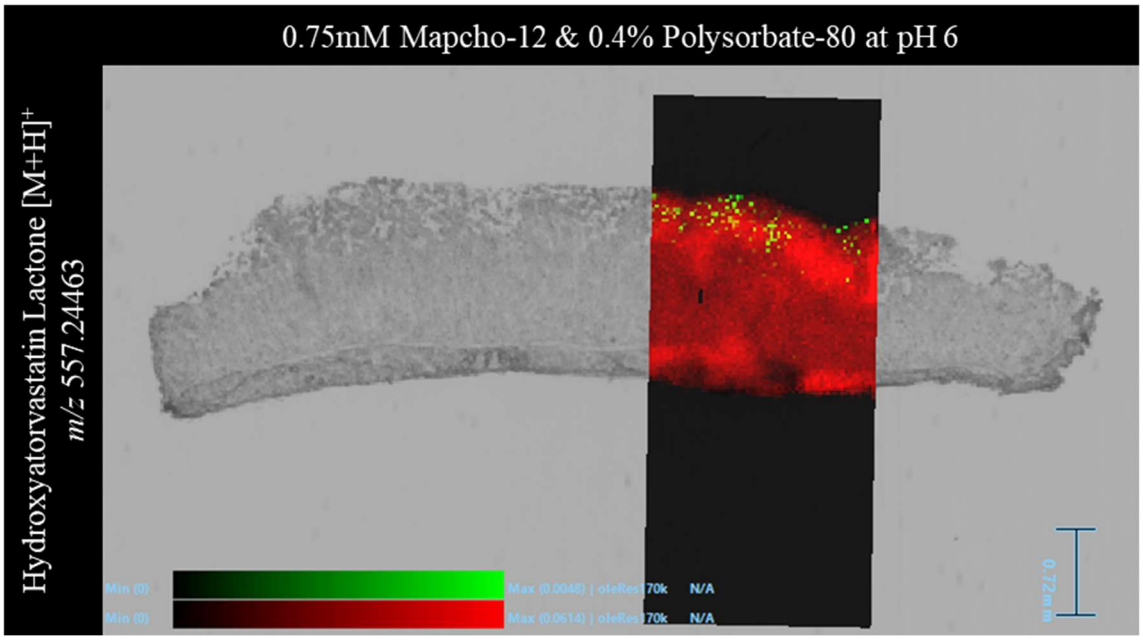

Figure 4.87: *DESI image overlaid onto an optical image of the tissue section it was acquired from with the surface of the tissue facing upwards. The tissue section was acquired from a fresh tissue absorption experiment with 0.75mM mapcho-12 and 0.4% polysorbate-80 in the donor circuit buffered to pH 6 and 10% FBS in the acceptor circuit. The distribution of the lipid ion m/z 780.5 and the protonated metabolite hydroxyatorvastatin lactone was displayed in a red and green colour scale, respectively. The metabolite ion was within 1 ppm.*

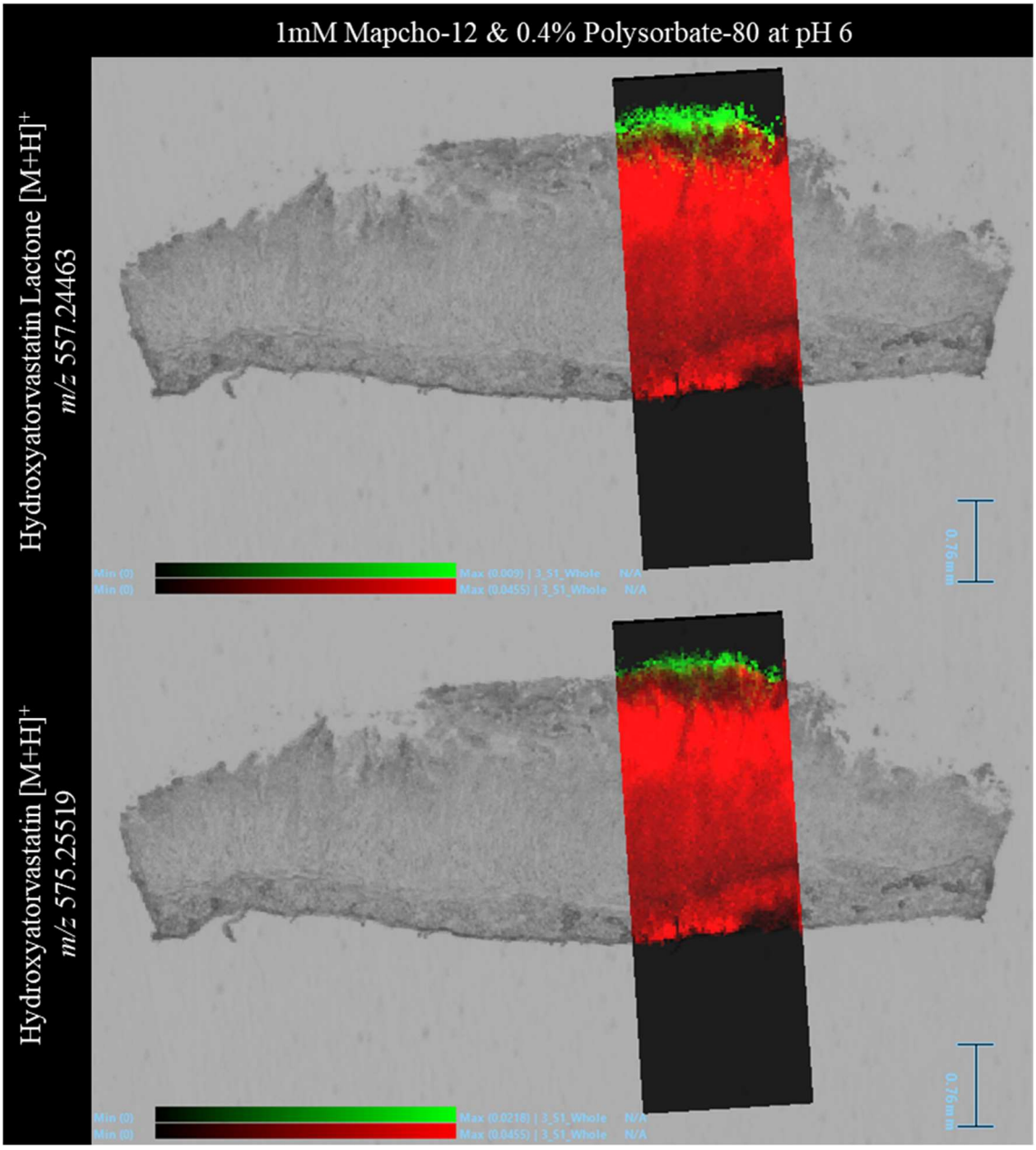

Figure 4.88: *DESI images overlaid onto an optical image of the tissue section they were acquired from with the surface of the tissue facing upwards. The tissue section was acquired from a fresh tissue absorption experiment with 1 mM mapcho-12 and 0.4% polysorbate-80 in the donor circuit buffered to pH 6 and 10% FBS in the acceptor circuit. The distribution of the lipid ion m/z 780.5 has been displayed in a red colour scale. The distribution of the protonated metabolites, hydroxyatorvastatin lactone and hydroxyatorvastatin were shown in the top and bottom window, respectively, using a green colour scale. The metabolite ions were within 1 ppm.*

Metabolites hydroxyatorvastatin and hydroxyatorvastatin lactone were identified throughout the study. The distribution of these ions was within that of the corresponding atorvastatin acid ion. This, along with the extremely low mass error, corroborated the ion assignment. Notably, the metabolite distribution covered much less surface area than the atorvastatin acid ions. The previous ROIs were checked for signals from any of the known atorvastatin metabolite ions; the findings were summarised and shown in Table 4.13. In this case, there was only one instance in which a metabolite ion was detectable on the tissue away from the visual drug distribution.

Table 4.13: *A summary of whether the named atorvastatin metabolites were detectable in different ROIs in the DESI image. The ROIs specified here included the whole tissue, an area on the tissue with no drug signal and an area away from the tissue. All data here relates to DESI images collected from the mapcho-12 and polysorbate-80 study performed at pH 6.*

Mapcho-12 with 0.4% Polysorbate-80 Study at pH 6					
Atorvastatin Metabolites	ROI	Ion present in ROI? Concentration of Mapcho-12 (mM)			
		0	0.5	0.75	1
Hydroxyatorvastatin $[M+H]^+$ *m/z* 575.25519	Whole tissue?	✓	✓	✓	✓
	Within tissue away from drug distribution?	×	×	×	×
	Away from tissue?	×	×	×	×
Hydroxyatorvastatin $[M+Na]^+$ *m/z* 597.23713	Whole tissue?	✓	✓	×	✓
	Within tissue away from drug distribution?	×	×	×	×
	Away from tissue?	×	×	×	×
Hydroxyatorvastatin Lactone $[M+H]^+$ *m/z* 557.24463	Whole tissue?	✓	✓	✓	✓
	Within tissue away from drug distribution?	×	✓	×	×
	Away from tissue?	×	×	×	×
Hydroxyatorvastatin Lactone $[M+Na]^+$ *m/z* 579.22657	Whole tissue?	×	✓	×	✓
	Within tissue away from drug distribution?	×	×	×	×
	Away from tissue?	×	×	×	×

The tissue rinsing solutions collected from this study were analysed to see how much atorvastatin remained on the surface of the tissue. The amount of atorvastatin acid recovered from the tissue rinse solution was plotted against the concentration of mapcho-12 present in the donor circuit and is displayed in Figure 4.89.

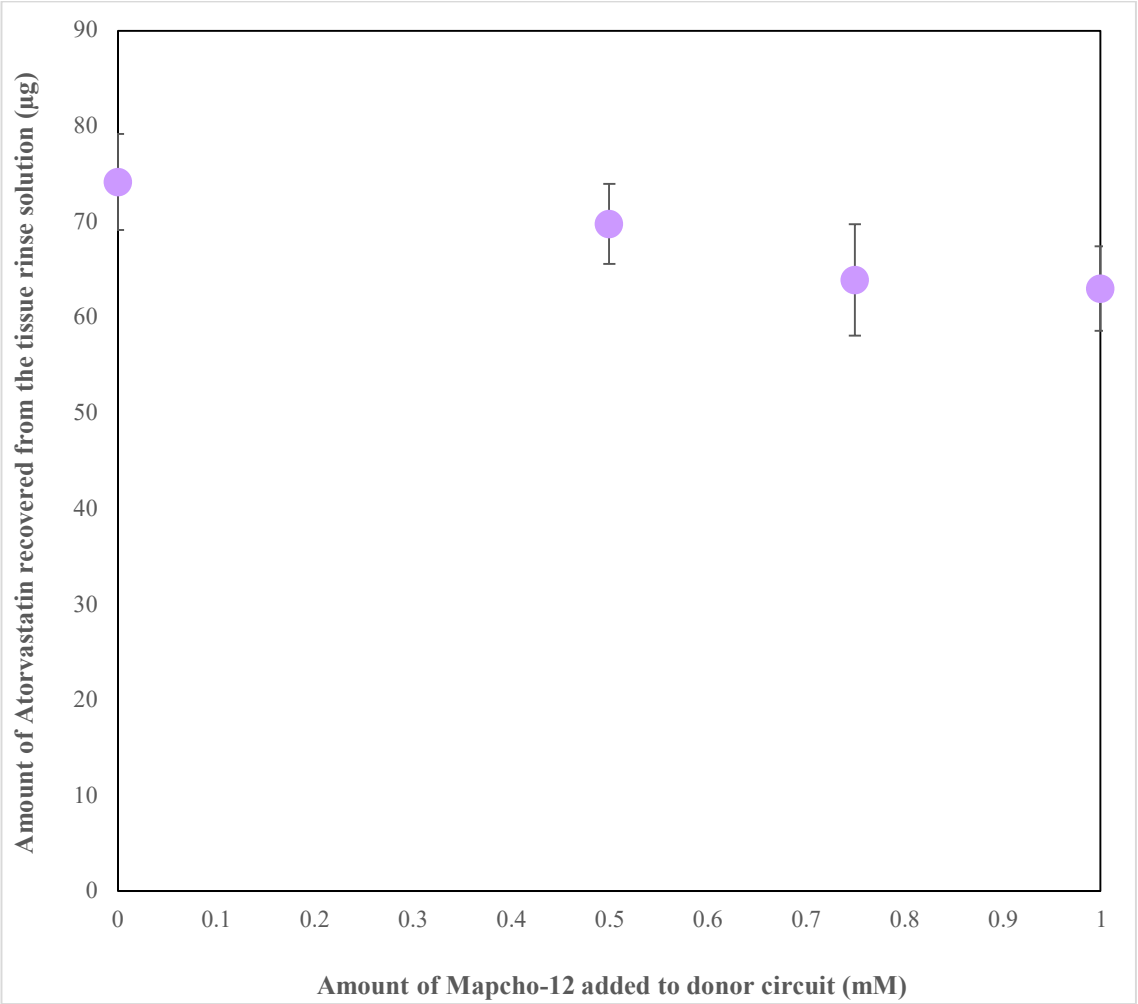

Figure 4.89: *A graph to show the amount of Atorvastatin that was rinsed from the tissue discs plotted against the concentration of mapcho-12 added to 0.4% Polysorbate-80 in the donor circuit (pH 6) of the corresponding absorption experiment. The data presented here is from the Mapcho-12 with 0.4 % (v/v) Polysorbate-80 study performed at pH 6 (n=3).*

A one-way ANOVA test found that as the concentration of mapcho-12 in the donor circuit was increased, there were no significant differences in the amount of atorvastatin acid recovered from the tissue rinsing solution. In addition to this, a similar amount of atorvastatin was recovered in comparison to other experiments which used the highest amount of polysorbate-80. Thus, indicative that the drug remained relatively in solution. Importantly, atorvastatin would always remain detectable in this solution to some extent as a film of donor circuit solution would be present on the tissue surface.

The amount of atorvastatin recovered from the initial system rinse solution was plotted against the concentration of mapcho-12 in the donor circuit and shown in Figure 4.90. A similar pattern was observed in the solution used to rinse the system after it had been drained following an absorption experiment. A one-way ANOVA test confirmed that as the concentration of mapcho-12 in the donor circuit was increased, there were no statistically significant differences in the amount of atorvastatin acid recovered from the solution used to rinse the system. This would suggest that the presence of mapcho-12 had no significant effect on the solubility of atorvastatin in PBS.

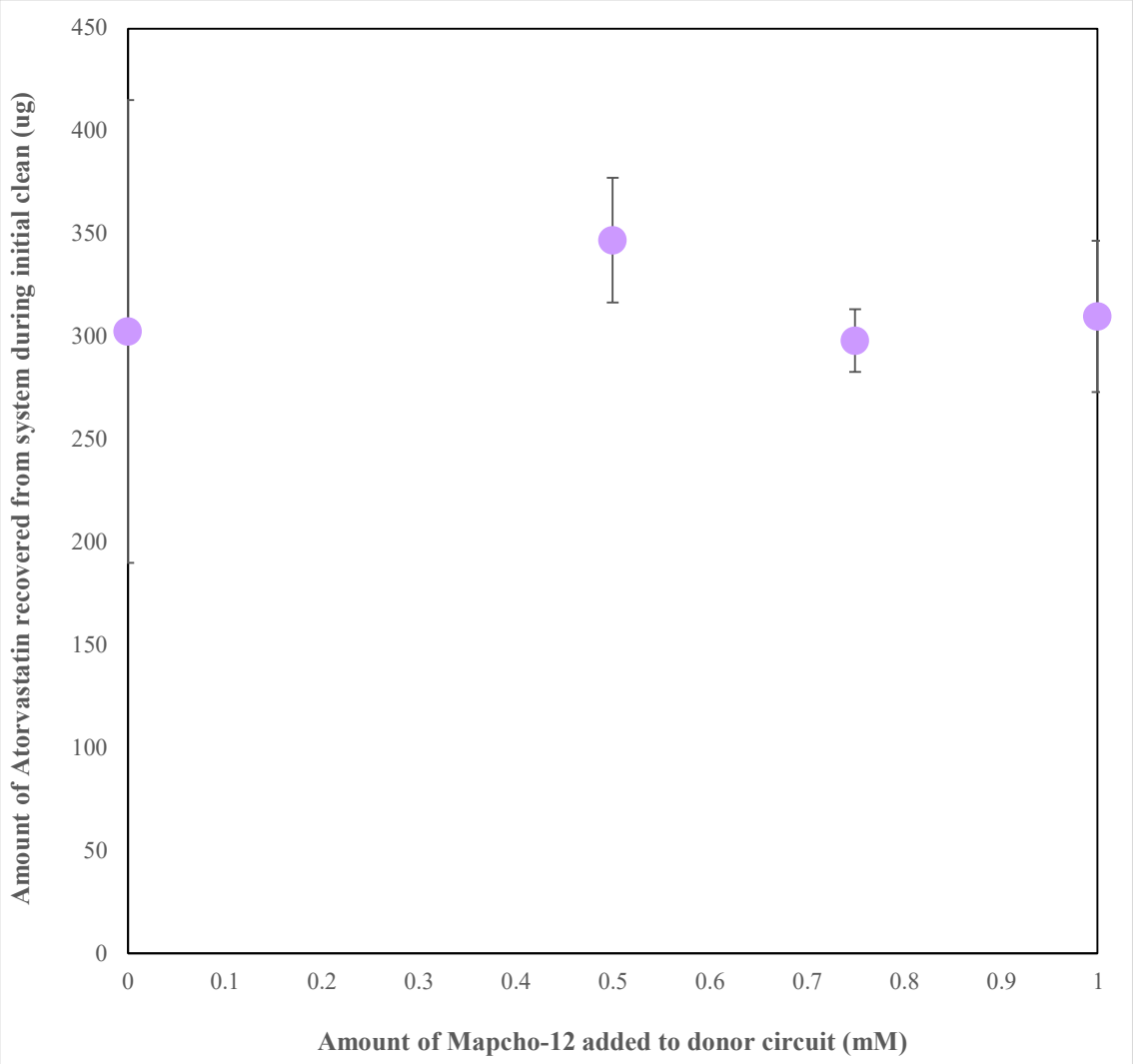

Figure 4.90: *A graph showing the amount of Atorvastatin that was recovered from the QV600 LLI after the system had been drained following an absorption experiment with varied concentrations of mapcho-12 along with 0.4% Polysorbate-80 in the donor circuit (pH 6) of the corresponding absorption experiment. The data presented here is from the Mapcho-12 with 0.4 % (v/v) Polysorbate-80 study performed at pH 6 (n=3).*

Both rinsing solutions, tissue and system, strongly suggest that minimal amounts of atorvastatin acid had fallen out of solution and settled on the surface of the tissue. However, all DESI images from this study demonstrated a saturated layer of atorvastatin acid on the surface of the tissue despite rinsing the surface prior to imaging. A logical explanation for this would be that the drug became saturated within the sticky mucus layer that surrounds the surface of the villi. Considering the issues with thresholding data on the DESI MRT previously discussed, this would provide a rational justification for the over-powering signal consistently shown on the surface throughout all studies, regardless of the drug solubility.

4.4.5 Partial Mucus Removal Study

In attempt to assess the effects of the mucus layer on the visualisation and permeation of atorvastatin, a small study was conducted in which the mucus layer was partially removed. The study consisted of an experiment ran in triplicate in which 0.4% polysorbate-80 was buffered to pH 6 in the donor circuit. It was not possible to completely remove the mucus layer without jeopardising the structure and integrity of the tissue. Therefore, a partial removal method previously reported (Arnold et al., 2019) was employed. Ice-cold KRS was added to the transport bags to help loosen the mucus away from the surface of the tissue. Once the tissue had reached the lab, a small portion of the tissue was thoroughly rinsed with more ice-cold KRS. This process was repeated until the rinsing solution was clear. Photographs were taken of the tissue when it reached the lab and after the intensive rinsing at the start of each experiment in the study. The images acquired are displayed in Figure 4.91.

Figure 4.91 highlights the differences in volume, appearance and texture of the mucus present between individual tissue samples. In addition to this, it shows the inconsistency of mucus deposition across the intestine within the same individual. The images also show the degree in which mucus had been removed to the naked eye. For example, in Figure 4.91B some mucus can be seen to remain after the intensive rinsing step.

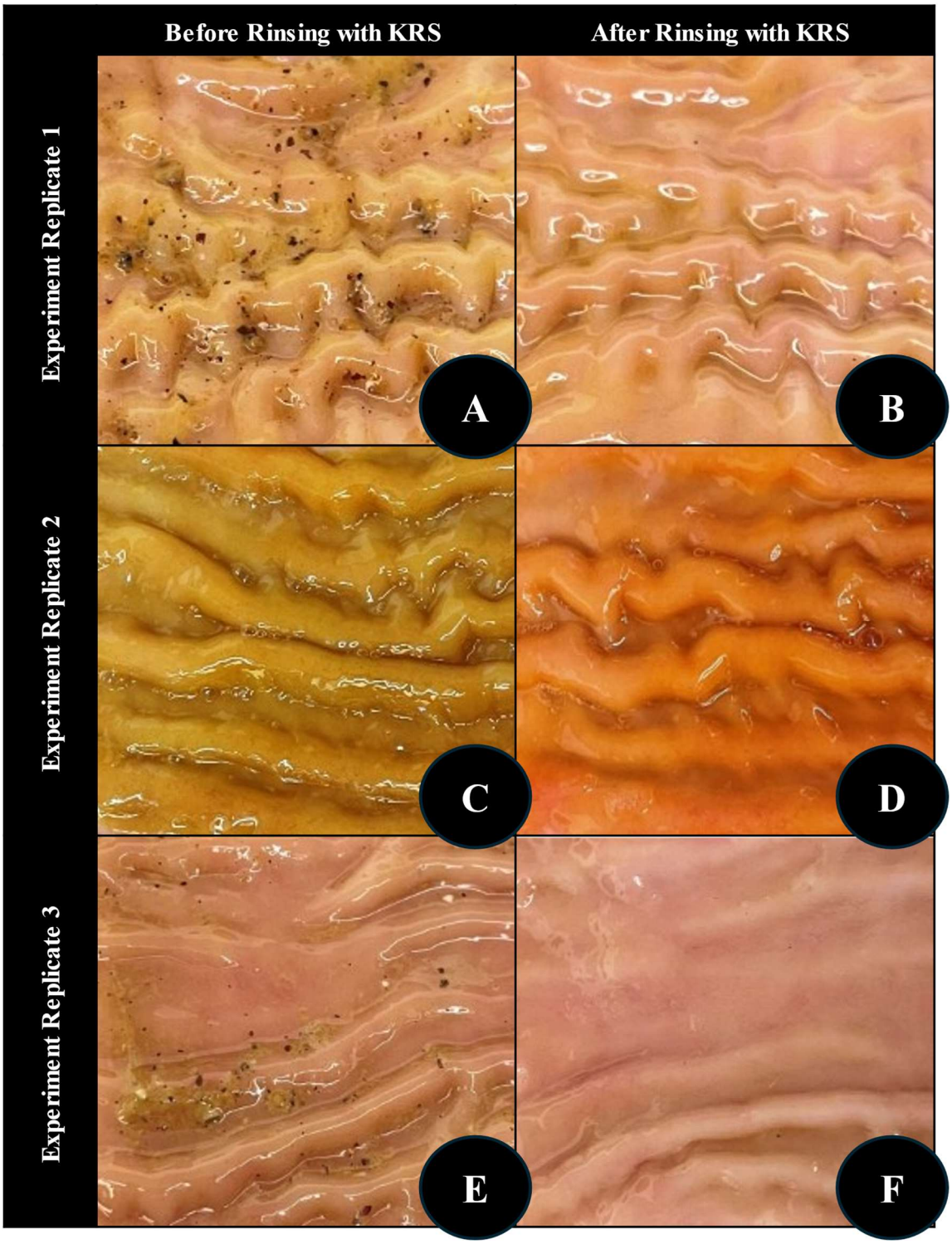

Figure 4.91: *A collection of optical images taken of intestinal tissue taken prior to and immediately after intensive rinsing with KRS. Each experiment replicate refers to a different absorption experiment performed on separate days and thus, use different pigs.*

A tissue disc was taken and extracted from each of the experiments in this study and plotted as yellow data points in Figure 4.92. From other studies performed at pH 6,

experiments with the same formulation (only 0.4% polysorbate-80 in the donor circuit) were also plotted and were essentially replicates that spanned over many studies.

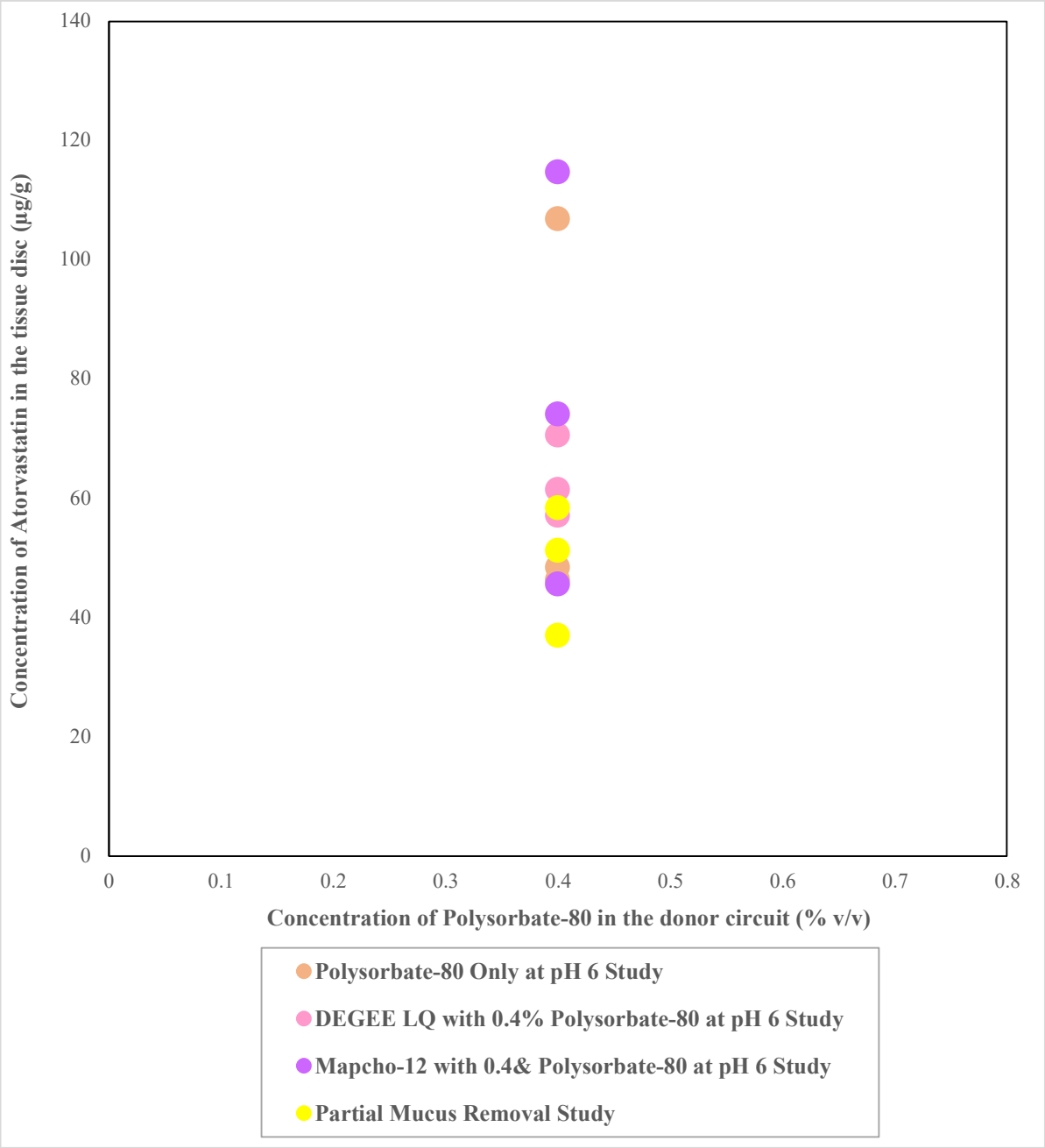

Figure 4.92: *A graph to show the concentration of atorvastatin calculated in the tissue extracts plotted against the amount of polysorbate-80 in the donor circuit from numerous studies. From the studies listed in the graph legend, experiments with only 0.4% polysorbate-80 in donor circuit buffered to pH 6 were plotted and were essentially replicates spanned over many studies.*

All absorption experiments plotted in Figure 4.92 were essentially replicate experiments despite spanning over several studies. The only exception being the current study, represented by yellow markers, as the mucus was intentionally removed. Despite this, a large variation can be seen in the concentration of atorvastatin calculated from each tissue disc across all of the experiments. While a clear distinction could not be made between the 'partial mucus removal' study and the other studies statistically, all data points were consistently shown on the lower end of the average. This was rather interesting considering that the optical images shown in Figure 4.91 highlight how little mucus can be naturally present in some cases. In addition, not all mucus could be removed from the tissue surface in this study. Thus, it remains possible that the amount of atorvastatin retrieved from the tissue extracts was more of a reflection of the amount trapped in the mucus layer. Nevertheless, this remains to be a theory as there was no definitive distinction shown between the studies.

A tissue disc from one of the experiments was then analysed by DESI MSI to visualise how a partial mucus removal would affect the atorvastatin acid distribution that could be visualised. DESI images were acquired for common atorvastatin acid adducts and are displayed in Figure 4.93 and 4.94.

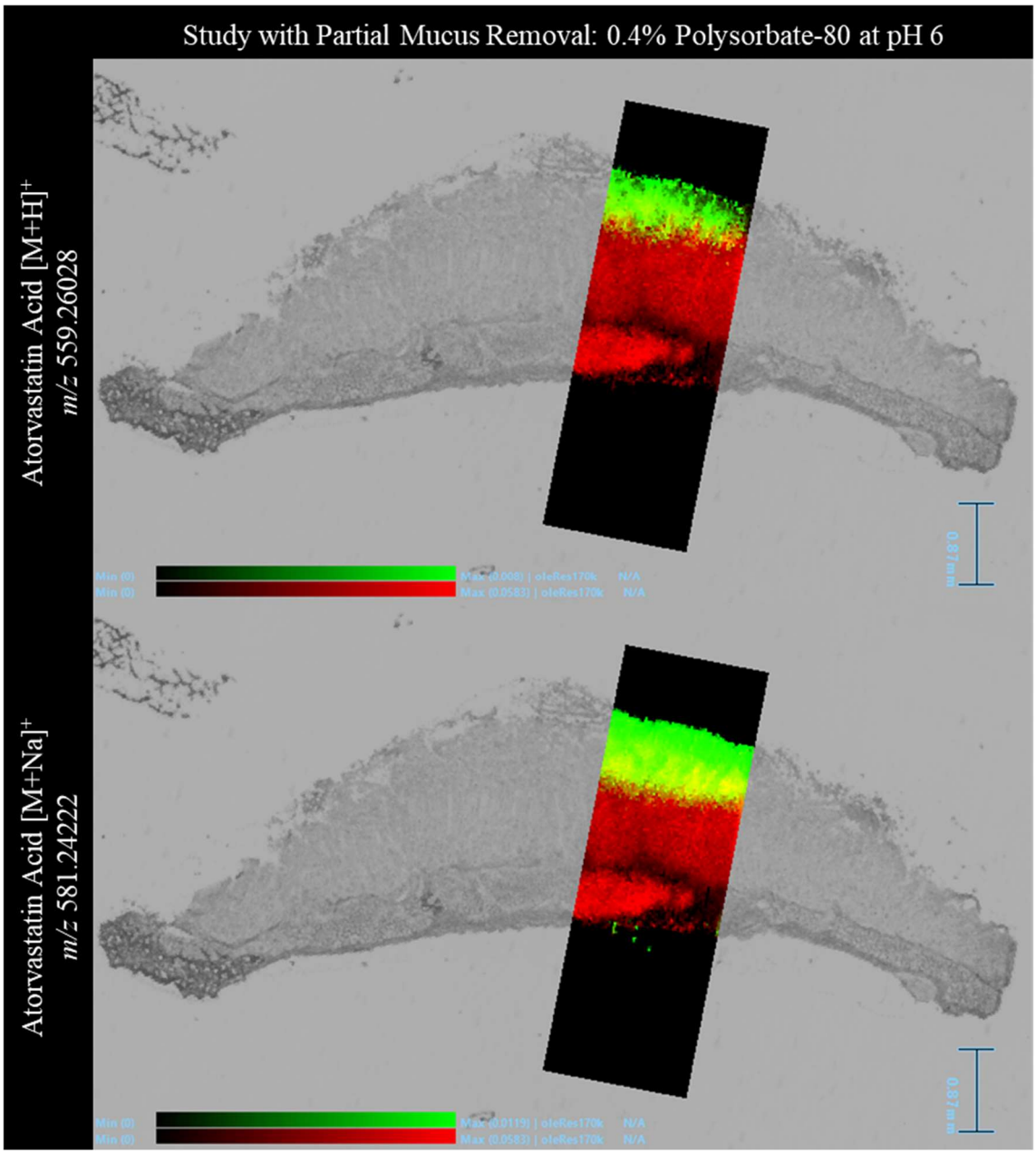

Figure 4.93: *DESI images overlaid onto an optical image of the tissue section they were acquired from with the surface of the tissue facing upwards. The tissue section was acquired from a fresh tissue absorption experiment with 0.4% polysorbate-80 in the donor circuit buffered to pH 6 and 10% FBS in the acceptor circuit. The tissue had been thoroughly rinsed with ice-cold KRS prior to starting the experiment. The distribution of the lipid ion m/z 780.5 has been displayed in a red colour scale. The distribution of protonated atorvastatin acid and its sodium adduct were shown in the top and bottom window, respectively, using a green colour scale. All identified drug related ions were within 1ppm.*

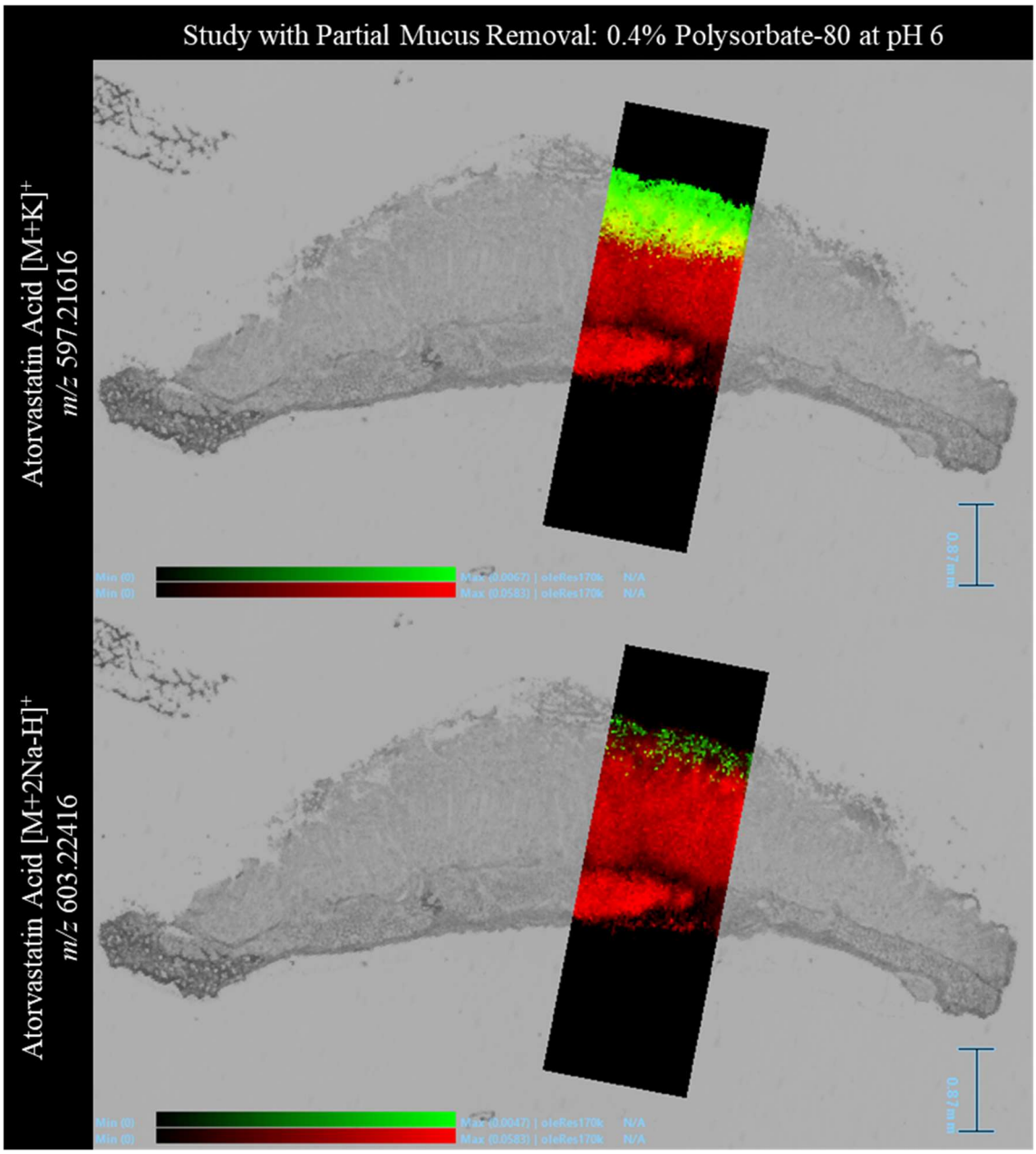

Figure 4.94: *DESI images overlaid onto an optical image of the tissue section they were acquired from with the surface of the tissue facing upwards. The tissue section was acquired from a fresh tissue absorption experiment with 0.4% polysorbate-80 in the donor circuit buffered to pH 6 and 10% FBS in the acceptor circuit. The tissue had been thoroughly rinsed with ice-cold KRS prior to starting the experiment. The distribution of the lipid ion m/z 780.5 has been displayed in a red colour scale. The distribution of potassium and $[M+2Na-H]^+$ adducts of atorvastatin acid were shown in the top and bottom window, respectively, using a green colour scale. All identified drug related ions were within 1ppm.*

A similar distribution of atorvastatin was observed in the DESI images from this study compared to the studies reported earlier where the mucus was fully intact. Atorvastatin acid ions did not appear to penetrate deeper into the tissue sections with exception of the sodium adduct. In this particular DESI image, a few pixels showing the atorvastatin acid sodium adduct ion could be seen on the very bottom of the tissue section with a few outside the perimeter of the lipid ions. Nevertheless, atorvastatin ions were not shown in the mid range of the tissue section. ROIs were drawn on the tissue away from any drug-related pixels in attempt to detect any lower levels of atorvastatin acid in the tissue. ROIs were also drawn around the whole tissue and an area away from the tissue for comparison. The results of this investigation were summarised in Table 4.14 and the specific location of each ROI have been detailed in Appendix I Figure 25.

Table 4.14: *A summary of whether the named atorvastatin related ions were detectable in different ROIs in the DESI image. The ROIs specified here included the whole tissue, an area on the tissue with no drug signal and an area away from the tissue. All data relates to DESI images collected from partial mucus removal study performed at pH 6.*

Study with Partial Mucus Removal using 0.4% Polysorbate-80 at pH 6		
Atorvastatin and Related Ions	ROI	Ion present in ROI?
Atorvastatin Acid $[M+H]^+$ *m/z* 559.26028	Whole tissue?	✓
	Within tissue away from drug distribution?	×
	Away from tissue?	×
Atorvastatin Acid $[M+Na]^+$ *m/z* 581.24222	Whole tissue?	✓
	Within tissue away from drug distribution?	×
	Away from tissue?	×
Atorvastatin Acid $[M+K]^+$ *m/z* 597.21616	Whole tissue?	✓
	Within tissue away from drug distribution?	×
	Away from tissue?	×
Atorvastatin Acid $[M+2Na-H]^+$ *m/z* 603.22416	Whole tissue?	✓
	Within tissue away from drug distribution?	×
	Away from tissue?	×

No atorvastatin acid related ions were detected in the ROIs drawn away from the visual drug distribution. The DESI MS data was checked for any visual signals from known atorvastatin metabolites. The DESI images acquired are displayed in Figure 4.95.

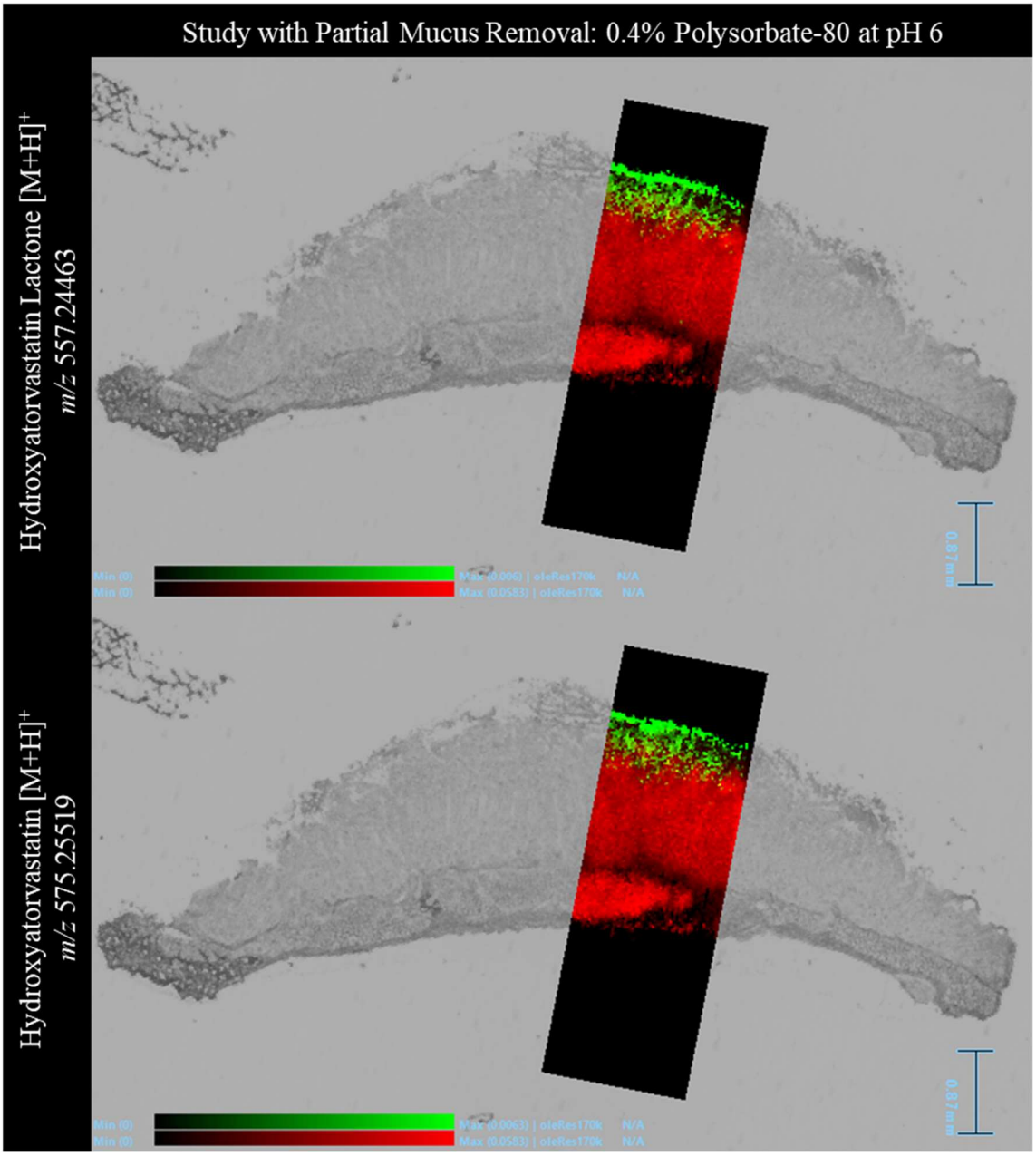

Figure 4.95: *DESI images overlaid onto an optical image of the tissue section they were acquired from with the surface of the tissue facing upwards. The tissue section was acquired from a fresh tissue absorption experiment with 0.4% polysorbate-80 in the donor circuit buffered to pH 6 and 10% FBS in the acceptor circuit. The tissue had been thoroughly rinsed with ice-cold KRS prior to starting the experiment. The distribution of the lipid ion m/z 780.5 has been displayed in a red colour scale. The distribution of protonated metabolites hydroxyatorvastatin and hydroxyatorvastatin lactone were shown in the top and bottom window, respectively, using a green colour scale. All identified metabolite ions were within 1ppm.*

Metabolites hydroxyatorvastatin and hydroxyatorvastatin lactone were shown to be present in the tissue section. Both metabolites presented a near identical distribution on the upper layer of the tissue. This distribution was localised in a similar area to the atorvastatin acid ions shown previously although, both metabolites covered a much smaller surface area of the tissue. The same ROIs as previously discussed were analysed for any signals from all known atorvastatin metabolites. The results were summarised in Table 4.15.

Table 4.15: *A summary of whether the named atorvastatin metabolite ions were detectable in different ROIs in the DESI image. The ROIs specified here included the whole tissue, an area on the tissue with no drug signal and an area away from the tissue. All data relates to DESI images collected from partial mucus removal study*

Study with Partial Mucus Removal using 0.4% Polysorbate-80 at pH 6		
Atorvastatin Metabolites	ROI	Ion present in ROI?
Hydroxyatorvastatin $[M+H]^+$ *m/z* 575.25519	Whole tissue?	✓
	Within tissue away from drug distribution?	×
	Away from tissue?	×
Hydroxyatorvastatin $[M+Na]^+$ *m/z* 597.23713	Whole tissue?	✓
	Within tissue away from drug distribution?	×
	Away from tissue?	×
Hydroxyatorvastatin Lactone $[M+H]^+$ *m/z* 557.24463	Whole tissue?	✓
	Within tissue away from drug distribution?	×
	Away from tissue?	×
Hydroxyatorvastatin Lactone $[M+Na]^+$ *m/z* 579.22657	Whole tissue?	✓
	Within tissue away from drug distribution?	×
	Away from tissue?	×

As was found with atorvastatin acid, no metabolite ions were detectable in the mass spectra collected from the ROI on the tissue away from the visual drug distribution. This interpretation alone would suggest that the drug has not moved into the lower layers of the tissue however, the permeation values suggest otherwise. The permeation

coefficient values from the 'partial mucus removal' study have been plotted against the concentration of polysorbate-80 in Figure 4.96.

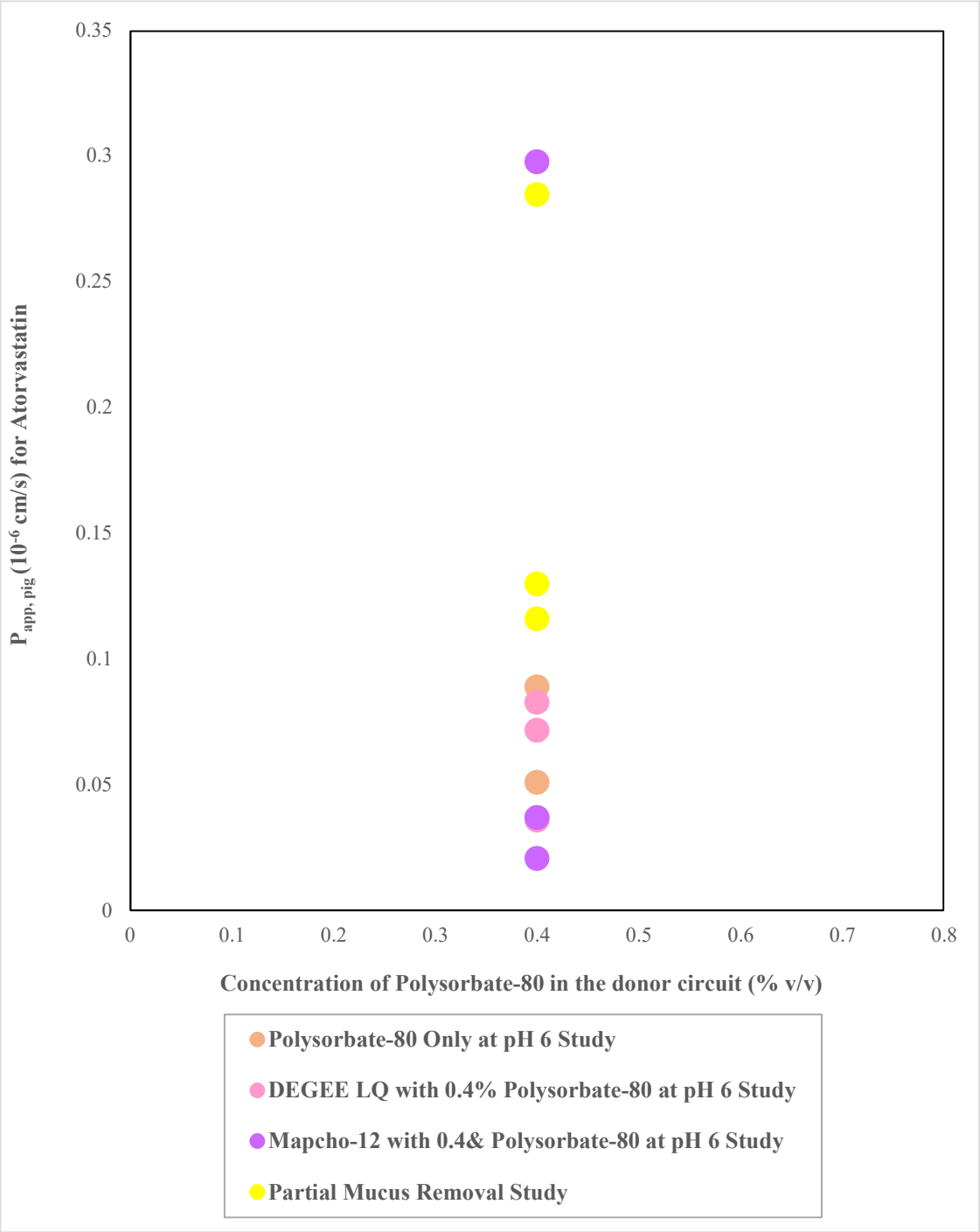

Figure 4.96: *The calculated permeation coefficient values plotted against the amount of polysorbate-80 in the donor circuit for numerous studies. From the studies listed in the graph legend, experiments with only 0.4% polysorbate-80 in donor circuit buffered to pH 6 were plotted and were essentially replicates spanned over many studies.*

The values from the ‘partial mucus removal’ study were plotted against other studies that used the same pH and amount of excipient, and thus were essentially replicate experiments. When the mucus was partially removed, the permeation coefficients were on the higher end of the scale than those without physical interference to the mucus. There was one exception where a permeation coefficient slightly exceeded that of the data points from the partial mucus removal study. Using an unpaired t test, no statistically significant differences were identified between those with and without mucus. As was observed in the optical images, there was great variation in the mucus present on the intestinal surface and one image in particular showed an area with no apparent mucus prior to removal. Therefore, it remains possible that some data points reflect this scenario and as such, skewed the statistics.

While this study highlighted the variation in mucus between individuals and hinted at a source of variation for the permeation observed, this should still be regarded as an essential obstacle to be studied as it poses a real-life challenge. The work reported here represents a model much closer to the real-life situation than models without mucus.

4.4.6 Mass Balance Evaluation

Before any conclusions were drawn, the mass balances for each experiment were calculated. The percentage of atorvastatin recovered was plotted against the experiment number and this is shown in Figure 4.97. The experiments were numbered in order of study occurrence followed by the increasing excipient concentration. Each study is represented with different coloured data points that linked with the colours used in previous graphs. The lowest percentage considered to be an acceptable mass balance was also plotted onto the graph in the form of a thick black line. From the graph, it was clear that the majority of the absorption experiments conducted gave recoveries that fell under the normal acceptable range.

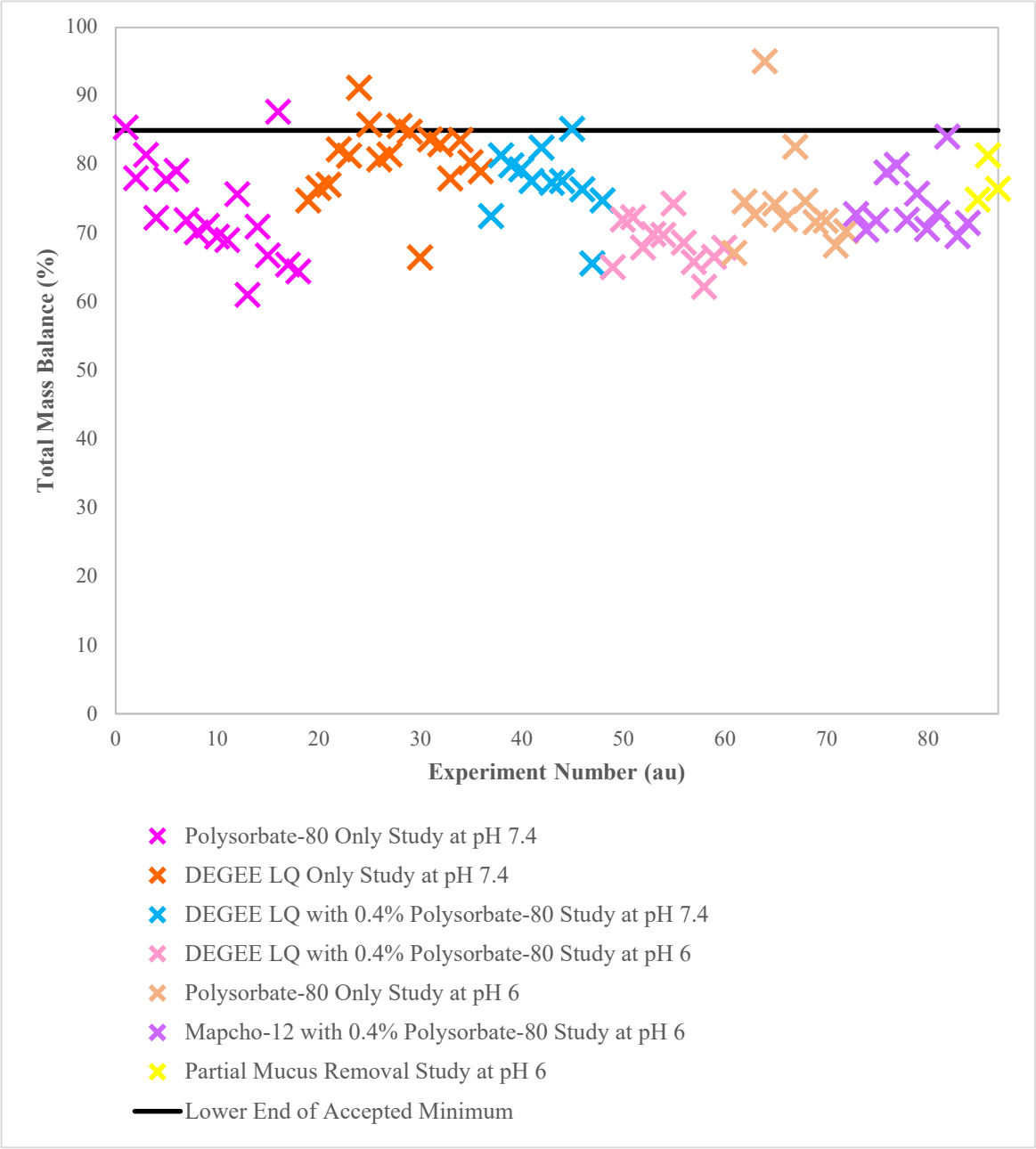

Figure 4.97: *The total percentage mass balance from each experiment plotted against the corresponding experiment number. The absorption experiments from different studies were denoted by the colour of the data point as shown in the legend. The experiment number increased with the timeline of the study and increase in excipient concentration per study.*

In chapter 2, all mass balances reported were within the accepted range. A key difference in the analysis of the data from chapter 2 and the data shown here were the extraction techniques. After frequent LC-MS/MS runs of the matrix-matched experiment samples prepared as detailed in Chapter 2, the column life was significantly reduced. A rise in back-pressure was observed along with drifting peak retention times and blockages. Therefore, certain samples in this chapter were prepared with an extra

sample preparation step as detailed in the methods section to improve the column life which in turn saved time, costs and reduced sample loss. The tissue extracts and initial system rinse solutions were primarily made up from 70-90% methanol and so, did not need further extraction. However, other samples made primarily from PBS and DMEM/F12 required further extraction. While steps were taken to increase the efficiency of extraction, it is clear that further improvements need to be made.

Two different formulations of atorvastatin were made in PBS and buffered to pH 6. One of the standards contained 0.4% polysorbate-80 in order to test the effect of an excipient on the extraction efficiency. Additionally, each standard was made in triplicate and extracted separately to assess the reproducibility between extractions. On the instrument, each extract was analysed in triplicate to provide information on the reproducibility of the data. The findings were summarised and shown in Table 4.16.

Table 4.16: *The extraction efficiencies calculated from two differently formulated atorvastatin standards that were made in triplicate. Atorvastatin was extracted from each standard replicate and analysed on the LC-MS/MS in triplicate; the extraction recovery from each instrument replicate was calculated in addition to the average for the instrument and standard replicates.*

		Atorvastatin Standard (0.5 mg/mL) in PBS at pH 6					
		No Excipient			0.4% Polysorbate-80		
Standard Replicate		1	2	3	1	2	3
Extraction Recovery (%)	1	74.46	78.42	77.76	76.11	78.21	77.47
Instrument Replicate	2	75.30	78.93	78.22	78.02	77.05	79.16
	3	77.49	77.84	76.34	77.59	75.51	76.30
Instrument Replicate Average		75.75	78.40	77.44	77.24	76.92	77.64
Total Average		77.19			77.27		

The extraction efficiency from known atorvastatin acid standards was found to be less than 80%. This finding was consistent between standards, regardless as to whether polysorbate-80 was present. The average extraction efficiency was indistinguishable between the standards with and without 0.4% polysorbate-80. This would suggest that the presence of polysorbate-80 in that quantity had no significant impact on the efficiency of extraction. There were very slight variances in all of the instrument replicates that were ran; similar variances were also observed between standard replicates. Thus suggesting that the standard replicates made were fairly reproducible.

The less-than-perfect extraction efficiencies shown could most definitely be responsible for the large portion of atorvastatin missing from the mass balance. The donor circuit fluid accounted for a large proportion of the mass balance and so, a reduction in extraction efficiency would have had a significant effect on the mass balance. Additionally, this would provide a logical explanation for the near-acceptable mass balances shown for 'DEGEE LQ only' study; due to the poor drug solubility exhibited in the donor circuit, a significantly higher portion of the mass balance was comprised from the system rinsing solution and this particular sample type required no extraction. The effect of other environmental factors should also be considered for an overall consensus of the extraction efficiency for all studies. Varied amounts of DEGEE LQ, mapcho-12, polysorbate-80 (in higher concentrations) as well as varied pH could have a profound impact on the efficiency of atorvastatin extraction.

Since the reduced extraction efficiency for PBS-based samples was proven to account for a large loss in the mass balance, it was imperative to assess the extraction efficiency for the acceptor circuit samples which contribute to the permeation coefficient values. A slightly different extraction method was used for the acceptor circuit values to take into consideration the presence of proteins and reverse any protein-binding that would affect the recovery of atorvastatin. A similar experiment was performed on atorvastatin standards to assess the extraction efficiency. Two different formulations of atorvastatin standards were used; one with 10% FBS and the other without. Each formulation was made in triplicate. From each standard replicate, three aliquots were taken for extraction. The intention was to ascertain how reproducible the extractions were when taken from the same standard. As with the other experiment, all extraction replicates were ran in triplicate on the LC-MS/MS. From the results, the extraction efficiencies were calculated and summarised in Table 4.17.

Table 4.17: *The extraction efficiencies calculated from two differently formulated atorvastatin standards that were made in triplicate. Three aliquots were taken from each standard replicate, underwent extraction and were analysed on the LC-MS/MS in triplicate; the percentage of atorvastatin recovered from each instrument replicate was calculated in addition to the average for the instrument and standard replicates.*

Atorvastatin Standard (0.5 mg/mL) in DMEM/F12																			
		Without FBS									With 10% FBS								
Extraction Recovery (%)	Standard Replicate	1			2			3			1			2			3		
	Extraction Replicate	1	2	3	1	2	3	1	2	3	1	2	3	1	2	3	1	2	3
	Instrument Replicate 1	66.1	76.0	68.4	61.3	67.9	69.6	71.3	71.4	58.0	63.4	66.9	63.7	56.1	50.8	58.1	68.3	73.0	74.4
	Instrument Replicate 2	65.8	74.5	71.2	63.9	68.8	68.3	71.9	71.0	57.4	63.2	64.8	64.6	54.0	50.7	57.8	68.2	72.5	74.6
	Instrument Replicate 3	68.9	75.4	69.4	59.1	68.3	68.8	71.8	71.2	57.1	64.0	66.8	63.7	55.1	51.3	59.6	66.0	73.6	76.4
	Instrument Replicate Average	67.0	75.3	69.7	61.5	68.3	68.9	71.7	71.2	57.5	63.5	66.2	64.0	55.1	50.9	58.5	67.5	73.1	75.1
	Standard Average	70.6			66.2			66.8			64.6			54.8			71.9		
	Total Average	67.89									63.8								

As compared to the previous data, the variation between instrument replicates appeared to be very similar as expected. However, there was much higher variation between the extraction replicates despite some of them being aliquots from the same standard replicate. The largest variance between aliquots extracted from the same standard replicate was 14.2%; this would be indicative of either the aliquot taken not being representative of the sample or the extraction process being not entirely reproducible.

The greatest variability observed was from the standards that contained 10% FBS. The average extraction efficiency calculated from each of the three standard replicates spanned over 17.1%. Such large discrepancies could have a profound effect on the interpretation of data from this sample type, especially with the recovered concentrations being so small. While the PBS extractions could be improved by using LC standards prepared in the same manner, the inconsistency with the DMEM-based extractions would require further optimisation to improve reproducibility as well as efficiency.

Focusing on the overall average extraction efficiency, less than 70% of atorvastatin acid was recovered from the known atorvastatin standards, regardless of whether FBS was added or not. Nevertheless, this percentage of loss would still not account for the difference between the permeation coefficients commonly presented here and those in work published by (Iqbal et al., 2021).

Since the discovery of metabolites in the DESI MS images after the studies were completed, this fuelled the very likely theory that significant metabolism had occurred within the tissue. Theoretically, this would be a logical explanation as in real-life scenarios, the bioavailability of atorvastatin was reported to be as low as 14% due to metabolism by CYP3A4 enzymes present in the gut. As the metabolite ions were able to be visualised in the tissue section, the concentration must be significant or at least in a similar range to the detected atorvastatin acid ions. Although the images provide no quantitative information, an estimated value was calculated per tissue section using the tissue extracts to give a rough figure. From the lowest to the highest concentrations in the tissue extracts, an estimated 0.00352 – 0.25312 µg of atorvastatin acid was present in each section taken from the centre of the disc. Although these were very rough estimations, it gave a valuable insight into the proportion of atorvastatin that may have metabolised and remained in the tissue. With atorvastatin metabolites detected in the tissue disc, there was a possibility that they too would have permeated into the acceptor

circuit; especially considering that the metabolite patterns mirrored that of the atorvastatin acid distributions.

The successful detection and quantification of atorvastatin metabolites in both the tissue extracts and acceptor circuit would increase the mass balance but more importantly, the amount of atorvastatin that had permeated through the tissue. Whether the increase would be significant remains unknown without further work. It would provide valuable information to quantify the metabolite alongside atorvastatin acid. The variation in surface area of the tissue due to pilace ciraces and irregular villi would lead to the expectation that CYP3A4 enzyme production would fluctuate. Additionally, the effectiveness of the metabolising enzymes would be limited by the viability of the tissue. Although the viability of the tissue was assessed under standard conditions, perhaps in-line measurements would be more suitable to check each tissue batch. Due to the tissue being acquired from the abattoir and in addition to a medley of environmental conditions used for different studies, the viability of the tissue may fluctuate. Thus, further modification of the model should be considered to allow in-line viability assessments without compromising the system set-up conditions.

After upgrading the o-ring fitting, there was still the occurrence of the odd outlier in the permeation coefficients. The cause of these outliers was unknown however, there were a few theories that should be investigated to improve the reproducibility and variation of the data. The first theory, given evidence of metabolite presence, was the idea that this particular tissue was not viable and so, more intensive permeation of atorvastatin acid was seen. To verify this hypothesis, it would be critical going forward to quantify both atorvastatin acid and all known metabolites. Most permeation coefficients obtained were less than those published, by 1-2 orders of magnitude, and yet the outliers were more comparable to those published. A post-observation was that despite the pressure difference remaining the same, in some cases the pressure in the donor circuit was slightly above atmospheric rather than general atmospheric pressure. This was suspected to be caused by small air bubbles hidden in the donor circuit reservoir bottle that could not easily been seen without intervention. The elevated pressure in the donor circuit could have encouraged permeation into the donor circuit. A short study with elevated pressure in the donor circuit would highlight whether the dubbed ‘outlier’ was in fact reproducible. If this was proven to be the case, the system should be permanently modified to achieve this in a reproducible manner. This could be achieved by tilting the

reservoir to release bubbles prior to elevating the donor circuit reservoir above the system at a reproducible height.

4.5 Conclusions

The adapted millifluidics system allowed several large successful absorption studies to be performed and provided interesting trends from varied excipient concentrations and combinations. The sheer number of experiments performed using the model demonstrated variability in the ex vivo experiments and perhaps, highlighted areas where the model could be improved even further. Sporadic, yet significant, permeation coefficients have paved the way for follow-up studies to explore the impact of metabolism and pressure in hope to create a more reproducible and realistic model. With the trade-off between instrument health and extraction efficiency, further optimisation is needed to improve reproducibility between extractions and thus, permeation coefficients. In this early period of trialling the adapted millifluidics model combined ex vivo tissue, DESI mass spectrometry highlighted a promising future for the possibilities of drug and metabolite identification and thus, mapping. Going forward, the studies would benefit from imaging serial tissue sections on another more sensitive instrument after metabolite presence had been confirmed. Instruments such as the Waters DESI TQ offer a much higher level of sensitivity that would allow the visualisation of lower levels of atorvastatin acid and its metabolites and potentially, highlight the absorption pathway. In addition to reducing potential masking effects, this would allow more information to be collected on the tissue structure it co-localises with which could not be achieved in this study. To allow more intuitive comparisons between DESI images from different studies, the development of a QMSI method would give more meaning to the distributions of atorvastatin and its metabolites observed.

Whilst the absolute values for $P_{app,pig}$ obtained in this study are affected by the issues around extraction efficiencies and drug metabolism described, important data showing the qualitative effects of excipients used alone or in combination have been obtained. In particular the concentration limit to the positive effects obtained by use of the tight junction modifier Mapcho-12 in combination with the solubilizer Polysorbate 80 were clearly demonstrated to apply here to viable tissue as well as to cells layers as had been shown in previous studies.

References

Agrawal, A. G., Kumar, A., & Gide, P. S. (2015). Formulation of solid self-nanoemulsifying drug delivery systems using N-methyl pyrrolidone as cosolvent . *Drug Development and Industrial Pharmacy, 41*(4), 594-604. 10.3109/03639045.2014.886695

Al-Kazemi, R., Al-Basarah, Y., & Nada, A. (2019). *Dissolution enhancement of atorvastatin calcium by cocrystallization*. Maad Rayan Publishing Company. 10.15171/apb.2019.064

Arnold, Y. E., Thorens, J., Bernard, S., & Kalia, Y. N. (2019). *Drug transport across porcine intestine using an ussing chamber system: Regional differences and the effect of P-glycoprotein and CYP3A4 activity on drug absorption*. MDPI AG. 10.3390/pharmaceutics11030139

Iqbal, R., Qureshi, O. S., Yousaf, A. M., Raza, S. A., Sarwar, H. S., Shahnaz, G., Saleem, U., & Sohail, M. F. (2021). *Enhanced solubility and biopharmaceutical performance of atorvastatin and metformin via electrospun polyvinylpyrrolidone-hyaluronic acid composite nanoparticles*. Elsevier BV. 10.1016/j.ejps.2021.105817

Khan, F. N., & Dehghan, M. H. G. (2011). *Enhanced bioavailability of atorvastatin calcium from stabilized gastric resident formulation*. Springer Science and Business Media LLC. 10.1208/s12249-011-9673-3

LECO Corporation. (2018). *Encoded frequent Pushing Improving duty cycle in the folded flight path high resolution time-of-flight mass spectrometry.*

Lennernas, H. (2003). Clinical pharmacokinetics of atorvastatin. *Clinical Pharmacokinetics, 42*(13), 1141-1160. 10.2165/00003088-200342130-00005

Liu, D., Lecluyse, E. L., & Thakker, D. R. (1999). *Dodecylphosphocholine-mediated enhancement of paracellular permeability and cytotoxicity in caco-2 cell monolayers*. American Geophysical Union (AGU). 10.1021/js990094e

Mapcho®-12. (2024, April,). Avanti Polar Lipids Products. https://avantilipids.com/product/850336

Sugita, K., Takata, N., & Yonemochi, E. (2021). *Dose-dependent Solubility–Permeability interplay for poorly soluble drugs under non-sink conditions*. MDPI AG. 10.3390/pharmaceutics13030323

Super refined™ DEGEE . (2024, April,). CRODA Pharma Product Finder. https://www.crodapharma.com/en-gb/product-finder/product/5421-super_1_refined_1_degee

Wu, X., Whitfield, L. R., & Stewart, B. H. (2000). Atorvastatin transport in the caco-2 cell model: Contributions of P-glycoprotein and the proton-monocarboxylic acid co-transporter.*17*, 209-215.

Chapter 5:

Concluding Remarks

The initial proof-of-concept study detailed in Chapter 2 demonstrated the versatility of the QV600 LLI system. The commercially available system has only ever been advertised and implemented as a dynamic system for the culture of 2D cell lines. However, the study presented here has demonstrated that the system is capable of housing much larger samples such as ex vivo tissue. The preliminary work detailed in Chapter 2 has shown that atorvastatin was able to penetrate the tissue and diffuse into the acceptor circuit in levels comparable with those in published works that use porcine tissue and other BCS II oral drugs (Arnold et al., 2019). The combination of LC-MS/MS and MALDI-MSI has allowed the confirmation of atorvastatin within the tissue to verify the movement of the drug through the tissue. While this study has clearly proven that the adapted QV600 LLI system is suitable for the study of atorvastatin through the GI tract using previously frozen ex vivo porcine tissue, it was essential to not limit the model to drug classes that move by passive diffusion. While frozen studies are ideal for model development and the study of passive diffusion, the host of absorption mechanisms that become available when tissue is viable should not be overlooked. Further work was therefore carried out to adapt the model to incorporate and maintain viable porcine tissue for the purpose of drug absorption experiments; this has been described and discussed in subsequent chapters.

Chapter 3 explores the practical challenges of converting a cell culture system into a millifluidics system suitable for viable tissue. A great deal of work was required to balance the set-up timings with the robustness of the tissue fittings. Further work was required to optimise the efficiency and robustness of the system and this led to the development of the syringe filling method. The dual outcomes of using this technique were that it allowed the system to be filled quickly whilst simultaneously highlighting any flaws in the fitting. Thus, providing an extra level of confidence that the barrier between the two circuits maintained intact. With the improvements made, the millifluidics model could be successfully set-up in a much more time-efficient manner than was reported in Chapter 2. The modular nature of the QV600 LLI allowed for the incorporation of real-time pressure monitoring sensors that were instrumental in diagnosing and thus solving issues encountered during the set-up optimisation process. A short excipient study comparing different flow rates demonstrated that the model was capable of producing permeation coefficients that fell within the range of those produced by another ex vivo model; the study explored drug absorption across porcine

intestine using an array of drugs within the same BCS group as atorvastatin. The use of real-time pressure monitoring sensors highlighted the detrimental, and sometimes lasting, effect that bubble formation had on system pressure. The system was re-configured to create a more significant pressure gradient between the two circuits, which in turn, improved the robustness of the system and minimised the effect of air bubbles. With the new modifications made to the system and configuration implemented, the model proved to be capable of performing drug absorption experiments on ex vivo porcine tissue without having a detrimental effect on the viability of the tissue.

In Chapter 4, the use of the adapted millifluidics system for a range of drug absorption studies is described. These explored the effects of different excipients and environmental factors on the permeation of atorvastatin through viable ex vivo porcine tissue. The DEGEE LQ study produced permeation coefficient values for atorvastatin that were similar to those reported by a previous ex vivo study of atorvastatin. The earlier study focused on the absorption of atorvastatin through goat intestine using a Franz cell (Iqbal et al., 2021). The permeation coefficients reported were used to optimise the efficiency of the modified model. With the exception of the DEGEE LQ study, most of the other excipient studies fell 1-2 orders of magnitude below the reported values. Nevertheless, the model allowed for internally comparative studies to be conducted that assessed the effect of altering the excipient formulation and environment on drug absorption and permeation. It was demonstrated how altering the pH of some formulations could increase the permeation coefficients by a whole order of magnitude. Trends were seen in several formulations including mapcho-12; the optimal concentration of mapcho-12 for increased permeation of atorvastatin was reflected in the findings of another reported study (Liu et al., 1999).

The large number of experiments and whole studies conducted in the adapted millifluidics system demonstrated variability and highlighted potential areas for further improvement of the model. Seemingly sporadic, yet significant, changes in the permeation coefficients obtained have demonstrated the need for follow-up studies to explore why these occurred since this would lead to the creation of a more reproducible system. Significant permeation coefficients were attained for non-formulated atorvastatin during the optimisation stages of the model prior to re-configuration and pressure monitoring. Retrospectively, too much focus may have been put on

maintaining a significant pressure gradient and consequently, allowed pressure fluctuations in the donor circuit to go unnoticed. Generally, the donor circuit sits at atmospheric pressure however, fluctuations above this had been observed but overlooked due to the significant gradient being maintained. While the exact cause of these fluctuations is unclear, there were several occurrences where a large air bubble was discovered hidden in the reservoir tubing; the work described in Chapter 3 addressed the effect that bubble formation can have on system pressure. It is plausible that unnoticed bubble formation in the donor circuit could have raised the pressure in the donor circuit above atmospheric pressure; thus, increasing the driving force and producing seemingly sporadic permeation coefficient values. It would be ideal to raise the donor circuit reservoir (same principle as applied to the acceptor circuit) above the system to create a more significant pressure in the donor circuit and test the theory.

The combination of DESI MSI with the adapted millifluidics model proved to be a useful tool in the discovery and mapping of atorvastatin and its metabolites within the tissue sections. The high mass accuracy of the DESI MRT allowed for confident identification of atorvastatin metabolites. The use of an imaging method, such as DESI MSI, was proven to be essential in the work reported here. The interpretation of atorvastatin in tissue by LC-MS/MS analysis of tissue extracts alone was misleading; DESI MSI provided important spatial information that mainly demonstrated saturation of atorvastatin in the upper layers of the tissue section. Even with significant permeation coefficients, the low levels of atorvastatin and its metabolites within a tissue section were seemingly below the detection limits of the methodology. After metabolite identification on the MRT, it would be beneficial to analyse serial sections on more sensitive instruments such as the Waters DESI TQ and potentially map the absorption routes of both drug and metabolite.

As the QV600 LLI system is commercially available, a number of modular accessories exist that modify the system further. Simple modifications such as the addition of more chambers allow for more samples to be tested, or better still, the study of the different intestinal regions within the same system, simultaneously. Attachments such as sampling ports allow for time point studies. The modular nature of the system allows for easy re-configuration to open the circuit which would allow the sink effect to be studied. Furthermore, it seems plausible that other organ models could be connected to construct a multi-organ model. The newly recognised versatility of the system presents

an exciting possibility to perform comparative studies on larger sample types such as ex vivo tissue, organoids and even human biopsies within the same environment. This would be particularly useful for researchers who were hoping to explore other sample types in a relatively inexpensive manner. Before this future projection of the model can become a reality, further troubleshooting and refinement of the model and workflow must firstly be addressed.

In terms of troubleshooting, a short comparative excipient study with an elevated donor circuit reservoir would deduce whether a significant positive pressure in the donor circuit would produce significant permeation coefficients and simultaneously eliminate the apparent 'outliers'. With the trade-off between instrument robustness and extraction efficiency, further optimisation is needed to improve reproducibility between extractions and thus, permeation coefficients. An ideal modification for the refinement and streamline of the system would be to incorporate built-in probes that allow in-line viability testing via TEER measurements. The development of an LC-MS/MS method for the detection and quantification of atorvastatin metabolites would provide valuable information and better understanding. In addition to seeking a more sensitive DESI MS, the development of a QMSI method would allow for quantitative comparisons between the DESI images generated from different studies and thus, give more meaning to the distribution of atorvastatin and metabolites alike.

Overall, the millifluidics model adapted to house viable ex vivo porcine intestinal tissue has already been modified to allow for successful drug absorption studies that can be manipulated to generate significant permeation coefficients on a level similar to other ex vivo models. The combination of the millifluidics model with DESI MSI and LC/MS-MS has demonstrated great promise and future prospects as a powerful workflow for drug absorption studies.

References

Arnold, Y. E., Thorens, J., Bernard, S., & Kalia, Y. N. (2019). *Drug transport across porcine intestine using an ussing chamber system: Regional differences and the effect of P-glycoprotein and CYP3A4 activity on drug absorption*. MDPI AG. 10.3390/pharmaceutics11030139

Iqbal, R., Qureshi, O. S., Yousaf, A. M., Raza, S. A., Sarwar, H. S., Shahnaz, G., Saleem, U., & Sohail, M. F. (2021). *Enhanced solubility and biopharmaceutical performance of atorvastatin and metformin via electrospun polyvinylpyrrolidone-hyaluronic acid composite nanoparticles*. Elsevier BV. 10.1016/j.ejps.2021.105817

Liu, D., Lecluyse, E. L., & Thakker, D. R. (1999). *Dodecylphosphocholine-mediated enhancement of paracellular permeability and cytotoxicity in caco-2 cell monolayers*. American Geophysical Union (AGU). 10.1021/js990094e

Publications and Presentations

Scientific Article

Spencer, C. E., Rumbelow, S., Mellor, S., Duckett, C. J., & Clench, M. R. (2022). Adaptation of the Kirkstall QV600 LLI Microfluidics System for the Study of Gastrointestinal Absorption by Mass Spectrometry Imaging and LC-MS/MS. Pharmaceutics, 14(2), 364. https://doi.org/10.3390/pharmaceutics14020364

Book Chapter

Spencer, C.E., Duckett, C.J., Rumbelow, S., Clench, M.R. (2023). The Adaptation of the QV600 LLI Milli-Fluidics System to House Ex Vivo Gastrointestinal Tissue Suitable for Drug Absorption and Permeation Studies, Utilizing MALDI MSI and LC-MS/MS. In: Cole, L.M., Clench, M.R. (eds) Imaging Mass Spectrometry. Methods in Molecular Biology, vol 2688. Humana, New York, NY. https://doi.org/10.1007/978-1-0716-3319-9_7

Review Article

Spencer CE, Flint LE, Duckett CJ, Cole LM, Cross N, Smith DP, Clench MR. Role of MALDI-MSI in combination with 3D tissue models for early stage efficacy and safety testing of drugs and toxicants. Expert Rev Proteomics. 2020 Nov-Dec;17(11-12):827-841. doi: 10.1080/14789450.2021.1876568. Epub 2021 Feb 2. PMID: 33440126; PMCID: PMC8396712.

Poster Presentations

American Society of Mass Spectrometry (ASMS) Conference

- The absorption of drugs through porcine gastrointestinal tissue analysed by mass spectrometry imaging - 2020 (Online)
- The absorption of drugs through porcine gastrointestinal tissue analysed by Mass Spectrometry Imaging - 2021 (Online)
- The adaptation of QV600 LLI for comparative excipient studies using ex vivo tissue and mass spectrometry - 2022
- The adaptation of QV600 LLI for comparative excipient studies using ex vivo tissue and mass spectrometry -2023

British Mass Spectrometry Society (BMSS) Special Interest Group (SIG) Conference

- The adaptation of QV600 LLI for comparative excipient studies using ex vivo tissue and Mass Spectrometry - 2022
- Improved Performance of a Milli fluidic System for Drug
- Absorption Studies using ex vivo tissue and Mass Spectrometry - 2023

OurCon Conference

- The absorption of drugs through porcine gastrointestinal tissue analysed by Mass Spectrometry Imaging - 2021

Winter Poster Conference

- Enhanced absorption of drugs in the GI tract studied by Mass Spectrometry Imaging - 2019
- The absorption of drugs through porcine gastrointestinal tissue analysed by mass spectrometry imaging - 2020
- The absorption of drugs through porcine gastrointestinal tissue analysed by Mass Spectrometry -2021
- The adaptation of QV600 LLI for comparative excipient studies using ex vivo tissue and Mass Spectrometry - 2022

Conference Talks

Advances in Cell & Tissue Culture (ACTC) Conference

- Absorption of drugs in the GI tract studied by mass spectrometry imaging - 2021
- Effect of Excipients on the Absorption of Drugs in the GI Tract - 2022

British Mass Spectrometry Society (BMSS) Special Interest Group (SIG) Conference

- Absorption of drugs in the GI tract studied by mass spectrometry imaging - 2021
- Enhanced Absorption of Drugs in the GI Tract Studied by Mass Spectrometry Imaging - 2023

Mass Spectrometry Imaging and Integrated Topics (IMSIS) Conference

- Enhanced Absorption of Drugs in the GI Tract Studied by Mass Spectrometry Imaging - 2023 (Accepted only)

Appendix I:

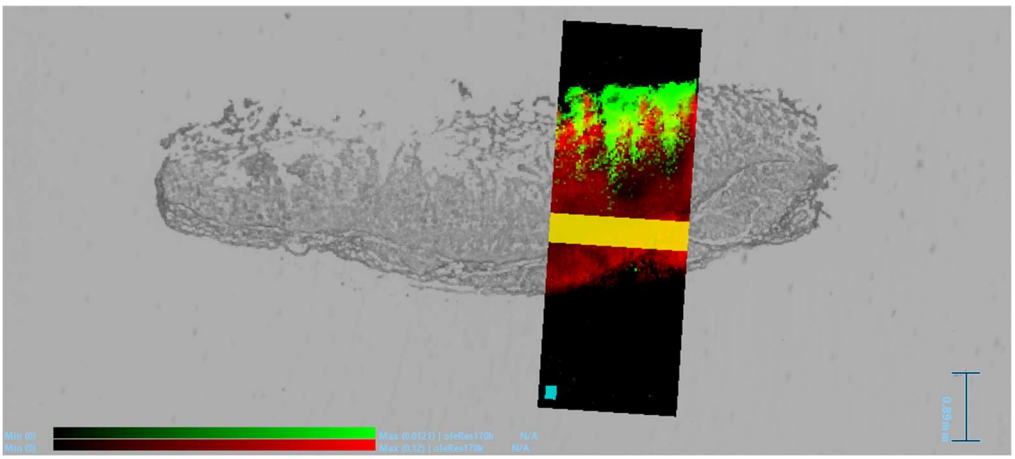

Appendix I Figure 1: *A DESI MSI image from a fresh tissue absorption experiment with no polysorbate-80 in the donor circuit buffered to pH 7.4 (Polysorbate-80 only pH 7.4 study) from Figure 4.10 now annotated with ROIs. The specific ROIs "within tissue away from drug distribution" and "away from tissue" referred to in Table 4.2-4.3 for 0% (v/v) polysorbate-80 have been represented by the yellow and blue shapes burned into the original DESI MSI image, respectively.*

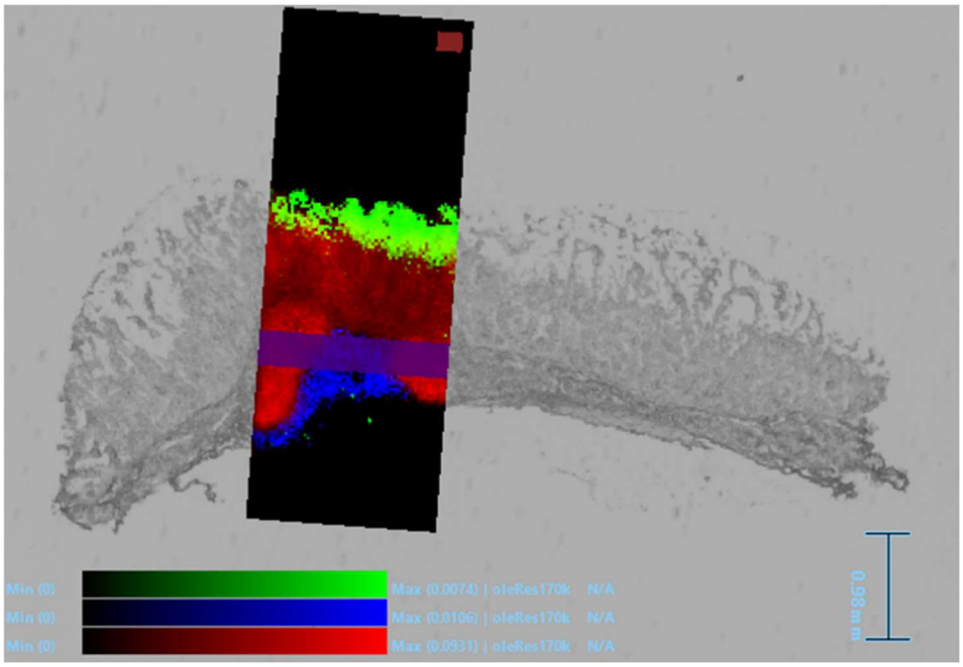

Appendix I Figure 2: *A DESI MSI image from a fresh tissue absorption experiment with 0.4% (v/v) polysorbate-80 in the donor circuit buffered to pH 7.4 (Polysorbate-80 only pH 7.4 study) from Figure 4.6 now annotated with ROIs. The specific ROIs "within tissue away from drug distribution" and "away from tissue" referred to in Table 4.2-4.3 for 0.4% (v/v) polysorbate-80 have been represented by the purple and red shapes burned into the original DESI MSI image, respectively.*

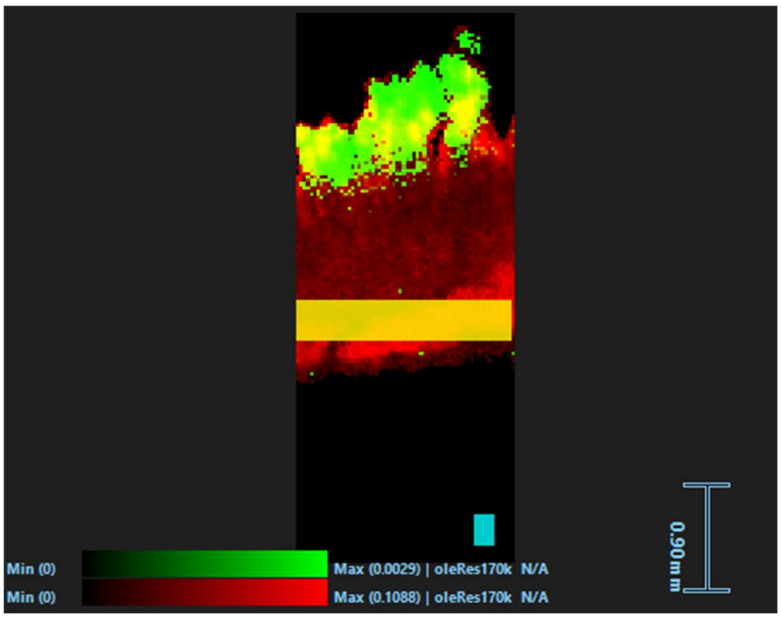

Appendix I Figure 3: *A DESI MSI image from a fresh tissue absorption experiment with 1% (v/v) polysorbate-80 in the donor circuit buffered to pH 7.4 (Polysorbate-80 only pH 7.4 study) from Figure 4.7 now annotated with ROIs. The specific ROIs "within tissue away from drug distribution" and "away from tissue" referred to in Table 4.2-4.3 for 1% (v/v) polysorbate-80 have been represented by the yellow and blue shapes burned into the original DESI MSI image, respectively.*

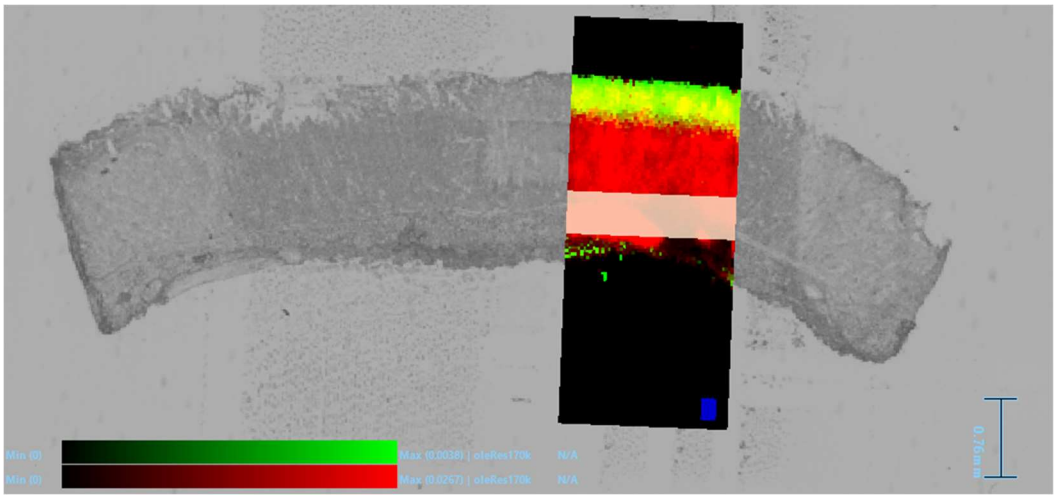

Appendix I Figure 4: *A DESI MSI image from a fresh tissue absorption experiment with 2% (v/v) polysorbate-80 in the donor circuit buffered to pH 7.4 (Polysorbate-80 only pH 7.4 study) from Figure 4.9 now annotated with ROIs. The specific ROIs "within tissue away from drug distribution" and "away from tissue" referred to in Table 4.2-4.3 for 2% (v/v) polysorbate-80 have been represented by the white and blue shapes burned into the original DESI MSI image, respectively.*

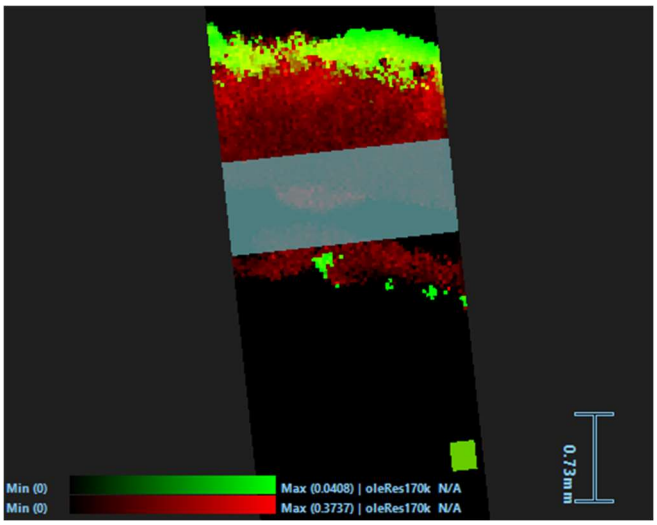

Appendix I Figure 5: *A DESI MSI image from a fresh tissue absorption experiment with no DEGEE LQ in the donor circuit buffered to pH 7.4 (DEGEE LQ only pH 7.4 study) from Figure 4.17 now annotated with ROIs. The specific ROIs "within tissue away from drug distribution" and "away from tissue" referred to in Table 4.4-4.5 for 0% (v/v) DEGEE LQ have been represented by the blue and green shapes burned into the original DESI MSI image, respectively.*

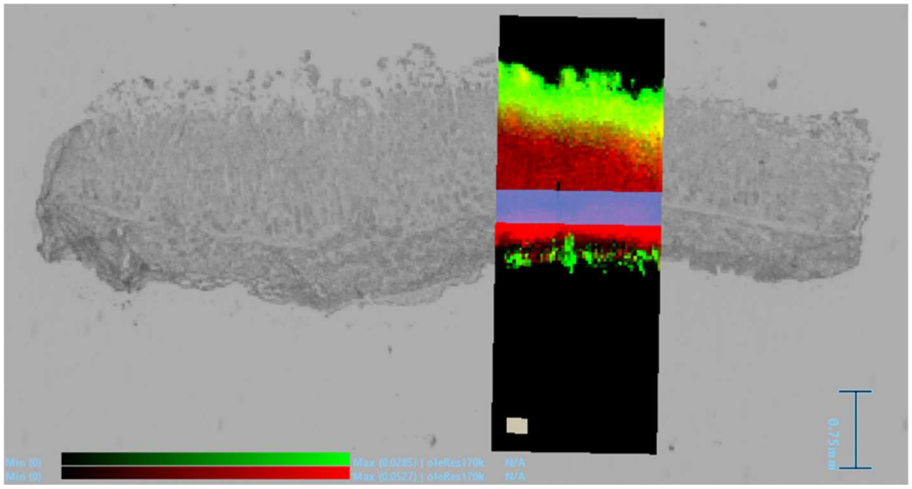

Appendix I Figure 6: *A DESI MSI image from a fresh tissue absorption experiment with 0.4% (v/v) DEGEE LQ in the donor circuit buffered to pH 7.4 (DEGEE LQ only pH 7.4 study) from Figure 4.19 now annotated with ROIs. The specific ROIs "within tissue away from drug distribution" and "away from tissue" referred to in Table 4.4-4.5 for 0.4% (v/v) DEGEE LQ have been represented by the purple and white shapes burned into the original DESI MSI image, respectively.*

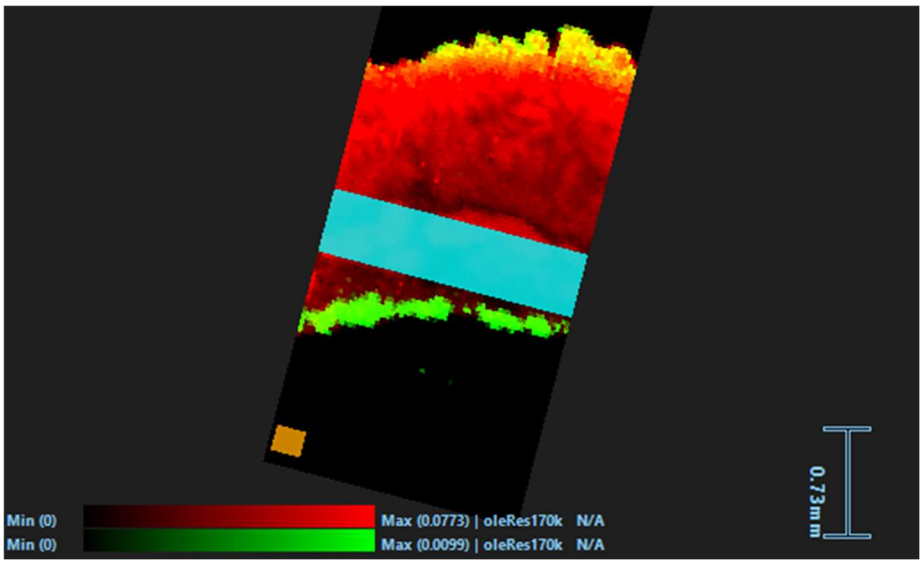

Appendix I Figure 7: *A DESI MSI image from a fresh tissue absorption experiment with 1% (v/v) DEGEE LQ in the donor circuit buffered to pH 7.4 (DEGEE LQ only pH 7.4 study) from Figure 4.21 now annotated with ROIs. The specific ROIs "within tissue away from drug distribution" and "away from tissue" referred to in Table 4.4-4.5 for 1% (v/v) DEGEE LQ have been represented by the blue and orange shapes burned into the original DESI MSI image, respectively.*

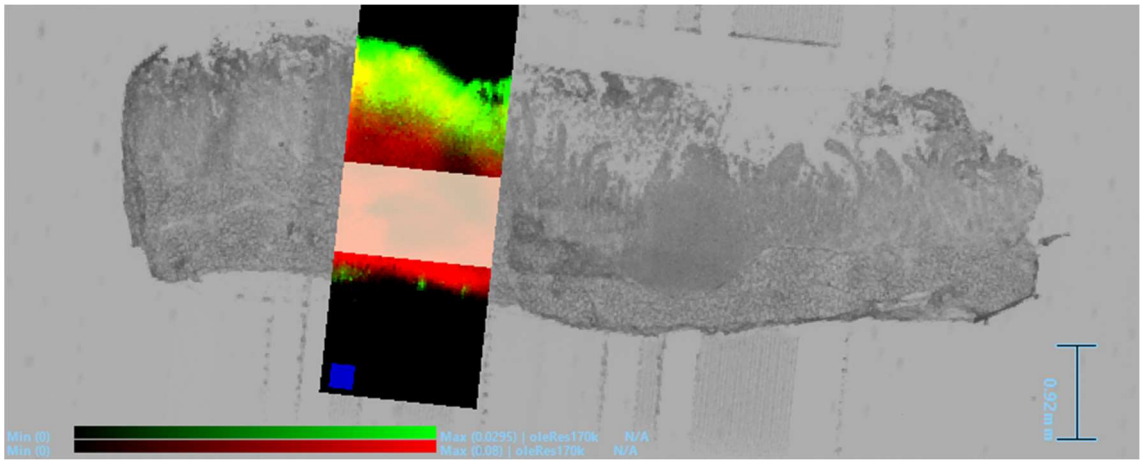

Appendix I Figure 8: *A DESI MSI image from a fresh tissue absorption experiment with 2% (v/v) DEGEE LQ in the donor circuit buffered to pH 7.4 (DEGEE LQ only pH 7.4 study) from Figure 4.24 now annotated with ROIs. The specific ROIs "within tissue away from drug distribution" and "away from tissue" referred to in Table 4.4-4.5 for 2% (v/v) DEGEE LQ have been represented by the white and blue shapes burned into the original DESI MSI image, respectively.*

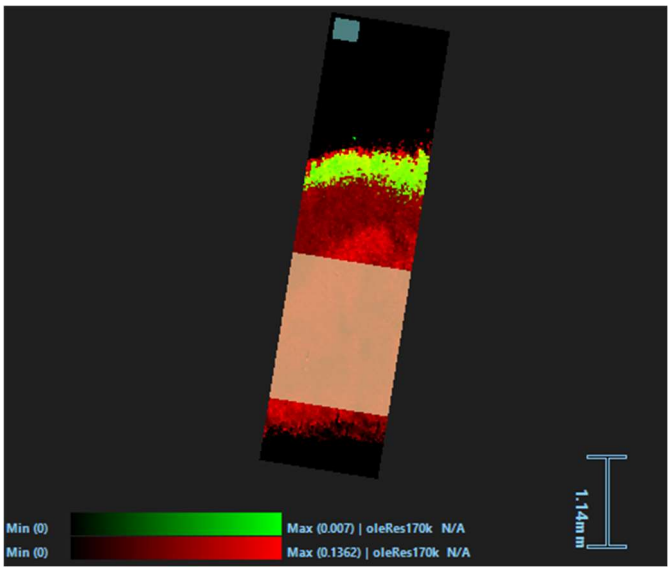

Appendix I Figure 9: *A DESI MSI image from a fresh tissue absorption experiment with no DEGEE LQ in the donor circuit buffered to pH 7.4 (Polysorbate-80 & DEGEE LQ pH 7.4 study) from Figure 4.30 now annotated with ROIs. The specific ROIs "within tissue away from drug distribution" and "away from tissue" referred to in Table 4.6-4.7 for 0% (v/v) DEGEE LQ have been represented by the orange and blue shapes burned into the original DESI MSI image, respectively.*

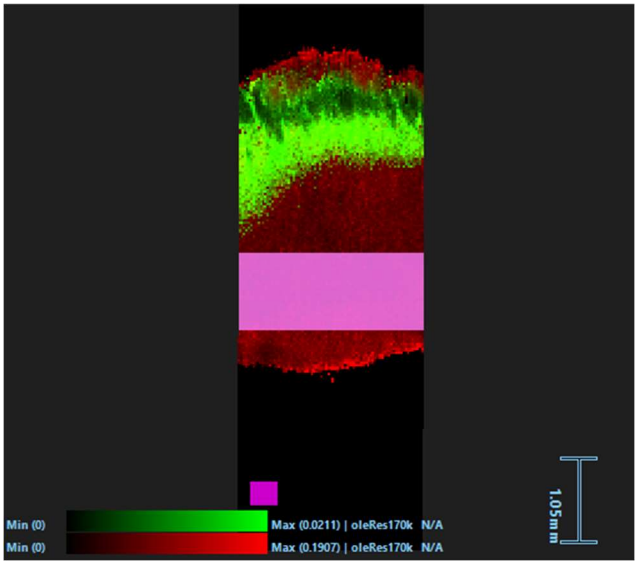

Appendix I Figure 10: *A DESI MSI image from a fresh tissue absorption experiment with 0.4% (v/v) DEGEE LQ in the donor circuit buffered to pH 7.4 (Polysorbate-80 & DEGEE LQ pH 7.4 study) from Figure 4.32 now annotated with ROIs. The specific ROIs "within tissue away from drug distribution" and "away from tissue" referred to in Table 4.6-4.7 for 0.4% (v/v) DEGEE LQ have been represented by the light pink and dark pink shapes burned into the original DESI MSI image, respectively.*

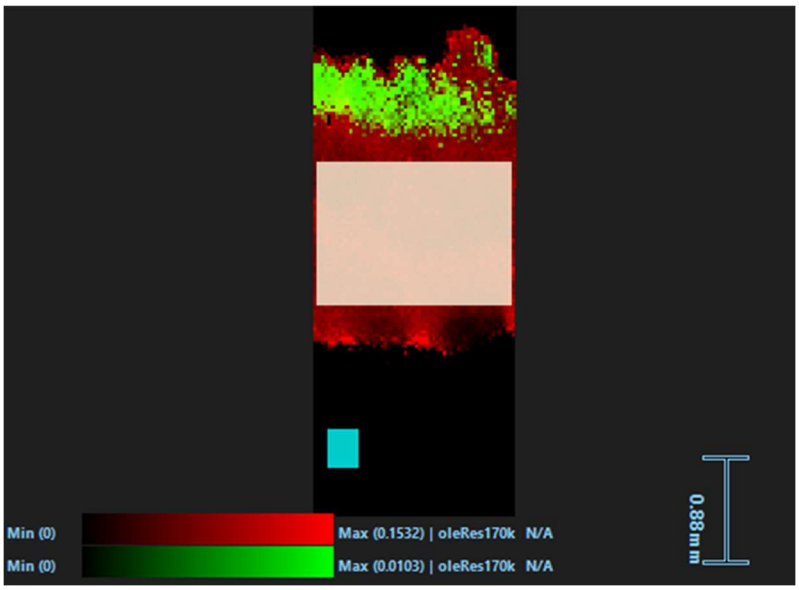

Appendix I Figure 11: *A DESI MSI image from a fresh tissue absorption experiment with 1% (v/v) DEGEE LQ in the donor circuit buffered to pH 7.4 (Polysorbate-80 & DEGEE LQ pH 7.4 study) from Figure 4.34 now annotated with ROIs. The specific ROIs "within tissue away from drug distribution" and "away from tissue" referred to in Table 4.6-4.7 for 1% (v/v) DEGEE LQ have been represented by the white and blue shapes burned into the original DESI MSI image, respectively.*

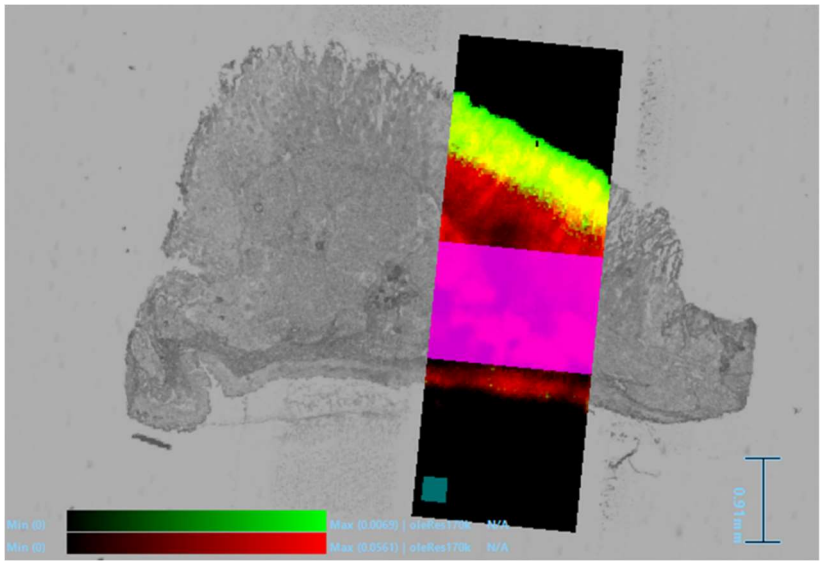

Appendix I Figure 12: *A DESI MSI image from a fresh tissue absorption experiment with 2% (v/v) DEGEE LQ in the donor circuit buffered to pH 7.4 (Polysorbate-80 & DEGEE LQ pH 7.4 study) from Figure 4.36 now annotated with ROIs. The specific ROIs "within tissue away from drug distribution" and "away from tissue" referred to in Table 4.6-4.7 for 2% (v/v) DEGEE LQ have been represented by the pink and blue shapes burned into the original DESI MSI image, respectively.*

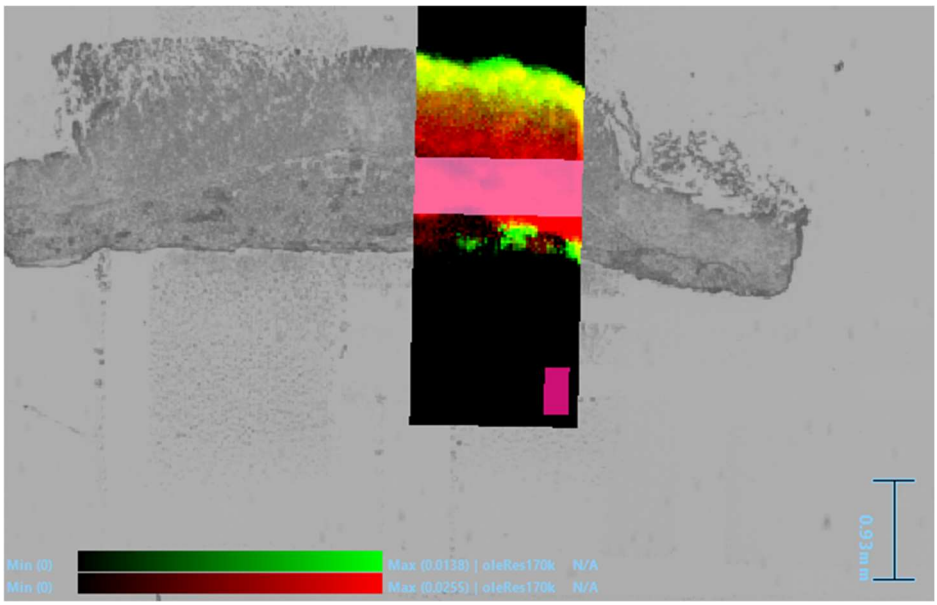

Appendix I Figure 13: *A DESI MSI image from a fresh tissue absorption experiment with no polysorbate-80 in the donor circuit buffered to pH 6 (Polysorbate-80 only pH 6 study) from Figure 4.45 now annotated with ROIs. The specific ROIs "within tissue away from drug distribution" and "away from tissue" referred to in Table 4.8-4.9 for 0% (v/v) polysorbate-80 have been represented by the light pink and dark pink shapes burned into the original DESI MSI image, respectively.*

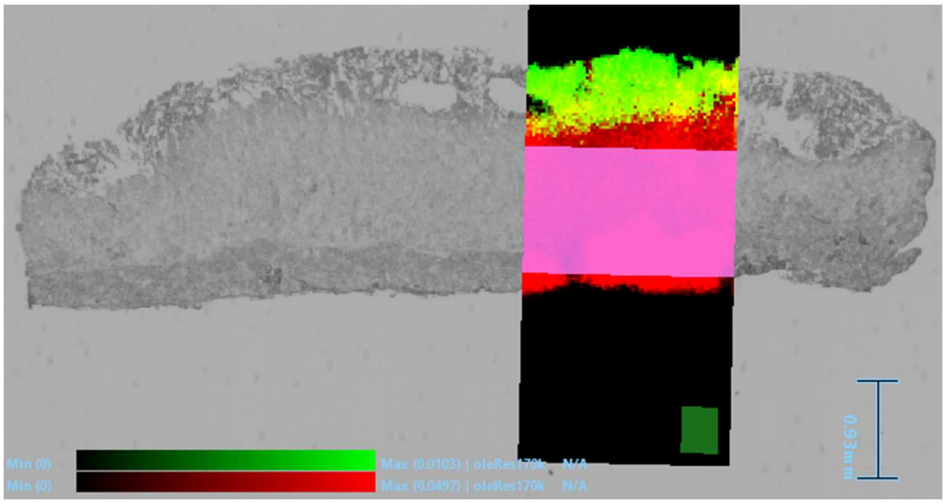

Appendix I Figure 14: *A DESI MSI image from a fresh tissue absorption experiment with 0.4% (v/v) polysorbate-80 in the donor circuit buffered to pH 6 (Polysorbate-80 only pH 6 study) from Figure 4.47 now annotated with ROIs. The specific ROIs "within tissue away from drug distribution" and "away from tissue" referred to in Table 4.8-4.9 for 0.4% (v/v) polysorbate-80 have been represented by the pink and green shapes burned into the original DESI MSI image, respectively.*

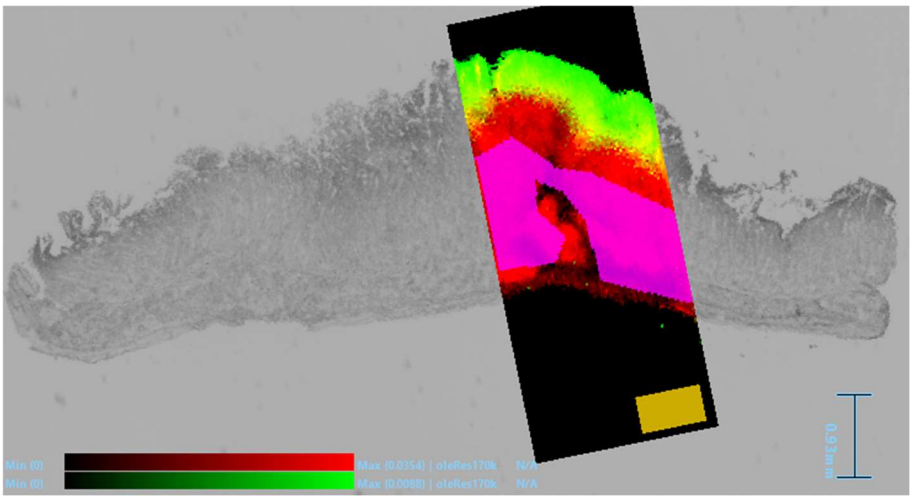

Appendix I Figure 15: *A DESI MSI image from a fresh tissue absorption experiment with 1% (v/v) polysorbate-80 in the donor circuit buffered to pH 6 (Polysorbate-80 only pH 6 study) from Figure 4.49 now annotated with ROIs. The specific ROIs "within tissue away from drug distribution" and "away from tissue" referred to in Table 4.8-4.9 for 1% (v/v) polysorbate-80 have been represented by the pink and orange shapes burned into the original DESI MSI image, respectively.*

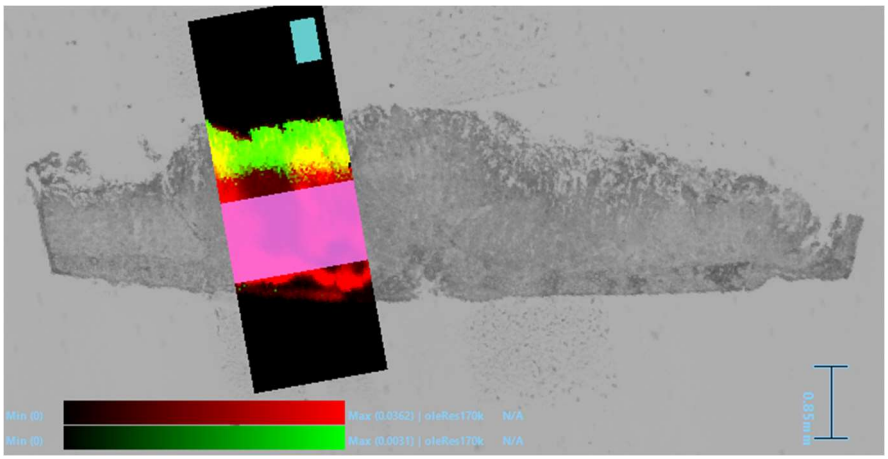

Appendix I Figure 16: *A DESI MSI image from a fresh tissue absorption experiment with 2% (v/v) polysorbate-80 in the donor circuit buffered to pH 6 (Polysorbate-80 only pH 6 study) from Figure 4.51 now annotated with ROIs. The specific ROIs "within tissue away from drug distribution" and "away from tissue" referred to in Table 4.8-4.9 for 2% (v/v) polysorbate-80 have been represented by the pink and blue shapes burned into the original DESI MSI image, respectively.*

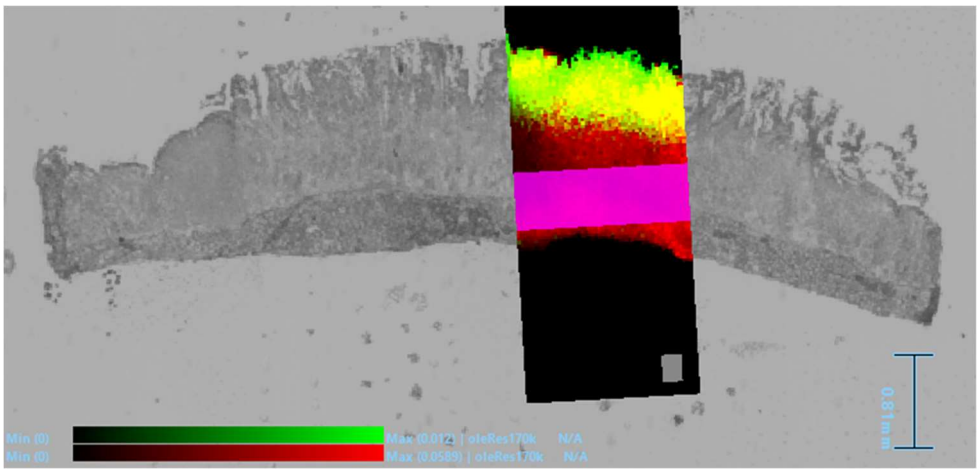

Appendix I Figure 17: *A DESI MSI image from a fresh tissue absorption experiment with no DEGEE LQ in the donor circuit buffered to pH 6 (Polysorbate-80 & DEGEE LQ pH 6 study) from Figure 4.58 now annotated with ROIs. The specific ROIs "within tissue away from drug distribution" and "away from tissue" referred to in Table 4.10-4.11 for 0% (v/v) DEGEE LQ have been represented by the pink and grey shapes burned into the original DESI MSI image, respectively.*

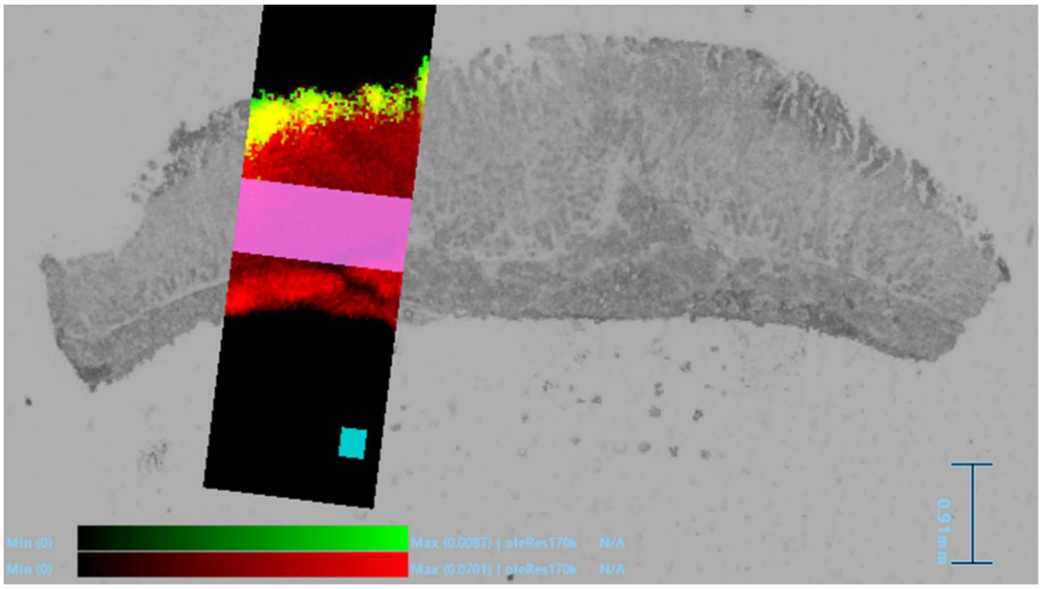

Appendix I Figure 18: *A DESI MSI image from a fresh tissue absorption experiment with 0.4% (v/v) DEGEE LQ in the donor circuit buffered to pH 6 (Polysorbate-80 & DEGEE LQ pH 6 study) from Figure 4.60 now annotated with ROIs. The specific ROIs "within tissue away from drug distribution" and "away from tissue" referred to in Table 4.10-4.11 for 0.4% (v/v) DEGEE LQ have been represented by the pink and blue shapes burned into the original DESI MSI image, respectively.*

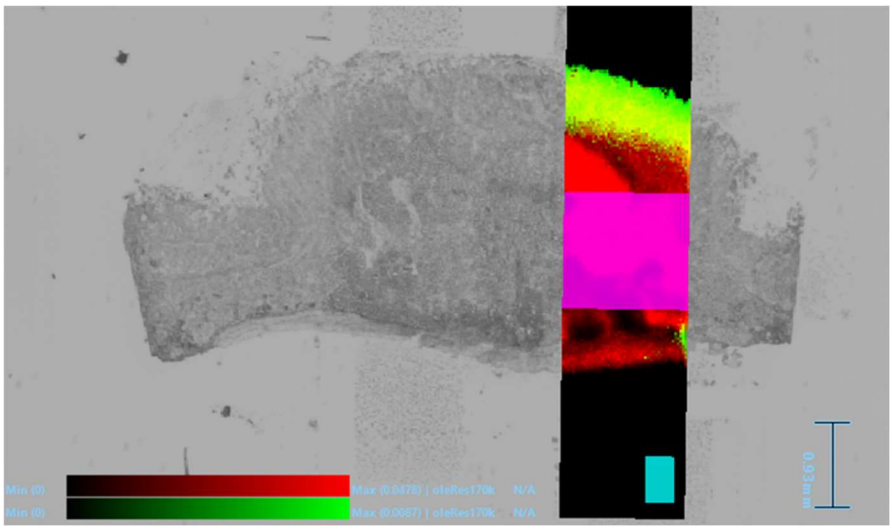

Appendix I Figure 19: *A DESI MSI image from a fresh tissue absorption experiment with 1% (v/v) DEGEE LQ in the donor circuit buffered to pH 6 (Polysorbate-80 & DEGEE LQ pH 6 study) from Figure 4.62 now annotated with ROIs. The specific ROIs "within tissue away from drug distribution" and "away from tissue" referred to in Table 4.10-4.11 for 1% (v/v) DEGEE LQ have been represented by the pink and blue shapes burned into the original DESI MSI image, respectively.*

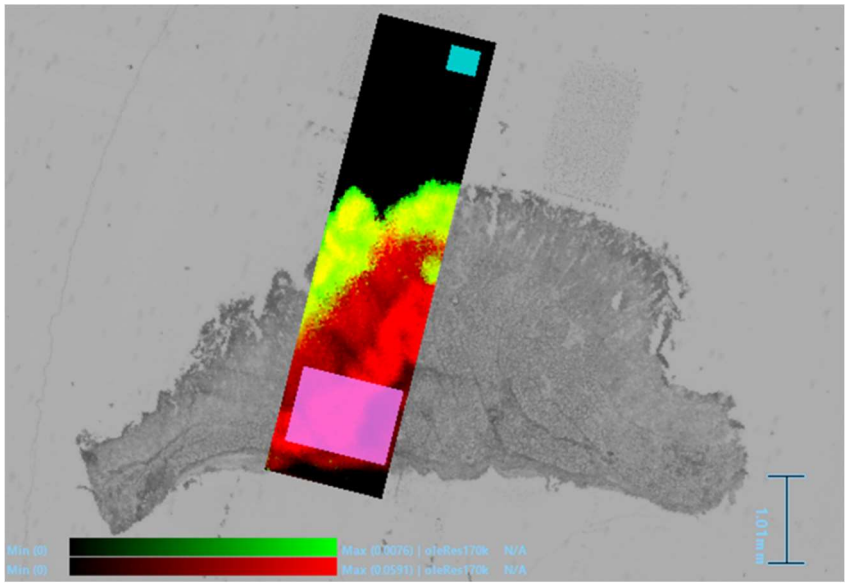

Appendix I Figure 20: *A DESI MSI image from a fresh tissue absorption experiment with 2% (v/v) DEGEE LQ in the donor circuit buffered to pH 6 (Polysorbate-80 & DEGEE LQ pH 6 study) from Figure 4.64 now annotated with ROIs. The specific ROIs "within tissue away from drug distribution" and "away from tissue" referred to in Table 4.10-4.11 for 2% (v/v) DEGEE LQ have been represented by the pink and blue shapes burned into the original DESI MSI image, respectively.*

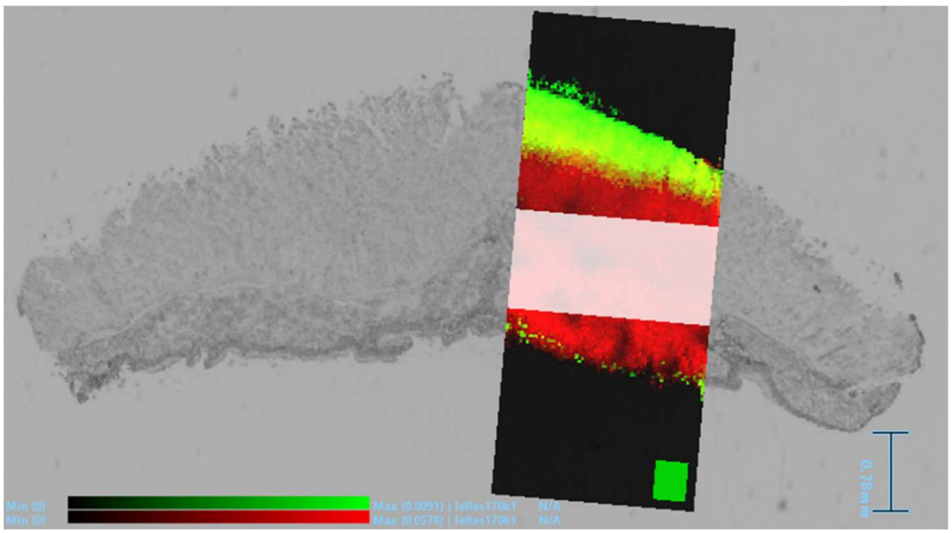

Appendix I Figure 21: *A DESI MSI image from a fresh tissue absorption experiment with no Mapcho-12 in the donor circuit buffered to pH 6 (Polysorbate-80 & Mapcho-12 pH 6 study) from Figure 4.76 now annotated with ROIs. The specific ROIs "within tissue away from drug distribution" and "away from tissue" referred to in Table 4.12-4.13 for 0 mM Mapcho-12 have been represented by the white and green shapes burned into the original DESI MSI image, respectively.*

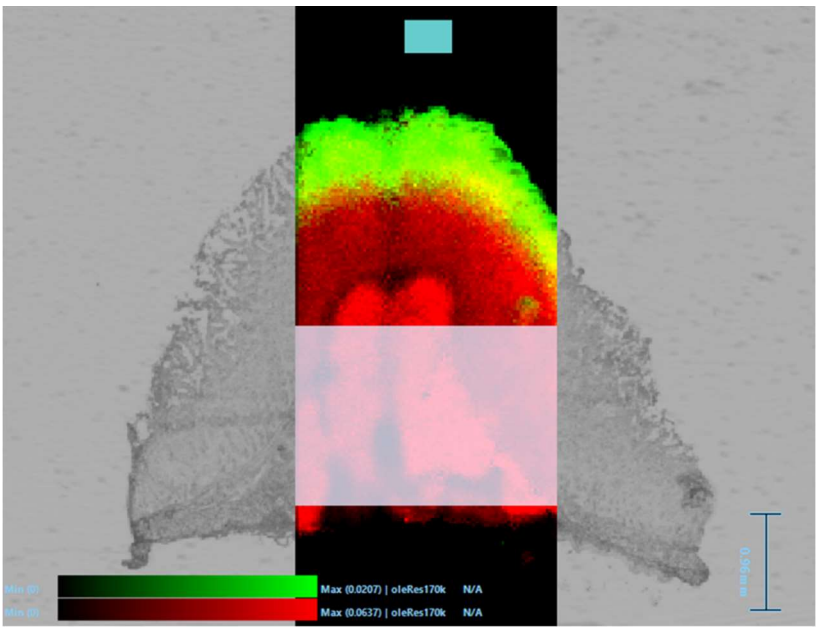

Appendix I Figure 22: *A DESI MSI image from a fresh tissue absorption experiment with 0.5mM Mapcho-12 in the donor circuit buffered to pH 6 (Polysorbate-80 & Mapcho-12 pH 6 study) from Figure 4.78 now annotated with ROIs. The specific ROIs "within tissue away from drug distribution" and "away from tissue" referred to in Table 4.12-4.13 for 0.5 mM Mapcho-12 have been represented by the white and blue shapes burned into the original DESI MSI image, respectively.*

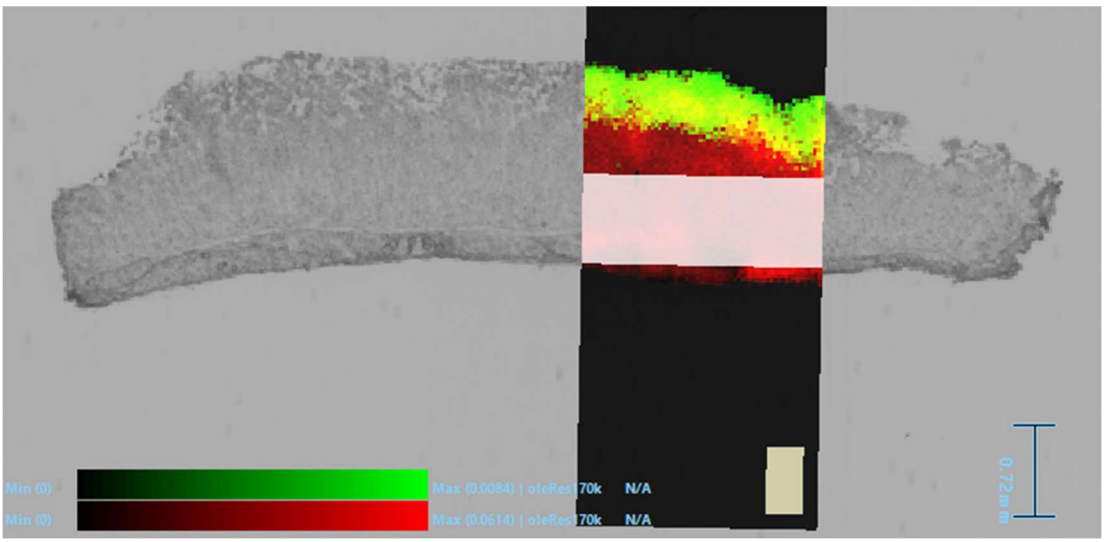

Appendix I Figure 23: *A DESI MSI image from a fresh tissue absorption experiment with 0.75 mM Mapcho-12 in the donor circuit buffered to pH 6 (Polysorbate-80 & Mapcho-12 pH 6 study) from Figure 4.80 now annotated with ROIs. The specific ROIs "within tissue away from drug distribution" and "away from tissue" referred to in Table 4.12-4.13 for 0.75 mM Mapcho-12 have been represented by the white and yellow shapes burned into the original DESI MSI image, respectively.*

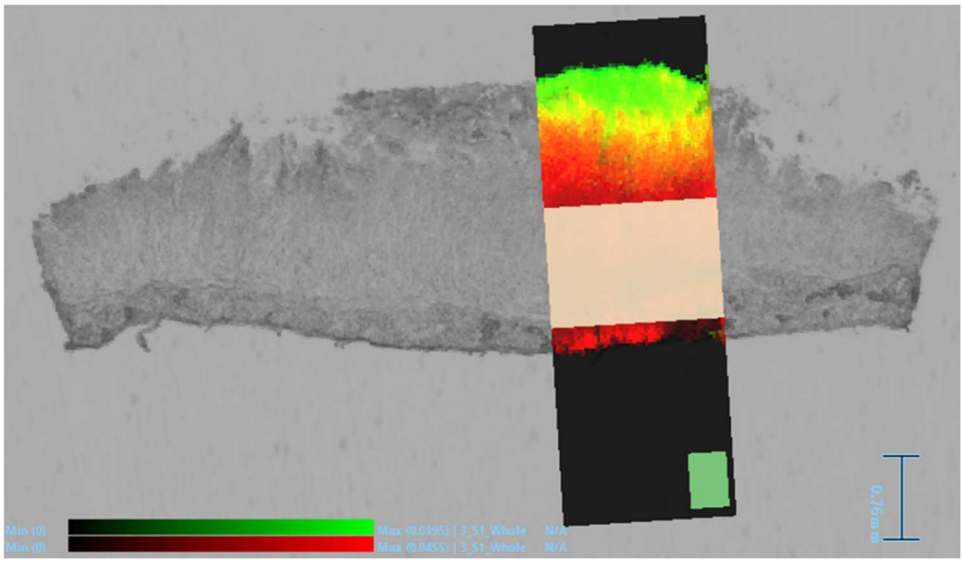

Appendix I Figure 24: *A DESI MSI image from a fresh tissue absorption experiment with 1 mM Mapcho-12 in the donor circuit buffered to pH 6 (Polysorbate-80 & Mapcho-12 pH 6 study) from Figure 4.82 now annotated with ROIs. The specific ROIs "within tissue away from drug distribution" and "away from tissue" referred to in Table 4.12-4.13 for 1 mM Mapcho-12 have been represented by the white and green shapes burned into the original DESI MSI image, respectively.*

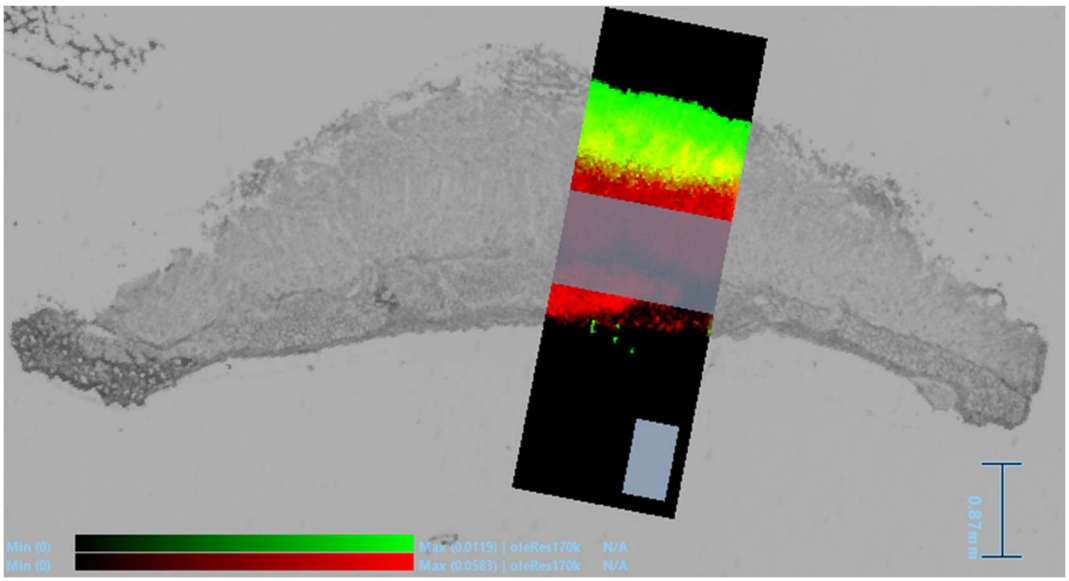

Appendix I Figure 25: *A DESI MSI image from a fresh tissue absorption experiment with 0.4% (v/v) Polysorbate-80 in the donor circuit buffered to pH 6 (Partial Mucus Removal pH 6 study) from Figure 4.93 now annotated with ROIs. The specific ROIs "within tissue away from drug distribution" and "away from tissue" referred to in Table 4.14-4.15 have been represented by the grey shapes burned into the original DESI MSI image.*